Ultrasensitive SERS detection of organophosphorus compounds via surface modified silver nanostructures

A thesis presented in partial fulfilment of the requirements for the degree of Master of Science in Chemistry

André Buzás Stowers-Hull

Supervisors: Professor Mark Waterland
Associate Professor Catherine Whitby
Associate Professor Gareth Rowlands

School of Natural Sciences,
Massey University, New Zealand

July, 2022

Acknowledgements

Thanks for Prof. Paul Plieger for supplying desks in his group's office area after our group was removed from our previous room.

Many thanks to my supervisor, Prof. Mark Waterland for being very supportive.

Abstract

The detection of target analytes with high specificity and sensitivity within fluids or on substrates is essential in many analytical applications. Surface-enhanced Raman spectroscopy (SERS) is a variation on vibrational Raman spectroscopy which uses plasmonic nanostructures or nanoparticles to amplify the Raman signal of various molecules via the formation of surface plasmons; concentrated areas of surface plasmons are known as 'hot spots,' often influenced by the morphology of the chosen nanostructure. SERS can be attractive because it can provide greatly improved sensitivity and selective identification of an analyte in a mixture without separation, despite having different selection rules to normal Raman scattering. A variation of this technique, the slippery liquid-infused porous substrate (SLIPS) method, has also been shown to increase SERS signal enhancement considerably, allowing the detection of certain compounds at even lower initial concentrations. SLIPS-SERS involves the use of a Teflon-based microporous filter coated with a polyfluorinated oil to dry a drop of nanoparticles to a single condensed spot, which increases the likelihood of hotspot interactions with analytes. Despite increasing the overall sensitivity of SERS, some analytes still pose a challenge in SLIPS-SERS. One way to overcome this is modifying the surfaces of chosen nanoparticles, in the case of this research, this is done with a thin outer layer of SiO_2 or TiO_2 (ideally less than 5 nm thick). This is known as Shell-isolated Nanoparticle Enhanced Raman Spectroscopy (SHINERS), which can increase sensitivity by another order of magnitude than normal SERS, decreases particle agglomeration and the oxidation of the plasmonic core. In this research, we combine known SERS techniques: SLIPS-SERS, SHINERS and utilizing various nanoparticle shapes to greatly increase the sensitivity and detection of organophosphorus compounds.

Contents

Acknowledgements **iii**

Abstract **v**

Contents **x**

List of tables **xi**

List of figures **xxiii**

1 Introduction **1**
1.1 Organophosphorus compounds in the environment 1
1.2 General overview of Raman Spectroscopy and Surface Enhanced Raman Spectroscopy (SERS) 2
1.2.1 Raman spectroscopy 2
1.2.2 The Quantum Description 9
1.2.3 Resonant states 10
1.2.4 Surface Plasmons 10
1.2.5 Surface Enhanced Raman Spectroscopy (SERS) 13
1.2.6 SERS selection rules 14
1.2.7 Electromagnetic and Chemical description of SERS 15
1.2.8 A brief Quantum description of SERS 16
1.2.9 Enhancing SERS: Slippery Liquid-infused Porous Surface Enhanced Raman Spectroscopy (SLIPSERS) 17
1.2.10 Enhancing SERS: Shell-isolated Nanoparticle Enhanced Raman Spectroscopy (SHINERS) 18
1.3 The Synthesis of Metallic Nanoparticles 20
1.3.1 Mechanisms of nanoparticle nucleation and growth 21
1.3.1.1 Nanoparticle Stability 26
1.3.2 The preparation of silver nanoparticles (AgNPs) 29
1.3.2.1 Inorganic reducing agents 29
1.3.2.2 Organic reducing agents 30
1.4 Applications of AgNPs for the detection of Organophosphorus compounds *via* SERS 30
1.4.1 Overcoming detection Issues 31
1.4.1.1 Detection *via* specificity 32

1.5 Combining non-specific methods: SHIN-SLIPSERS . . . 33
1.6 Analyte Selection . . . 33
1.6.1 Dyes . . . 33
1.6.2 Organophosphorus Compounds . . . 34
1.7 Project Hypotheses and Goals . . . 36

2 Experimental Methods 39
2.1 Silver nanospheres . . . 39
2.1.1 Ag@SiO_2 nanospheres . . . 39
2.1.2 Ag@SiO_2@Ag core-shell-satellite nanospheres . . . 40
2.2 Silver nanocubes . . . 41
2.3 Silver nanoparticle dispersion . . . 41
2.3.1 Ag@SiO_2 Silver nanoparticle dispersion . . . 41
2.4 Silver nanoprisms / triangular nanoplates . . . 42
2.4.1 Ag@SiO2 Nanoprisms . . . 43
2.5 Slippery Liquid Infused Porous Substrate (SLIPS) . . . 43
2.6 Raman spectroscopy . . . 44
2.6.1 SLIPS-SERS . . . 44
2.7 UV-vis Spectroscopy . . . 44
2.8 Electron microscopy . . . 45
2.9 Data Analysis via Python . . . 45

3 Results and Method Development 47
3.1 Identifying the LSPR peaks of the chosen nanoparticles *via* UV-vis spectroscopy . . . 47
3.2 Transmission Electron Microscopy . . . 50
3.3 Navigating through capping agents . . . 54
3.3.1 Trisodium Citrate . . . 54
3.3.2 Polyvinylpyrrolidone (PVP) . . . 59
3.4 Optimising nanoparticle concentrations . . . 61
3.5 Evaluating drying methods with Rhodamine 6G . . . 62
3.5.1 Glass . . . 62
3.5.2 Filter paper . . . 66
3.5.3 Cellulose acetate filter . . . 68
3.5.4 SLIPS . . . 72

4 SLIP-SERS Detection of Dyes 75
4.1 SLIPSERS Spectra . . . 75
4.1.1 Rhodamine 6G (R6G) . . . 75
4.1.1.1 'Yellow' and 'Yellow'@SiO2 Nanoparticles . . . 79
4.1.1.2 'Blue' Nanoprisms . . . 81
4.1.1.3 Nanocubes . . . 83
4.1.1.4 Spherical Nanoparticles . . . 84
4.1.1.5 Comparison of all nanoparticle types for R6G . . . 90
4.1.2 Ponceau 4R (P4R) . . . 91
4.1.2.1 'Yellow' and 'Yellow'@SiO2 Nanoparticles . . . 92

4.1.2.2 'Blue' Nanoprisms . . . 95
4.1.2.3 Nanocubes . . . 97
4.1.2.4 Spherical Nanoparticles . . . 98
4.1.2.5 Comparison of All Nanoparticle Types . . . 100
4.2 Linear Discriminant Analysis of the dye spectra . . . 103

5 SLIP-SERS Detection of Glyphosate 111
5.1 Raman spectrum . . . 111
5.2 SLIPSERS Spectra . . . 113
5.2.0.1 'Yellow' and 'Yellow'@SiO2 Nanoparticles . . . 117
5.2.0.2 'Blue' Nanoprisms . . . 120
5.2.0.3 Spherical Nanoparticles . . . 124
5.2.0.4 Nanocubes . . . 127
5.2.0.5 Comparison of All Nanoparticle Types . . . 128
5.3 Linear Discriminant Analysis of Glyphosate SLIPSERS spectra . . . 129

6 SLIP-SERS Detection of Diazinon 131
6.1 Raman spectrum . . . 131
6.2 SLIPSERS Spectra . . . 133
6.2.0.1 'Yellow' and 'Yellow'@SiO2 Nanoparticles . . . 136
6.2.0.2 'Blue' Nanoprisms . . . 139
6.2.0.3 Nanocubes . . . 141
6.2.0.4 Spherical Nanoparticles . . . 142
6.2.0.5 Comparison of All Nanoparticle Types . . . 145
6.3 Linear discriminant analysis and comparison of the diazinon and glyphosate SLIPSERS spectra . . . 147

7 Conclusions 153
7.1 Linear Discriminant Analysis of all of the collected SLIPSERS spectra 153
7.2 SLIPSERS detection of Dyes . . . 155
7.2.1 Efficacy of SHIN-SLIPSERS for the detection of dyes . . . 156
7.3 SLIPSERS detection of glyphosate . . . 156
7.3.1 Efficacy of SHIN-SLIPSERS for the detection of glyphosate . . . 157
7.4 SLIPSERS detection of diazinon . . . 157
7.4.1 Efficacy of SHIN-SLIPSERS for the detection of diazinon . . . 157
7.5 Future Work . . . 158

Bibliography 159

A Appendix 179
A.1 Miscellaneous Spectra . . . 179
A.1.1 Ponceau 4R . . . 179
A.1.2 Glyphosate . . . 179
A.1.3 Diazinon . . . 184
A.2 Nanoparticle Distributions . . . 188
A.2.1 All Analytes . . . 188

A.2.2 Dyes 189
A.2.3 Glyphosate 196
A.2.4 Diazinon 200
A.3 Tables 203

List of Tables

2.1 Summary of nanoparticle types used in this thesis, and the names they are referred to in graphs. 39

3.1 Summary table of the important Raman active modes in trisodium citrate for the experimentally collected Raman (532 nm), experimentally collected SERS (532 nm), and the literature values for Raman and SERS.[216] It is important to note that often in SERS spectra of organic compounds that the -CH2 stretching modes can broaden, often looking like one very strong, somewhat broad peak. Note: exper. is the experimental data and lit. is the literature values. 56

4.1 Summary table of the important Raman active modes found in the SERS spectra of R6G using literature values [217–219] and collected experimental SERS spectra of Rhodamine-6G (Fig.(4.5) using a 532 nm wavelength. 75

4.2 Summary table of key concentration Raman active modes in the literature values[220] and collected experimental SLIP-SERS spectra of P4R. Excitation wavelength: 532 nm. 92

5.1 Summary table of the important Raman active modes in the experimental and calculated spectra (B3LYP and B3LYP and 6-311++G(3d,2p) basis set. of glyphosate. Collected at 532 nm. 113

5.2 Summary table of the observed SERS modes present in the average of the three spectra containing excess glyphosate with silica capped nanoparticles compared with the experimental Raman spectra and calculated Raman spectra of glyphosate. Collected at 532 nm. 114

6.1 Summary of the observed modes for diazinon of the literature values for modes and the experimental Raman modes[221] collected in a 532 nm setup as described in Sec.(2.6). 131

6.2 Summary of the observed modes for diazinon in the experimental Raman modes for the standard Raman spectrum and SERS spectrum. 134

A.1 Table of modes common for each initial concentration of R6G for the silver nanocube substrate. 203

List of Figures

1.1 A Jablonski Diagram that shows the electronic (bold lines between the curve) and rotational/vibrational (thin lines between the curve) energy levels of a molecule. Potential transitions between states are shown by arrows, where dotted lines are for radiative (dipole-allowed) transitions and the solid lines are for non-radiative transitions. 4

1.2 (a) Diagram of Rayleigh and Raman scattering processes. (b) A typical Morse curve for an electronic state showing the fundamental tone levels for a single vibration and as horizontal tie lines which represent vibronic states. 6

1.3 Representation of how bond stretching in CS2 (S=C=S) changes with the polarizability α of the molecule, where q is the momentum change of the scattering event. When the sulfur atoms (yellow) are further apart from the carbon atom (grey), it will be easier for the electric field to move the electron clouds (the opposite being true when the sulfur atoms are closer to the carbon atom), and thus polarize the molecule. Polarizability, therefore, is an oscillatory behaviour that occurs with the molecular vibration. 7

1.4 Diagram showing the difference between longitudinal and transverse waves. Reused under CC-BY-2[38] 11

1.5 The potential orientations of diazinon from Section 1.6 and how it could interact with the surface plasmons when bonded to a silver nanoparticle 15

1.6 Figure showing SERS processes on a plasmonic nanoparticle at off resonance. Schematics of (a) the off-resonant SERS process in a plasmonic particle and a vibrating molecule and (b) the SERRS process, both depicted with their corresponding level structure. Image reused with permission from APS physics from the article by Neumann *et. al.*,[93] license number RNP/22/MAR/051922, the license can be found in the LaTeX folder for this thesis. 16

1.7 Simplified diagram showing the steps involved in creating a SLIPS sample. 18

1.8 Left: the general design of a SHIN, with a plasmonic core such as silver or gold; right: the thin SiO_2 or TiO_2 layer provides extra stability to the nanoparticle, and can minimise the amount of agglomeration, and prevent oxidation of the plasmonic core; bottom: provided the shell thickness is small enough, the distance between the core of an analyte can still enable the SERS effect to be taken advantage of as the surface plasmons are still able to interact with the molecule close to or absorbed to the surface of the SHIN. 19
1.9 Schematic plot of the free energy barrier (ΔG^*) of nucleation at constant temperature for homogeneous nucleation (green line) and heterogeneous nucleation (blue line). ΔG is the change in free energy in the respective conditions; the surface of growing seeds, or in the bulk phase. 23
1.10 Illustration showing the contact angle, θ for "germs" that form on surfaces of structural inhomogeneities. 25
1.11 LaMer model showing the process of nucleation and growth of nanoparticles and its growth stages.[157] 26
1.12 Structures of the chosen SERS dyes, Rhodamine-6G (a); and Ponceau 4R 34
1.13 Structures of the chosen organophosphorus compounds 35
1.14 Diagram showing the structure of glyphosate at different pKa values. 35
1.15 Summary table showing how pH affects silica at the same pKas of glyphosate 36

2.1 From left: nanoparticle solution of 2.3 after washing using method 2 to immediately after adding TEOS. 42
2.2 From left: silver nanoprisms after capping with SiO_2 shell, right: silver nanoprisms before addition of SiO_2. 43
2.3 (a) Drops of silver nanoparticles drying in the oven; (b) a spot of silver nanoparticles dried in an oven using the SLIPs method described above. 44

3.1 Overlay of washed nanoparticle dispersion (red line) compared to capped Ag@SiO2 (blue line), and a second attempt for silica capping (green). 47
3.2 UV-vis spectra of the silver prisms and the silica capped prisms used throughout this thesis. 48
3.3 UV-vis spectra of the silver nanocubes used throughout this thesis. A broad peak is seen at around 550 nm. 49
3.4 UV-Vis spectra overlaying Spheres (red), Stöber method capped $Ag@SiO_2$ spheres from method (blue) and the $Ag@SiO_2$-Ag satellites. 50
3.5 Transmission electron micrograph of the typical sample of the Silver dispersion ("yellow" nanoparticles); note the variation of shapes. . . . 50
3.6 (a) An isolated TEM image of a single nanoprism; (b) a different area of the TEM sample showing the variation of nanoparticles present in the silver nanoprism dispersion. 51
3.7 TEM micrograph of the Silver nanoprisms capped with silica, described in Section2.4.1 52

3.8 Transmission electron micrograph of the typical sample of silver nanocubes used in the SERS experiments. 53
3.9 Transmission electron micrograph of the typical sample of silver nanopsheres used in the SERS experiments. 53
3.10 A SLIPSERS spectrum of the "yellow" nanoparticle dispersion described in Section 2.3. 54
3.11 Raman spectra of trisodium citrate collected on a 532nm incident beam. 55
3.12 Raman spectra of trisodium citrate from 150 cm-1 to 1800 cm-1. Excitation wavelength: 532 nm. 56
3.13 SLIPSERS spectrum of citrate using silica capped silver nanoparticles. This was done by concentrating the nanoparticles as described in Sec.3.4, and using a concentration of 0.01 M of aqueous trisodium citrate, then doing the SLIPS method as described in Section 2.5. Excitation wavelength: 532 nm. 57
3.14 The Raman intensity change in an aqueous SERS spectrum of the peak at 1392 cm^{-1} after adding successive amounts of 100μL of 0.1 M NaCl solution. Excitation wavelength: 532 nm. 58
3.15 Raman spectrum of PVP (M_w = 40 000). Excitation wavelength: 532 nm. 59
3.16 PVP (40,000 Da, 0.1 M) SLIPSERS spectrum using the Ag@SiO_2 yellow nanoparticles. 60
3.17 Stacked SLIPSERS spectra showing the effect of five consecutive washes of the spherical nanoparticles made in Sec.2.1 using MilliQ water following an initial wash of acetone. Excitation wavelength: 532 nm. . 61
3.18 (a) Peak-fitted averaged SERS spectrum of R6G on glass; (b) Raw SERS data of R6G using the same drying method of (a). R6G at an initial concentration of 10^{-7} M. Excitation wavelength: 532 nm. . . . 63
3.19 The standard deviation of all the spectra collected using glass as the main substrate for the drying method. R6G at an initial concentration of 10^{-7} M. Excitation wavelength: 532 nm. 64
3.20 Histograms showing the distribution of intensities at given peaks for drying a sample on glass only, over 120 frames of data. (a) At 617 cm^{-1}; (b) at 1350 cm^{-1}; (c) at 1501 cm^{-1}; (d) at 1637 cm^{-1}. R6G at an initial concentration of 10^{-7} M. Excitation wavelength: 532 nm. . . . 65
3.21 (a) Peak-fitted averaged SERS spectrum of R6G using the Whatman Grade 4 filter paper as the drying substrate method ; (b) Raw SERS data of R6G using the same drying method of (a). R6G at an initial concentration of 10^{-7} M. Excitation wavelength: 532 nm. 66
3.22 The standard deviation of all the spectra collected for the R6G on the Whatman Grade 4 Qualitative Filter Papers drying method. Excitation wavelength: 532 nm. 67
3.23 Histograms showing the distribution of intensities at given peaks for drying on filter paper, over 120 frames of data. (a) At 617 cm^{-1}; (b) at 1350 cm^{-1}; (c) at 1501 cm^{-1}; (d) at 1637 cm^{-1}. R6G at an initial concentration of 10^{-7} M. Excitation wavelength: 532 nm. 68

3.24 (a) Averaged spectrum across 120 frames of the 'yellow' dispersion using the cellulose acetate drying method and R6G at an initial concentration of 10^{-7} M, (b) all 120 frames of the yellow dispersion using the cellulose acetate drying method (left), (right) averaged spectrum across 120 frames. Excitation wavelength: 532 nm. 69
3.25 The standard deviation of all the spectra collected using the cellulose acetate filter as the drying substrate method. Centre line is the averaged spectrum. Excitation wavelength: 532 nm. 70
3.26 Histograms showing the distribution of intensities at given peaks for drying on Cellulose Acetate filters with R6G at an initial concentration of 10^{-7} M, over 120 frames of data. (a) At 617 cm^{-1}; (b) at 1350 cm^{-1}; (c) at 1501 cm^{-1}; (d) at 1637 cm^{-1}. Excitation wavelength: 532 nm. . 71
3.27 (a) Peak-fitted averaged SERS spectrum of R6G using the SLIP as the drying substrate method ; (b) Raw SERS data of R6G using the same drying method of (a). R6G at an initial concentration of 10^{-7} M Excitation wavelength: 532 nm. 72
3.28 The standard deviation of all the spectra collected for the SLIPs drying method, R6G at an initial concentration of 10^{-7} M, excitation wavelength: 532 nm. 73
3.29 Histograms showing the distribution of intensities at given peaks prepared using the SLIPS method, over 120 frames of data. R6G at an initial concentration of 10^{-7} M. Excitation wavelength: 532 nm. . 74

4.1 A SLIP-SERS spectrum of Rhodamine 6G using the "yellow" nanoparticle substrate and 10^{-7} M initial concentration used as the "standard" spectrum. 76
4.2 A SLIP-SERS spectrum of Rhodamine 6G using the "yellow" nanoparticle substrate and at various concentrations. 77
4.3 Comparison of the intensity of the peak at 1500 cm^{-1} across all nanoparticle types. 78
4.4 Comparison of the intensity of the peak at 600 cm^{-1} across all nanoparticle types. 78
4.5 Stacked spectra showing the range of initial concentrations of R6G to evaluate the sensitivity of the 'yellow' nanoparticles. Excitation wavelength: 532 nm. 79
4.6 Stacked spectra showing the range of initial concentrations of R6G to evaluate the sensitivity of the yellow@SiO_2 nanoparticles. Note that the range of concentrations are larger in this graph because it appeared to be more sensitive - with possible R6G signals being observed from an initial concentration of 10^{-15} M. Excitation wavelength: 532 nm. . 81
4.7 Stacked spectra showing the range of initial concentrations of R6G to evaluate the sensitivity of the silver nanoprisms. Excitation wavelength: 532 nm. Excitation wavelength: 532 nm. 82

4.8 Stacked spectra showing the range of initial concentrations of R6G to evaluate the sensitivity of the blue@SiO_2 nanoparticles. Note that the 'dead' pixel at around 2592 cm-1 is exaggerated at the low signal-to-noise. Excitation wavelength: 532 nm. 83
4.9 Stacked spectra showing the range of initial concentrations of R6G to evaluate the sensitivity of the silver nanocubes. Excitation wavelength: 532 nm. 84
4.10 Stacked spectra showing the range of initial concentrations of R6G to evaluate the sensitivity of the spherical nanoparticles. Excitation wavelength: 532 nm. 85
4.11 Stacked spectra showing the range of initial concentrations of R6G to evaluate the sensitivity of the Spheres@SiO_2 nanoparticles. Excitation wavelength: 532 nm. 86
4.12 (a) The silica capped spherical nanoparticles at an initial concentration of 10^{-7} M, 10^{-11} M, 10^{-12} M R6G compared to the SERS standard using the silica capped yellow nanoparticles; (b) the silica capped spherical nanoparticles at an initial concentration of 10^{-9} M, 10^{-10} M, 10^{-10} M R6G compared to the SERS standard using the silica capped yellow nanoparticles and a spectra to show how the spectra are forming d/g bands (dotted line). Excitation wavelength: 532 nm. 87
4.13 Stacked spectra showing the range of initial concentrations of R6G to evaluate the sensitivity of the 'Spheres@SiO2-Sat' nanoparticles. Excitation wavelength: 532 nm. 88
4.14 (a) The silica capped spherical nanoparticles with Ag satellites at an initial concentration of, 10^{-9} M, 10^{-10} M R6G compared to the SERS standard using the silica capped yellow nanoparticles and a d/g band spectra. Excitation wavelength: 532 nm. (b) The silica capped spherical nanoparticles with Ag satellites at initial concentrations of 10^{-11} M, 10^{-12} M R6G compared to the SERS standard using the silica capped yellow nanoparticles and a d/g band spectra. Excitation wavelength: 532 nm. 89
4.15 Stacked SLIPSERS spectra for all nanoparticle types for Rhodamine 6G. Excitation wavelength: 532 nm. 90
4.16 SLIPSERS spectra of P4R and the "yellow" nanoparticle dispersion at an initial concentration of 10^{-7} M. Excitation wavelength: 532 nm. . 91
4.17 Stacked SLIPSERS spectra showing the initial concentration of added P4R in aqueous mixture (50μL) to 50μL of concentrated "yellow" nanoparticle dispersion. Arbitrary intensity. Excitation wavelength: 532 nm. 93
4.18 Zoomed in detail on the 'yellow' nanoparticle Raman spectra from Fig.(4.17), for the ranges 500-1900 cm^{-1}. Excitation wavelength: 532 nm. 94

4.19 Stacked SLIPSERS spectra showing the initial concentration of added P4R in aqueous mixture (50μL) to 50μL of concentrated "yellow@SiO_2" nanoparticle dispersion. Arbitrary intensity. Excitation wavelength: 532 nm. 95
4.20 Stacked SLIPSERS spectra showing the initial concentration of added P4R in aqueous mixture (50μL) to 50μL of concentrated "blue" nanoprisms. Arbitrary intensity. Excitation wavelength: 532 nm. 96
4.21 Using the silver nanoprisms capped with silica as a SERS substrate, stacked SLIPSERS spectra showing the initial concentration of added P4R in aqueous mixture (50μL) to 50μL of concentrated "blue@sio2" nanoprisms. Arbitrary intensity. Excitation wavelength: 532 nm. . . . 97
4.22 Using the silver nanocubes as a SERS substrate, stacked SLIPSERS spectra showing the initial concentration of added P4R in aqueous mixture (50μL) to 50μL of nanocubes. Arbitrary intensity. Excitation wavelength: 532 nm. 98
4.23 Stacked SLIPSERS spectra showing the initial concentration of added P4R in aqueous mixture (50μL) to 50μL of concentrated nanospheres. Arbitrary intensity. Excitation wavelength: 532 nm. 99
4.24 Stacked SLIPSERS spectra showing the initial concentration of added P4R in aqueous mixture (50μL) to 50μL of concentrated spheres@SiO_2. Arbitrary intensity. Excitation wavelength: 532 nm. 100
4.25 Stacked SLIPSERS spectra showing the initial concentration of added P4R in aqueous mixture (50μL) to 50μL of concentrated spheres@sio2 with Ag Satellites. Arbitrary intensity. Excitation wavelength: 532 nm. 101
4.26 Summary of selected SERS spectra based on their nanoparticle substrate type for P4R. Excitation wavelength: 532 nm. 102
4.27 Linear Discriminant Analysis of all of the P4R SLIPSERS spectra, organised by their nanoparticle type. 103
4.28 Linear Discriminant Analysis of all of the P4R SLIPSERS spectra which use SHINs as their substrate, organised by their nanoparticle type. 104
4.29 Linear Discriminant Analysis of all of the R6G SLIPSERS spectra, by their nanoparticle type. 105
4.30 Linear Discriminant Analysis of all of the R6G SLIPSERS spectra which use SHINs as their substrate, organised by their nanoparticle type. 106
4.31 Linear Discriminant Analysis comparing of all of the P4R and R6G SLIPSERS spectra, by the type of dye. 107
4.32 Linear Discriminant Analysis of all of the dye SLIPSERS spectra which use SHINs as their substrate, organised by their nanoparticle type. . . 108
4.33 Linear Discriminant Analysis of all of the dye SLIPSERS spectra which use SHINs as their substrate, organised by the analyte. 109

5.1 Peak labelled Raman spectra of a sample of PESTANAL analytical grade (99%) Glyphosate sandwiched between two cover slips. Collected at 532 nm. 111
5.2 Calculated Raman spectra of the glyphosate anion using B3LYP and 6-311++G(3d,2p) basis set. 112

5.3 Overlayed comparison of the calculated Raman spectra (B3LYP 6-311++G(3d,2p)) (orange) and the experimental Raman spectra (teal) collected at 532 nm. Frequencies are scaled. 112
5.4 Comparison of glyphosate calculated and experimental Raman spectra with SERS spectra containing an excess of glyphosate, and an average of the three collected spectra (top). Collected at 532 nm. 115
5.5 Averaged spectra of the three spectra collected of excess glyphosate with the yellow Ag@SiO_2 substrate. Collected at 532 nm. 116
5.6 Comparison of collected glyphosate SERS spectra and the average of these spectra with the calculated and experimental Raman spectra. Collected at 532 nm. 117
5.7 Stacked SERS spectra using the 'yellow' substrate over a range of initial concentrations of glyphosate. Collected at 532 nm. 118
5.8 Initial concentration dependence of glyphosate at 211, 733, 1576, and 2939 cm^{-1} for the 'yellow' substrate for the average spectra shown in Fig.(5.7). Collected at 532 nm. 119
5.9 Stacked SERS spectra using the Yellow@SiO_2 substrate over a range of initial concentrations of glyphosate. Collected at 532 nm. 120
5.10 Stacked SERS spectra using the 'blue' silver nanoprism substrate over a range of initial concentrations of glyphosate. Collected at 532 nm. . 121
5.11 Initial concentration dependence of glyphosate at 211 cm^{-1}, 733 cm^{-1}, 1576 cm^{-1}, and 2939 cm^{-1} for the 'blue' silver nanoprism substrate. . 122
5.12 Stacked SERS spectra using the Blue@SiO_2 nanoprism substrate over a range of initial concentrations of glyphosate. Collected at 532 nm. . 123
5.13 Stacked SERS spectra using the silver nanospheres substrate over a range of initial concentrations of glyphosate. Excitation wavelength: 532 nm. 124
5.14 Stacked SERS spectra of the the silica capped silver nanosphere substrate over a range of initial concentrations of glyphosate. Excitation wavelength: 532 nm. 126
5.15 Stacked SERS spectra using the silver nanocube substrate over a range of initial concentrations of glyphosate. Excitation wavelength: 532 nm. 127
5.16 Stacked SERS spectra the different silver substrates over a range of initial concentrations of glyphosate compared to the Raman spectrum. Excitation wavelength: 532 nm. 128
5.17 LDA plot of all of the glyphosate SLIPSERS spectra separated by the nanoparticle type. 129
5.18 Linear Discriminant Analysis of all of the glyphosate SLIPSERS spectra which use SHINs as their substrate, organised by their nanoparticle type. 130

6.1 A Raman spectrum of an analytical grade sample (Pestanal, 99%) of diazinon on a 532 nm incident beam, captured by using a small drop on a welled microscope slide. 132
6.2 The Raman spectra for Diazinon in the 150-1800 cm^{-1} range. 532 nm excitation wavelength. 133

6.3 The SERS spectrum for diazinon using an $Ag@SiO_2$ substrate and excess diazinon (about 0.01 M initial concentration). 135
6.4 The SERS spectrum of diazinon using an $Ag@SiO_2$ substrate and excess diazinon (about 0.01 M), in the range 150cm-1 to 1800cm-1. . 135
6.5 Stacked spectra comparing the Raman spectra of diazinon, a SERS spectra containing excess diazinon with the "yellow" nanoparticles, and SLIPSERS spectra collected at various initial concentrations of diazinon with silver nanoparticle dispersion ("yellow") as a SERS substrate. 137
6.6 Stacked spectra using the silica capped "yellow" nanoparticle dispersion, and comparing the Raman spectra of diazinon, a SERS spectra containing excess diazinon and various initial concentrations of diazinon. 138
6.7 Stacked spectra comparing the Raman spectra of diazinon, a standard SLIPSERS spectra containing excess diazinon and various initial concentrations of diazinon with silver nanoprisms as a SERS substrate. 140
6.8 Stacked spectra with the silica capped nanoprism substrate, comparing the Raman spectra of diazinon, a standard SLIPSERS spectra containing excess diazinon and various initial concentrations of diazinon with the silica capped prisms as the SERS substrate. 141
6.9 Stacked spectra with the nanocube substrate, comparing the Raman spectra of diazinon, a standard SLIPSERS spectrum containing excess diazinon and various initial concentrations of diazinon with the silver nanocubes as a SERS substrate. 142
6.10 Stacked spectra with the nanospheres substrate, compared with the Raman spectra of diazinon, a standard SLIPSERS spectra containing excess diazinon and various initial concentrations of diazinon with the nanospheres as the SERS substrate. Incident beam at 532 nm. 143
6.11 Stacked spectra with the nanospheres substrate, compared with the Raman spectra of diazinon, a standard SLIPSERS spectrum containing excess diazinon and various initial concentrations of diazinon with the nanospheres as the SERS substrate. Zoomed in to 250 cm^{-1} to 1800 cm^{-1}. Incident beam at 532 nm. 144
6.12 Stacked spectra with the silica capped nanospheres substrate, compared with the Raman spectra of diazinon, a standard SLIPSERS spectrum containing excess diazinon and various initial concentrations of diazinon with the silica capped nanospheres as the SERS substrate. Incident beam at 532 nm. 145
6.13 A comparison of all of the "best" SLIPSERS spectra of diazinon for each of the silver nanoparticle types, compared to the SERS standard and its Raman spectrum. As most of the variation between the spectra occurs at the 300 cm^{-1} to 1800 cm^{-1}, the rest of the wavenumbers will be omitted from this figure. 146
6.14 Linear Discriminant Analysis of all of the diazinon spectra according to the types of nanoparticles used. 147

6.15 Linear Discriminant Analysis of all of the diazinon SLIPSERS spectra which use SHINs as their substrate, organised by their nanoparticle type. 148
6.16 Linear Discriminant Analysis comparing all of the diazinon and glyphosate spectra. 149
6.17 Linear Discriminant Analysis of all of the diazinon and glyphosate SLIPSERS spectra which use SHINs as their substrate, organised by their nanoparticle type. 150
6.18 Linear Discriminant Analysis of all of the diazinon and glyphosate SLIPSERS spectra which use SHINs as their substrate, organised by their analyte type. 151

7.1 Linear Discriminant Analysis of all of the SLIPSERS spectra according to the analytes in the sample. 154
7.2 Linear Discriminant Analysis of all of the SLIPSERS spectra according to the types of nanoparticle substrates in the sample. 155

A.1 Ponceau-4R absorbed onto the silica capped silver nanosphere substrate with silver nanosphere satellites at an initial concentration of 10^{-9} M. Excitation wavelength: 532 nm. 179
A.2 Glyphosate absorbed onto the silica capped silver nanoparticle dispersion "yellow" substrate satellites at an initial concentration of 10^{-3} M. Excitation wavelength: 532 nm. 180
A.3 Glyphosate absorbed onto the silica capped silver nanoparticle dispersion "yellow" substrate satellites at an initial concentration of 10^{-10} M. Excitation wavelength: 532 nm. 180
A.4 Glyphosate absorbed onto the silica capped silver nanoparticle dispersion "yellow" substrate satellites at an initial concentration of 10^{-9} M. Excitation wavelength: 532 nm. 181
A.5 Glyphosate absorbed onto the silica capped silver nanosphere substrate satellites at an initial concentration of 10^{-10} M. Excitation wavelength: 532 nm. 181
A.6 Glyphosate absorbed onto the silver nanospheres substrate at an initial concentration of 10^{-6} M. Excitation wavelength: 532 nm. 182
A.7 Glyphosate absorbed onto the silver nanospheres substrate at an initial concentration of 10^{-11} M. Excitation wavelength: 532 nm. 182
A.8 Glyphosate absorbed onto the silica capped silver nanospheres substrate at an initial concentration of 10^{-10} M. Excitation wavelength: 532 nm. 183
A.9 Glyphosate absorbed onto the silver nanocube substrate at an initial concentration of 10^{-10} M. Excitation wavelength: 532 nm. 183
A.10 A Raman spectrum of diazinon on a 532 nm incident beam, captured by using a small drop on a microcope slide. 184
A.11 Diazinon absorbed onto a "yellow" substrate at an initial concentration of 10^{-9} M. Excitation wavelength: 532 nm. 185
A.12 Diazinon absorbed onto the silver nanoprism substrate at an initial concentration of 10^{-10} M. Excitation wavelength: 532 nm. 186

A.13 Diazinon absorbed onto the silver nanocube substrate at an initial concentration of 10^{-10} M. Excitation wavelength: 532 nm. 187
A.14 Loadings plot of the SLIPSERS spectra for all analytes for each of the principle components. 188
A.15 For the all of the spectra, a scattermatrix plot with distribution curves and scatterplots showing the distribution of spectra by the nanoparticle type using their principle components 189
A.16 For the all of the spectra, a collection of PCA scattermatrix plots with distribution curves and scatterplots showing the distribution of spectra by the analyte type by the first five principle components. 190
A.17 For the all of the SLIPSERS spectra containing SHINs as nanoparticles, and all of the analytes a collection of loadings plots for principle components 1-5 showing which modes contribute more variation between the samples. 191
A.18 For the all of the R6G spectra, a collection of PCA scattermatrix plots with distribution curves and scatterplots showing the distribution of spectra by the nanoparticle type by the first five principle components. 192
A.19 For the all of the P4R spectra, a collection of PCA scattermatrix plots with distribution curves and scatterplots showing the distribution of spectra by the nanoparticle type by the first five principle components. 193
A.20 For the R6G, a scattermatrix plot with distribution curves and scatterplots showing the distribution of spectra by the analyte type using their principle components. 194
A.21 For the all of the SLIPSERS spectra containing SHINs as nanoparticles, and all of the dyes as analytes, a collection of loadings plots for principle components 1-5 showing which modes contribute more variation between the samples. 195
A.22 Loadings plot of principle components 1 to 6 for all glyphosate spectra. 196
A.23 For the glyphosate spectra, a scattermatrix plot with distribution curves and scatterplots showing the distribution of spectra by the nanoparticle type using their principle components 197
A.24 For the glyphosate spectra, a scattermatrix plot with distribution curves and scatterplots showing the distribution of spectra by the analyte type using their principle components. 198
A.25 For the all of the SLIPSERS spectra containing SHINs as nanoparticles and glyphosate and diazinon as analytes, a collection of loadings plots for each principle component show which modes contribute more variation between the samples. 199
A.26 Loadings plot of the SLIPSERS of diazinon for each of the principle components. 200
A.27 For the diazinon spectra, a scattermatrix plot with distribution curves and scatterplots showing the distribution of spectra by the nanoparticle type using their principle components. 201

A.28 For the diazinon spectra, a scattermatrix plot with distribution curves and scatterplots showing the distribution of spectra by the analyte type using their principle components. 202

1. Introduction

1.1 Organophosphorus compounds in the environment

Organophosphorus compounds (also known as phosphate esters), have a general formula of $O{=}P(OR)_3$, and find themselves in use as an additive to flame retardants,[1–3] and as nerve agents.[4] As flame retardants, they have found more common usage since the ban on brominated flame retardants (BFRs) in the USA and New Zealand in 2004, and in the EU in 2006. As a result, organophosphate flame retardants (OPFRs) have been found in waster water or housing materials around the world,[5] such as China,[6] the USA,[7] and New Zealand.[8] In addition, organophosphorus compounds have found widespread use in the agricultural industry as they are effective at pest control. In New Zealand, several pests have even developed resistance towards organophosphorus pesticides, such as several species of blowfly[9–11] A good case study in New Zealand, is the Lightbrown apple moth, *Epiphyas postivittana*, populations in orchards in the country during the 1960s through to the late 1980s had developed resistance to organophosphate and carbamate insecticides.[12–15] The pest problem of this moth was only solved by discontinuing the use of organophosphorus insecticides in the orchards, biological control[15] and introducing existing native natural enemies into the orchards;[16, 17] today the moth is controlled successfully by the use of Integrated Pest Management (IPM). The importance of detecting these compounds is therefore obvious: due to their widespread use, it is important to monitor their environmental levels because of their effect on local ecologies, such as effects on bee populations,[18–20], and the potential human health impacts.[21–23] However, methods that are used quite often such as GC-MS, LC-MS and HPLC are time consuming.[24–30] Other methods, such as ultrasensitive biosensors[31, 32], enzymatic electrochemical biosensors,[24, 33], and fluorescence sensors[34] are otherwise high cost and/or immobile. Thus the need to develop low-cost, portable (for potential use in the field or onsite location-by-location data collection), ultra-sensitive, rapid methods for the detection of organophosphorus compounds provides the motivation for this research thesis. However, SERS methods are not necessarily applicable to every organophosphorus compound. This is because SERS sensitivity is affected by factors such as: the power of the incident laser beam, the kind of nanoparticle, the homogeneity of the nanoparticle, the chosen analyte and its binding affinity, and the concentration of the nanoparticle, and the concentration of the analyte. Surface binding, in particular, is dependent on the features of the nanoparticle and the analyte's affinity for the nanoparticle substrate. What

is expected is that the surface chemistry of the nanoparticle plays a key role in the binding of the substrate and that the nanoparticle resonance is just as important. Therefore, the main goal of this research is to develop and optimise a SERS system for the detection of selected organophosphorus compounds (in Sec.1.6).

1.2 General overview of Raman Spectroscopy and Surface Enhanced Raman Spectroscopy (SERS)

Vibrational spectroscopies, mainly Infrared (IR) and Raman spectroscopies are dependent on infrared absorption and Raman scattering, respectively. These techniques are used to provide information on chemical structure and physical forms, based on so-called "fingerprints" in their recorded spectra. In addition, this information can be used to semi-quantitatively or quantitatively determine the amount of a certain substance in a sample – whether they are in solid, liquid, or gaseous form. A given sample to be analysed can vary in temperature, exist in bulk, crystalline, as microscopic particles or as surface layers. Both Raman and mid-IR spectroscopy are complementary techniques and usually, both are required to completely measure the vibrational modes of a molecule. Although some vibrations may be active in both Raman and IR. In general, Raman spectroscopy is best at the detection of symmetric vibrations of non-polar groups while IR spectroscopy is best at the detection of asymmetric vibrations of polar groups. Raman spectroscopy utilises a single wavelength of radiation to irradiate the sample, which is then scattered from the molecule, one vibrational unit of energy different from the incident beam. This event occurs roughly one in every million photons. Of the large body of work surrounding Raman spectroscopy, Surface-Enhanced Raman Spectroscopy (SERS) now makes up a large portion of the literature.

1.2.1 Raman spectroscopy

Unlike IR spectroscopy, the Raman scattering process utilises a single wavelength of incident radiation, which is then scattered off the sample. The Raman is by all accounts, an inelastic scattering process. This scattering process results in a distortion (polarization) of the cloud of electrons around the nuclei of a molecule, causing it to form a virtual state, which is short-lived, and the photon is re-radiated. In this thesis, the Fergie (IsoPlane 81) detector detects these re-radiated photons via its fast-response time Charge Coupled Device (CCD) detector, where each wavelength detected is captured in an 'image' of 1024 x 256 pixels (much like a digital camera the spectra can be considered to be made of 'pixels'). These pixels, or 1024 wavenumbers per spectra, make up the observed spectra, which is collected over a certain amount of exposure time (multiple exposures are common to detect SERS events). In cases where nuclear motion is induced, energy can either be transferred from the incident photon or from the molecule to the scattered photon - this is regarded as inelastic scattering. Inelastic scattering of radiation in this manner is known as Raman scattering, which is an inherently weak process (occurring in about one in every 10^6 to 10^8 photon that

is scattered. In a Raman scattering process, the incident photon ($E_i = E_{\text{laser}}$) and momentum ($p_i = p_{\text{laser}}$) scatters to produce E_s (energy of scattered photon) and p_s (momentum of scattered photon). We get Eqn. 1.1:

$$E_s = E_i \pm E_q \text{ and } p_s = p_i \pm q \tag{1.1}$$

Where E_q and q are the energy and momentum changes during a scattering event. Two key vibrations in Raman spectroscopy are *normal modes* and *phonons*. The normal modes are vibrations within a system (such as an extended solid material or a molecule), where the atoms are vibrating at the same frequency and phase of the incident beam. Phonons are a subset of the normal modes; as they are normal modes which involve the displacement of atoms within unit cells over a crystalline solid. Normal modes are key to understanding the Raman spectra, as each normal mode within a molecule occurs due to the electrons following the incoming electric field, changing the polarizability of the molecule, and the displacement of these electrons is what drives the vibration. In comparison, in an IR vibration, instead of the polarizability of the molecule changing, the electron cloud shifts and forms a dipole, resulting in the observed IR vibrational modes. In non-linear molecules, their degrees of freedom have a $3N - 6$ dependence, whereas a linear molecule has a $3N - 5$ degrees of freedom dependence.

To simplify matters, when in the presence of no external field, the molecular energy has no dependence on its orientation in space. Thus its potential energy is made up only of its vibration degrees of freedom. This potential energy difference (in a harmonic oscillator) is given by:

$$\begin{aligned} \Delta V &= V(q_1, q_2, q_3, ..., q_n) - V(0, 0, 0, ..., 0) \\ &= \frac{1}{2} \sum_{i=1}^{N_{vib}} \sum_{j=1}^{N_{vib}} \left(\frac{\delta^2 V}{\delta q_i \delta q_j} \right) q_i q_j \\ &= \frac{1}{2} \sum_{i=1}^{N_{vib}} \sum_{j=1}^{N_{vib}} f_{ij} q_i q_j \end{aligned} \tag{1.2}$$

Where q represents the equilibrium displacement; and N_{vib} is the number of vibrational degrees of freedom. For simplicity, the anharmonic terms are ignored in this equation. Classical mechanics determines that the cross terms can be eliminated from Eq.(1.2), matrix algebra then reveals a new set of coordinates Q_j is revealed:

$$\Delta V = \frac{1}{2} \sum_{j=1}^{N_{vib}} F_j Q_j^2 \tag{1.3}$$

This new equation shows no cross terms (so the energy does not get transferred to other modes), however, these coordinates, Q, are normal modes (or normal coordinates). With Eq.(1.3), we can then get the Hamiltonian operator for the vibrations:

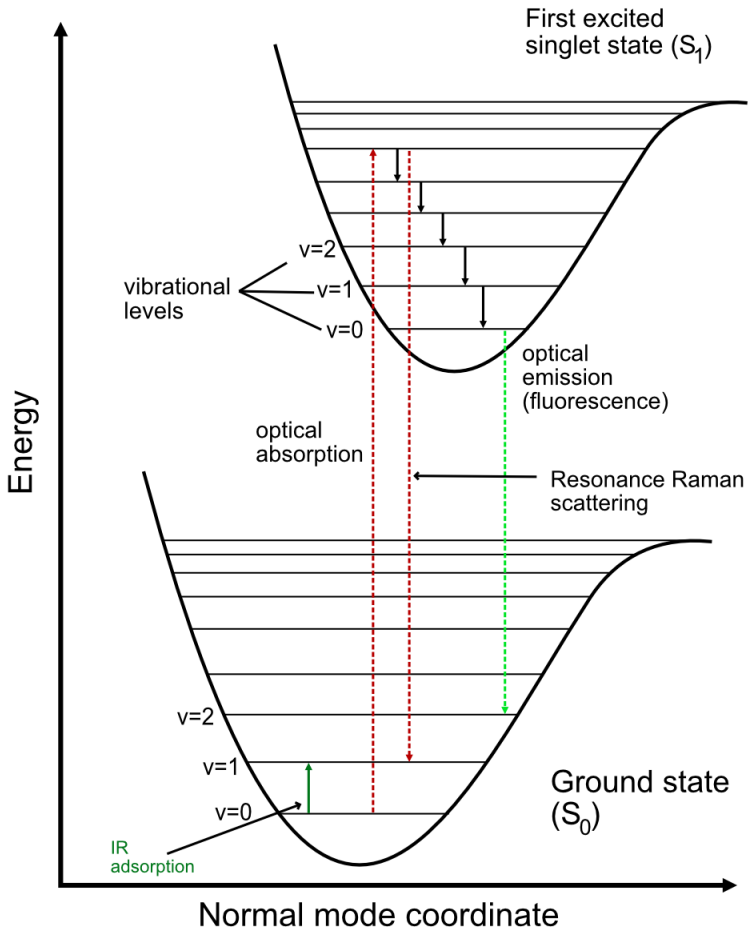

Figure 1.1: A Jablonski Diagram that shows the electronic (bold lines between the curve) and rotational/vibrational (thin lines between the curve) energy levels of a molecule. Potential transitions between states are shown by arrows, where dotted lines are for radiative (dipole-allowed) transitions and the solid lines are for non-radiative transitions.

$$\hat{H}_{vib} = -\sum_{j=1}^{N_{vib}} \frac{\hbar^2}{2\mu_i} \frac{d^2}{dQ_j^2} + \frac{1}{2} \sum_{j=1}^{N_{vib}} F_j Q_j^2 \tag{1.4}$$

The total wavefunction is a product of the individual wavefunctions and the energy is the sum of independent energies. This leads to:

$$\hat{H}_{vib} = \sum_{j=1}^{N_{vib}} = \sum_{j=1}^{N_{vib}} \left(\frac{-\hbar^2}{2\mu_j} \frac{d^2}{dQ_i^2} + \frac{1}{2} \sum_{j=1}^{N_{vib}} F_j Q_j^2 \right) \tag{1.5}$$

The total vibrational energy of a molecule is therefore given by the sum of all of the vibrational modes within a molecule:

$$E_{vib} = \sum_{j=1}^{N_{vib}} hv_j \left(v_j + \frac{1}{2} \right) \tag{1.6}$$

Where $v_j = 0, 1, 2, ...$etc.. N_{vib}, therefore, is the number of harmonic oscillations occurring that correspond to the number of vibrational modes present in the molecule. At the ground vibrational state (m), the energy of the molecule is $(1/2)hv_j$, this is often referred to as the zero point energy. Vibrational transitions, as seen in Fig.(1.1), are induced when it absorbs a quanta of energy according to $E = hv$, where the first excited state ($v_j = 1$), is separated from the ground state by $E_{vib} = (3/2)hv$, and the next ($v_j = 2$) is $(5/2)hv$ and so on. Whilst the harmonic approximation can be sufficient, a better approximation is the Morse potential (see Fig.(1.1)), which takes into the anharmonicity where the energy levels become closer together at higher energies, and bond dissociation at very high vibrational energies. There are two types of Raman scattering, dependent on the initial state of the molecule. In general, an anti-Stokes process is one in which a photon scattering off a molecule has higher energy than the incident photon, thereby leaving the molecule in a lower vibrational energy state (Fig.(1.2a), $n \rightarrow m$). Conversely, a Raman Stokes process is one in which the Raman scattering process results in a molecule going to a higher energy state than it started with, and the scattered photon having less energy than the incident photon (Fig.(1.2a), $m \rightarrow n$). Therefore, experiments that are done at room temperature, will result in the majority of Raman scattering to be Stokes Raman scattering. The ratio of Stokes and anti-Stokes scattering present can be calculated from the Boltzmann equation (Eqn. 1.7):

$$\frac{N_n}{N_m} = \frac{g_n}{g_m} exp \left[\frac{-(E_n - E_m)}{kT} \right] \tag{1.7}$$

N_n is the number of molecules at the excited vibrational energy level (n)
N_m is the number of molecules at the ground vibrational energy level (m)
g is the degeneracy in of m and n.
$E_n - E_m$ is the difference in energy between the vibrational energy levels
k is the Boltzmann constant

For a given molecule, it consists of a series of electronic states that contain both vibrational and rotational states. In Fig. 1.2b where the y-axis represents energy, x-axis represents internuclear distance, the curved line represents a single vibration, where $v = 0$ is the ground state, and $v = 1$ is the first excited state, and so on. The curved line represents an energy electronic state that shows that at large internuclear separation atoms are essentially free. However, as the internuclear distance decreases, they are then attracted to each other to form a bond, but if the atoms approach too closely, they repel each other (shown by the steep rise in energy). The bond length is therefore represented by the lowest point in the curved line. Within the curve, the tie lines represent a quantized vibrational state, also referred to as a vibronic state of a specific electronic state. As this line represents a single vibration, one quantum

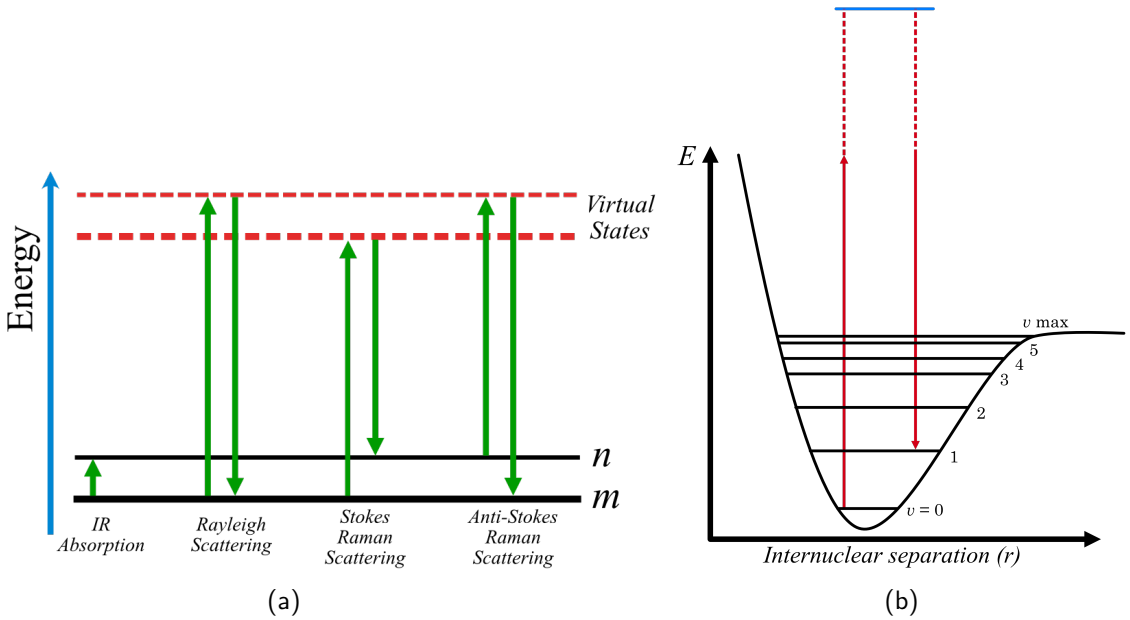

Figure 1.2: (a) Diagram of Rayleigh and Raman scattering processes. (b) A typical Morse curve for an electronic state showing the fundamental tone levels for a single vibration and as horizontal tie lines which represent vibronic states.

of absorbed energy can cause the molecule to vibrate, for example: $v = 0 \rightarrow v = 1$. The anharmonic shape of the Morse curve means that it is somewhat complex to calculate the energy of vibronic levels (which becomes important in computational calculations of Raman spectra), so it is replaced with a parabolic curve (harmonic) that considers the molecule as a mass attached to a spring, giving Hooke's law, showing the relationship between frequency, mass, vibration and the bond strength:

$$\tilde{v} = \frac{1}{2\pi c}\sqrt{\frac{K}{\mu}} \tag{1.8}$$

where c is the velocity of light, K is the force constant of the bond between atom A and atom B, μ is the reduced mass of atoms A and B of masses M_A and M_B:

$$\mu = \frac{M_A M_B}{M_A + M_B} \tag{1.9}$$

The simplified nature of Hooke's Law means that it is much easier to understand the approximate order of energies of specific vibrations - lighter atoms and stronger bonds mean higher frequencies. For example, C-H vibrations lie around 3000 cm^{-1} for aliphatic and aromatic systems, whereas C-I vibrations lie at around 500 cm^{-1} and the -C=C- stretch will be in higher energy than the -C-C- stretch. However - the harmonic approximation means that the overtones of a molecule will be equally spaced, but in a real system (which is closer to an anharmonic system) the energy separation between levels will decrease as shown in Fig. 1.2b. The change in polarizability (α) where one quantum unit change is possible ($\Delta\omega = \pm 1$) plays an important role in determining the observed Raman signals - this is the basic selection rule of Raman scattering. If

a vibration has the same symmetry species as the translational vectors, it will be IR active; while if it is the same as the quadratic functions, it will be Raman active. $\Delta\omega = \pm 1$ applies to both Raman scattering and IR absorption.

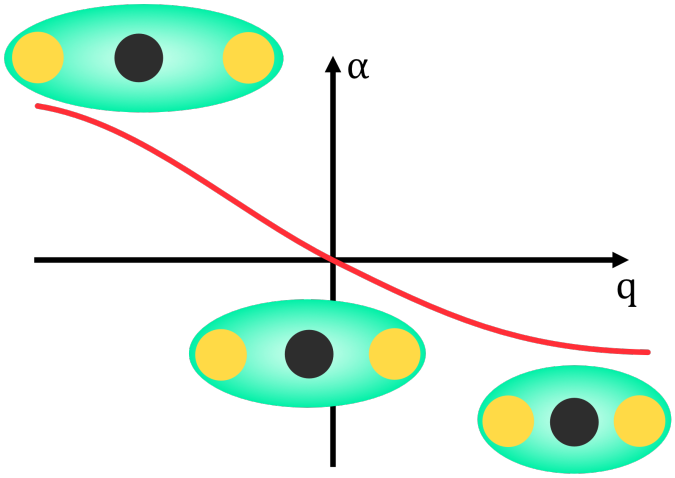

Figure 1.3: Representation of how bond stretching in CS2 (S=C=S) changes with the polarizability α of the molecule, where q is the momentum change of the scattering event. When the sulfur atoms (yellow) are further apart from the carbon atom (grey), it will be easier for the electric field to move the electron clouds (the opposite being true when the sulfur atoms are closer to the carbon atom), and thus polarize the molecule. Polarizability, therefore, is an oscillatory behaviour that occurs with the molecular vibration.

Classically, Raman scattering can be described as an electromagnetic wave that fluctuates with time. The electric field strength (E) of this event is given in the equation below:

$$E = E_0 \cos 2\pi v_0 t \tag{1.10}$$

Where E_0 is the amplitude of the electric field, and v_0 is the frequency of the laser. An electric dipole moment (P) is induced when a diatomic molecule is exposed to the incident laser, giving:

$$p = \alpha E_{\text{local}} = \alpha E_0 \cos 2\pi v_0 t \tag{1.11}$$

In Eqn. (1.11) α is a proportionality constant called *polarizability*. When a molecule vibrates with a frequency v_m, atoms are displaced (for example in Fig. 1.3), and the nuclear displacement of this vibration is given by q:

$$q = q_0 \cos 2\pi v_m t \tag{1.12}$$

Where q_0 is the vibrational amplitude. In smaller amplitudes, α is a linear function of q, which means it becomes:

$$\alpha = \alpha_0 + \left(\frac{\delta\alpha}{\delta q}\right)_0 q_0 + ... \tag{1.13}$$

In Eqn. (1.13), α_0 is the polarizability at the equilibrium position, and $(\delta\alpha/\delta q)_0$ is the rate of change of α with respect to the change in nuclear displacement, q at the equilibrium position. As polarization α is an atomic property, and the dielectric constant ϵ of a material is dependent on arrangement of atoms, Equations (1.11), (1.12), and (1.13) can be combined to give the full classical description of the electric dipole moment:

$$\begin{aligned}
\mathbf{P} &= \alpha E_0 \cos 2\pi v_0 t \\
&= \alpha E_0 \cos 2\pi v_0 t + \left(\frac{\delta\alpha}{\delta q}\right)_0 \alpha E_0 \cos 2\pi v_0 t \\
&= \alpha E_0 \cos 2\pi v_0 t + \left(\frac{\delta\alpha}{\delta q}\right)_0 \alpha E_0 \cos 2\pi v_0 t \cos 2\pi v_m t \\
&= \alpha E_0 \cos 2\pi v_0 t + \frac{1}{2}\left(\frac{\delta\alpha}{\delta q}\right)_0 E_0[\cos 2\pi(v_0 + v_m)t + \cos 2\pi(v_0 - v_m)t]
\end{aligned} \tag{1.14}$$

From Eq. 1.14 we can see that light will be scattered elastically and inelastically. Rayleigh scattering, a type of elastic scattering of light occurs at frequency v_0, shown by the first term. The second term however shows that light can be scattered inelastically (Raman scattering). The Raman scattering process is given by the frequency $v_0 + v_m$ (Stokes scattering) and $v_0 - v_m$ (anti-Stokes scattering), this is represented graphically in Fig. (1.2a). If $(\delta\alpha/\delta q)_0$ is zero, the vibration is not Raman active. Stokes and anti-Stokes processes are very important in the Raman scattering process - where an incident photon decreases or increases its energy by creating (Stokes) or destroying (anti-Stokes) a phonon excitation in the sample. This is shown simply in Eqn. (1.1) and inside the parenthesis in Eqn. (1.14) by the plus-minus signs, which applies when the energy has been transferred to the medium excited by the Raman signal. The probability of the Stokes and anti-Stokes processes from happening can be found based on the energy of the incident photon E_i, scattered photon energy E_s and the temperature. This probability is given by the Bose-Einstein distribution function:

$$n = \frac{1}{\exp(E_q/k_B T) - 1} \tag{1.15}$$

where:
n is the average number of phonons
E_q is phonon energy
k_B is the Boltzmann constant
T is the temperature.

The probability of the Stokes and anti-Stokes processes is different because of the

way the phonons are affected. In the Stokes process, phonons go from n phonons to $n+1$ phonons, whilst the anti-Stokes process results in the opposite. The intensity ratio of these processes is given by:

$$\frac{I_S}{I_{aS}} \propto \frac{n+1}{n} = \exp(E_q/k_B T) \tag{1.16}$$

Where I_S and I_{aS} are the intensity of the Raman Stokes and anti-Stokes peaks.

1.2.2 The Quantum Description

In the previous section, it was established that Raman scattering processes are practically instantaneous, so a virtual state is created to conceptualise the process whereby Raman scattering occurs. However, in Resonance Raman scattering, where the incident laser wavelength corresponds to an electronic transition in say, a target molecule, an actual state exists - an electronic or a vibronic state, given by $|r\rangle$. The key to understanding the underlying quantum theory behind Raman spectroscopy as a whole relies on understanding the quantum description of polarizability and Raman resonance. Previously, polarizability was described classically in Eqn. (1.11) also with CS_2 in Fig. 1.3 as an example. In a Raman transition between states $i, |i\rangle$ (initial state), and $f, |f\rangle$ (final state), the intensity of the scattered light perpendicular to the incident beam is given by the equation:

$$I_{fi}(\pi/2) = \frac{\pi^2}{\varepsilon_0^2}(\bar{v}_0 \pm \bar{v}_{fi})^4 \mathcal{I}_0 \sum_{\rho,\sigma} [\alpha_{\rho\sigma}]_{fi} [\alpha_{\rho\sigma}]^*_{fi} \tag{1.17}$$

For a transition between two states $i, |i\rangle$ (initial state), and $f, |f\rangle$ (final state), in a scattering system, the polarizability tensor for the transition is given by the equation:[35]

$$[\alpha_{\rho\sigma}]_{fi} = \frac{1}{hc} \sum_r \left[\frac{[\mu_\rho]_{fr}[\mu_\sigma]_{ri}}{\tilde{v}_{ri} - \tilde{v}_0 + i\Gamma_r} + \frac{[\mu_\sigma]_{fr}[\mu_\rho]_{ri}}{\tilde{v}_{rf} + \tilde{v}_0 - i\Gamma_r} \right] \tag{1.18}$$

Where, $[\mu_\rho]_{fr}$ is the ρth component of the transition dipole moment that is related to the $|f\rangle \leftarrow |r\rangle$ ($|r\rangle$ being an intermediate state).

$$[\alpha_{\rho\sigma}]_{gn,gm} = \frac{1}{hc} \sum_{ev} \left(\frac{\langle n|[\mu_\rho]_{ge}|v\rangle\langle v|[\mu_\sigma]_{eg}|m\rangle}{\tilde{v}_{ev,gm} - \tilde{v}_0 + i\Gamma_{ev}} + \frac{\langle n|[\mu_\sigma]_{ge}|v\rangle\langle v|[\mu_\rho]_{eg}|m\rangle}{\tilde{v}_{ev,gn} - \tilde{v}_0 + i\Gamma_{ev}} \right) \tag{1.19}$$

The temperature also affects the Raman polarizability, as the vibrational modes are quanta of a harmonic oscillator, and are therefore bosons that follow Bose-Einstein statistics. The Bose factor, $n_k^B(T)$, for the vibrations over all possible states for a given molecule at thermal equilibrium at temperature T is implicitly an average. This is given by the equation:

$$n_k^B(T) = [\exp(\frac{\hbar\omega_k}{k_B T}) - 1] \tag{1.20}$$

Where ω_k is the frequency of a given normal mode.

1.2.3 Resonant states

Excitation of states in a given system under resonance conditions gives rise to some simplifications with respect to Eqn. (1.19), because as $\tilde{v}_0$ (the laser/incident beam frequency) approaches a given transition wavenumber $\tilde{v}_{ev.gm}$ the resulting excited state will dominate over the others. Any non-resonant transitions can be ignored at the point of resonance in the transition polarizability equation, and the polarizability can be expressed as the sum of four terms:

$$[\alpha_{\rho\sigma}]_{gn,gm} = A + B + C + D \tag{1.21}$$

For the purpose of this thesis, only the A and B terms from Eqn. (1.21) are of any note, because the C and D terms relate to very rare events that do not need to be considered.

$$A = \frac{1}{hc}[\mu_\rho]^0_{ge}[\mu_\sigma]^0_{eg} \sum_v \frac{\langle n_g|v_e\rangle\langle v_e|m_g\rangle}{\tilde{v}_{ev,gm} - \tilde{v}_0 + i\Gamma_{ev}} \tag{1.22}$$

The A-term in Eqn. (1.22) represents the resonance Raman effect occurring in only totally symmetric modes, such as in a pi-pi* transition in say, a cyanine dye like Rhodamine-6G.

$$\begin{aligned} B = &\frac{1}{h^2c^2}\sum_{s\neq e}[\mu_\rho]^0_{gs}[\mu_\sigma]^0_{eg}\frac{h^k_{se}}{\Delta\tilde{v}_{se}}\sum_v \frac{\langle n_g|Q_k|v_e\rangle\langle v_e|m_g\rangle}{\tilde{v}_{ev,gm} - \tilde{v}_0 + i\Gamma_{ev}} \\ &+ \frac{1}{h^2c^2}\sum_{s\neq e}[\mu_\rho]^0_{ge}[\mu_\sigma]^0_{sg}\frac{h^k_{es}}{\Delta\tilde{v}_{gs}}\sum_v \frac{\langle n_g|v_e\rangle\langle v_e|Q_k|m_g\rangle}{\tilde{v}_{eg,gm} - \tilde{v}_0 + i\Gamma_{ev}} \end{aligned} \tag{1.23}$$

The B-term, in Eqn.(1.23), represents the *coupling* of modes, both symmetric and non-symmetric modes are represented in this equation. As the Raman effect is instantaneous, this coupling of modes is can be considered a superposition of the new state and the ground state. The C and D terms in Eqn. (1.21) are rare events that are not relevant to this thesis.

1.2.4 Surface Plasmons

The precise description of plasmons in literature can be confusing because over the years the experiments involving the exact nature of the plasmonic effect have changed. The original definition of the term comes from Pines' review article from 1956:[36]

> "The valence electron collective oscillations resemble closely the electronic plasma oscillations observed in gaseous discharges. We introduce the term 'plasmon' to describe the quantum of elementary excitation associated with this high-frequency collective motion.„

From this, it can be gathered that plasmons are a type of quantum quasi-particle that represent the elementary excitations, or modes, of the oscillations present in the charge density in a plasma. In many ways, this is analogous to how photons are quantum particles that represent the excitations, modes or oscillations present in electromagnetic fields. In metals such as gold, silver, aluminium, or iron, the plasmonic effect is prominent. The free electrons in these metals move about in what can be considered a plasma or either a free-electron plasma or a solid-state plasma[37]. An important concept for understanding plasmons are longitudinal and transverse modes; modes are generally described by their frequency, ω, and their wave vector, $\mathbf{k}$. These are linked by the dispersion relation, $\omega(\mathbf{k})$. As electric fields, $\mathbf{E}$, are an oscillating quantity as a vector, isotropic and homogenous media can be distinguished: if E and k are parallel $\mathbf{E} \parallel \mathbf{k} = 0$ everywhere, then it is a longitudinal mode/wave, whereas if E and k are perpendicular $\mathbf{E} \perp \mathbf{k} = 0$, the mode or wave is transverse, as in 1.4.

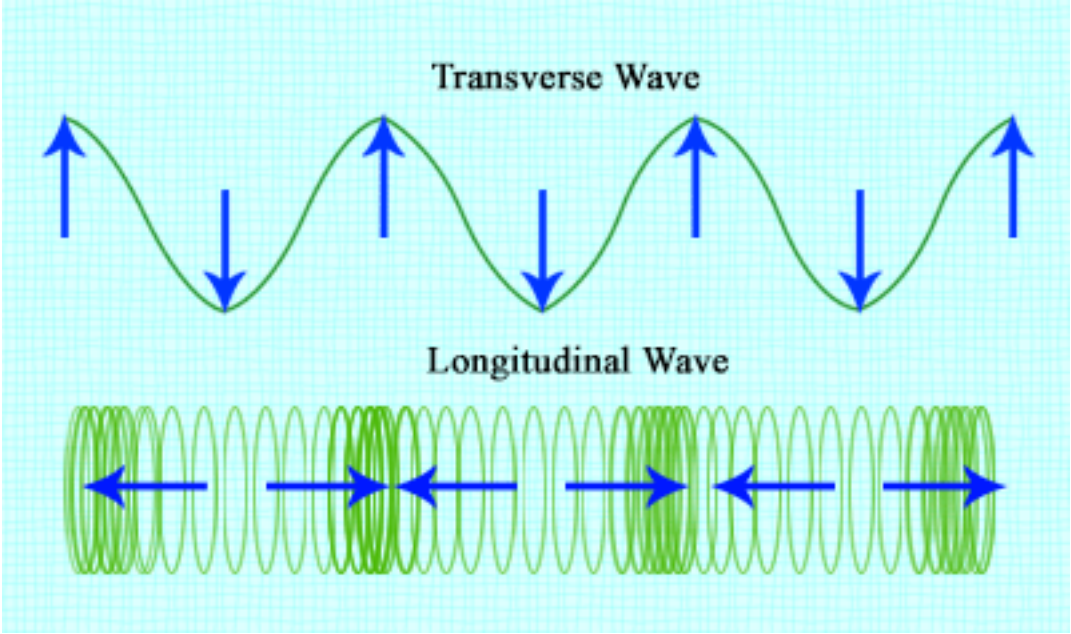

Figure 1.4: Diagram showing the difference between longitudinal and transverse waves. Reused under CC-BY-2[38]

The polarizability vector of a given molecule is given by the equation:

$$\vec{P} = N\vec{p} = N\hat{\alpha}(\omega)\vec{E}(\omega) \tag{1.24}$$

The Lorentz model describes the optical response of an electron in an atom or molecule, bound with a restoring force characterised by a resonant frequency given by ω_0. But because the electrons in a metal are not bound, they can be described without the restoring force, so $\omega \approx 0$. In reality, the linear optical polarizability is determined by and linked to the fundamental electronic structure of the molecule interacting with the incident beam. In metals, In addition, because the electrons in a metal are uniform and distributed randomly, the optical susceptibility is simply the

sum of the polarizabilities.

$$\epsilon(\omega) = 1 - \frac{ne^2}{m\epsilon_0}\frac{1}{\omega^2 + i\gamma_0\omega} \tag{1.25}$$

In Eqn. (1.25), where n (m^{-3}) is the number of free electrons per unit volume and m (kg) their [effective] mass. The damping term, γ_0 (rad s^{-1}), corresponds to the collision rate of free electrons with the crystal or impurities present in the system. Positive ions present represent a background real dielectric function, given by $\varepsilon_\infty \geq 1$, which affects the optical response of the crystal, so it must be incorporated into the dielectric function of the Drude model:

$$\epsilon(\omega) = \varepsilon_\infty \left(1 - \frac{\omega_p^2}{\omega^2 + i\gamma_0\omega}\right) \tag{1.26}$$

where ω_p (rad s^{-1}) is:

$$\omega_p = \sqrt{\frac{ne^2}{m\epsilon_0\epsilon_\infty}} \tag{1.27}$$

Without any external perturbation, ω_p is defined as the natural oscillation frequency of the solid-state plasma charge density, giving it the name of the *plasma frequency*. The corresponding wavelength of this plasma frequency is given by $\lambda_p = 2\pi c/\omega_p$. Separating the real and imaginary parts of Eqn. (1.26), we get:

$$\mathrm{Re}(\epsilon(\omega)) = \epsilon_\infty \left(1 - \frac{\omega_p^2}{\omega^2 + \gamma_0\omega}\right) \tag{1.28}$$

and the imaginary part:

$$\mathrm{Im}(\epsilon(\omega)) = \frac{\epsilon_\infty\omega_p^2\gamma_0}{\omega(\omega^2 + \gamma_0^2)} \tag{1.29}$$

For a metal described by the Drude model, the plasma frequency can be obtained from the real part in Eqn. (1.28), $\mathrm{Re}(\epsilon(\omega)) \approx 0$. This is because γ_0 is much smaller compared to ω. In the model described in the equations above, for situations were $\omega < \omega_p$, the real part becomes $\mathrm{Re}(\epsilon(\omega)) < 0$. In plasmonic materials, there exist phenomena called localized surface plasmon–polaritons (LSPs). The modes of these resonances are expressed with discrete values of ω. Ignoring the dampening term in the Drude model from Eqn. (1.26), we get:

$$\epsilon(\omega) = \epsilon_\infty(1 - \frac{\omega_p^2}{\omega^2}) \tag{1.30}$$

In plasmons, there are two main modes:

- The first modes are *bulk plasmon-polaritons* these are transverse modes and can be considered light or photons within a system, these change their properties based on their interaction with the metal and its electrons. These modes occur because of an interaction of the photons with a single electron excitation, not

from collective excitations within the plasmonic material. This is given by the equation:

$$\omega^2 = \omega_p^2 + \frac{c^2}{\varepsilon_\infty k^2} \tag{1.31}$$

- The second modes are *bulk plasmons*, these are longitudinal modes that correspond to oscillations in the internal charge density and a corresponding electric wave (not a magnetic wave). These modes do not couple to photons, making it not very relevant to SERS and a majority of plasmonic effects. The bulk plasmon frequency is determined by $\varepsilon(\omega) = 0$, which reduces to $\omega = \omega_p$, however, this frequency may be different from the plasma frequency ω_p because of inter-band transitions, this is the case for gold and silver.

1.2.5 Surface Enhanced Raman Spectroscopy (SERS)

SERS uses the plasmonic properties of materials and the structure of nanoparticles to enhance Raman signals of a selection of molecules. Different nanoparticle morphologies can enhance the Raman signal in different ways. Many different kinds of morphologies have been explored, from nanodimers,[39, 40] nanorods,[41–43] nanocubes,[44–47] nanotriangles or prisms,[48–52] pyramids or bipyramids,[53] nanostars or nanoflowers,[54, 55] nanocages,[56–58] and nanopores. In addition, the SERS effect has been found to occur in other techniques such as the use of plasmonic films, hybrid nanomaterials, high pressure, photo-induced Raman spectroscopy and shell-isolated Raman spectroscopy. SERS, therefore, offers exciting potential to enhance Raman signals that would otherwise go unnoticed in normal Raman spectroscopies. Typically, "good" SERS substrates are made of a plasmonic material such as gold or silver (or, more rarely, aluminium due to its difficult chemistry [59–62]) that support strong plasmonic resonances in the 400 nm to 1000 nm range. Highly localised plasmon resonances (or, hot spots) can form on the surface of the plasmonic material. The three main classes of SERS substrates are metallic particles, 'planar' metallic structures and metallic electrodes. SERS enhancement can be affected by several factors, five of these are identified by Le Ru *et. al.*, these are listed as:[63]

- Laser excitation characteristics; such as wavelength, polarization, and angle of incidence, etc.
- Detection setup; such as scattering configuration, solid angle for collection, polarized and/or unpolarized detection
- Selected SERS substrate; key characteristics such as material (such as silver, gold, *etc.*), orientation of the nanoparticle with respect to the incident beam direction, polarization and angle, and the refractive index of the environment (for example, is it in aqueous solution, another solvent environment or in air?)
- Intrinsic properties of the analyte; of note are the Raman polarizability tensors of the modes (or their intrinsic Raman cross-section)

- Analyte adsorption properties; important to note are properties such as adsorption efficiency and analyte concentration (surface coverage), distance from the surface and the orientation of adsorbed properties (fixed or randomly oriented).

As a general rule, most molecules exhibit a SERS spectrum can share modes that are present in their Raman spectra at the same excitation wavelength, with predictable peaks such as C-H vibrations at around 2600-3100 cm^{-1} however, factors such as the selected plasmonic substrate, the morphology of the substrate surface, and the concentration of the molecules with respect to the plasmonic substrate can all have an effect on the observed SERS spectrum.

1.2.6 SERS selection rules

As mentioned in Sec.(1.2.5), surface selection rules play a large role in what is seen in the observed SERS spectra, these are thoroughly discussed by Le Ru *et. al.*;[63, 64] a molecule might change it's signature vibrational modes, in essence, it's 'identity' when it adsorbs onto the plasmonic surface and forms a surface complex. This could result in small shifts (or more) and/or broadening of modes observed in the Raman spectra. In some cases, modes observed in Raman spectra will completely disappear or lose much intensity under SERS conditions, while other modes might get enhanced that would normally not appear at all. As a result of the plasmonic resonance of the nanoparticle substrate used, SERS signals can differ in their polarization properties compared to those found in a Raman spectrum. Sometimes, broad backgrounds occur in SERS spectra and are usually caused due to impurities or fluorescence scattering that might occur at the same time as SERS. While fluorescence will effect SERS spectra, it is suggested that the broad background associated with SERS spectra is due to a SERS continuum, whose origin is still controversial.[65] However, it has been observed that the SERS continuum fluctuates like the SERS signals, and has the same polarization properties.[64]. In addition to all of these, many SERS probes, such as laser dyes like Rhodamine-6G, photobleach under non-SERS conditions (although this usually requires high laser power). In addition, the orientation of the molecules with respect to the surface plasmons can have an effect on the observed SERS modes.[66–70] For example, using diazinon from Section 1.6, it should bond to the silver surface (the R-P=S-Ag bond itself will also change the Raman spectra as it connects the molecule to the electronic system of the silver surface, changing its polarization properties), the orientation of the ring will change how it interacts with the plasmon, which can change how it interacts with the plasmon, thereby changing its observed vibrational modes. This can occur with other molecules, regardless if they form a bond with the silver surface or not.

Due to the relatively high energy of surface plasmon "hotspots" that form in SERS-appropriate nanoparticles, it is no surprise that molecules can undergo significant photobleaching/photo-chemistry. Hotspots are, in effect, highly localised regions of intense localised plasmon resonances (LSPR) which tend to form in rough nanostructures, such as in interstitial crevices on the nanoparticle surface, or even between two nanoparticles.[39, 51, 71–77] Increasing the likelihood of hotspot formation or increasing their formation to higher densities, becomes important for SERS, as

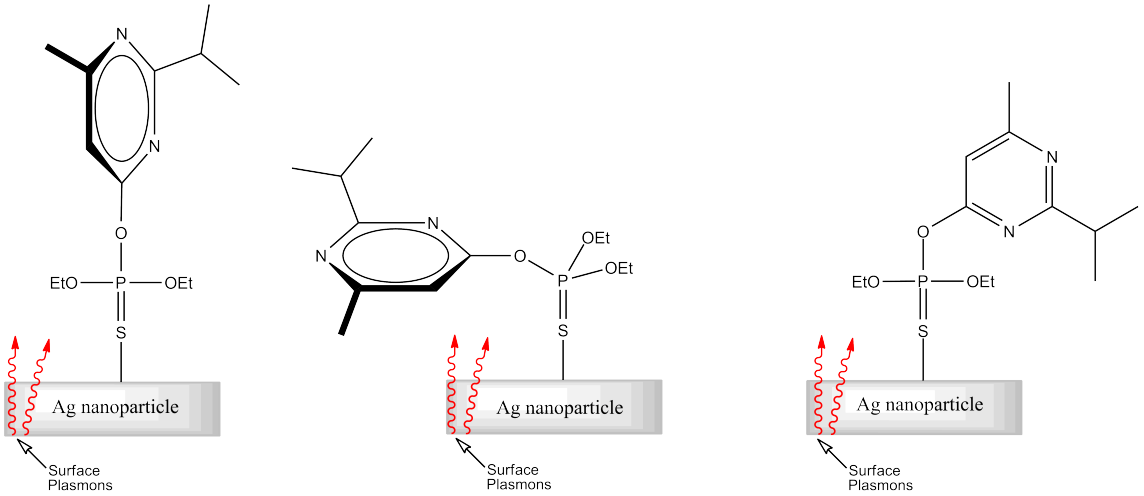

Figure 1.5: The potential orientations of diazinon from Section 1.6 and how it could interact with the surface plasmons when bonded to a silver nanoparticle

they have been shown to increase detection of SERS signals by several orders of magnitude.[75, 78] This effect has been observed experimentally, and in some cases, the photo-products of these photochemical products are observed.[73] Signals can also fluctuate, due to effects not present in conventional Raman spectroscopy conditions. The fluctuations could be due to changes in the substrate conditions (for example, in a more aqueous environment, Brownian motion of the colloid), photo-bleaching, single-molecule sensitivity, or due to the dielectric properties of the nanoparticles, which can affect how the incident beam interacts with the substrate, thereby affecting observed modes. Also, there is an effect called called the single molecule detection regime,[79–82] whereby the concentration of the absorbed molecule is significantly low enough, single-molecule fluctuations are observed as an average over the detection area. This results in what appears to be strong SERS signals at low concentrations where it would not be expected to occur. This differs from the many-molecule regime, where at higher concentrations, many molecules are SERS enhanced, and the observed spectrum is an average of all of these molecules; this is typical of most SERS spectra.

1.2.7 Electromagnetic and Chemical description of SERS

As described previously in 1.2.1, Raman intensities scale as a product of the polarizability and the incident laser (electric field) intensity, this means when it comes to SERS, there are two widely accepted descriptions of the SERS effect: a chemically derived one which involves charge-transfer excited states;[83–90] and another that describes SERS as enhancements in the field intensity due to plasmon resonance excitation.[91] In the latter description, the enhancement factor of a single molecule is given by the equation:

$$E = |E(\omega)|^2 |E(\omega')|^2 \tag{1.32}$$

where $E(\omega)$ is the local electric field enhancement factor at the incident frequency

ω, and $E(\omega')$ is the electric field enhancement factor at the Stokes-shifted frequency ω'. In conventional SERS (explored in this thesis), E is averaged over the surface area of the nanoparticle substrate where molecules can adsorb onto the surface. The resulting value generated from this is called the observed SERS enhancement factor, given by $\langle E \rangle$. Most calculations find that this value is roughly 10^6,[92] which accounts for most of the observed enhancement in SERS (around $10^6 - 10^8$), which is why the non-resonant chemical contribution to SERS is assumed to be small (usually less than 10^2).

1.2.8 A brief Quantum description of SERS

For the purposes of this thesis, the full quantum mechanical description of the Raman effect is not needed for SERS, however, it will be briefly touched on to get an understanding of the Raman cross-section (another name for the Raman polarizability) and the link to the microscopic properties of normal modes. This is important for interpreting the DFT calculations of Raman spectra, as DFT calculations produce a list of the vibrations according to their Raman activity. Normal modes can be interpreted as quantum harmonic oscillators, this is because all of the atoms in a normal mode oscillate at the same frequency.

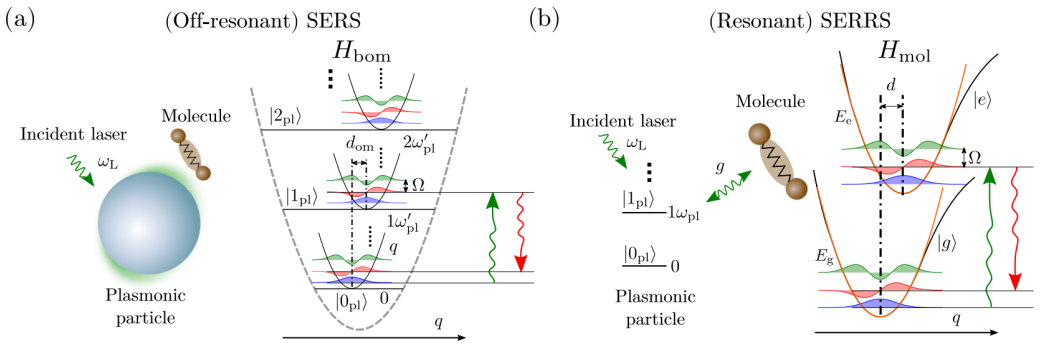

Figure 1.6: Figure showing SERS processes on a plasmonic nanoparticle at off resonance. Schematics of (a) the off-resonant SERS process in a plasmonic particle and a vibrating molecule and (b) the SERRS process, both depicted with their corresponding level structure. Image reused with permission from APS physics from the article by Neumann *et. al.*,[93] license number RNP/22/MAR/051922, the license can be found in the LaTeX folder for this thesis.

However, for this thesis, a full assignment of normal modes will not be the most practical, nor the most useful. This is because more than one normal mode could contribute to any given Raman peak, particularly in more complex a molecules. This often makes it difficult to identify which mode is responsible for which peak. In addition, some normal modes may either be too weak, or significantly overlap, making it difficult to be detected by a Raman spectrometer. This is especially the case if these modes have a low polarizability, or contain symmetry-forbidden transitions.

Some normal modes may even be affected by external factors such as temperature, pressure, solvent, or intermolecular interactions. This makes it hard to compare the experimental spectrum with the theoretical predictions or reference data. It can therefore be demanding to account for every possible mode of vibration that contributes to a single peak.

1.2.9 Enhancing SERS: Slippery Liquid-infused Porous Surface Enhanced Raman Spectroscopy (SLIPSERS)

Slippery Liquid-Infused Porous Surfaces (SLIPS) came out of research surrounding ways to amplify the effects of non-wetting surface chemistry by using micro-, or nano-texturing to create superhydrophobic and superoleophobic surfaces with low sliding angles. However, a newer approach infuses the micro-, or nano-textured surface with immiscible lubricating liquids, thus creating a Slippery Liquid-infused porous surface.[94] As these are low surface-energy liquids, the nanoporous structure will hold onto the liquid on the surface due to capillary action, making the surface of the filter omniphobic. The advantage of using an omniphobic surface such as this (as opposed to a glass slide or a piece of cellulose acetate filter), is that it avoids an effect called contact line pinning, which causes a drop to dry at a low angle, concentrating the contents of a drop into a 'coffee ring'-like shape. Pinning-free evaporation, as exploited by the SLIPS method, allows the drop to dry at a high angle. This high angle of evaporation can provide an increase in concentration and removal of a significant amount of solvent. This results in a final "spot" which contains a high concentration of analyte and nanoparticles, and if used in conjunction with SERS, can lead to further enhancement of signals due to the high-density ratio of nanoparticles (and therefore hotspots) to the chosen analyte(s). This technique has been previously used by the research group[95], and others.[96, 97] In addition, this technique is not limited to liquid-phase extraction/detection, and can also be used for gas-phase and solid-phase extraction/detection.[97]

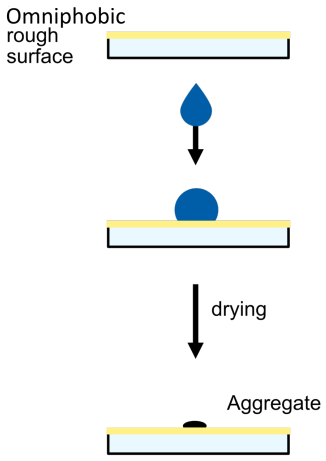

Figure 1.7: Simplified diagram showing the steps involved in creating a SLIPS sample.

1.2.10 Enhancing SERS: Shell-isolated Nanoparticle Enhanced Raman Spectroscopy (SHINERS)

Shell-isolated nanoparticles (SHINs) usually consist of a metallic core encased in a layer of silica, alumina or titanium dioxide. SHINs emerged from the research surrounding core-shell structures such as quantum dots, and the need for stable nanoscale catalysts, and have since expanded to applications in electrochemistry, and detection methods such as SERS and phosphorescence.[98, 99] Typically, SHINs have a plasmonic core, and a thin layer of either silica or titanium dioxide, the thin layer can be of any size below 10 nm, depending on the use-case of the SHIN. However, the surface chemistry of the silica shell must be considered; at low pH silica has little [negative] to no charge, weakly negatively charged at around pH 3 to 5, more strongly at pH 8, and the highest charge density at more basic pH.[100–103] If, for example, using silica (or titanium dioxide), the shell is also capable of being modified by the hydrolysis of silyl-based compounds, opening SHINs to a wide range of applications, such as nanoresonators [104], phosphorescence platforms,[99], cellulose nanocomposites,[105], and as SERS platforms.[43, 104, 106–111]

Under normal circumstances, a silica or a titanium dioxide shell would separate the plasmonic core from any molecules touching, or absorbed onto the surface. However, if the shell is controlled to be thin, the surface plasmons can penetrate the silica shell and still influence the polarization of a nearby absorbed molecule upon the exposure of an incident beam. Thus, by combining a thin shell and a plasmonic core, SHINERS (Shell Isolated Nanoparticle Enhanced Raman Spectroscopy) can maintain an enhanced Raman signal, whilst isolating the plasmonic core. In practice, this should increase the shelf-life of the SERS platform, and reduce agglomeration of the plasmonic cores, which is unfavourable for SERS. For SHINERS, then, the optimal thickness of this shell-isolating layer is 2-5 nm in thickness.[107, 112]
Concerning coating metallic nanoparticles with silica, the most common method

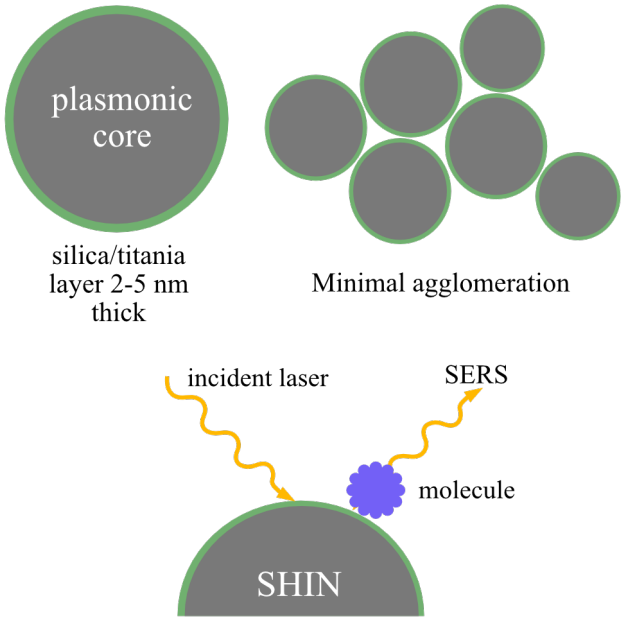

Figure 1.8: Left: the general design of a SHIN, with a plasmonic core such as silver or gold; right: the thin SiO_2 or TiO_2 layer provides extra stability to the nanoparticle, and can minimise the amount of agglomeration, and prevent oxidation of the plasmonic core; bottom: provided the shell thickness is small enough, the distance between the core of an analyte can still enable the SERS effect to be taken advantage of as the surface plasmons are still able to interact with the molecule close to or absorbed to the surface of the SHIN.

is using the Stöber method.[113] The Stöber method uses alkoxysilanes (for example tetraethoxysilane) as the SiO_2 precursor, which attaches onto the surface of nanoparticles, then under the catalytic addition of ammonia, an SiO_2 layer grows on the nanoparticle surface. It is a highly kinetic-dependent process, which occurs via the hydrolysis of the alkoxysilane, where condensation and nucleation events allow the formation of the SiO_2 shell. The Stöber method has enabled the use of nanoparticles that would be unstable under normal conditions. Regardless of the Ag@SiO_2 application, precise control of the shell thickness is extremely important - more so in SHINERs, where a large shell will create a barrier between the plasmonic core and the surface of the SHIN (as in Fig.(1.8). Within the context of SHINERs, this is extremely unfavourable, as the interaction between the plasmonic surface and the analyte is the most important part of the SERS effect. As a result, SHINs find themselves in an interesting position about SERS where unfavourable shell thickness results in useless nanoparticles. The advantage of SHINs, then, is three-fold. First, the enhanced stability of the nanoparticles due to the silica layer protects the plasmonic core from oxidation. Secondly, the silica layer reduces the likelihood of agglomeration and aggregation of the plasmonic cores, allowing more edges to interact with each other and increasing the likelihood of hotspots forming between nanoparticles. Finally, the silica layer allows the nanoparticles to be deployed in situations where the bare plasmonic material would normally not be stable.

1.3 The Synthesis of Metallic Nanoparticles

Ggenerally speaking, nanoparticles (NPs) or nanomaterials exist in dimensions in the nanometer scale, usually, these nanomaterials exist in the range from 1 nm to 100 nm. Metallic nanoparticles have found themselves used in an ever-expanding range of applications, commercial products,[114] and research fields, these include electronics,[62, 115–118], bio-medicine,[119–124] catalysis,[125–127] photovoltaics,[128, 129] and analytical chemistry. Of key interest has been the controlled synthesis over size, shape and dispersity (where monodisperse nanoparticles find themselves of interest in commercial products) of metallic nanoparticles. Creating and controlling metallic NPs can be done in several ways, usually either by a physical or chemical method. Nanoparticles Can be produced in vapour, liquid or solid phase,[130] and the methods of producing nanoparticles are separated into two main groups: the (a) top-down and (b) bottom-up approach. Physical methods usually rely on the "top-down" approach, whereby NPs are created by breaking down large structures (either bulk or from the etching of microscopic particles) into smaller particles.[115, 131] Widely used top-down methods include nanolithography,[132–137] and electron-beam nanolithography,[138–141] which involve the etching of nanostructures on a substrate, and then growth of nanoparticles using the nanostructured substrate as a mould to grow nanoparticles of the desired shape. In contrast, chemical methods tend to approach NP synthesis by the "bottom-up" approach. Simply put, this approach involves bringing in metal atoms from a source such as a salt or another precursor *via* a reduction, then controlling the aggregation of these metallic atoms into nanoparticles. In comparison to top-down methods like nanolithography or electron-beam lithography, the bottom-up approach is much less suited to producing controlled shape and size of the nanoparticle, however, it is by far the most common type of method for producing metallic nanoparticles with top-down methods require expensive, dedicated setups. The research in this thesis exclusively prepares metallic NPs *via* wet chemical methods (and therefore a bottom-up approach, explored more in Sec.(1.3.2) and Sec.(2).

As mentioned, the production of metallic nanoparticles (whether it's Au, Ag, Pd, Pt, Cu, Al...) is usually prepared by dissolving the chosen metallic salt (such as $AgNO_3$) or precursor (such as CF_3COOAg) in an aqueous or non-aqueous medium (such as ethylene glycol) and then reducing it with a reducing agent such as sodium borohydride, trisodium citrate, ascorbic acid, hydrazine or an alcohol [142]. Even producing a nanoparticle shape such as a sphere requires some kind of stabilising agent to prevent aggregation and eventually the production of a bulk metal. This tends to be done by utilising capping agents that adsorb onto the surface of nanoparticles that are forming. Stabilisation can occur with small capping agents like citrate ions *via* electrostatic stabilisation, or on a larger scale by utilising large sterically bulky polymers like poly(vinyl)alcohol (PVA) or polyvinylpyrrolidone (PVP). Other organic ligands, typically those with high binding affinity to the chosen atom (such as phosphines or thiols for silver or gold) can also suppress the aggregation of nascent nanoparticles. Thiols in particular are common capping agents and analytical model molecules for silver and gold nanoparticles, they range from disulfides, dendrimers or polymers.[143–145]

In addition to these methods, NPs can also be produced by utilising emulsions, where micelles or droplets are used as nano-scale reactors where the precursor/salt solution is localised, spatially separating NP formation in steps. [146] Size control is an important part of NP research, as such it can be obtained by changing factors such as thermodynamics, kinetics or stoichiometry. Stabilisers on the surface of nanoparticles can fulfil this role particularly if the stabiliser is strongly absorbed onto the metallic surface. Also, micelles can be used to control the stoichiometry by localising a certain amount of reactants within them, or nucleation events can be suppressed by utilising a seeded growth method (forming seeds *ex situ* as opposed to *in situ*), or *via* digestive ripening of nanoparticles. Of all these potential ways of limiting nanoparticle size, capping agents are the most common as they produce a thermodynamically stable capping agent-NP entity. Generally, capped nanoparticles are much more stable than their bare (washed) NP counterparts. Varying this capping agent stoichiometrically enables control over the size and even shape of NPs. Homogeneously size distributed large nanoparticles tend to be obtained *via* seeded growth.[143, 147] For NPs made of noble metals, typically small seeds are obtained quickly by using a strong reductant like $NaBH_4$ with a stabilising agent being present (like citrate), this is then succeeded by addition of a weak reducing agent (for example, ascorbic acid) and a second stabiliser which is generally bulkier or binds more strongly (for example CTAB).[145, 147–154] While metallic nanoparticles share many of their properties with the bulk material, they do differ in several properties which depend on the shape, size and surface structure of said nanoparticles.[155] As the main focus of this thesis is more specifically the sensitivity of the nanoparticles in SERS, it is important to get an understanding of how and why nanoparticles form the way they do, to explain not only why they behave in the way they do but also gain some insight into how their stability and nanoparticle growth leads to changes in the observed SERS spectra.

1.3.1 Mechanisms of nanoparticle nucleation and growth

The most important factors in nanoparticle synthesis can be boiled down to:

- What is the general growth mechanism of the given synthesis?
- How and when is the final particle and shape size determined?
- What determines the final particle size and shape?
- How do various synthesis parameters influence the particle growth and therefore the final size of nanoparticles?
- At what point can a given synthesis be considered to produce "monodisperse" or "heterogeneous" solutions of nanoparticles?

There are several mechanisms of the growth of nanoparticles,[156] such as the LaMer mechanism,[157, 158] Ostwald Ripening and Digestive Ripening[159], the Finke-Watzky

Two Step Mechanism,[160] Coalescence and Orientated Attachment[161] and Intraparticle Growth (or intraparticle ripening).[162, 163] The Finke-Watsky mechanism is a process in which two steps occur simultaneously:[160]

$$A \rightarrow B \tag{1.33}$$

$$A + B \rightarrow 2B \tag{1.34}$$

The first step in Eq.(1.33) is a slow, continuous nucleation from starting material A to product B; the second step in Eq.(1.34) is an autocatalytic surface growth where starting material A and B form two moles of B, this is not a diffusion-controlled mechanism. This model currently fits systems such as Iridium,[160, 164] platinum,[165] and rhodium or ruthenium.[166] For the sake of brevity, only the LaMer model, and Ostwald and Digestive ripening mechanisms will be briefly discussed here. Nucleation is a thermodynamic model of particle growth where a "nucleus" (a cluster of atoms) forms within a metastable primary phase (the solution containing precursor/metal salts) to act as templates for crystal growth. Primary nucleation as described by Mullin,[167] occurs when a nucleation event happens without the presence of any other crystalline matter, this has been used to describe many chemical syntheses.[168–170] In the case of many porous solids or nanocrystals, this does not always follow classical models of crystallisation in solution. And, in cases like calcium phosphate, Habraken *et. al.*[171] demonstrate that ion-association complexes combine both classical and non-classical theories. Classical Nucleation Theory (CNT), which was developed more than 70 years ago by Becker and Döring describes the condensation of liquids from the vapour phase.[158, 172] CNT describes nucleation and is based on the Gibbs capillary effect, so macroscopic properties such as the surface energy are used to describe the rate of nucleation. Since the paper by Becker and Döring, CNT has expanded to explain other types of phase transitions such as aerosols and nucleation of solids from the liquid phase.[173, 174] Further growth past nucleation is usually explained *via* growth processes such as diffusion-limited growth, aggregation or Ostwald ripening. Other models use rate equations to describe nanoparticle size distribution changes over time.[175]

In CNT, nucleation can be described to occur either homogeneously or heterogeneously. Homogeneous nucleation is when nucleation events occur somewhat uniformly, spontaneously and require a supercritical state like a supersaturated solution. On the other hand, heterogeneous nucleation is when nuclei form at some form of interface between the main phase and a structural irregularity - such as a container surface, impurities, grain boundaries or dislocations. Heterogeneous nucleation is much more common in the liquid phase because the solution and its container act as a nucleating surface. Homogeneous nucleation is defined thermodynamically by the total free energy of a given droplet can be represented by ΔG_{tot}, given by the equation (using the same symbols as in Fig. 1.9:

$$\Delta G_{tot} = \Delta G_{bulk} + \Delta G_{surface} \tag{1.35}$$

The "bulk" can also be referred to as the total volume, or simply the "volume" of

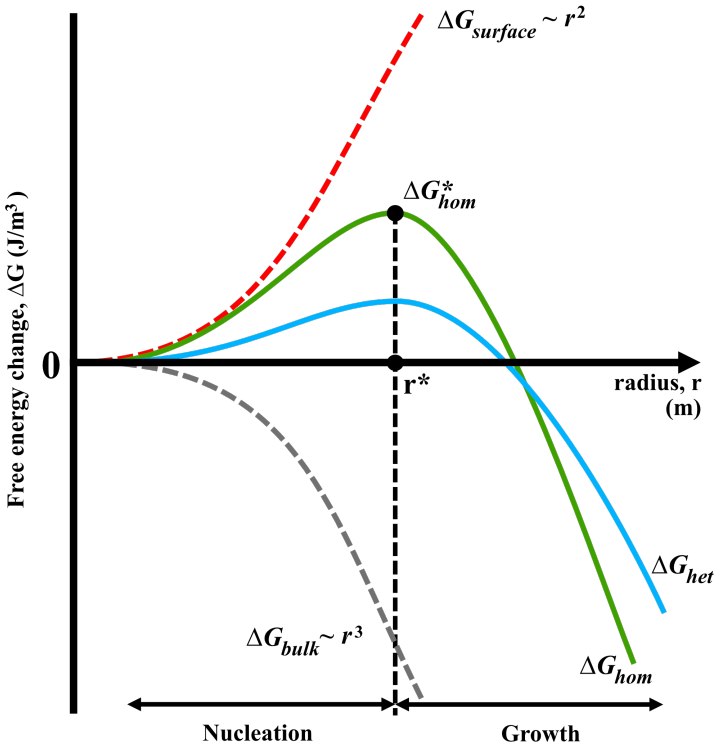

Figure 1.9: Schematic plot of the free energy barrier (ΔG^*) of nucleation at constant temperature for homogeneous nucleation (green line) and heterogeneous nucleation (blue line). ΔG is the change in free energy in the respective conditions; the surface of growing seeds, or in the bulk phase.

a given system. The surface free energy, $\Delta G_{surface}$ and the bulk (volume) free energy is given by the following equations:

$$\Delta G_{bulk} = \frac{4}{3}\pi r^3 \Delta G_v \tag{1.36}$$

$$\Delta G_{surface} = 4\pi r^2 \gamma \tag{1.37}$$

$$\Delta G_v = \frac{-k_B T \ \mathrm{In}(S)}{v} \tag{1.38}$$

For Eqn. (1.36), r is the nuclear radius, and ΔG_v is equal to $\Delta G_bulk/unitvolume$, the crystal free energy, defined in Eqn. (1.38) (where v is the molar volume and S is the supersaturation ratio). The crystal free energy is dependent on temperature In Eqn. (1.37), γ is the surface tension of the interface between the nucleus and its surroundings (it is always a positive value). Combining Eqns. (1.37) and (1.36) gives:

$$\Delta G_{tot} = \frac{4}{3}\pi r^3 \Delta G_v + 4\pi r^2 \gamma \tag{1.39}$$

In Eqn. (1.39) the second term (the surface) dominates, resulting in the r^3 term

to vary more rapidly and the r^2 dominates, resulting in positive ΔG values, as shown in Fig. (1.9) as the red line ($\Delta G_{surface}$). On the other hand, if the radius is larger the r^3 term dominates and the free energy trends negative, as shown in Fig. 1.9 as the grey line (ΔG_{bulk}).

$$\Delta G_{crit} = \frac{4\pi\gamma r_{crit}^2}{3} = \Delta G_{crit}^{hom} \tag{1.40}$$

$$r_{crit} = \frac{-2\gamma}{\Delta G_v} = \frac{2\gamma v}{k_B RT\ \mathrm{In}(S)} \tag{1.41}$$

r_{crit} is the critical radius, and corresponds to the minimum size required for a particle to be stable without being redissolved in solution. The free energy G_{crit} follows the same logic, as seen in Fig. 1.9. Metal clusters with a radius larger than r_c, are more thermodynamically stable, allowing them to undergo more growth *via* continuous reduction of metal atoms. Eqns. 1.41 and 1.40 show that the supersaturation ratio S, directly influences the critical radius r_c, where higher values of S decrease the r_c. This effectively means that a lower r_c value enables small clusters of metal atoms to facilitate nucleation. The nucleation rate $J(T, \Delta G_{crit})$ is therefore given by relating it to the Arrhenius equation because the energy barrier shown in Fig. 1.9 is an activation barrier:

$$J(T, \Delta G_{crit}) = \frac{dN}{dt} = A\ \exp\left(\frac{-\Delta G_{crit}}{k_B T}\right) \tag{1.42}$$

Where N is the number of particles and t is time. Relating the rate of nucleation to the previous equations we get:

$$\frac{dN}{dt} = A\ \exp\left(\frac{16\pi\gamma^3 v^2}{3{k_B}^3\ T^3(\mathrm{In}\ S)^2}\right) \tag{1.43}$$

To account for irregularities in the formation of nuclei in heterogeneous nucleation, a corrected term, ϕ is introduced into the free energy term for homogeneous nucleation:

$$\Delta G_{crit}^{het} = \phi \Delta G_{crit}^{hom} \tag{1.44}$$

ϕ is an angle dependent factor that is required because of the non-spherical nature of pre-nuclei "germs" that form on the first surface of a foreign body. It is defined by the equation:

$$\phi = \frac{(2 + \ \cos\ \theta)(1 - \ \cos\ \theta)^2}{4} \tag{1.45}$$

In CNT, so far it can be gathered that particles will grow larger above some critical radius, and below said critical radius, they will re-dissolve. However, not every nucleus will grow at the same rate, and often particles will vary in size. There is a size effect called Ostwald ripening which must be taken into account when growing nanoparticles. This is given by the equation below, which describes the change in particle size over time:

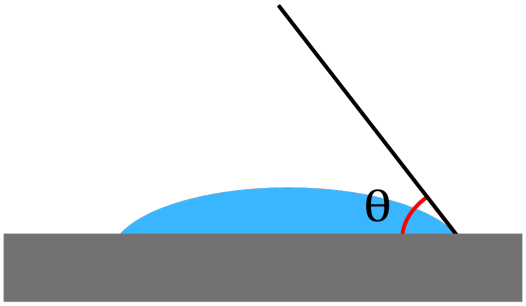

Figure 1.10: Illustration showing the contact angle, θ for "germs" that form on surfaces of structural inhomogeneities.

$$\frac{dr}{dt} = \frac{K_D}{r}\left(\frac{1}{r*} - \frac{1}{r}\right) \tag{1.46}$$

Where: r is the particle radius, $r*$ is the particle radius at equilibrium with the bulk solution, and t is time, K_D is defined as:

$$K_D = \frac{2\gamma D v^2 C_b}{k_B T} \tag{1.47}$$

where: γ is the surface energy, D is the diffusion coefficient, C_b is the bulk monomer concentration (an atom/molecule "building" the crystal) in the solution, k_B is the Boltzmann constant and T is the temperature. The standard deviation, Δr for a particle at a given radius at equilibrium is given by:

$$\frac{d\Delta r}{dt} = \frac{K_D \Delta r}{\bar{r}^2}\left(\frac{2}{\bar{r}} - \frac{1}{r*}\right) \tag{1.48}$$

where $\bar{r}$ is the mean particle radius. Eq. (1.48) is dependent on supersaturation of the solution. If $\bar{r}/r* \geq 2$ then the growth of the particle tends to result in a tighter distribution because $d(\Delta r)/dt \leq 0$. But if $\bar{r}/r*$ then $d(\Delta r)/dt$ and the size distribution of growing particles tends to broaden.

The LaMer mechanism is based on the idea of burst nucleation, where nuclei form spontaneously due to homogeneous nucleation, which then grows without any additional nucleation events occurring. This process is described in Fig.1.11, and is separated into three parts. The first part,(Phase I) can occur *via* liquid phase chemistry, where the supersaturated solution is generated by the reduction of metal atoms from their salt/precursor. Nucleation itself occurs only once a minimum concentration is reached (C_{min}), resulting in Phase II. From here, a critical concentration is reached and atoms will separate from the solution and form metallic clusters. As this progresses and the concentration of metal atoms decreases to a point where it is below the minimum critical supersaturation level, the nucleation process is terminated - from here nanocrystals will grow into larger particles (Phase III).

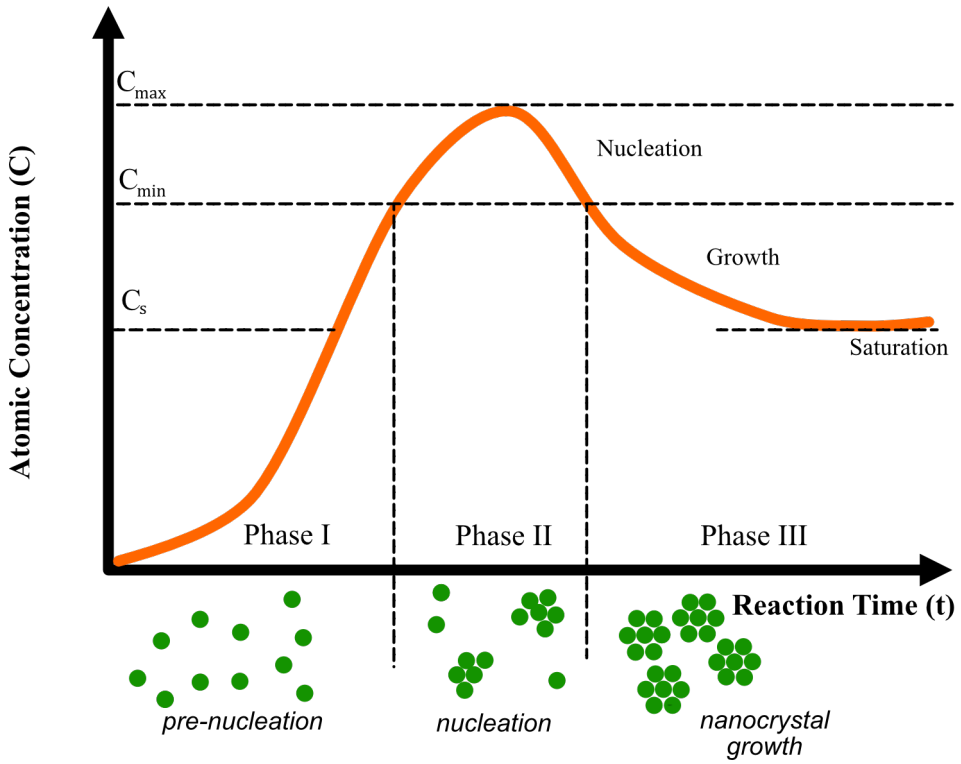

Figure 1.11: LaMer model showing the process of nucleation and growth of nanoparticles and its growth stages.[157]

1.3.1.1 Nanoparticle Stability

Generally speaking, nanoparticles are quite unstable and tend towards agglomeration and aggregation if they do not have a stabilising agent. Usually, nanoparticles are electrostatically stabilised as a result of the methods used to create them. Under ideal conditions, nanoparticles have an electrostatic double layer. The four main repulsive forces to consider are van der Waals interactions, Electrostatic interactions, DLVO theory, and steric stabilisation. van der Waals interactions are an attractive force for nanoparticles. The van der Waals interaction potential $W_a(D)$ between two particles with the radius R_1 and R_2 is given by the equation:

$$W_a(D) = -\frac{\pi^2 \rho_1 \rho_2}{6} C \left[\frac{2R_1R_2}{c^2-(R_1+R_2)^2} + \frac{2R_1R_2}{c^2-(R_1-R_2)^2} + \ln\left(\frac{c^2-(R_1+R_2)^2}{c^2-(R_1-R_2)^2} \right) \right] \tag{1.49}$$

where c is the centre-to-centre distance between two particles with radius R_1, R_2; and ρ is the electron density, the distance between the two surfaces, D, is $D = c - (R_1 + R_2)$. Then, taking into account two identical particles having $R = R_1 = R_2$ and $D << R$ The equation reduces down to:

$$W_a(D) = \frac{\pi^2 \rho_1 \rho_2 C R}{12D} = -\frac{AR}{12D} \tag{1.50}$$

Where A is the Hamaker constant. Eqns. (1.49) and (1.50) show that the surface interaction potential decays not as much with respect to D than with the interaction potential between the two particles - for example, $1/D$ compared to $1/r^6$, therefore showing that the potential is proportional to particle size $W_a(D\ R)$.
Electrostatic interactions are a nanoparticle repulsion force that comes from the overall surface charge of a nanoparticle. Nanoparticles tend to be surrounded by solvated ions that effectively "shield" the surface charge as described by Stern-Gouy-Chapman (SGC) theory. In SGC theory, the particle is surrounded by a compact and diffuse layer called the electric double layer (EDL). The EDL has a thickness determined by electrostatics called the Debye length ($\lambda(\kappa - 1)$). The layer is distributed according to the Poisson equation to give the distribution of the electric surface potential:

$$\varepsilon\varepsilon_0 \frac{d^2\Psi(x)}{dx^2} = -\rho(x) \tag{1.51}$$

where x is the distance from the particle surface, $\psi(x)$ is the electric potential, ε is the vacuum permittivity, ε_0 is the dielectric constant and ρ is the charge density. Applying Debye-Hückel linearization to the equation gives:

$$\varepsilon\varepsilon_0 \frac{d^2\psi(x)}{dx^2} = \sum_i \frac{z_i^2 e^2 n_{i\infty}^2 \Psi(x)}{k_B T} = \kappa^2 \Psi(x) \tag{1.52}$$

where $n_{i\infty}$ is the concentration of a given ion (i), and κ is the Debye constant. Eqn. (1.51 can be solved by defining $\lambda_D = \kappa^{-1}$, giving the equation describing the decrease of the electrical surface potential in the EDL:

$$\Psi(x) = \Psi_0(0)\exp(-\kappa x) \tag{1.53}$$

where $\Psi(x)$ is the surface potential at $x = 0$. Forces in the EDL are caused by an overlap of electrical potential distribution and ionic concentration. The interparticle force of the EDL is defined by the radius, R and distance between two surfaces D, using the Derjaguin approximation. The interparticle force, between the two EDL layers, is defined by the equation:

$$F(D) = -2\pi\varepsilon\varepsilon_0\kappa R\psi_\delta^2\ \exp(-\kappa D) \tag{1.54}$$

with the interparticle energy defined as:

$$W_R = \int_D^\infty F(D)dD \tag{1.55}$$

$$W_R(D) = 2\pi\varepsilon\varepsilon_0 R\psi_\delta^\infty\ \exp(-\kappa D) \tag{1.56}$$

where Eqn. (1.55) is the interparticle energy, and Eqn. (1.56) is the interparticle energy between the two layers of the EDL.
Nanoparticles can be prevented from aggregating by adsorbing large molecules (such as polymers) onto their surface. The repulsive interaction between particles with such a protective layer is described by DLVO theory, and is given by the equation:

$$W_{total}(D) = W_a(D) + W_r(D) + W_{steric} \tag{1.57}$$

where W_{steric} is the repulsive interaction potential, which is primarily dependent on polymer concentration, temperature, and chain length of the adsorbed polymer. DLVO theory (Derjaguin, Landau and Verwey, Overbeek) assumes that the total force between colloidal particles is the addition of the van der Waals and EDL interaction forces. The DLVO theory predicts a well-defined critical coagulation concentration (CCC), which separates the aforementioned types of aggregation: slow and fast aggregation. The CCC is defined as the minimum electrolyte concentration required to reach an energetic barrier that is equal to zero. Using silica nanoparticles as an example, DLVO theory predicts that as the pH increases, the surface charge of the nanoparticles increases, therefore increasing the CCC concentration. Therefore the attractive forces of van der Waals and the repulsive force from the EDL are combined, so the total interaction energy between two particles is given by:

$$W_{total}(D) = W_a(D) + W_r(D) \tag{1.58}$$

where W_a and W_r are the attractive and repulsive forces. Combining Eqn. (1.55) and (1.50 with the above Eqn. (1.58) gives:

$$\begin{aligned} W_{total}(D) &= W_a(D) + W_r(D) \\ &= -\frac{AR}{12D} + 2\pi\varepsilon\varepsilon_0 R\psi_\delta^2 \exp(-\kappa D) \end{aligned} \tag{1.59}$$

DLVO theory is better at predicting nanoparticle stability in weakly charged systems, where the potential barrier is found at distances greater than a few nanometers. Therefore, it is important to note that the limitations of DLVO theory arise mostly in more highly charged systems. In these kinds of systems, the CCC is located at much higher salt concentrations, making the potential barrier move into sub-nanometer distances. At these distances, variations in the nanoparticle surface can affect stability much more in the weakly charged systems, so any derivation from DLVO theory is likely due to the surface roughness and/or the charge of the nanoparticle itself. Silica nanoparticles, for instance, show the limits of DLVO theory; under low pH conditions, silica nanoparticles not only have little to no charge,[176–178] but are claimed to be stable. However DLVO theory incorrectly predicts that silica nanoparticles should be unstable at this pH. [100, 179–182] In addition, in other silica systems it has been found that, experimentally, the CCC has a minimum, which is a function of pH.[179–181] As mentioned above, DLVO theory instead, predicts a continuous increase in the CCC as the pH increases. However, it has been shown that DLVO theory in silica nanoparticles only applies to larger particles in the sub-micron range; conversely, the smaller particles in the nanometer range (approximately smaller than 25 nm radius),[183]

1.3.2 The preparation of silver nanoparticles (AgNPs)

Nanoparticle dispersions that are made of noble metals such as gold and silver, post-transition metals like Aluminium, or transition metals such as copper can be made into a wide range of colours which vary with the corresponding size and shape of the particles, which make them useful as plasmonic substrates for use in SERS. Noble metals such as silver or gold, are useful due to their stability and easily reproducible methods for nanoparticle creation. In addition to the growth mechanisms outlined in the previous section, noble metals nucleate and grow in their own way, dependent on their chemistry and their affinity for various chemicals that bind to them. Nanoparticles can also be produced non-chemically using methods such as laser ablation, vapour deposition, and nanolithography.[137] Silver has been studied in depth and under various conditions, such as by Rothberg *et. al.*[184] and by Henglein *et. al. via* γ-irradiation of silver perchlorate in propanol in the presence of N_2O, and sodium citrate.[185] In Henglein *et. al.*, there are a couple of proposed mechanisms: electron transfer via reduction is responsible for Ag^+ ions reducing on particles already present in solution. This mechanism suggests that low citrate concentrations lead to coalescence of silver nanoparticles, while very high citrate concentrations destabilise the nanoparticles as the ionic strength causes reduction to occur on the surface of particles that are forming, causing them to grow larger. With the use of small-angle X-ray scattering, more insights were gained into the growth of silver nanoparticles where Harada and Katagiri.[186] What they found was that silver particles form in two stages: the first phase is an initiation, where a rapid increase in the number of nanoparticles occurs within the first ten minutes - resulting in a solution which is 20% polydisperse. Further analysis found this first step to being an autocatalytic reduction–nucleation which is the two-step mechanism proposed by Finke and Watzky. The second phase of silver nanoparticle growth with citrate involves a decrease in the number of nanoparticles forming, while the size of nanoparticles increases, which is explained via Ostwald ripening.

1.3.2.1 Inorganic reducing agents

In many silver nanoparticle syntheses, sodium borohydride ($NaBH_4$) is a favourite in nanoparticle reactions because $NaBH_4$ is a strong reducing agent that tends to lead to the production of smaller-sized nanoparticles.[50]

$$AgNO_3 + NaBH_4 \longrightarrow Ag^0 + 0.5H_2 + 0.5B_2H_6 + NaNO_3 \tag{1.60}$$

On the other hand, reducing agents like hydrazine (N_2H_4) are also used as a common inorganic reducing agent. Stable solutions tend to be very basic, however, the silver nanoparticles are much less stable under these conditions.

$$2Ag^+ + N_2H_2 \longrightarrow 2Ag^0 + N_2 + 2H^+ \tag{1.61}$$

With hydrazine, it is possible to create nanoparticles with a 10-50 nm size range, but it is difficult to control their size and their polydispersity.[187] Although, there has been some effort to control the monodispersity of hydrazine-reduced nanoparticles.

[188]

1.3.2.2 Organic reducing agents

Among the reactions that produce nanoparticles, organic reducing agents offer an expansive collection of reagents for a single type of reducing agent - for example, using citrate (which began as the Turkevich method in 1951) for the synthesis of gold nanoparticles can be adapted to a wide range of particle size and shape. The original Turkevich method used chloroauric acid with sodium citrate under boiling conditions to produce a colloidal suspension of gold nanoparticles.[189] The basic process of this reaction when used with a source of silver ions is given by the Eqn. 1.62:

$$C_6H_5O_7^{3-} + 2Ag^+ \longrightarrow C_5H_4O_5^{3-} + H^+ + CO_2 + 2Ag \tag{1.62}$$

This method is the most popular due to it being an aqueous method, and the fact that under the right conditions, citrate acts as both a reducing agent, and then a stabiliser for silver nanoparticles, often being able to last weeks outside of low temperatures, and months in refrigeration conditions. Many variations on the Turkevich method have been made[190], resulting in various nanoparticle shapes, from rounded, prisms, to pentagonal nanoparticles. Another common method of producing nanoparticles via polyol reduction - usually involves either ethylene glycol or diethylene glycol as a solvent, and polyvinylpyrrolidone as a capping agent. This method is also very adaptable like the citrate reduction, allowing the formation of spheres,[39, 113, 127, 191, 192] cubes,[44, 46, 47, 193, 194] rods,[41–43, 147] wires,[195, 196], cages,[58] and more.[197] The polyol process is very popular, as a result, the reaction of an $AgNO_3$ precursor with ethylene glycol is as follows:

$$HOCH_2CH_2OH \rightarrow 2CH_3CHO + 2H_2O \tag{1.63}$$

$$2Ag^+ + 2CH_3CHO \rightarrow CH_3CO\text{-}OCCH_3 + 2Ag + 2H^+ \tag{1.64}$$

The moment silver atoms reach a supersaturated concentration, they will begin to nucleate and grow into silver nanostructures in the solution phase, thereby producing the nanoparticles.s

1.4 Applications of AgNPs for the detection of Organophosphorus compounds *via* SERS

The detection of pesticides and organophosphorus compounds is important in assessing environmental issues, as pesticides such as organophosphorus compounds can cause damage to the central nervous system. [23, 198]. Malathion and glyphosate are some of the more common compounds that are studied, as their use is more widespread due to them not being recognised as harmful to humans. This is relevant because the scientific evidence of pesticide carcinogenicity is always changing, cancer hazard classifications for specific pesticides also change over time, as do pesticide use profiles

as a result of agrichemical developments, legislation and pest resistance. Several pesticides currently known or suspected to cause cancer in humans are no longer used in New Zealand since the 1970s and 1980s, for example, DDT and parathion, which were banned for use in 2018 and 2017, respectively.[22] Many methods used to detect pesticides using SERS use methods already outlined here, for instance, just using SERS,[199] surface modification of the plasmonic surface,[200] or using SHINs,[106, 199, 201, 202] or using aptamers.[203]

1.4.1 Overcoming detection Issues

Detecting specific analytes using SERS can be difficult due to the variability in the observed Raman modes when enhanced by a plasmonic material - where physical constraints such as the orientation of molecules on the plasmonic surface, the orientation of plasmonic surfaces and their morphology/shape which affects "hot-spot" formation, or any leftover capping agents that could interfere with the detection of the selected analytes. Typically, when showing the effectiveness or efficiency of a nanoparticle, ideal molecules such as dyes are used, whose properties are known and Raman spectra are well understood. However, where this is not the case, and where the nanoparticles on their own are not enough to enhance the Raman signals, certain steps can be taken to enhance the SERS signals. Dilute solutions of nanoparticles should lead to a decrease in the intensity of the observed signals, even if the nanoparticle itself is ideal for SERS. In solution, one could also force aggregation by adding either NaCl or Na_2SO_4. Normally too much aggregation can decrease the efficiency of nanoparticles, however, if the goal is to increase the likelihood of a molecule encountering hotspot, an optimal amount of aggregation can be used to enhance the SERS signals observed. Another method is to remove the solvent factor completely - solvents such as water result in very large -OH peaks in the Raman signal. For molecules where their signals do not lie within the range, this is not a problem, but where this is not the case, removing the solvent is a good solution. Drying the nanoparticles with their analyte does have its downsides, however. In some cases, the chosen analyte will not be stable without the solvent, or, drying results in ‘coffee-ring’, which can be difficult to analyse, as the drying process is not completely uniform.

A solution to this drying problem is Slippery Liquid-infused Porous Surface Enhanced Raman Spectroscopy (SLIPSERS), which uses the advantages of a microporous structure (such as a filter) and an omniphobic liquid to create a drying surface which avoids contact pinning. This concentrates a given droplet into a very small spot, drastically improving observed SERS signals, as everything within the droplet is forced into a small spot, including analytes. In addition to the nanoparticle concentration and the initial analyte concentration, the size distribution of the selected nanoparticles also needs to be considered. Much research has gone into the effect of size distribution on the observed SERS enhancement factor has taken place. Generally speaking, the larger the average nanoparticle size is, the less effective it is as a SERS substrate.[204, 205]

Another issue with detection comes in the form of d/g bands. These can appear in areas of intense hotspot formation or the laser burning the sample due to user error

(caused by the laser having high output), effectively creating graphene and related compounds. The Raman spectrum of graphene and its derivatives exhibits two prominent features: the so-called "G band" and the "D band." The G band (1580 cm^{-1}) comes from the bond-stretching mode of sp2-hybridized carbon atoms at the center of the Brillouin zone (also known as the Γ point); whilst the D band (1350 cm^{-1}) comes from the breathing mode of sp2-hybridized carbon atoms at the edge of the Brillouin zone (K point). The D band is observed in the Raman spectra due to defects or disorder within the lattice of graphene; such as edges, vacancies or functional groups (such as graphene oxide, GO; or reduced graphene oxide, rGO). The intensity ratio between the D to G bands (I_D/I_G) is commonly used as an indicator of the defect density or quality of graphene and its derivatives. This ratio alone is not usually sufficient to evaluate the degree of reduction of GO or rGO, because it can be affected by other factors such as layer number, layers overlapping, doping, intramolecular strain or the wavelength used from the laser. Other Raman features have been proposed to assess the reduction process of GO or rGO, such as the D* band (roughly 1620 cm^{-1}) and the 2D band (roughly 2700 cm^{-1}). The D* band is a defect-induced overtone of the D band, whilst the 2D band is a second-order two-phonon process involving two phonons with an opposite momentum near the K point. Like the I_D/I_G ratio, the intensity ratio of the D* to G band (I_{D*}/I_G) has been shown to correlate well with the C/O atomic ratio of either GO or rGO; reflecting the removal of oxygen-containing functional groups during reduction. In more in-depth studies about graphene, the 2D band is used to provide information about the number of layers, how layers are stacked, and electronic structure of graphene and its derivatives within a given sample.

1.4.1.1 Detection *via* specificity

So far, only non-specific methods have been discussed (being most relevant to this thesis), however, it is important to note that there is a significant amount of research on modifications that are used to detect compounds by specifically binding to them *via* specificity. Typically, these come in the form of either a generalised binding structure or an aptamer. Aptamers are made by DNA synthesis and are single-stranded oligonucleotides that fold and bind to specific shapes. Aptamers are usually designed with biological compounds such as proteins in mind, however, a lot of research has also been done to detect other compounds using aptamers on plasmonic surfaces. Raman spectroscopy and SERS are finding more widespread use in biomedical and biochemical sciences, for example using aptamers to detect COVID-19 spike proteins.[206] In related research to this thesis, aptamers can be more used to detect pesticides such as malathion.[203] Aptamers are ideal candidates for specificity, as they can be tuned for the exact structure of the analyte of interest. However, their main downside is their means of synthesis, having to be constructed using a DNA synthesizer.

1.5 Combining non-specific methods: SHIN-SLIPSERS

As mentioned in Sec.1.4.1 and Sec.1.2.10, SHINERS and SLIPS are both very useful generalised methods - however, combining them has some potentially useful applications. It solves some of the issues in SLIP-SERS, namely:

- if nanoparticles are improperly washed, capping agent peaks may appear in spectra that they would otherwise be undetected;
- SLIP-SERS results in the nanoparticles being exposed, making them unstable and prone to oxidation, reducing shelf life;
- SLIP-SERS forces nanoparticles to agglomerate into a single spot. While the sheer concentration of nanoparticles in a single spot can overcome this, reducing the potential for even more 'hot spots' throughout the agglomerate;

For one, SHINs under favourable conditions are less likely to lead to the aggregation and agglomeration of the plasmonic core due to the SiO_2 layer, and, combining this with SLIPS means it should result in a spot where fewer nanoparticles are agglomerated as a result of the drying process. This should result in a higher likelihood of hot-spots forming plus the added likelihood of a molecule interacting with these hot spots due to the condensed spot. Combining the SHIN and SLIP-SERS methods has two major downsides:

- if the core-shell is improperly made, it will have the opposite effect as described above;
- for analytes that are sensitive to thermal degradation, so many hot-spots occurring in a single agglomerate might negate any potential benefits, as they would be degraded too rapidly or too easily to provide any benefit at all.

However, both downsides above can be minimised if the methods are effectively tuned if: a consistent core-shell method is found, and; incident laser power and concentrations are optimised. Combining the methods results in Shell Isolated Nanoparticle - Slippery Liquid Porous Surface Enhanced Raman Spectroscopy.

1.6 Analyte Selection

1.6.1 Dyes

Laser dyes such as rhodamine-6G (R6G or RH6G) are ideal candidates for probing the effectiveness of plasmonic surfaces, as they are highly emissive with distinct vibrational spectra. In SERS research, it is common to see R6G being used as a probe molecule, with it being involved since the beginning of SERS research in the 1970s and 1980s.[207] Fluorophores like R6G make it an ideal candidate for probing the effectiveness of the nanoparticles used in this thesis - however, this might not translate

to 'how effective they are at detecting organophosphorus compounds, particularly compounds with inherently less Raman scattering. Ponceau 4R is an azo dye used as a food additive and comes in many synonyms, such as cochineal red A or by its additive code, E124. It is much less emissive than R6G and was chosen due to its cheap and accessible availability.

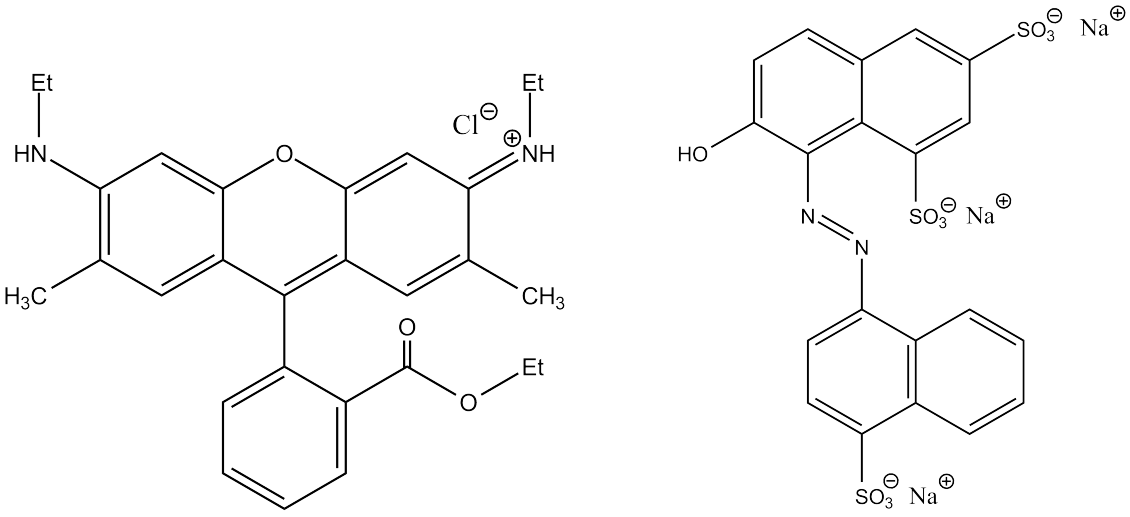

(a) (b)

Figure 1.12: Structures of the chosen SERS dyes, Rhodamine-6G (a); and Ponceau 4R

1.6.2 Organophosphorus Compounds

Diazinon for example, has been banned in New Zealand since 2015, and only approved handlers can use it up until 2028, however it has still been found in many New Zealand waterways despite the ban.[208]

Over the years, different pesticides and herbicides will be banned and others will come into use, it, therefore, becomes important to find ways of detecting pollutants quickly and with high sensitivity. Glyphosate has, in recent years, become somewhat of a controversial chemical, and frequently appears on the news due to its potential carcinogenicity to humans (though this is highly debatable, so far there is little evidence), and due to its widespread use its potential effects on local biodiversity. Therefore it became a logical choice as a chosen analyte, its structure is shown in Fig.(1.13b). Diazinon, on the other hand, being recently banned in the EU and currently going through a New Zealand EPA phase-out (though still available in restricted use) and still detectable in the environment, are 1,3-disubstituted diazines (pyrimidines) with three substituents attached to the ring, shown in Fig.(1.13a). In addition, the phosphate group also contains a sulfur atom in place of where a P=O would exist; in the context of a silver nanoparticle system like those in this thesis, diazinon would favour forming an R_3P=S-Ag bond.

One thing to note is that glyphosate is a polyprotic compound, and will have

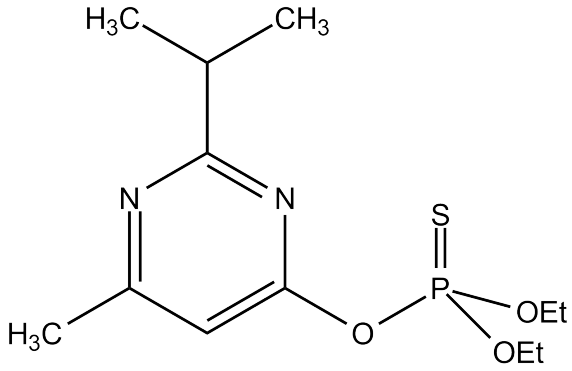

(a) Structure of diazinon

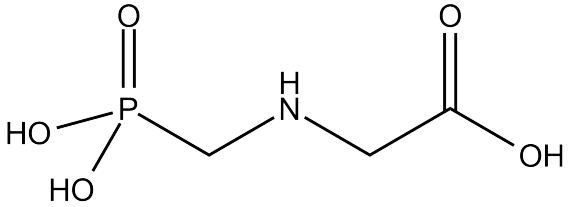

(b) Structure of glyphosate

Figure 1.13: Structures of the chosen organophosphorus compounds

varying structures depending on the pH of its environment, see Fig.(1.14). This, in turn, will change its electronic structure, its polarizability, and therefore its Raman and SERS spectra will change too. So the polyprotic nature of glyphosate might have to be considered as not all of the nanoparticles that will be used have the same aqueous environment.

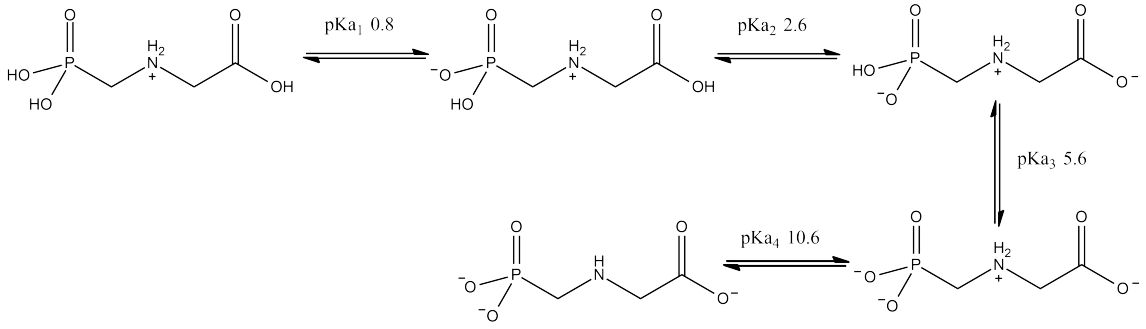

Figure 1.14: Diagram showing the structure of glyphosate at different pKa values.

However, one thing to consider about diazinon, is that it becomes relatively unstable once exposed to certain environmental conditions; Diazinon decomposes at temperatures above 1200degC. It is stable in alkaline media but is slowly hydrolysed by water and by dilute acids. In the pH range of 6.0 to 8.0, it is relatively stable, and the hydrolysis is very slow under these conditions. However, the hydrolysis process is quite rapid under acidic (usually at pH < 3.1 or lower) or alkaline conditions (usually at pH > 10.4 or lower).[209, 210] In addition to this, the pH of the SHINs versus the

glyphosate also needs to be considered, as the pH of the solutions will change the charges on the surface of the silica shell and, the structure of glyphosate itself, this comparison can be seen in Fig.(1.15) below.

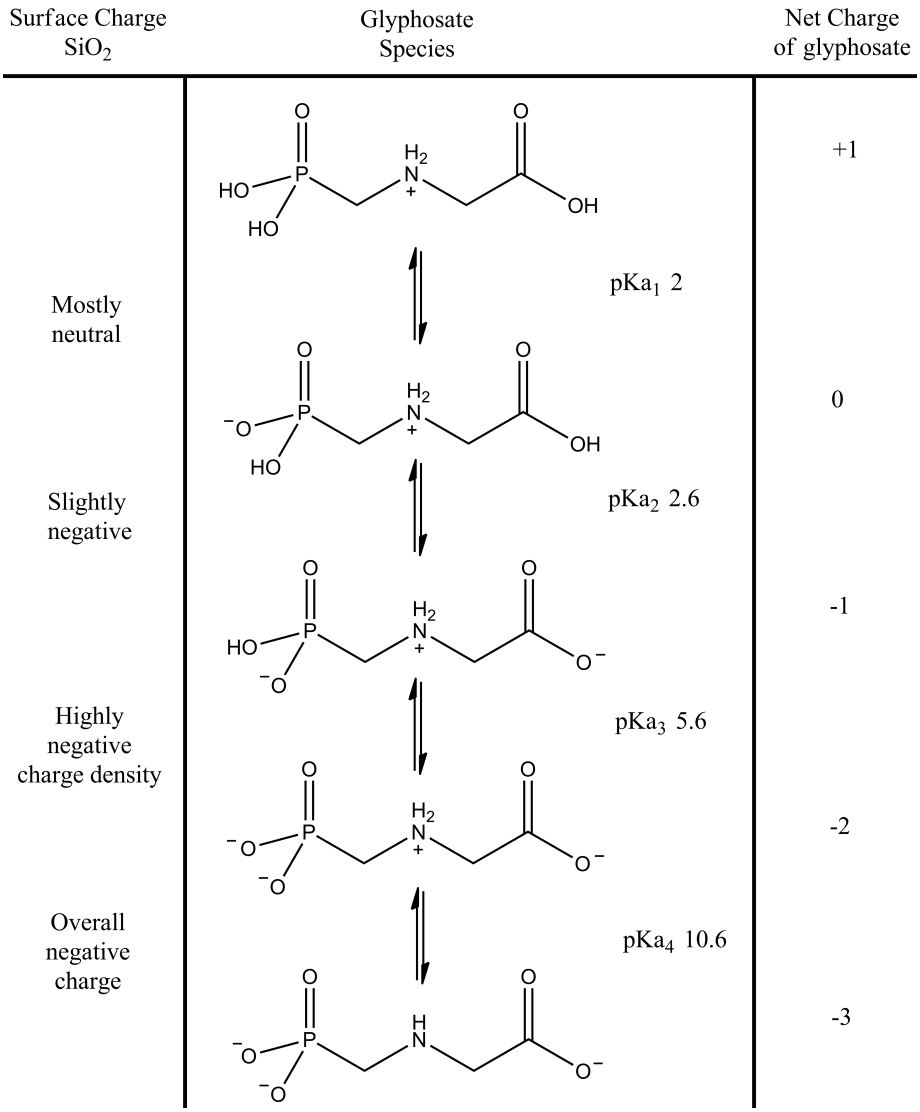

Figure 1.15: Summary table showing how pH affects silica at the same pKas of glyphosate

1.7 Project Hypotheses and Goals

This thesis will focus on these main goals:

- Produce a range of nanoparticle morphologies to test whether or not nanoparticle shape will have a significant effect on organophosphorus and dye detection using the SLIP method.

- Produce a SHIN version for each nanoparticle shape and compare to the standard shape SLIPSERS spectra, and what effect this has on their SLIPSERS spectra.
- Find out the limits of detection (in other words their lowest possible concentration they can detect SERS signals from) of selected analytes outlined in Section 1.6 on a range of analytes.

Based on previous literature, nanoparticle shape (is a key factor in hotspot formation,[40, 72] and due to the aggregate/agglomerate being formed by the nanoparticles in the SLIP method the likelihood of many interactions between sharp edges of nanoparticles will be stretched to its physical limit. Based on these reasons, the selected nanoparticles are, therefore:

- Nanopsheres, including silica capped nanospheres and SHINERs with smaller Ag nanoparticle satellites.
- Nanocubes.
- A nanoparticle dispersion containing a range of shapes, including a silica capped version.
- Nanoprisms, including a silica capped version.

In terms of SERS or SLIPSERS performance of the nanoparticles, the nanocubes or the nanoprisms will likely be the best performers in terms of sensitivity and limits of detection for both classes of nanoparticles (either standard nanoparticles or SHINs as explained in Sec.1.2.6). This is likely due to their shape having very sharp edges; for example, in the case of nanocubes, the vertices will have 90deg angles. Conversely, the silver nanospheres are likely to be the worst at detection limits, at least relative to the other nanoparticle types. In addition, the silver nanoparticle dispersion will sit firmly in between the rest, as the variation in nanoparticle shape and size should hinder its SERS performance somewhat, as shape homogeneity is shown to increase SERS performance in other applications.[78, 139, 211–213] The behaviour of nanoparticles in SERS is generally quite unpredictable; In the case of the analytes, R6G will be the best probe dye, due to its highly emissive nature. Detection of the organophosphorus compounds will probably be reliant on how well it adsorbs onto the surfaces of the chosen analyte, though the condensed spot due to the SLIP method might reduce this dependency by a small amount. Out of the two organophosphorus compounds chosen, diazinon will likely be the best in terms of limits of detection as it has a sulfur group on the phosphate, due to this it is likely to prefer to bind to the nanoparticles via the sulfur, as silver has a high affinity towards Ag-S bonds. The pyrimidine ring which will have some conjugation with the phosphate group will also have a significant effect on the scattering of light, much like in the dye systems.

2. Experimental Methods

In this thesis, the nanoparticles used are as follows:

Nanoparticle	Name used	Experiment code used
Silver nanospheres	"Spheres"	Ws
Silica-capped Silver nanospheres	"Spheres"@SiO2	WsSi
Silica-capped Silver nanospheres with Ag satellites	"Spheres"@SiO2 Sat	WsSiSat
Silver nanoprisms	"Blue"	Wb
Silica-capped Silver nanoprisms	"Blue"@SiO2	WbSi
Silver nanoparticle dispersion	"Yellow"	Wy
Silica-capped Silver nanoparticle dispersion	Yellow@SiO2	WySi

Table 2.1: Summary of nanoparticle types used in this thesis, and the names they are referred to in graphs.

2.1 Silver nanospheres

Nanospheres are produced via a polyol synthesis:
In a 250 mL round bottom flask, 50 mL of ethylene glycol was heated to 140°C with vigorous stirring, to this 6 g of polyvinylpyrrolidone (PVP, avg Mw = 40k g/mol), this was heated until all the PVP dissolved. Following PVP dissolving, 1 mL of silver nitrate (1 g/mL) was added, and the solution was heated for one hour, then quenched by submerging the flask in ice. The solution became yellow upon the addition of silver nitrate, then slowly turned turbid and formed a green-grey colour once completed. The nanoparticle solution was washed via centrifugation (using a 1-14 Sigma Micro Centrifuge) at 5000 rpm (18447 x g) for 30 mins with acetone three times to remove PVP, and then re-dispersed in 21.7 mL of ethanol.

2.1.1 Ag@SiO_2 nanospheres

Silica coating was produced via two main methods, primarily via the Stöber method.

Method 1 - Stöber method 1
At room temperature with constant stirring, and with 21.7 mL of solution from above, in Section 2.1 in a 250 mL round bottom flask, 68.5 mL ethanol was added, then 2.4 mL of ammonia (29%) followed by drop-wise addition of an ethanolic solution of 5.14 mL TEOS (Tetra-ethyl orthosilicate, or tetraethoxysilane), (2.5 vol%) over 3 min. Following this, the reaction was allowed to stir for 20 hours. The particles were then washed via centrifugation using acetone and the resulting solution was re-suspended in 20 mL ethanol.

Method 1.5 - Stöber method 2
A faster alternative to the above method is the following: At room temperature, with vigorous stirring, 125 μL of a concentrated solution of the nanoparticles produced in Section 2.1, and 125 μL of pure TEOS, were stirred for about a minute. Then, 3 mL of an ethanolic solution containing 250 μL of ammonia (29% stock) was added. The solution was then stirred for 4 min and then quenched with 20 mL ethanol. This solution was then washed by centrifugation at 9000 rpm (59768 x g) via re-suspension in MilliQ water. The shell size can be controlled by changing the initial amount of TEOS added.

Method 2 - Hydrolysis via sodium silicate
At room temperature with constant stirring, an ethanolic suspension of 30 mL of re-suspended particles from the Stöber method was made, and the added 400 μL of (3-aminopropyl)-tetraethylorthosilicate (1 mM) was added to the suspension and was stirred for 15 min. Following this, 3.4 mL of an aqueous sodium silicate (0.54 vol%) solution adjusted to pH 11, was added. Upon addition of sodium silicate, the solution was then stirred for a further 48 hours.

2.1.2 Ag@SiO_2@Ag core-shell-satellite nanospheres

Using a diluted sample of Ag@SiO_2 (Stöber method) made of the following: 1 mL nanoparticles in 19 mL ethanol. To this 20 mL solution, 10 mg of silver nitrate (99%) was added, and 20 μL of n-butylamine (98%) was added. This solution was then stirred gently in a Thermofisher ThermoMixer at 500 rpm at 50degC for 10 mins. The resulting solution was washed via centrifugation using MilliQ filtered water. This was also attempted using a round bottom flask to avoid having to split up the solution into smaller parts after adding the silver nitrate, which could add errors concerning reaction timing; the UV-vis comparison can be seen in Fig.(3.4) in Section 3.1.

2.2 Silver nanocubes

Silver nanocubes were produced in two main ways - via a polyol synthesis and an aqueous method.

Polyol 1 - Ethylene glycol (EG)[194]
At 150°C, constant stirring, in a 50 mL round bottom flask, to 6 mL of anhydrous EG, 2 mL of $AgNO_3$ (0.2 M, in EG), then shortly, 2 mL of polyvinylpyrrolidone (PVP) (111 mg/mL, avg M_w = 40-50g/mol) was added over 3 min via drop-wise addition. The solution became yellow upon the addition of PVP, and after 70 min, became turbid and resulted in a green-grey solution. This solution was then washed 3 times via centrifugation at 9000 rpm (59768 x g) for 10 min, and re-suspended in MilliQ water each time.

Aqueous method
Aqueous solutions of CTAC (5 mL, 20 mM) and AA (0.5 mL, 100 mM) were added into a 20 mL glass vial and heated to 60 °C for 10 min. Following this, aqueous solutions of CF_3COOAg (50 μL, 10 mM) and $FeCl_3$ (80 μL, 4.29 μM) were then added in one shot. The reaction solution had a pH value of about 3.1 during the entire synthesis. After 6 h, the products were collected by centrifugation at 8000 rpm (47224 x g) and re-dispersed in DI water.

2.3 Silver nanoparticle dispersion

All reagents are made with MilliQ filtered water. In 20 mL vials with constant stirring at room temperature and added in order, 2 mL of trisodium citrate (1.25×10^{-2} M), 5 mL of silver nitrate (3.75×10^{-4} M), 5 mL H_2O_2 (5×10^{-2} M), 40 μL KBr (10^{-3} M), and finally, 2.5 mL of freshly prepared $NaBH_4$ (5×10^{-3} M) was added. The solution begins with a pale yellow colour, goes to an orange-brown and eventually to a brighter yellow than it began, it takes about 4-8 mins to reach this point and the colour does not change further.[52]

2.3.1 Ag@SiO_2 Silver nanoparticle dispersion

At room temperature, using 6 mL of the final dispersion from the previous section 2.3, it was concentrated and washed via centrifugation (three times at 8000 rpm (47224 x g)), and re-dispersed in ethanol to a final volume of 125μL. This solution was then added to 125μL of TEOS (Tetra-ethyl orthosilicate, or tetraethoxysilane). Then a 3 mL ethanolic solution containing 250μL ammonia (20%) was added. The solution was then stirred for a further 4 min before being quenched with 20 mL ethanol. The resulting solution was then washed with water three times and then concentrated via centrifugation to about 2 mL.

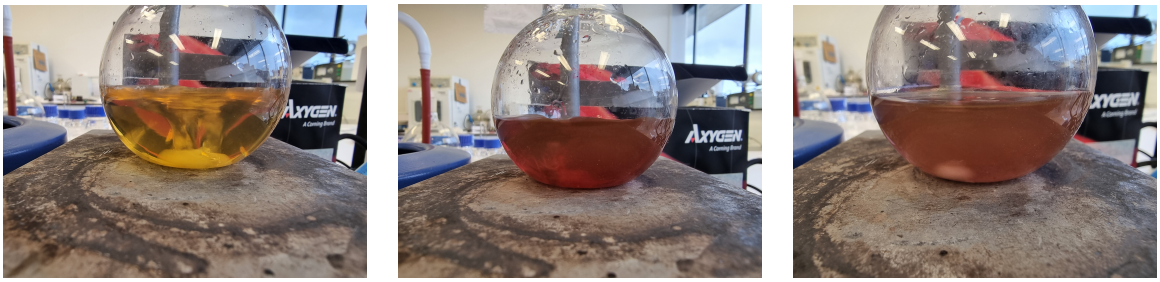

Figure 2.1: From left: nanoparticle solution of 2.3 after washing using method 2 to immediately after adding TEOS.

A second method was attempted, where it was the exact same process as the one described above, but with half the amount of ammonia solution and TEOS. The difference in the UV-vis spectra can be seen in Fig.(3.4) in Section 3.1.

2.4 Silver nanoprisms / triangular nanoplates

There were two main methods used in producing triangular nanoprisms, both are based in the citrate and borohydride reduction of silver.

Method One[52]
In 20 mL vials with constant stirring at room temperature added in order, 2 mL of trisodium citrate (1.25× 10^{-2} M), 5 mL of silver nitrate (3.75×10^{-4} M), 5 mL hydrogen peroxide (29%v/v, 5×10^{-2} M), finally, 2.5 mL of freshly prepared sodium borohydride (5×10^{-3} M) was added. The solution begins with a pale yellow colour, goes to an orange-brown and eventually to a dark blue, it takes about 4-8 mins to reach this point and the colour does not change anymore. This method is the primary one chosen, as it is the simplest and produces a solution with sufficient uniformity for the SERS experiments.
Method Two[214]
To 200 mL MilliQ filtered water and vigorous stirring at room temperature, added 12 mL trisodium citrate (0.075 M), 200 μL silver nitrate (0.1 M), and 480 uL hydrogen peroxide (29%v/v) then 1.2 mL of freshly prepared sodium borohydride (0.01 M) was added. The solution goes through various colour changes, from light yellow to brown-grey colour, shifting to orange, reddish-orange and then finally finishing at a deep blue. This is an indicator of when the reaction has stopped, as the solution no longer changes colour at this point. For use with the SLIPSERS measurements, 6 mL of this solution was washed via centrifuge at 9000 rpm (59768 x g) for 10 min, and then re-suspended in water three times. For the final re-suspension, they are combined with 500 μL of MilliQ water and used within a few days, as triangular nanoprisms are susceptible to etching.

Method Three [190]

To 24.04 mL of MilliQ filtered water, trisodium citrate (75 mM, 0.5 mL), poly(vinyl)-pyrrolidone (PVP) (17.5 mM, 0.1 mL, avg M_w = 29 000 g/mol), H_2O_2 (30 wt%, 60μL), was added and stirred at room temperature. Then sodium borohydride was added (100 mM, 0.25 mL) was added quickly and resulted in a light yellow solution. Over about 30 minutes, the solution changed colours from yellow, brown, red, and then green and eventually turning blue. Once this occurs, the reaction was complete. Nanoparticles are washed three times with water and then concentrated to a volume of 5 mL.

2.4.1 Ag@SiO2 Nanoprisms

At room temperature, using 6 mL of the final solution in Method One from Section 2.4, it was concentrated and washed via centrifugation, and re-dispersed in ethanol to a final volume of 125μL, which was then added to 125μL of tetraethyl orthosilicate (TEOS). Then a 3 mL ethanolic solution containing 250μL ammonia. The solution was stirred for a further 4 min before being quenched with 20 mL ethanol. The resulting solution was then washed three times with MilliQ water and then concentrated via centrifugation to about 400 μL.

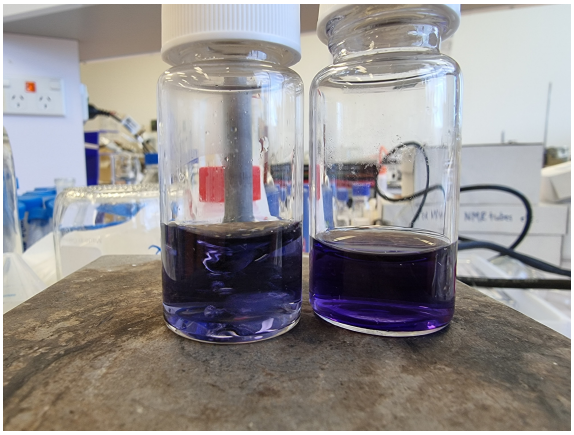

Figure 2.2: From left: silver nanoprisms after capping with SiO_2 shell, right: silver nanoprisms before addition of SiO_2.

2.5 Slippery Liquid Infused Porous Substrate (SLIPS)

SLIPS surfaces are prepared by placing a PTFE unlaminated filter, with a pore size of 0.2μm, 13 mm diameter, (provided by Sterlitech, SKU PTU021350), on a glass slide, placing a drop of a polyfluorinated oil (Krytox GLP100 or 105, about 80μL). This was then spun at about 1000 rpm using a Spin-coater, taking care for the oil to spread thinly without the filter falling off the glass slide. Next, in an oven set to 70°C a drop of nanoparticle solution (80μL) was pipetted onto the filter. The slide was then allowed to dry in the oven until the drop concentrates into a spot.

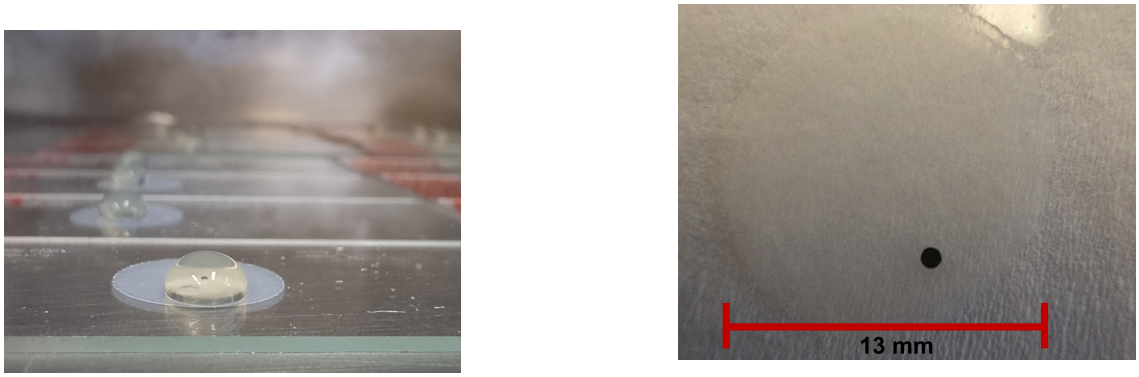

(a) (b)

Figure 2.3: (a) Drops of silver nanoparticles drying in the oven; (b) a spot of silver nanoparticles dried in an oven using the SLIPs method described above.

2.6 Raman spectroscopy

Raman spectra were recorded under ambient conditions with a custom-built Raman microscope. A 532 nm or 633 nm excitation (Laser Quantum Torus 532) was focused onto the silver nanoparticle/analyte aggregate via an N.A. = 0.65 (40× magnification) microscope objective. The laser power at the sample was <1 mW. Back-scattered Raman and Rayleigh scattered light was collected by the same objective, and the Rayleigh component was rejected by a 532 nm Raman edge filter (Iridian Spectral Technologies) and focused onto the entrance slit of a Teledyne (Princeton) Instruments Isoplane81 (FERGIE) spectrograph. Spectral data was acquired using LightField 6.1 software. No background removal was applied during data collection. The detector exposure time was 1 s and between 30 and 120 exposures (or 'frames') were captured and stored separately before data analysis. As discussed in Sec.1.2.1, these 'frames' of the spectra (which are spectra in of themselves) are 1024 x 256 pixels in size (meaning 1024 wavenumbers can be observed) are then averaged over the 30 or 120 exposures - leading to the final spectra shown in later sections.

2.6.1 SLIPS-SERS

The SLIPS samples prepared in 2.5 was placed upside down on the inverted microscope described in 2.6. The laser was focused on the spot of nanoparticles, adjusting focus when necessary to optimise the collection of data.

2.7 UV-vis Spectroscopy

All UV-vis spectra are acquired using a Shimadzu UV-1800, with scan speed selected to 'Quick', and the wavelength range set from 190 nm to 1100 nm.

2.8 Electron microscopy

Collection of Transmission electron microscopy data were collected on a FEI Tecnai G2 Spirit BioTWIN courtesy of the MMIC at Massey University.

2.9 Data Analysis via Python

Data was analysed using a custom Python 3 notebook, a Principal Component Analysis and a Linear Discriminant Analysis was done using the scikit-learn package. The purpose of a Principal Component Analysis (PCA) is to reduce the dimensionality of a large dataset containing a high number of features per observation, while preserving as much of the information and variation in the data as possible. In the case of this thesis, each spectrum contains essentially 120 spectra (called 'frames' in the detector's software) averaged over time, so doing this allows us to compare the effect certain bands have on the overall spectra, and their distribution across those 120 spectra. It does this by transforming the data into a new coordinate system where the features are linearly uncorrelated and ordered by their importance. The new features are called principal components (PCs) and they are linear combinations of the original features. PCA can be used for data exploration, visualisation, compression, and denoising of data. Similarly, Linear Discriminant Analysis (LDA) is used to find a linear combination of features that separates two or more 'classes' of objects or events within a dataset. In the case of this thesis the 'classes' were defined as either the nanoparticle type, or the analyte, and an average of each spectrum is a data point (rather than using the 120 'frames' per spectra). It can be used for either classification or a dimensionality reduction of the dataset. LDA is based on the assumption that the features follow a multivariate normal distribution and have an equal covariance matrix for each class. These assumptions may not hold for every dataset, meaning issues can arise when interpreting a dataset that does not work well with LDA. For example, not all data sets follow a normal distribution; if the data is not normally distributed, the performance of LDA may be suboptimal. LDA attempts to maximise the variance between the defined classes, and to minimise the within-class variance of the projected data, so that the classes are maximally distinct from one another. This allows a visualisation of the dataset into distinct classes. LDA should not be used as evidence for the existence of classes within the dataset as the user is predefining classes (supervised learning). Whereas PCA shows the existence of classes within the dataset without user input (unsupervised learning).

3. Results and Method Development

3.1 Identifying the LSPR peaks of the chosen nanoparticles *via* UV-vis spectroscopy

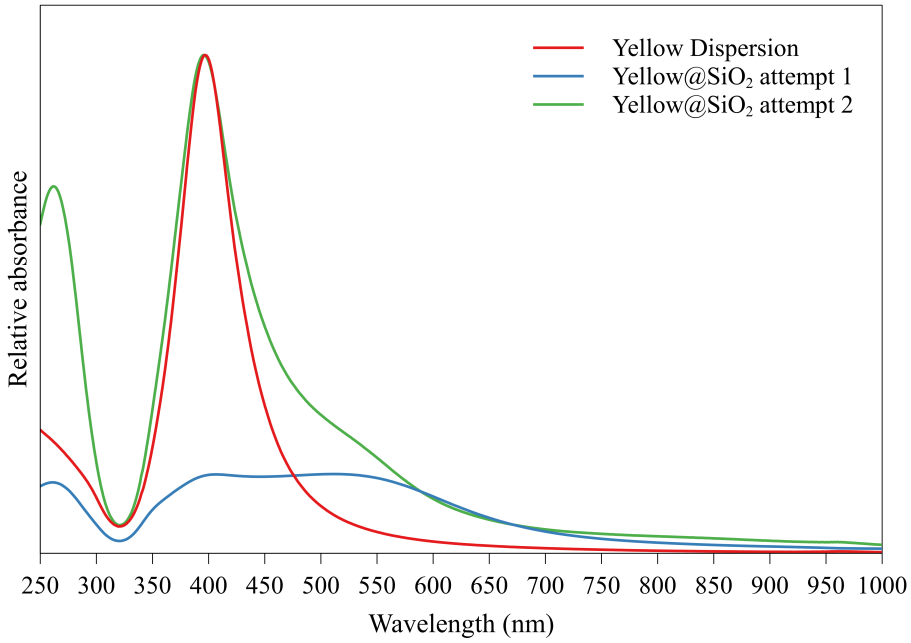

Figure 3.1: Overlay of washed nanoparticle dispersion (red line) compared to capped Ag@SiO2 (blue line), and a second attempt for silica capping (green).

As explained in Section 1, the Localised surface plasmons are the key factor in determining the type of laser used in the SERS measurements for the nanoparticles. As a result, a quick analysis of the nanoparticles using UV-vis spectroscopy or UV–vis extinction spectroscopy to determine the localised surface plasmon resonances of the nanoparticles, and therefore the appropriate laser wavelength to use for running the SERS measurements. All of the UV-vis spectra below have been normalised by dividing the absorbance values by their maximum, making sure each spectrum is relative to each other. In Fig.(3.1), the main peak (λ_{max}) occurs at 397 nm, with

another peak appearing beyond 250 nm, this peak is relatively sharp. Similarly, the third spectra (green line, attempt 2) has a peak at practically the same λ_{max} of the yellow dispersion. However, there is some peak broadening, which can be expected as the silica would the nanoparticles larger overall, changing how the light scatters. In addition, the peak that appears beyond the 250 nm limit appears to have shifted to higher wavelengths, it is unclear what this peak is from. In the first attempt (blue) appears that too much silica was added there was broadening and shifting of UV-vis spectra, this sample was ignored.

In Fig.(3.2), the λ_{max} for the prisms (red line) is at 599 nm, with a secondary peak appear at 334 nm. Overall, the peak is very wide, which means the nanoparticles might have varied uses in terms of the incident beam used, however, it might favour the 633 nm laser, as the λ_{max} is closer to this than the 532 nm which is used in the majority of the SERS spectra in this thesis. In addition, for the silica capped nanoprisms, the λ_{max} has shifted to a higher wavelength of 614 nm. This might be due to how the silica shell forms on the prisms. This might indicate that the nanoparticle shell must be controlled more precisely in future work.

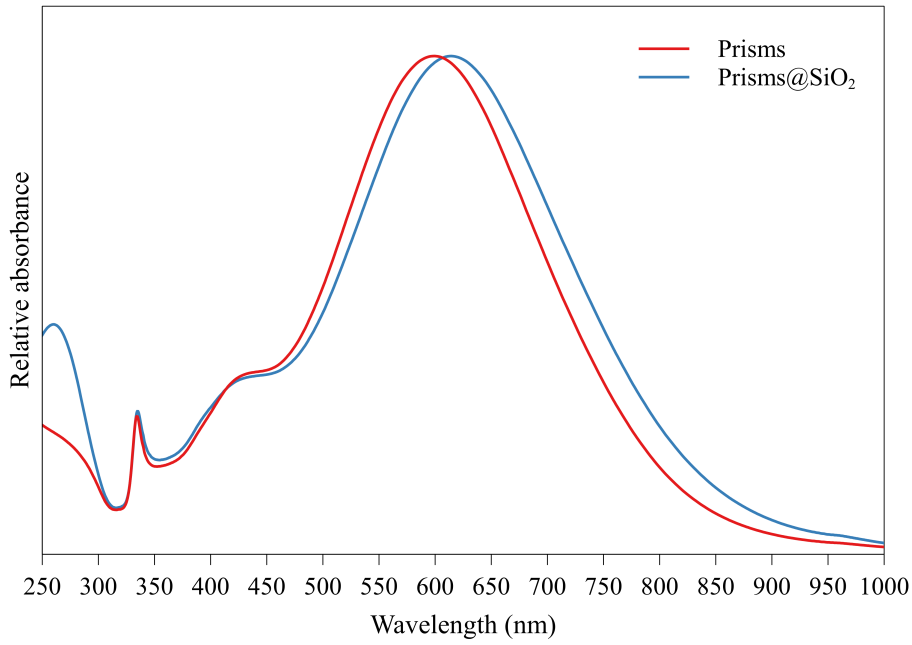

Figure 3.2: UV-vis spectra of the silver prisms and the silica capped prisms used throughout this thesis.

In Fig.(3.3), there is a broad peak with a λ_{max} at 532 nm, which makes this potentially an ideal candidate for the SERS experiments. Combined with a large amount of homogeneity, these nanoparticles have the potential to be the most sensitive. The aqueous method (blue) has a broader peak and a slight shift in wavelength of the λ_{max} to about 530 nm. As the polyol process produced a much sharper, more intense peak compared to the aqueous method. However, it was not worth tuning this reaction beyond this point, as there is significantly more research surrounding the polyol process. Therefore polyol method was used for the remaining experiments

in the TEM and the SERS experiments.

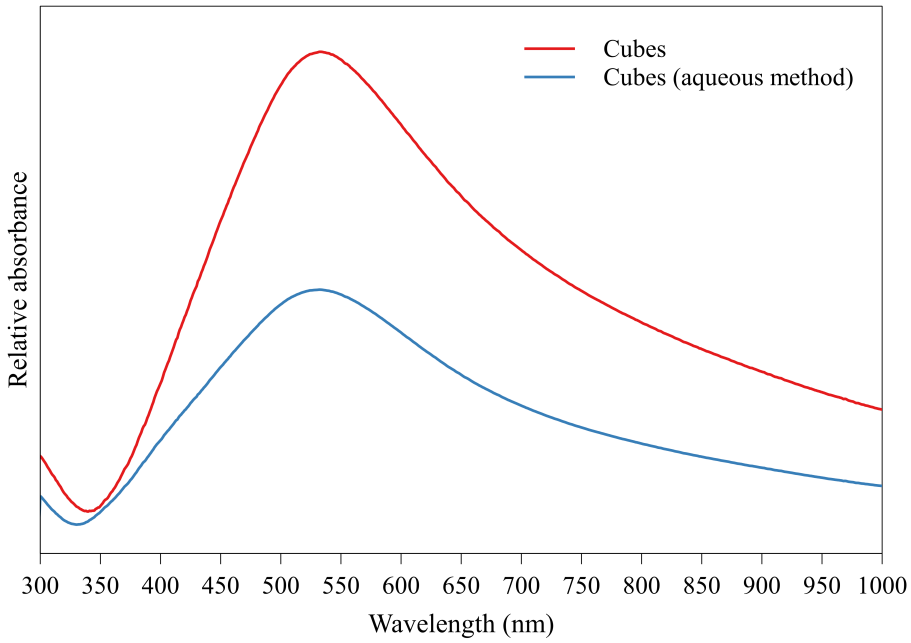

Figure 3.3: UV-vis spectra of the silver nanocubes used throughout this thesis. A broad peak is seen at around 550 nm.

In Fig.(3.4), the sphere's UV-vis spectrum (red dashed line) is very intense due to a high concentration, leading to a small amount of noise at the λ_{max}, which lies at 439 nm, there is also another peak that appears beyond the 250 nm limits. The Stöber method of producing a silica shell (blue) showed much sharper λ_{max} than the sodium silicate hydrolysis spectra (green dotted line), and also displays some more broadening toward high wavelengths to about 650 nm, though it is not a lot of broadening. The spherical nanoparticles with satellites had overall broader and less intense spectra. In particular, the method involving the Thermomixer is shifted more towards the λ_{max} of the spherical nanoparticles. due to the introduction of many smaller nanoparticles, which won't all form spherical nanoparticles, these smaller silver nanoparticles will also scatter the light more, leading to broader overall peaks. This might explain why the sodium silicate method was broad too, as silica nanoparticles scatter the light and broaden the observed peak.

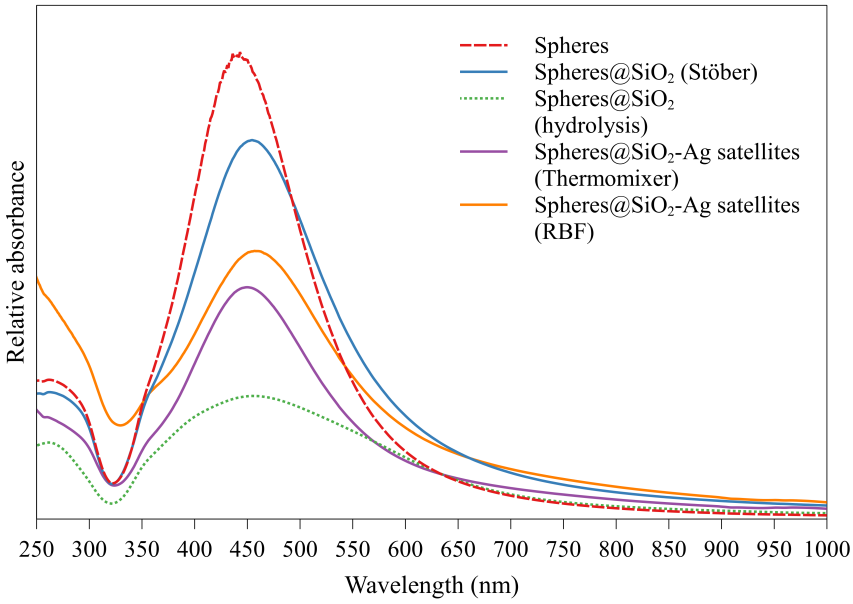

Figure 3.4: UV-Vis spectra overlaying Spheres (red), Stöber method capped Ag@SiO_2 spheres from method (blue) and the Ag@SiO_2-Ag satellites.

3.2 Transmission Electron Microscopy

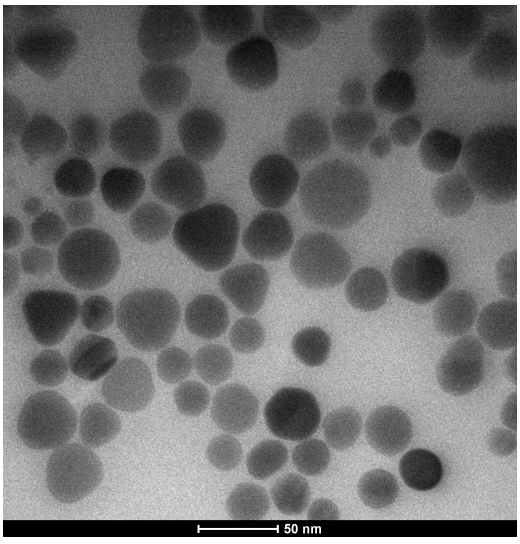

Figure 3.5: Transmission electron micrograph of the typical sample of the Silver dispersion ("yellow" nanoparticles); note the variation of shapes.

TEM was used to verify that the nanoparticles are approximately the desired shapes and size distribution, which has an affect on the . The silver nanoparticle dispersion ("yellow") below in Fig.(3.5), shows that this method produces a wide range of shapes that appear similar to the ones sold by Sigma-Aldrich (SKU:730785-25ML),[215] as they also the same colour and similar production method. However, as this method

was used previously in this research group, this is the expected the nanoparticle morphology from this method.[95] From Fig.(3.6a), the silver nano prisms have a size of about 45-50 nm. In the wider picture, from Fig.(3.6b), the nanoparticles have a broad range of nanoparticle morphology, though the most common is the prism shape, with some scattered truncated prisms. Though it is known that polydispersity of the nanoparticle sizes and the heterogeneity of the nanoparticle shapes has a negative effect on the SERS performance of a sample. However, as these nanoparticles will be concentrated into a small aggregate via SLIPS, this effect might be reduced as hotspots will form at edges between aggregated nanoparticles. What this entails is that monodispersity is *better* for increased sensitivity. For the purpose of this thesis, exact control is not as important.

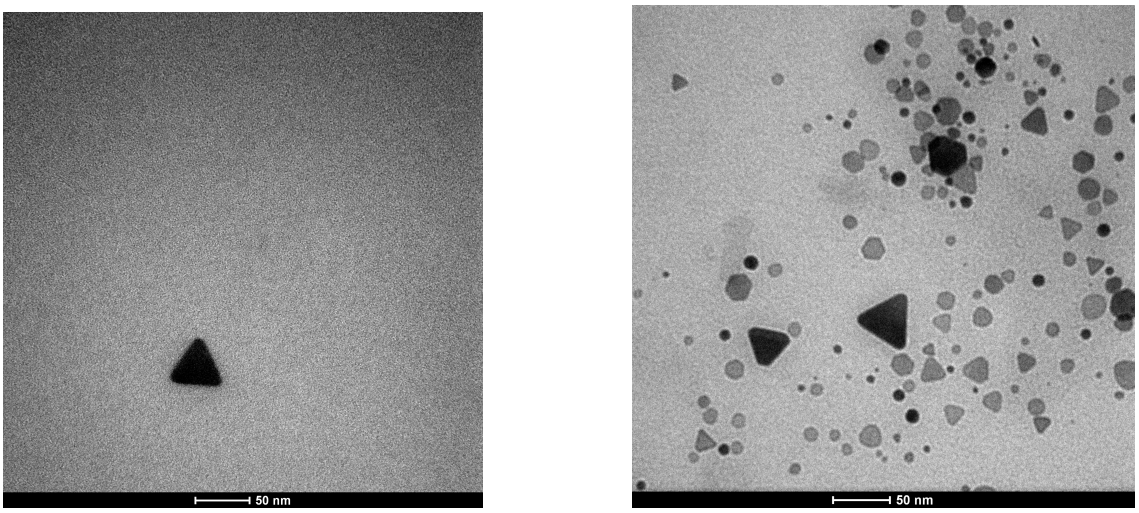

(a) (b)

Figure 3.6: (a) An isolated TEM image of a single nanoprism; (b) a different area of the TEM sample showing the variation of nanoparticles present in the silver nanoprism dispersion.

In the TEM image of the silver nanoprisms in Fig.(3.7) appears that some of the nanoparticles have been capped, though the micrograph is quite noisy/fuzzy for this so it is unclear if it's truly capped or just the electron beams producing this halo effect. Looking at the literature, more high-quality TEM micrographs show that silica shells are very lightly coloured compared to the silver core and the silica shell, unlike the TEM below in Fig.(3.7). However, the decision was made to continue with this particular sample for the SLIPSERS experiments.

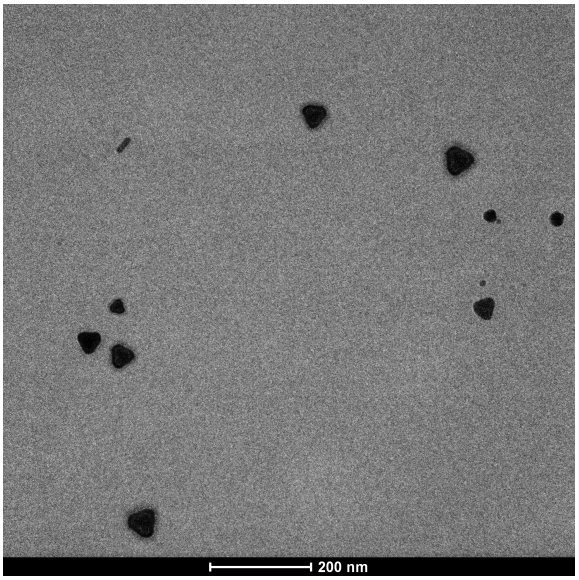

Figure 3.7: TEM microgrpah of the Silver nanoprisms capped with silica, described in Section2.4.1

In Fig.(3.8) it can be seen that despite the presence of some highly anisotropic silver nanorods, the nanocubes are relatively monodisperse and have a mostly homogeneous distribution of shapes. These should perform well as a SLIPSERS substrate. And given the high amount of sharp edges, at least compared to both the "yellow" nanoparticles and the silver nanoprisms, it in all likelihood should have the highest sensitivity.

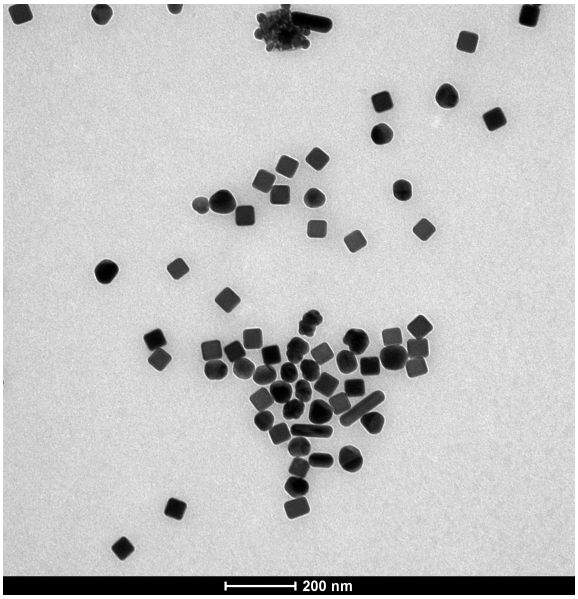

Figure 3.8: Transmission electron micrograph of the typical sample of silver nanocubes used in the SERS experiments.

The silver nanospheres in Fig.(3.9) show a lot of similarity with the nanoparticle dispersion in Fig.(3.5), however, and have much less density than compared to the silver nanocubes in Fig.(3.8), which share a similar method. Note that the silver nanospheres with satellites were a last-minute idea at the end of the project, so no time was available to use the TEM as it was under a lot of maintenance at the time.

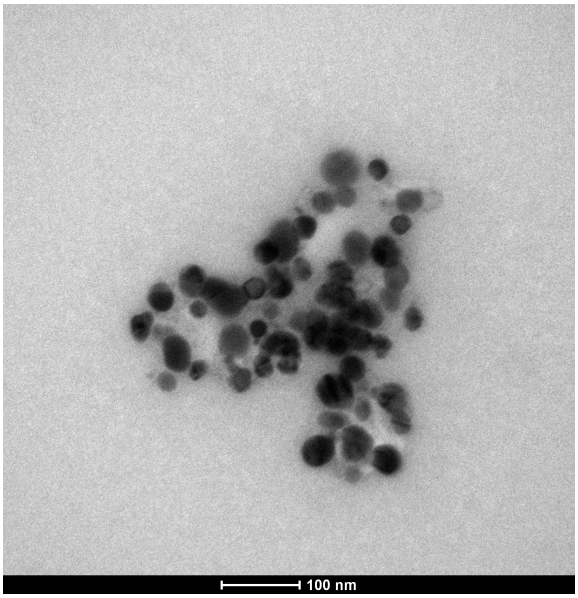

Figure 3.9: Transmission electron micrograph of the typical sample of silver nanopsheres used in the SERS experiments.

3.3 Navigating through capping agents

Capping agents play a key role in nanoparticle synthesis, as they enable the nanoparticles to gain their signature shapes. As a result, they have the potential to interfere with the analysis of selected analytes, as SERS can be somewhat unpredictable with how these capping agents or any contaminants can affect the observed signals. Generally speaking, these capping agents are removed via a washing process where the nanoparticles are centrifuged, the pellet is re-dispersed with a solvent such as water, acetone or ethanol several times, and then re-dispersed into a concentrated solution used for SERS and SLIPSERS measurements. Note that not all of the modes are assigned as this can get difficult to do under SERS conditions, although some modes can be assigned more easily than others. Identifying what the capping agents appear to be in their Raman and SERS spectra, respectively, will help in the analysis of the organophosphorus and dye probe data.

3.3.1 Trisodium Citrate

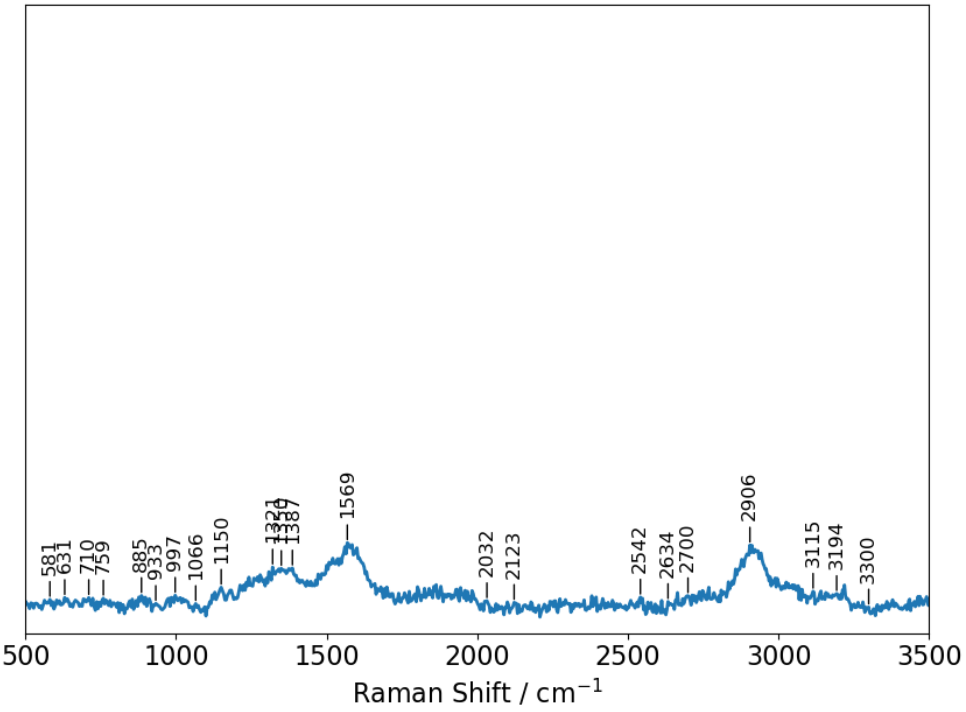

Figure 3.10: A SLIPSERS spectrum of the "yellow" nanoparticle dispersion described in Section 2.3.

Trisodium citrate is a common capping and reductant; is a relatively stable capping agent, especially when the surface charge is balanced correctly and nanoparticles produced with this compound can have quite long shelf lives if stored correctly (up to several months in a fridge). However, if this charge balance is disturbed, nanoparticles will easily destabilise and the nanoparticles will agglomerate and aggregate. This

means trisodium citrate is easy to remove - only requiring about two to three washes to remove the capping agent. Another way to remove citrate is to use NaCl, and given silver's affinity for Cl- ions NaCl is quite effective at displacing citrate, reducing the number of washes needed. Raman spectra of citrate were acquired by grinding the small trisodium citrate crystals into a powder and placing a small amount between two microscope coverslips, seen in Fig.(3.11).

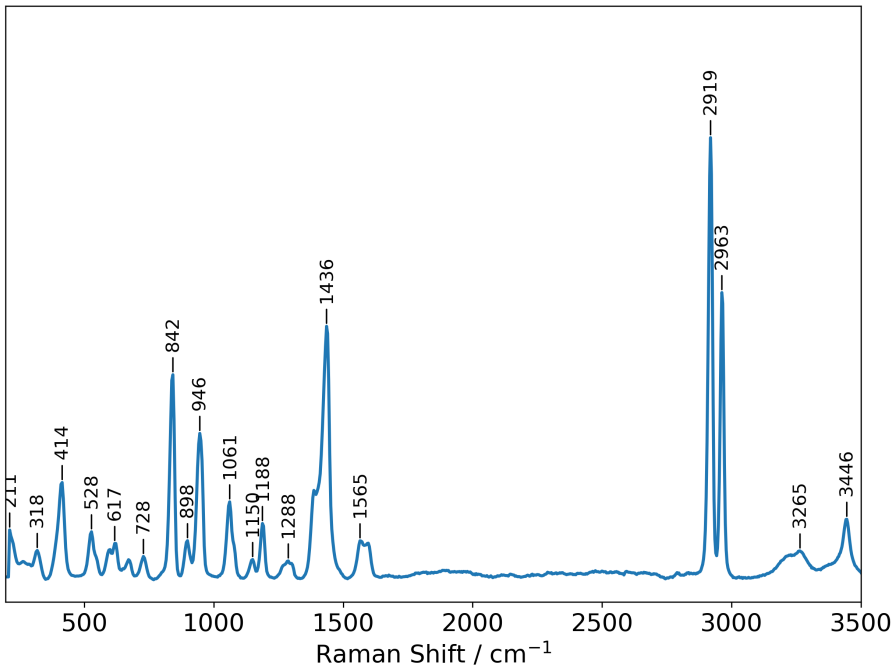

Figure 3.11: Raman spectra of trisodium citrate collected on a 532nm incident beam.

It is important to note that the SERS spectra in Fig.(3.13) will display peak broadening, likely due to the silica cap and the effects described in Sec.1.2.6.
A comparison of the spectra from the literature below in Table 3.1 shows that there is some agreement; however, the Raman spectrum from this paper is done in an aqueous media, and using 633 nm excitation, and not in the solid form or the 532 nm laser, as was done in this thesis. For this SERS spectrum in this thesis, citrate was adsorbed onto silver nanoparticles and dried using SLIPS, whilst the literature uses a silicon wafer as a substrate to dry their nanoparticle and citrate mixture.

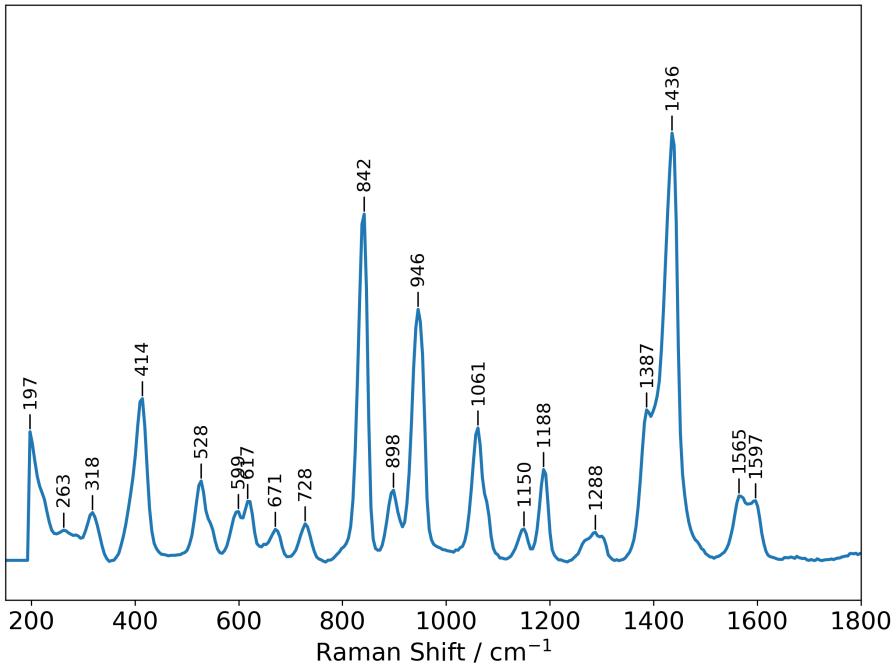

Figure 3.12: Raman spectra of trisodium citrate from 150 cm-1 to 1800 cm-1. Excitation wavelength: 532 nm.

Mode(s)	Frequency (cm^{-1})			
	Lit. Raman[216]	Raman exper.	Lit. SERS[216]	SERS exper.
$v_s(C-H)$	–	2963	–	–
$v_a(C-H)$	–	2919	–	2919
$v_a(COO)$	1567-1630	1565, 1597	1600-1603	1517, 1585, 1680
$v_s(COO)$	1406	1387, 1436	1375-1382	1346, 1391
$\delta(COO)$	1257-1282	1288	1279	1263
$v(C-OH)$	1042-1082	1061	1079	1019
$v(C-COO)$	943	946	924	
$v(C-C)$	830	842 824-846	838	
$\delta_{\text{out-of-plane}}(COO)$	667	671	791	617

Table 3.1: Summary table of the important Raman active modes in trisodium citrate for the experimentally collected Raman (532 nm), experimentally collected SERS (532 nm), and the literature values for Raman and SERS.[216] It is important to note that often in SERS spectra of organic compounds that the -CH2 stretching modes can broaden, often looking like one very strong, somewhat broad peak. Note: exper. is the experimental data and lit. is the literature values.

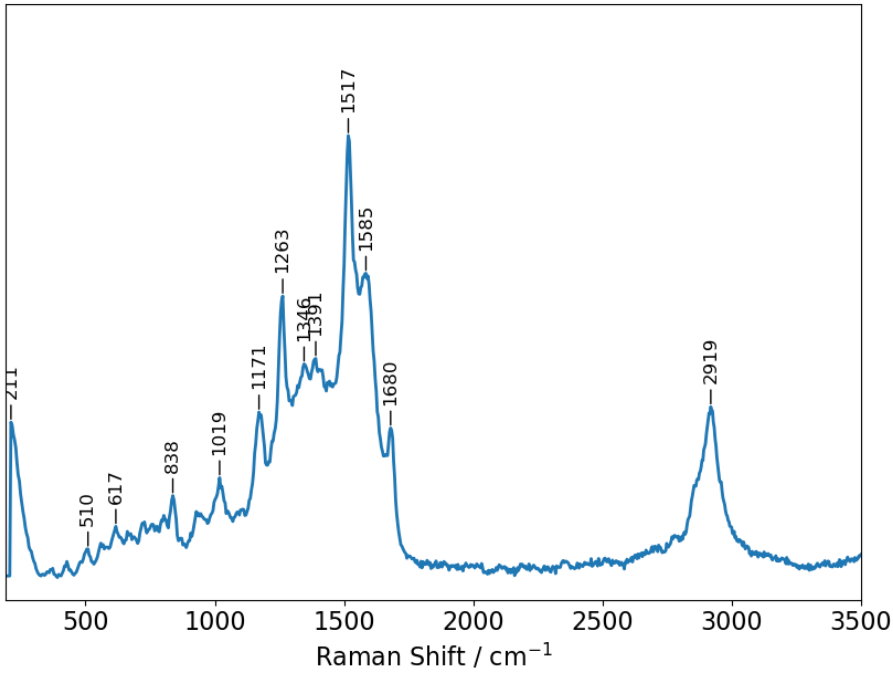

Figure 3.13: SLIPSERS spectrum of citrate using silica capped silver nanoparticles. This was done by concentrating the nanoparticles as described in Sec.3.4, and using a concentration of 0.01 M of aqueous trisodium citrate, then doing the SLIPS method as described in Section 2.5. Excitation wavelength: 532 nm.

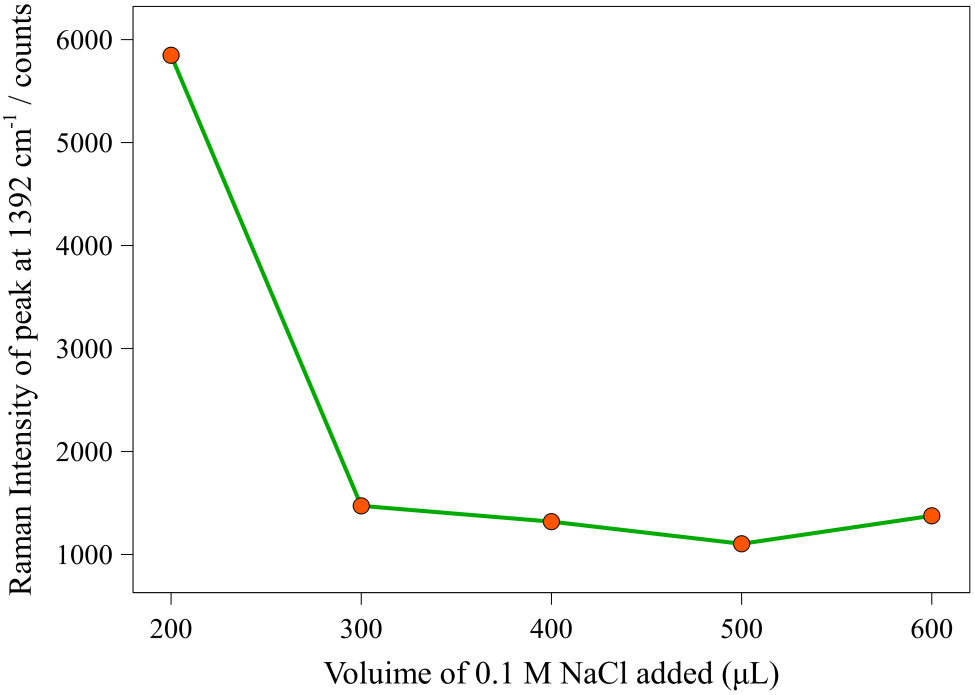

Figure 3.14: The Raman intensity change in an aqueous SERS spectrum of the peak at 1392 cm^{-1} after adding successive amounts of 100μL of 0.1 M NaCl solution. Excitation wavelength: 532 nm.

3.3.2 Polyvinylpyrrolidone (PVP)

PVP will contribute significantly to the observed Raman spectrum due to its size, and is typically used in 30k-55 kDa in size. PVP contains many oxygen atoms that will be attracted to both the silver surface and the silica surface of the nanoparticle that is used to create the SERS standard in Figure (3.16). Therefore it is necessary to attempt to completely remove it from the nanoparticles - this does however result in lower stability of the re-suspended nanoparticles. Removing PVP will require more washing steps when compared to cirtrate. A Raman spectrum of PVP was acquired by placing a small amount of PVP (Mw = 40 000 kDa) between two microscope coverslips. The glass on coverslips is quite thin, and will only have minimal affect on the observed Raman spectra. This spectra is in Fig.(3.15). Here there are the usual -CH_2 asymmetric and symmetric peaks combined at 2926 cm^{-1}.

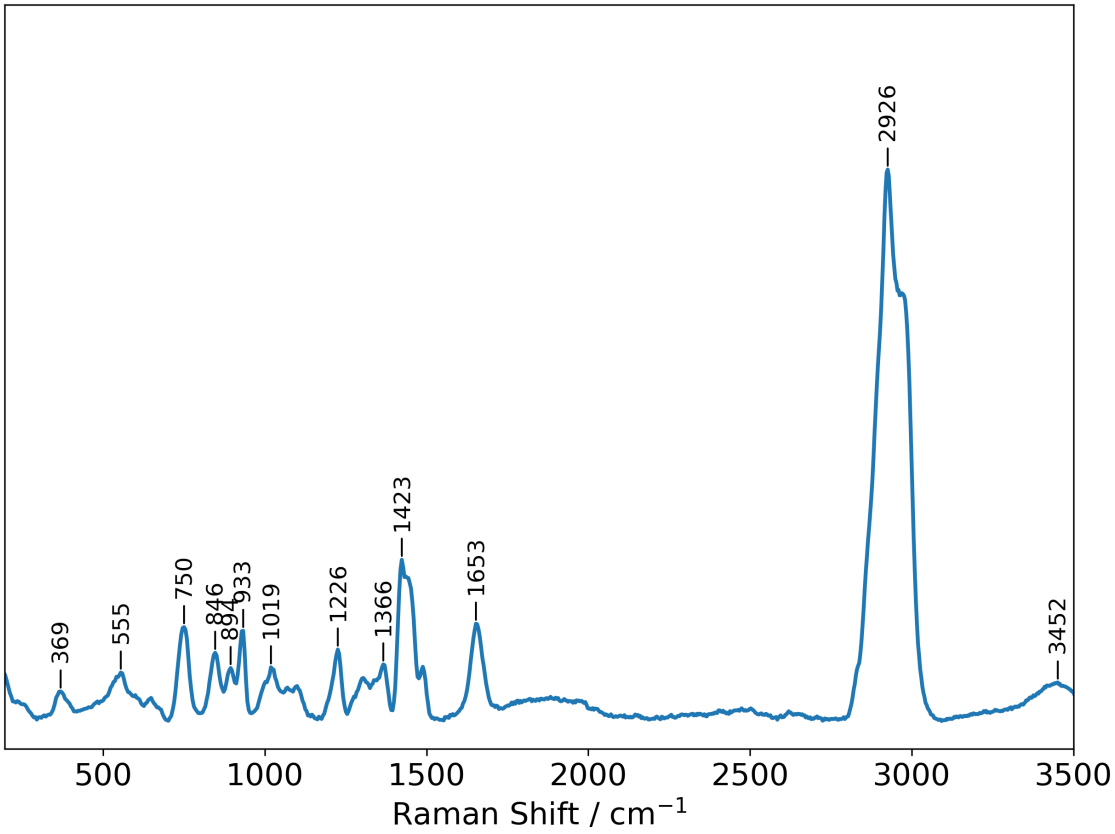

Figure 3.15: Raman spectrum of PVP (M_w = 40 000). Excitation wavelength: 532 nm.

PVP was removed by doing one wash with acetone (at 8000 rpm (47224 x g)) for the nanocubes or spherical nanoparticles and then washed five times using MilliQ water (at 8000 rpm (47224 x g)). In Fig.(3.17), the peaks from the PVP SERS spectrum are being reduced significantly up to the fifth wash. It's important to note that the reference SERS spectra appear different, despite sharing some modes, it is most likely due to the reference spectra using the silica capped nanoparticle dispersion

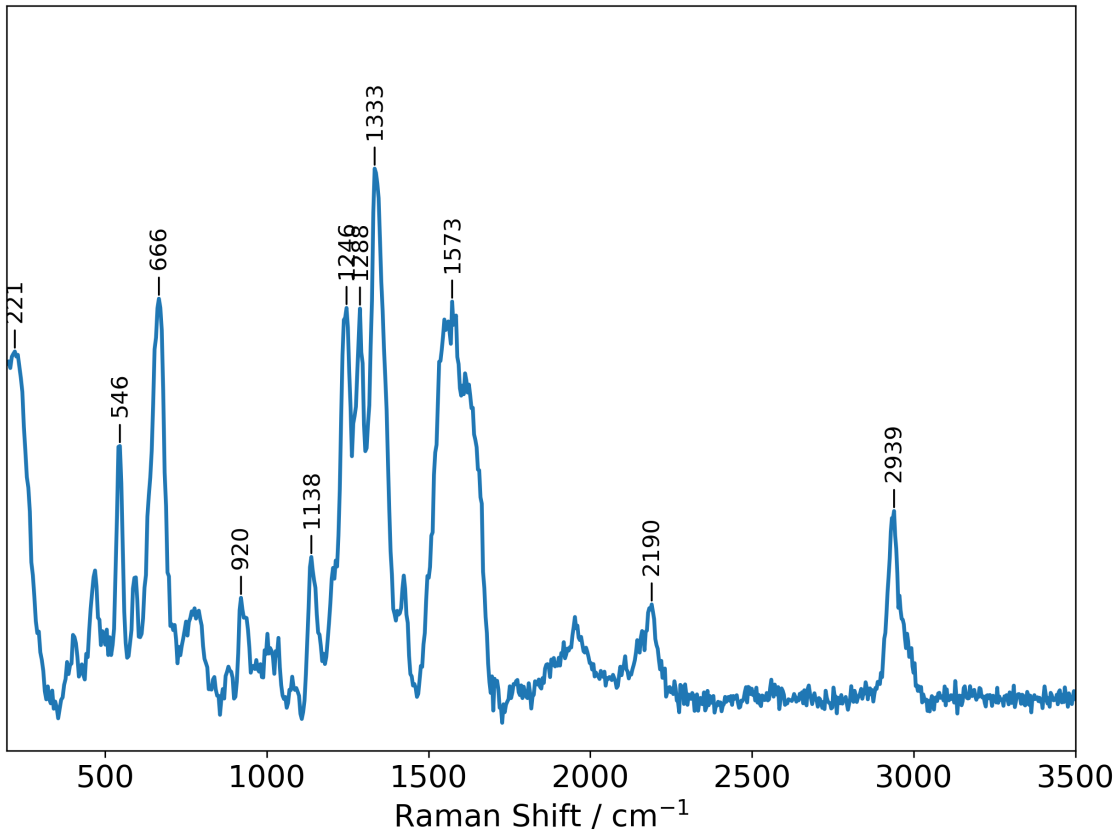

Figure 3.16: PVP (40,000 Da, 0.1 M) SLIPSERS spectrum using the Ag@SiO_2 yellow nanoparticles.

described in Sec.2.3.1, which, as mentioned in Sec.1.2.6, differing substrates can shift the spectra slightly. The PVP in these spectra is not in excess, which can improve the SERS spectra due to competition with adsorption onto the nanoparticle surface. By the final wash, the spectra is noisier, indicating that both the PVP and/or ethylene glycol has been more or less removed from the nanoparticle environment. For use in the SLIPSERS spectra, there is one final 'wash,' or rather, a concentration step, which should minimise any influence from PVP in subsequent SLIPSERS experiments.

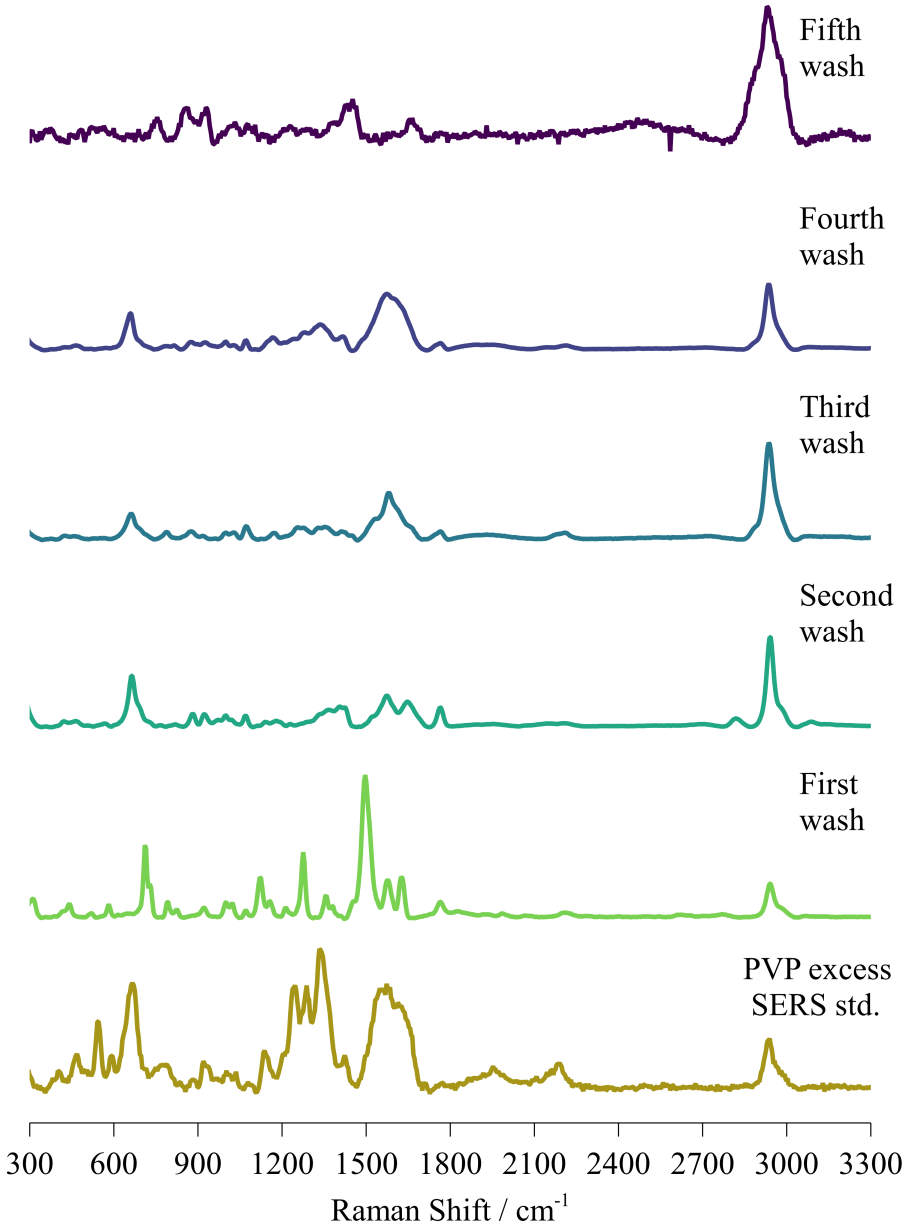

Figure 3.17: Stacked SLIPSERS spectra showing the effect of five consecutive washes of the spherical nanoparticles made in Sec.2.1 using MilliQ water following an initial wash of acetone. Excitation wavelength: 532 nm.

3.4 Optimising nanoparticle concentrations

Optimal nanoparticle concentrations are determined by washing the nanoparticles thoroughly. In this case, the "yellow" nanoparticle method (Section 2.3) will be used for determining the approximate optimal nanoparticle concentration: It is therefore appropriate for the citrate reduced nanoparticles, that the nanoparticles be washed at least 3 times with MiliQ filtered water, then as a baseline, concentrating 6 mL (or four 1.5 mL microcentrifuge tubes) into 400 μL. For the nanoparticles created

with PVP capping agents, it requires at least two washing steps with acetone, then at least four or more washing steps with MiliQ filtered water. As these nanoparticles are much more concentrated from the beginning, nanoparticles were instead diluted by adding 100 μL to 300 μL of MilliQ filtered water.

3.5 Evaluating drying methods with Rhodamine 6G

To determine how a drying method affects the observed SERS spectrum, some experiments were done using the mixed yellow dispersion (Section 2.3, Method 2), and a prepared solution of 10^{-7} M of R6G. This was prepared by concentrating 12 mL of nanoparticle solution and then re-dispersing in 185 μL of water, to this, 185μL of R6G solution was added and the mixture was allowed to sit for about 1 hour to allow R6G to adsorb onto the surface of the nanoparticles. None of the spectra in this section has had any post-processing applied aside from averaging of the spectra, to demonstrate the raw differences between the drying methods.

3.5.1 Glass

The drying method on glass involves taking an 80μL drop of nanoparticle-R6G mixture and drying it on a microscope slide in the same oven settings as the SLIPs substrates, resulting in a coffee ring-shaped spot. This method has one advantage over the rest: the glass provides more of a surface to transfer energy as heat to the glass and then the filter substrates. This could explain the relatively tighter distribution seen in Fig.(3.19).

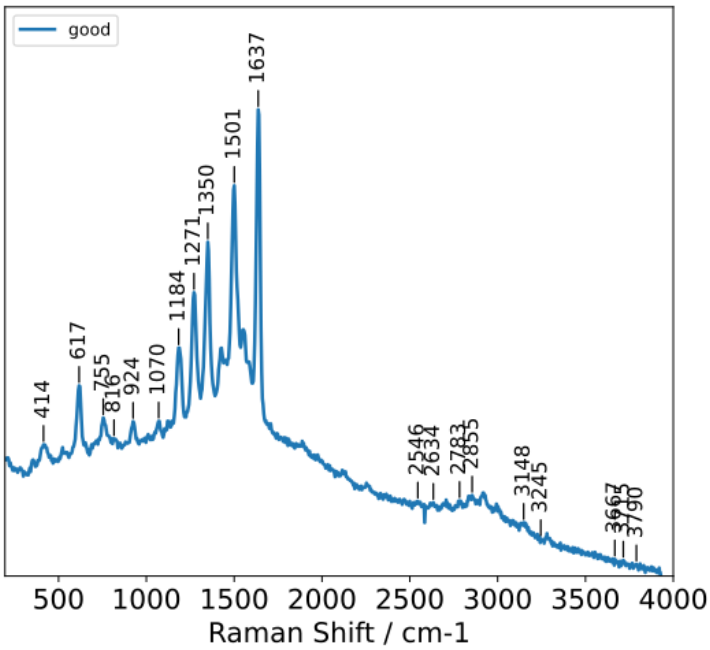

(a) Raman spectra averaged over 120 frames with peak picking

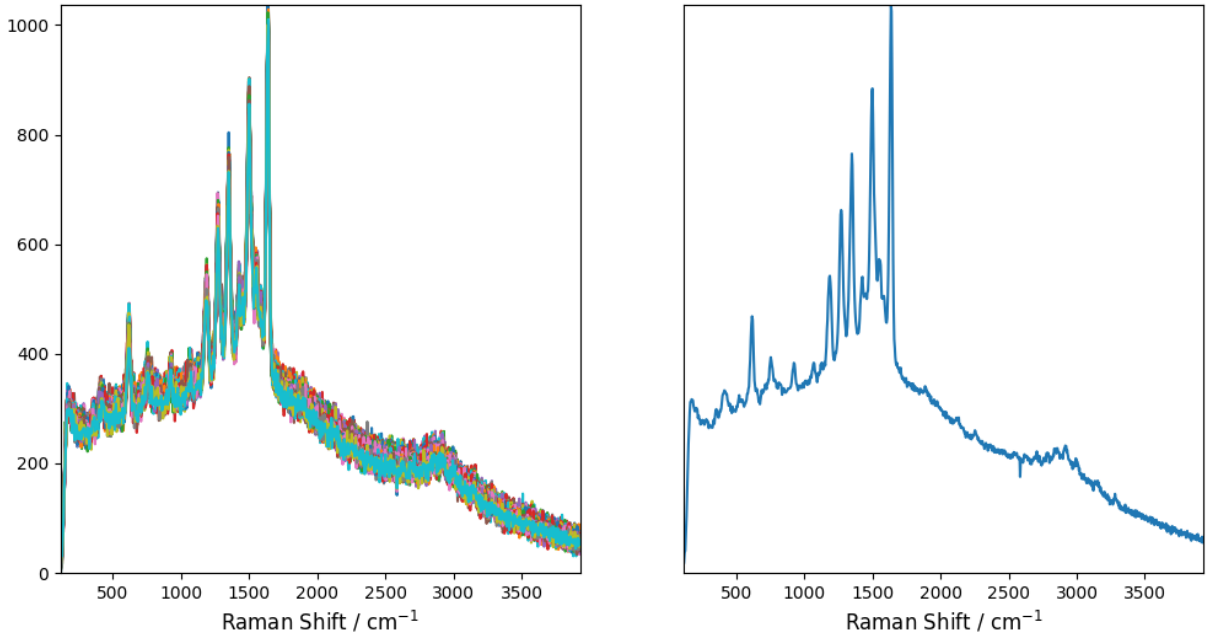

(b) Raman spectra over 120 frames stacked (left) and averaged over these frames (right)

Figure 3.18: (a) Peak-fitted averaged SERS spectrum of R6G on glass; (b) Raw SERS data of R6G using the same drying method of (a). R6G at an initial concentration of 10^{-7} M. Excitation wavelength: 532 nm.

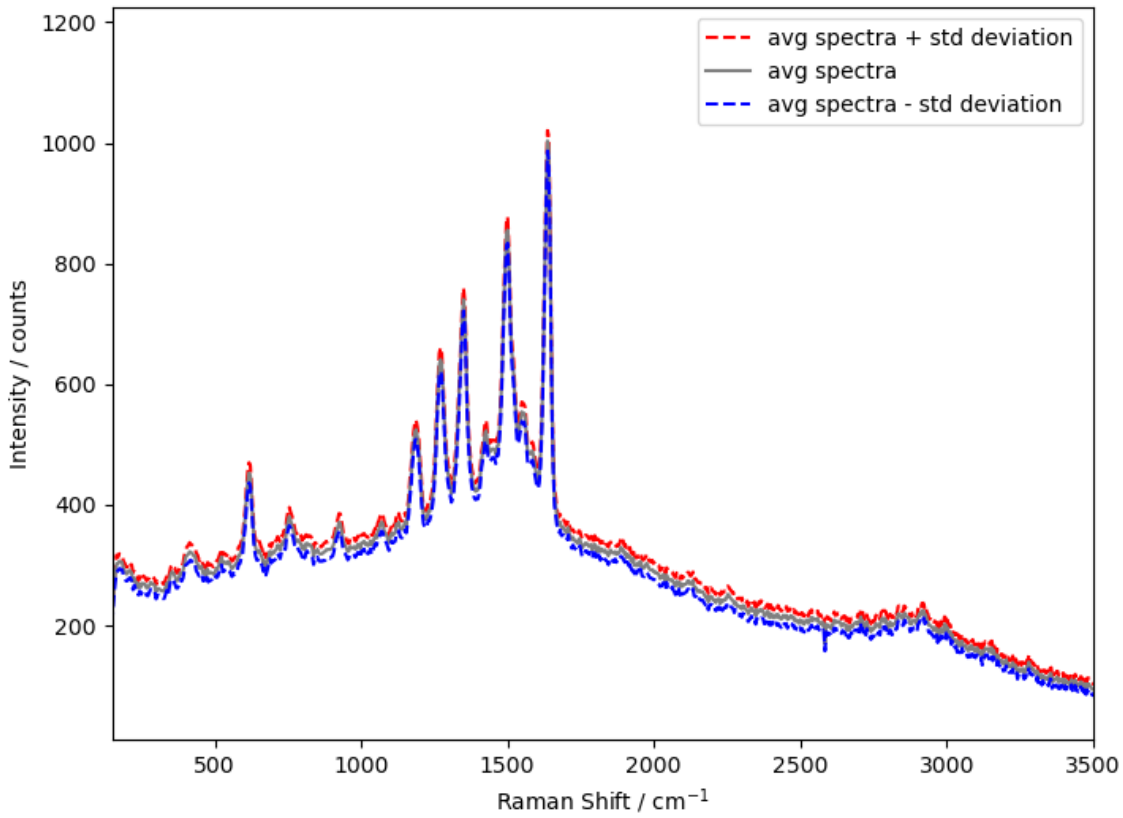

Figure 3.19: The standard deviation of all the spectra collected using glass as the main substrate for the drying method. R6G at an initial concentration of 10^{-7} M. Excitation wavelength: 532 nm.

The histograms in Fig.(3.20) show distributions that would be expected from sample with a tight distribution seen in Fig.(3.19), where the distribution is roughly normal (as the individual frames in Fig.(3.18b) do not show much variability.

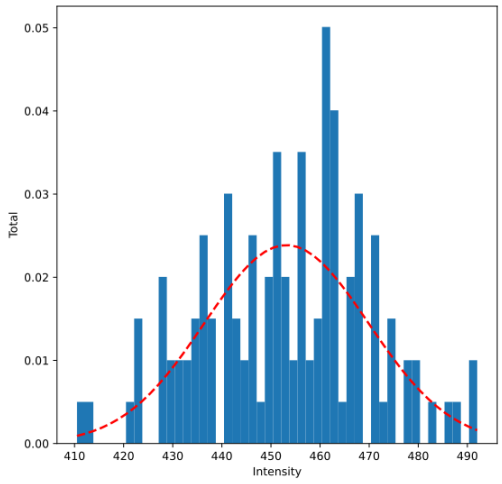

(a) 617 cm^{-1}

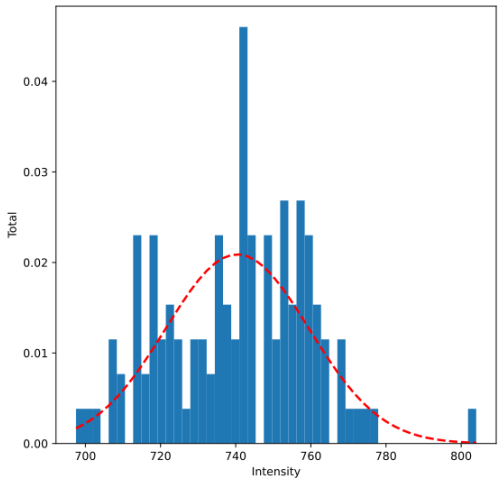

(b) 1350 cm^{-1}

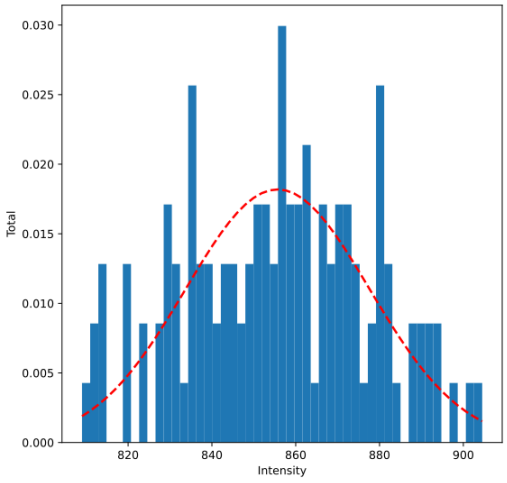

(c) 1501 cm^{-1}

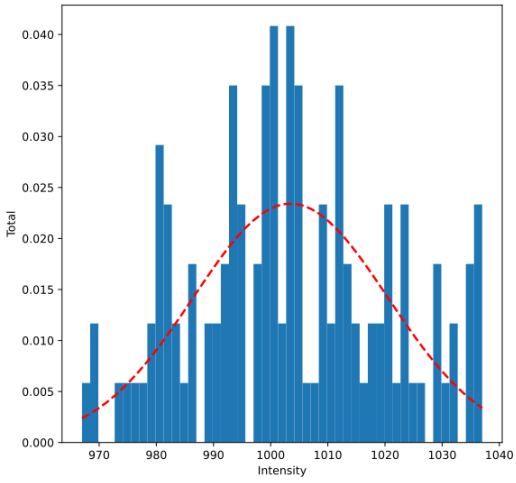

(d) 1637 cm^{-1}

Figure 3.20: Histograms showing the distribution of intensities at given peaks for drying a sample on glass only, over 120 frames of data. (a) At 617 cm^{-1}; (b) at 1350 cm^{-1}; (c) at 1501 cm^{-1}; (d) at 1637 cm^{-1}. R6G at an initial concentration of 10^{-7} M. Excitation wavelength: 532 nm.

The histograms above can be considered to somewhat approximate a normal distribution, with some skewing to the right in the 617cm-1 band and the skewing to the left in the 1350 cm-1 band. This corresponds to the distribution of frames there are in Fig.(3.18(b)).

3.5.2 Filter paper

The second drying method is to demonstrate what occurs when providing a paper-based form of drying surface. The filter paper used is Whatman Grade 4 filter paper and then a 100 μL drop of nanoparticle-dye (50 μL nanoparticles, 50 μL dye at an initial) solution was placed on the filter paper and dried in the oven in the same oven settings as the SLIPs substrates, this resulted in a grey spot. From Fig.(3.21), the variation between spectra is greater than those observed in the previous glass spectra in Fig.(3.18), and the spectra are more broad.

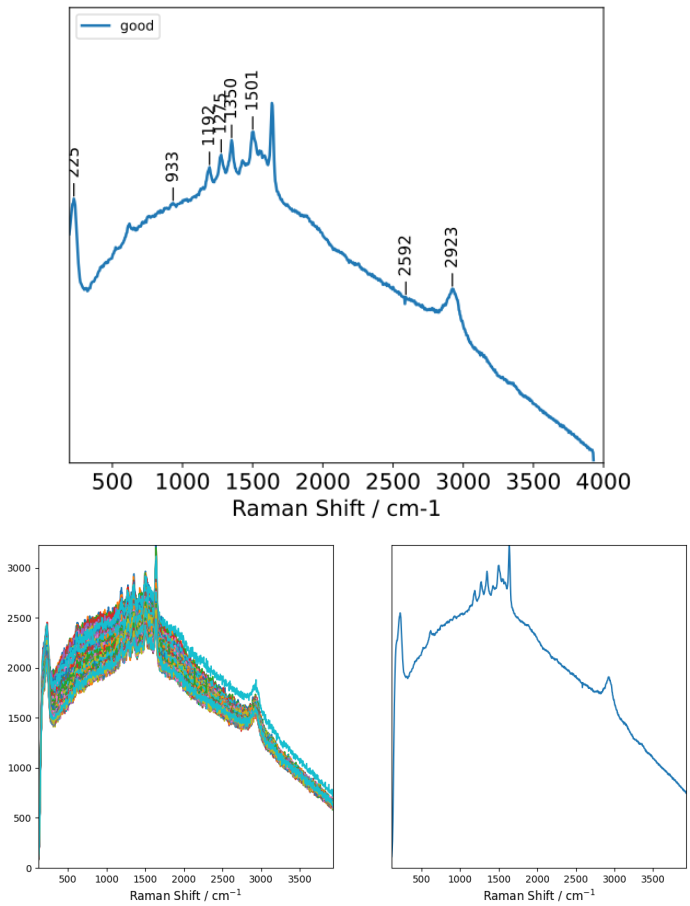

Figure 3.21: (a) Peak-fitted averaged SERS spectrum of R6G using the Whatman Grade 4 filter paper as the drying substrate method ; (b) Raw SERS data of R6G using the same drying method of (a). R6G at an initial concentration of 10^{-7} M. Excitation wavelength: 532 nm.

The standard deviation of the frames in Fig.(3.22) correlates with the observed variation between frames in Fig.(3.21).
Based on the spectra in Fig.(3.21), it can be noted that the spectra have significantly less defined peaks with higher intensity, these are however more broad. This is likely due to the presence of high amounts of cellulose in the paper and the treatment that goes into making the filter paper. The histograms in Fig.(3.23) correlate with the

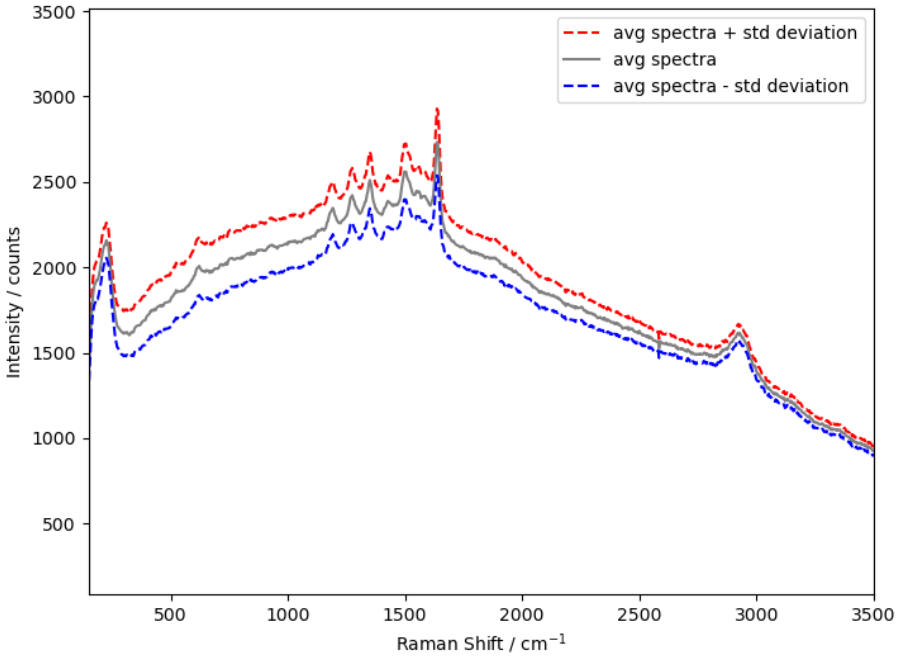

Figure 3.22: The standard deviation of all the spectra collected for the R6G on the Whatman Grade 4 Qualitative Filter Papers drying method. Excitation wavelength: 532 nm.

observed variation in frames seen in Fig.(3.21), where most of the spectra lie in the relatviely lower intensities.

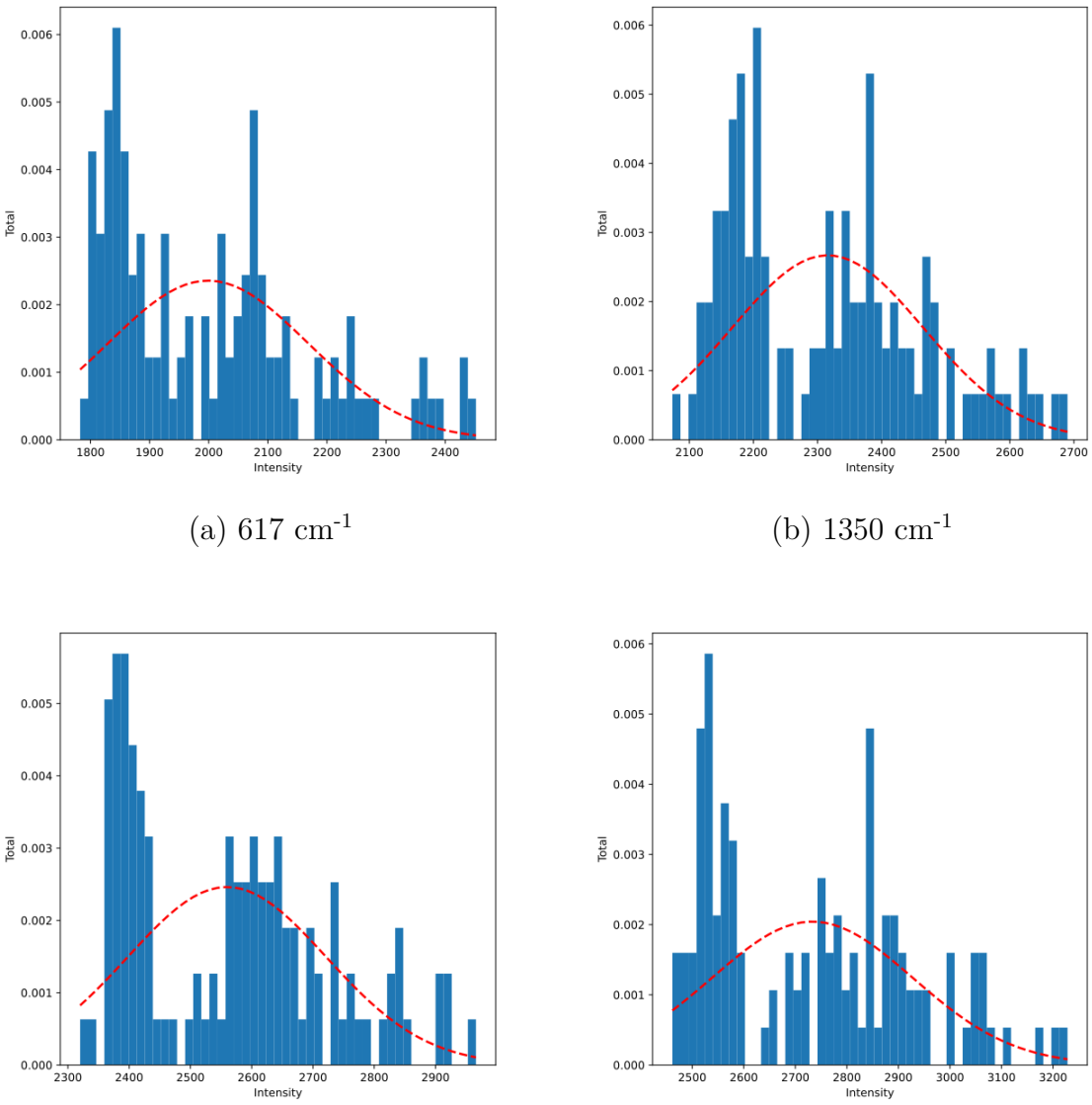

(a) 617 cm^{-1}

(b) 1350 cm^{-1}

(c) 1501 cm^{-1}

(d) 1637 cm^{-1}

Figure 3.23: Histograms showing the distribution of intensities at given peaks for drying on filter paper, over 120 frames of data. (a) At 617 cm^{-1}; (b) at 1350 cm^{-1}; (c) at 1501 cm^{-1}; (d) at 1637 cm^{-1}. R6G at an initial concentration of 10^{-7} M. Excitation wavelength: 532 nm.

3.5.3 Cellulose acetate filter

The chosen Sterlitech Cellulose acetate filters are hydrophilic filters made from cellulose diacetate and have a pore size of 0.45μm sized pores. This filter is significantly more porous than the filter paper and made of modified cellulose, it should be expected to perform similar to the filter paper. In Fig.(3.24), there does seem to be a similar effect with regards to the broadening of the overall spectra, ableit to a much lesser

extent. This is likely due to the manufacturing process of the filters, which attempts to have more uniform pores than the paper fibres in the filter paper. In addition, these have the highest intensities of all of the observed drying methods so far and the variation between frames seen in Fig.(3.24b) is more than the glass, but less than the filter paper.

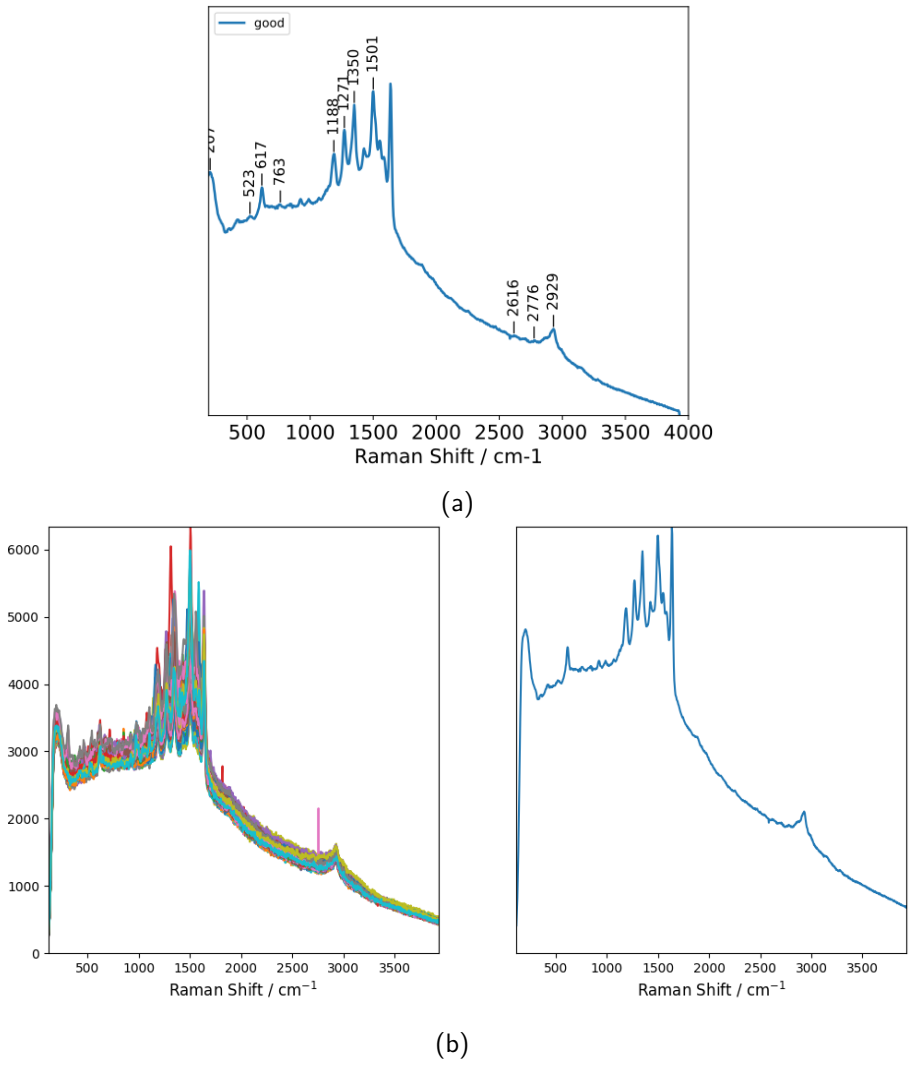

Figure 3.24: (a) Averaged spectrum across 120 frames of the 'yellow' dispersion using the cellulose acetate drying method and R6G at an initial concentration of 10^{-7} M, (b) all 120 frames of the yellow dispersion using the cellulose acetate drying method (left), (right) averaged spectrum across 120 frames. Excitation wavelength: 532 nm.

The standard deviation between all the frames in Fig.(3.25) appears to correlate with the observed variation between frames seen in Fig.(3.24b).

The histograms from Fig.(3.26) seem to correlate with what was observed in Figs.(3.24b) and (3.25), as the majority of spectra appear in the relatively lower-end of intensities.

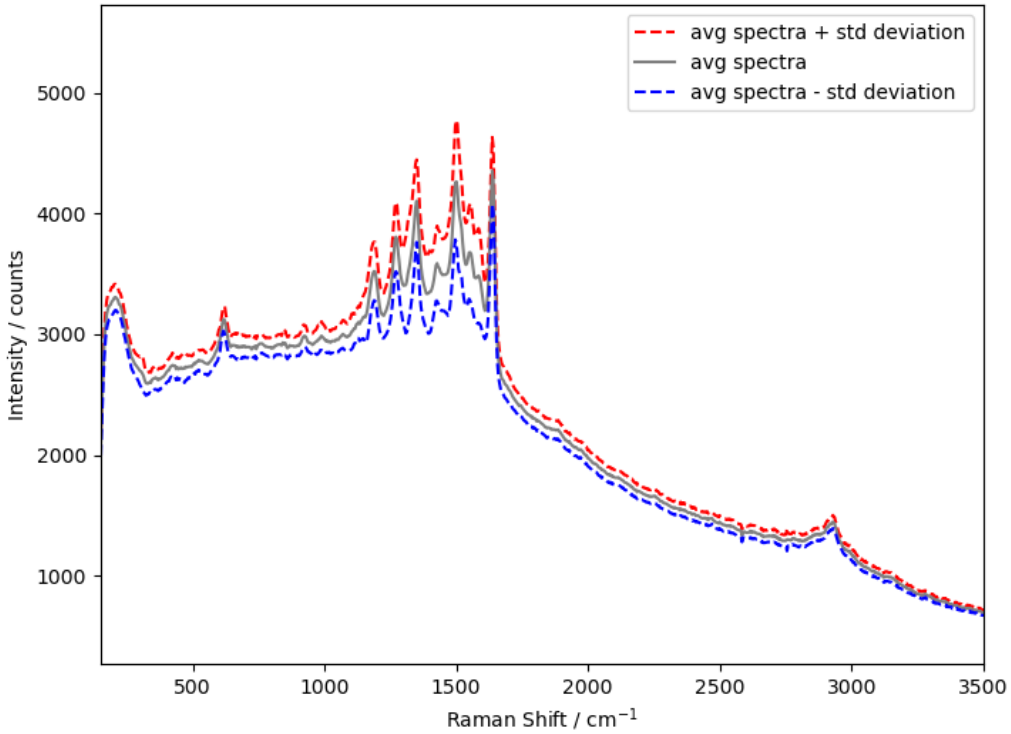

htpb]

Figure 3.25: The standard deviation of all the spectra collected using the cellulose acetate filter as the drying substrate method. Centre line is the averaged spectrum. Excitation wavelength: 532 nm.

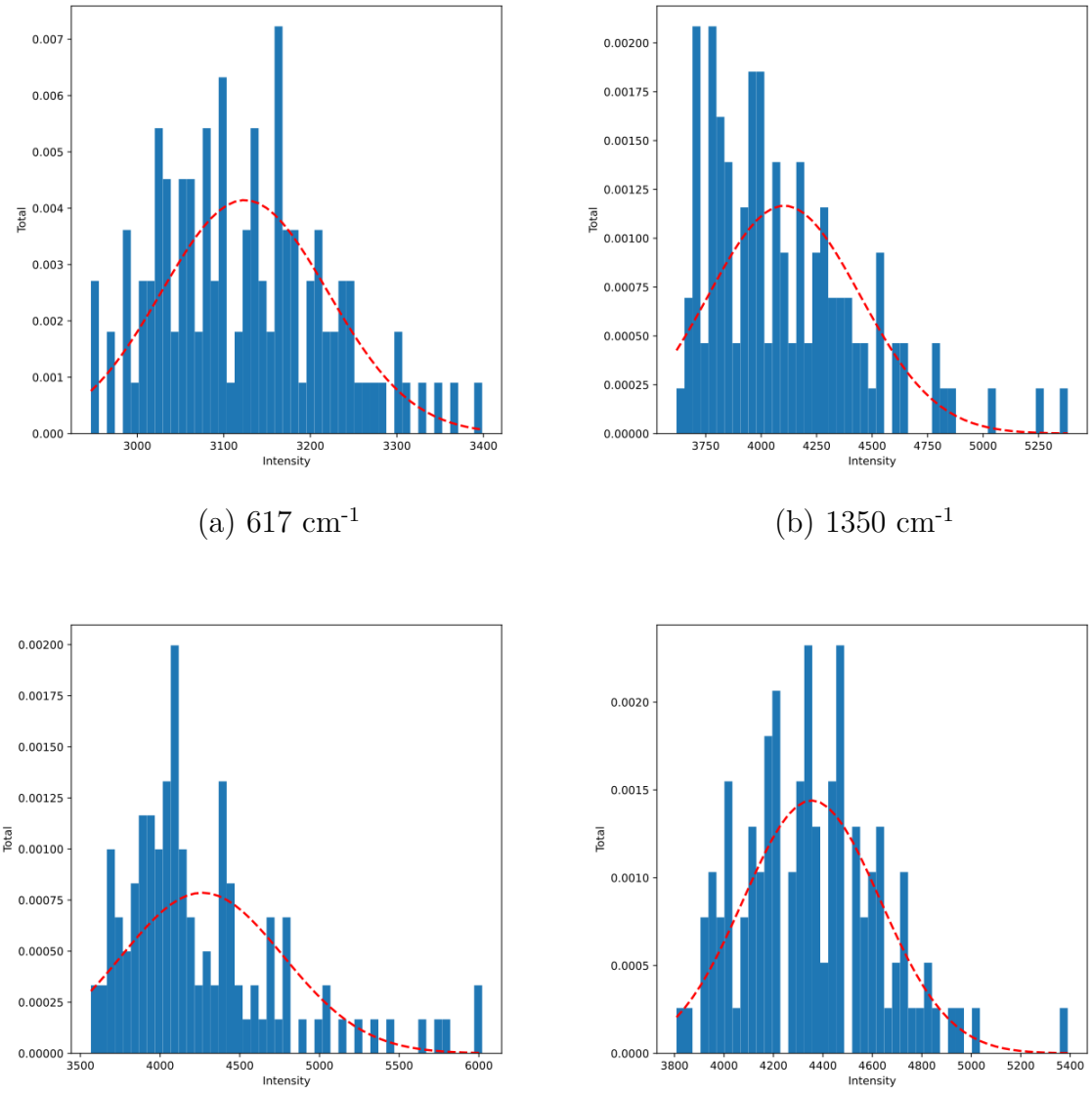

(a) 617 cm^{-1}

(b) 1350 cm^{-1}

(c) 1501 cm^{-1}

(d) 1637 cm^{-1}

Figure 3.26: Histograms showing the distribution of intensities at given peaks for drying on Cellulose Acetate filters with R6G at an initial concentration of 10^{-7} M, over 120 frames of data. (a) At 617 cm^{-1}; (b) at 1350 cm^{-1}; (c) at 1501 cm^{-1}; (d) at 1637 cm^{-1}. Excitation wavelength: 532 nm.

3.5.4 SLIPS

Finally, the SLIPS surface is made of an already omniphobic material - the PTFE filter and is combined with a thin layer of Teflon-based Krytox oil, the PTFE filters provide a much less absorbent drying surface than any of the methods described in the previous sections. The SLIPS sample is prepared in the same way described in 2.5 and 2.6.1. Unlike the Cellulose diacetate filters used in the previous section, these filters are hydrophobic, resulting in a condensed spot to form (see Fig.(2.3)).

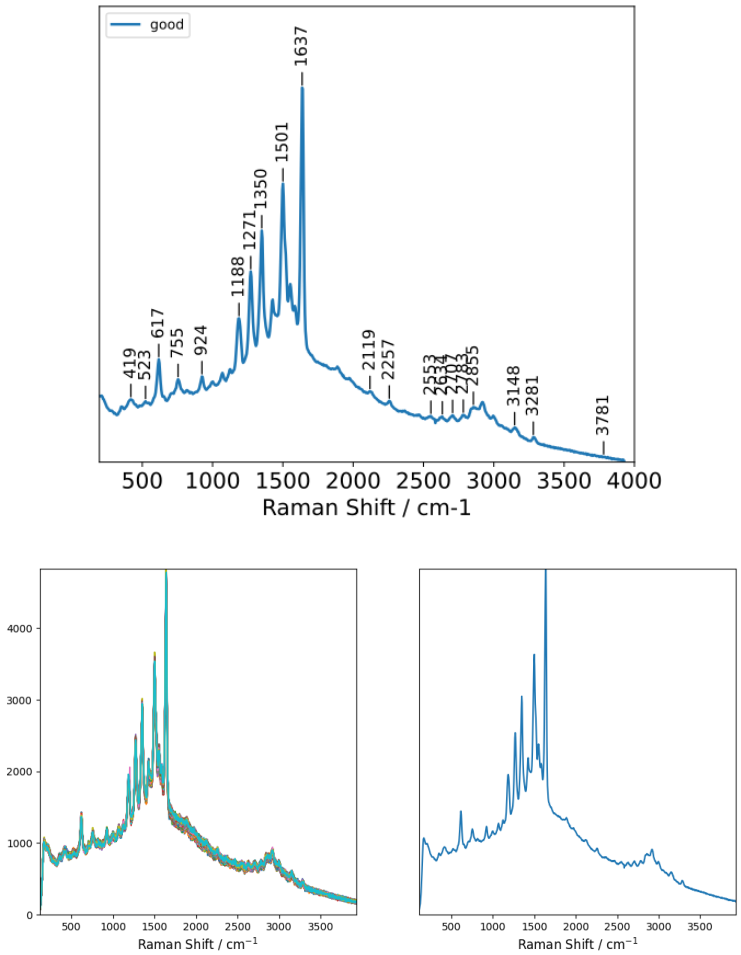

Figure 3.27: (a) Peak-fitted averaged SERS spectrum of R6G using the SLIP as the drying substrate method ; (b) Raw SERS data of R6G using the same drying method of (a). R6G at an initial concentration of 10^{-7} M Excitation wavelength: 532 nm.

. This method results in a tighter spread of observed spectra over the 120 frames collected (see Fig.(3.28), when compared to the cellulose acetate, filter paper. The drying method with glass has a similar standard deviation spread, however, the SLIPs surface produces a signal with at least four times as much intensity, and much less interference from fluorescent bands. This means that compared to the other methods

listed here, SLIPS appears to offer better potential for increasing the sensitivity of collecting SERS spectra.

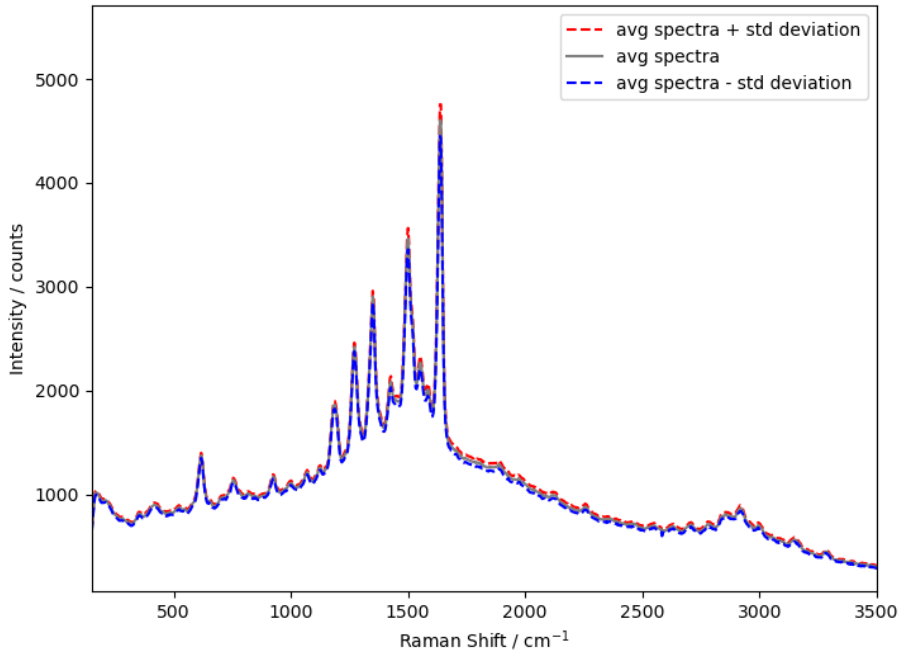

Figure 3.28: The standard deviation of all the spectra collected for the SLIPs drying method, R6G at an initial concentration of 10^{-7} M, excitation wavelength: 532 nm.

The histograms in Fig.(3.29) correlate with the observed variation in frames from Fig.(3.27) and the standard deviation of the frames in Fig. (3.28), where the spectra are more tightly spread and the standard deviations are small. For the SLIPS standard deviation, they seem much tighter than those observed in Fig.(3.19), and of those found in the cellulose acetate filter and paper filter.

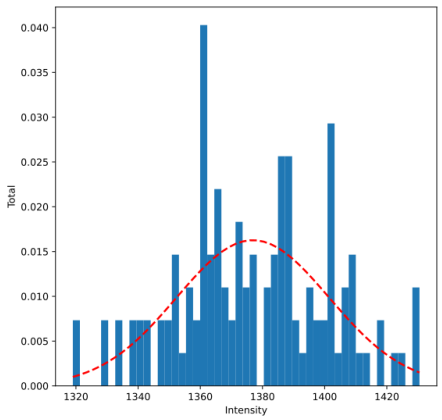

(a) 617 cm^{-1}

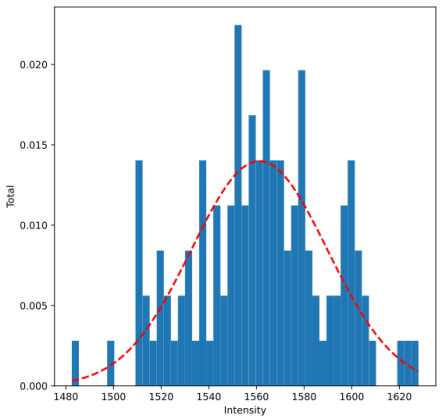

(b) 1350 cm^{-1}

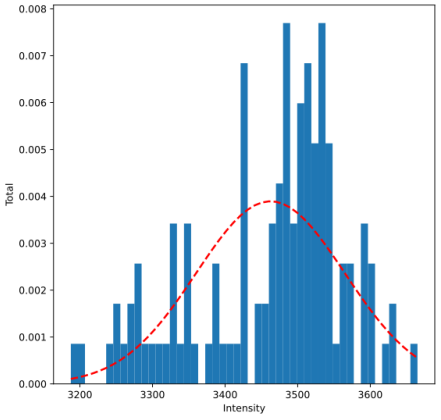

(c) 1501 cm^{-1}

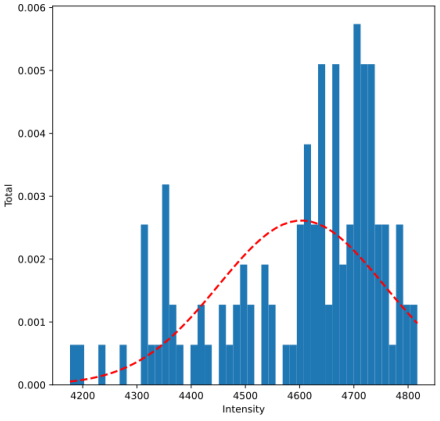

(d) 1637 cm^{-1}

Figure 3.29: Histograms showing the distribution of intensities at given peaks prepared using the SLIPS method, over 120 frames of data. R6G at an initial concentration of 10^{-7} M. Excitation wavelength: 532 nm.

4. SLIP-SERS Detection of Dyes

As explained in Sec.1.6.1, dyes represent good model molecules for figuring out the effectiveness of nanoparticles and their ability to enhance Raman signals in SERS. Rhodamine-6G is a common laser dye that has been used extensively in research to study laser emission and nanoparticle effectiveness in SERS substrates. In the case of Rhodamine-6G, its SERS spectrum is well known and therefore is a perfect compound to assess how well the nanoparticles perform as SERS substrates.

4.1 SLIPSERS Spectra

4.1.1 Rhodamine 6G (R6G)

As discussed above, R6G is a good probe compound for evaluating SERS performance - as it is extremely emissive.

	Raman Shift (cm^{-1})	
Mode(s)	Literature[217]	Experimental
C-C-C in plane ring bend	610	617
C-H out of plane bend	771	755
C-H in plane bend	1182	1188
Aromatic C-C stretch	1278	1271
Aromatic C-C stretch	1361	1350
	1509	1501
	1572	1561
	1652	1649

Table 4.1: Summary table of the important Raman active modes found in the SERS spectra of R6G using literature values [217–219] and collected experimental SERS spectra of Rhodamine-6G (Fig.(4.5) using a 532 nm wavelength.

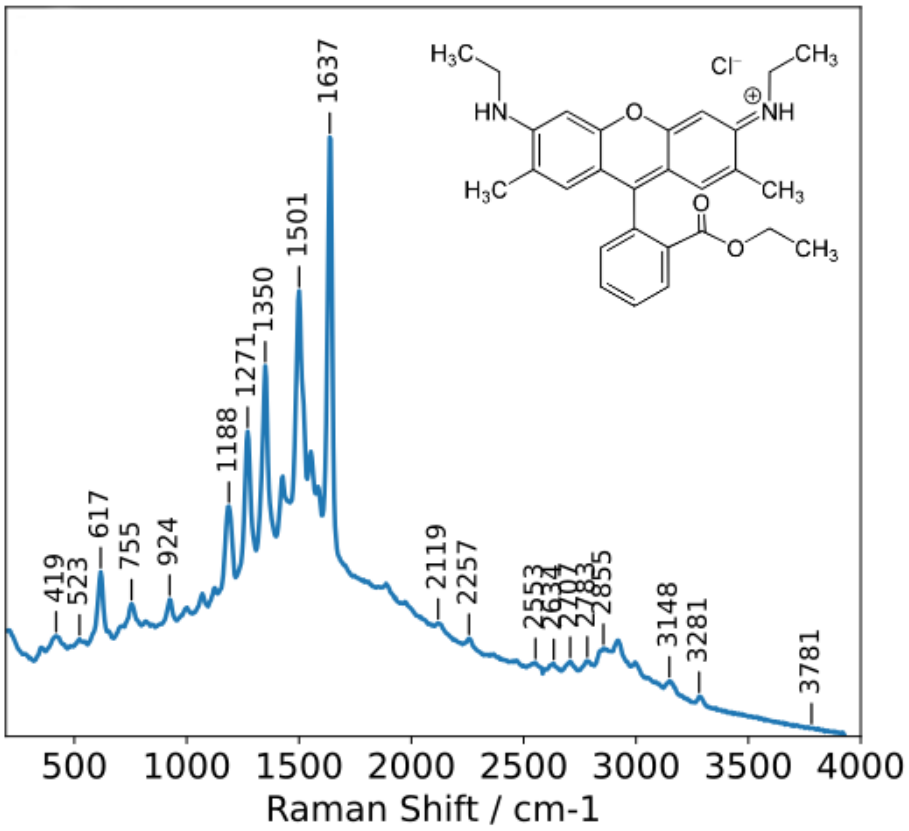

Figure 4.1: A SLIP-SERS spectrum of Rhodamine 6G using the "yellow" nanoparticle substrate and 10^{-7} M initial concentration used as the "standard" spectrum.

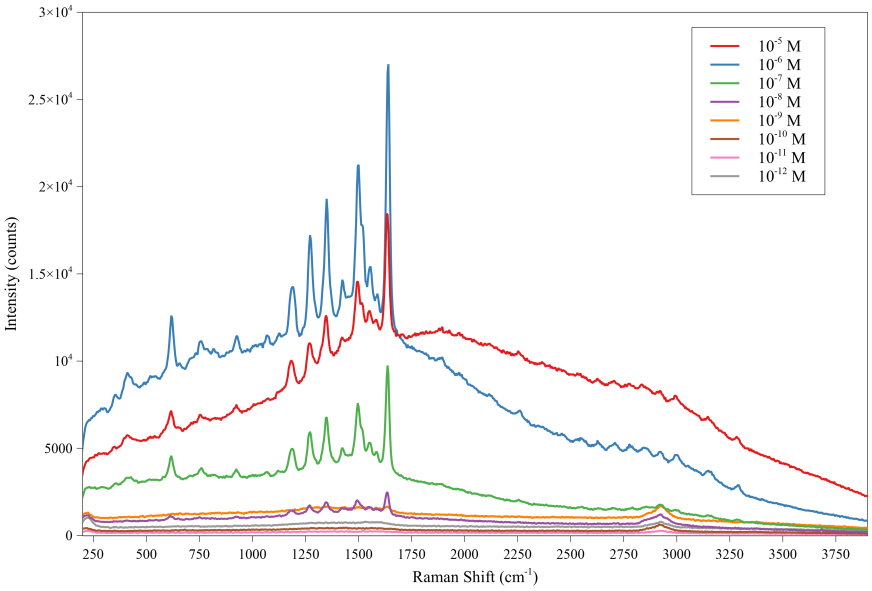

Figure 4.2: A SLIP-SERS spectrum of Rhodamine 6G using the "yellow" nanoparticle substrate and at various concentrations.

From Fig.(4.2 it can be inferred that the concentration dependence is non-linear, suggesting that either; contamination, adsorption of the dye to the glassware the solution was stored in, contamination from the SLIPS surface, or interference from the preparation of the SLIPS surface affects the limits of detection for the data collected on all of the analytes. The spectra in this figure are not normalised or baseline corrected, unlike in Fig.(4.1). Furthermore, if we compare all of the nanoparticle types in Fig.(4.3) and Fig.(4.4), it can be seen that the single molecule regime begins around the concentration region around 10^{-8} M to 10^{-9} M, as the intensity begins to diminish significantly, as seen in Fig.(4.2). This regime occurs when the probability of having zero molecules on the nanoparticles is about the same as having a single molecule on the nanoparticle surface, hence the decrease in intensity and overall decrease in likelihood of a "hot spot" enhancing a signal that can be observed. This means the ideal concentration to observe SERS events with a dye like R6G is around a concentration of 10^{-6} M, as it is likely to form a monolayer that does not interfere with signal enhancement or saturate the observed signal (observed as a fluorescent peak).

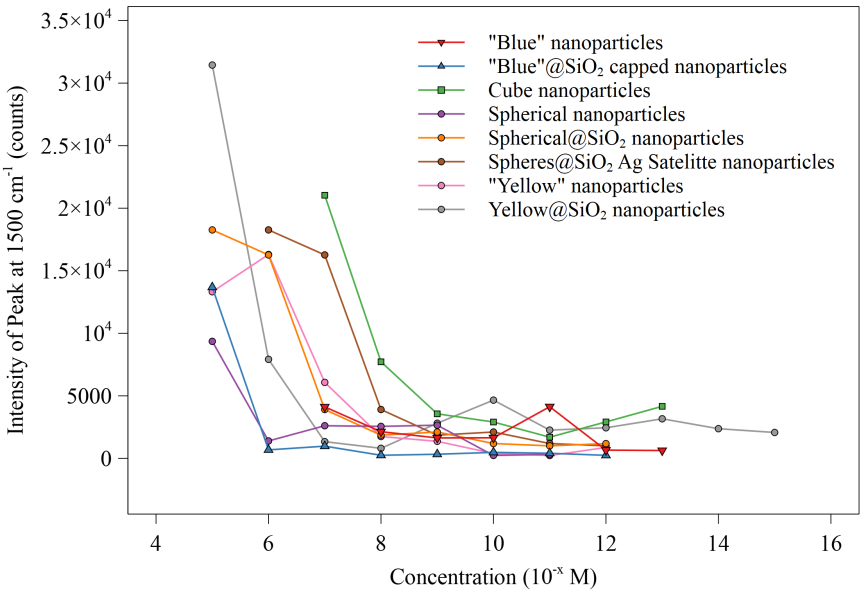

Figure 4.3: Comparison of the intensity of the peak at 1500 cm^{-1} across all nanoparticle types.

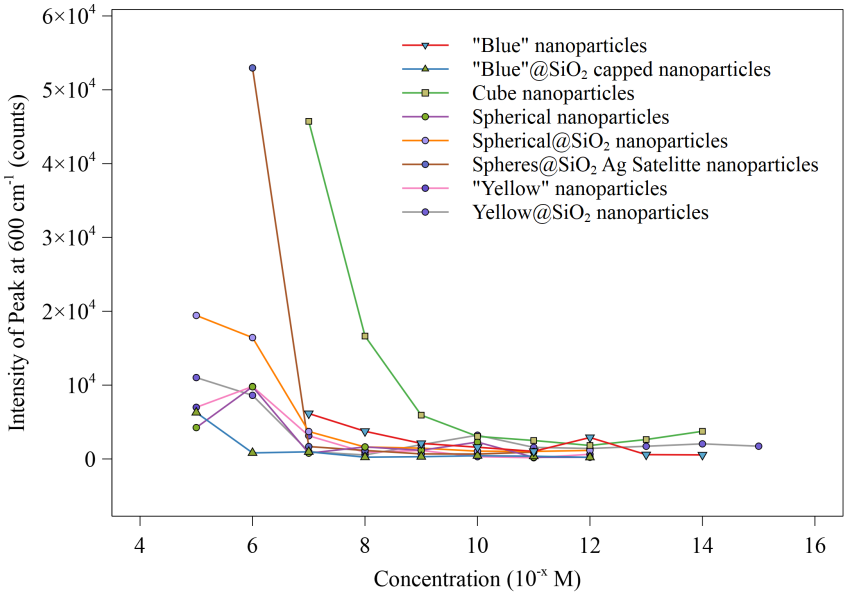

Figure 4.4: Comparison of the intensity of the peak at 600 cm^{-1} across all nanoparticle types.

4.1.1.1 'Yellow' and 'Yellow'@SiO2 Nanoparticles

The 'yellow' nanoparticles Fig.(4.5) appear to show some sensitivity up to about an initial concentration of $10^{-7}M$. The C-H peak appears to get stronger at an initial concentration of 10^{-8} M. It also appears that d-g bands are forming at the initial concentrations of 10^{-11} M and 10^{-12} M. However, there is at least some signals from R6G up to an initial concentration of 10^{-9} M.

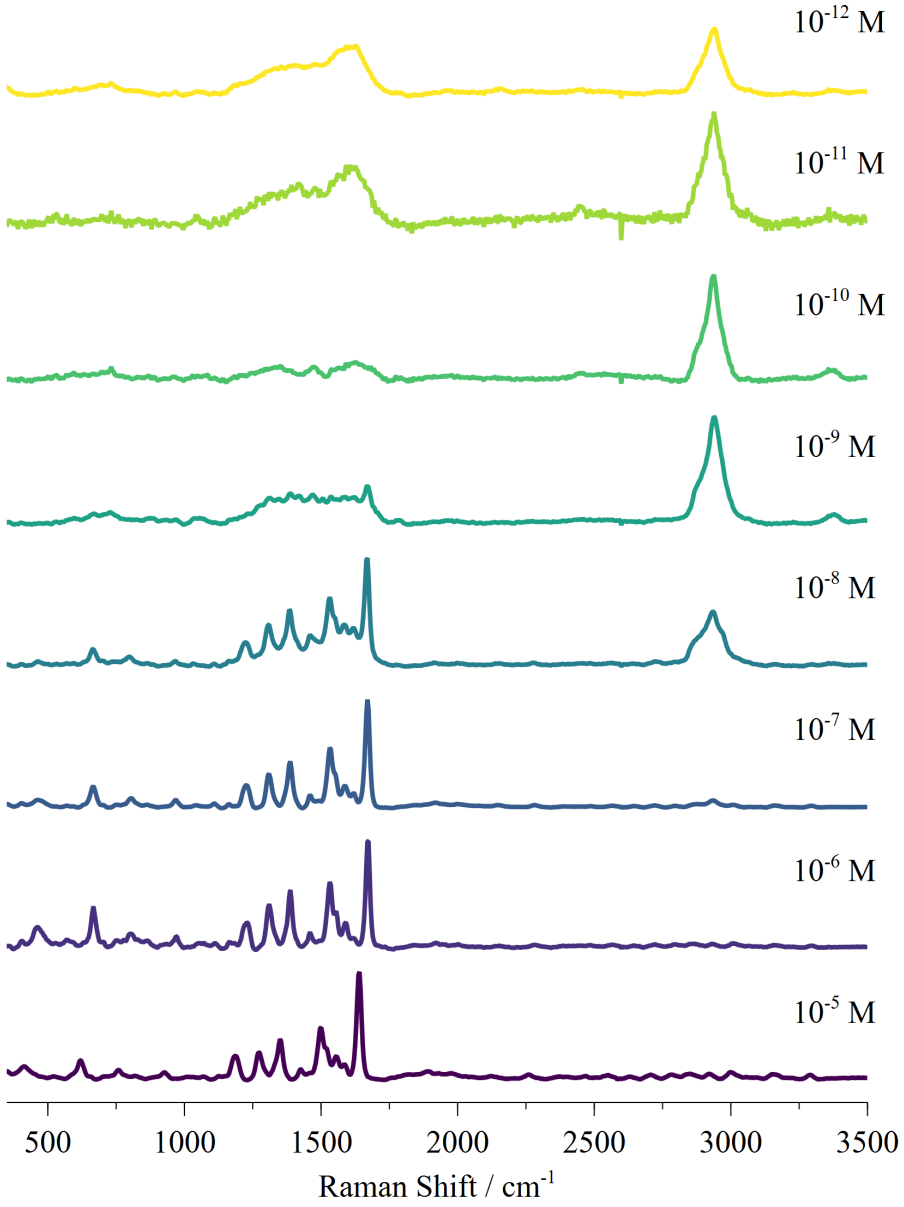

Figure 4.5: Stacked spectra showing the range of initial concentrations of R6G to evaluate the sensitivity of the 'yellow' nanoparticles. Excitation wavelength: 532 nm.

For the 'Yellow@SiO_2' nanoparticles (Fig.(4.6)), the silica shell appears to enhance

the signals somewhat, where it appears that some signals appear up to an initial concentration of 10^{-15} M. Similar to (Fig.(4.5)), there appears to be a sudden appearance of C-H bands starting at the spectra with an initial concentration of 10^{-8} M. In addition, at an initial concentration of 10^{-7} M, a peak at 2435 cm^{-1} appears, with varying intensities as the initial concentration decreases. Starting at about an initial concentration of 10^{-10} M, it appears that there is some d/g band contribution to the spectra, however the peaks at 997, 1234 and 1383 cm^{-1} still appear through the apparent d/g bands.

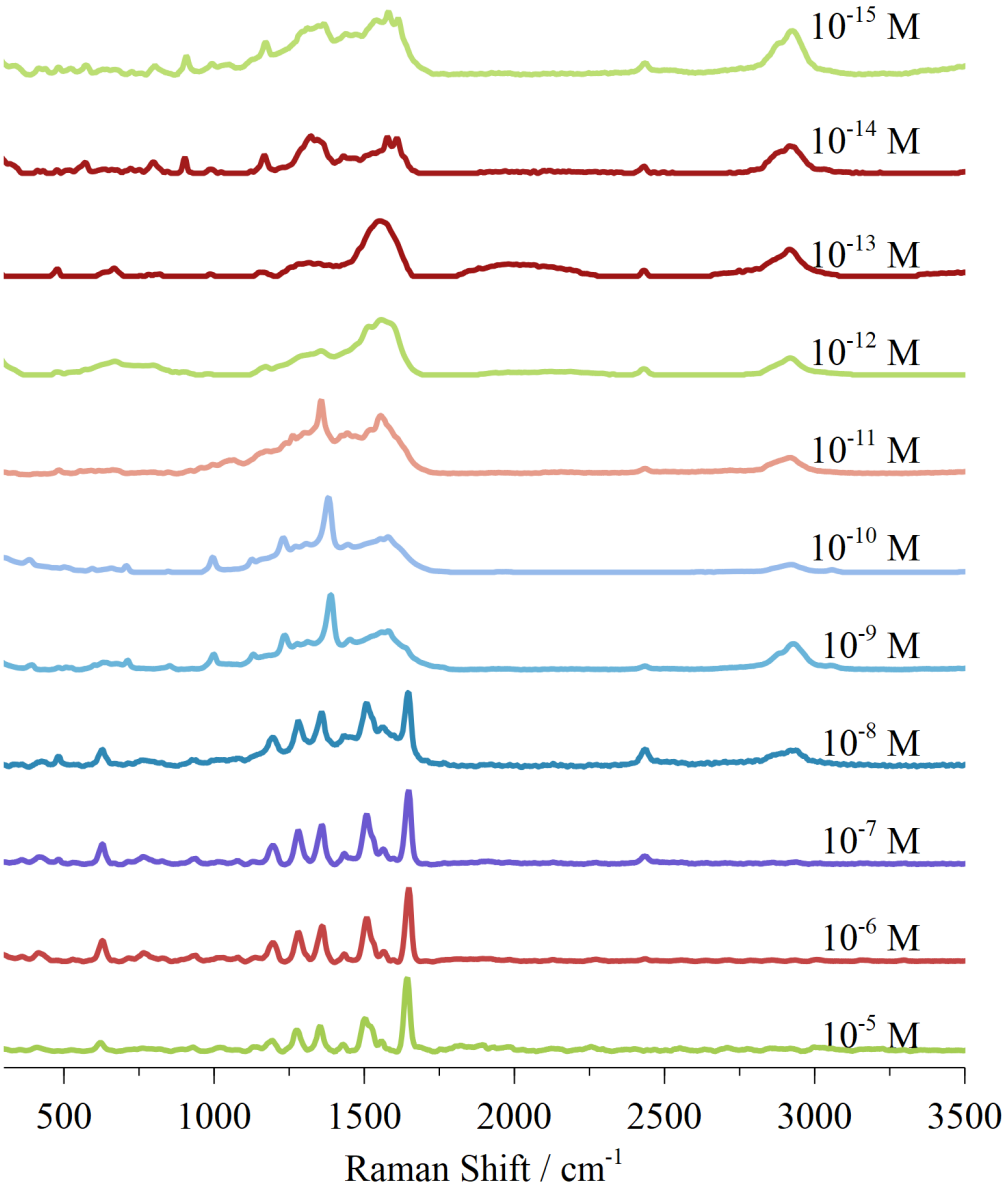

Figure 4.6: Stacked spectra showing the range of initial concentrations of R6G to evaluate the sensitivity of the yellow@SiO_2 nanoparticles. Note that the range of concentrations are larger in this graph because it appeared to be more sensitive - with possible R6G signals being observed from an initial concentration of 10^{-15} M. Excitation wavelength: 532 nm.

4.1.1.2 'Blue' Nanoprisms

For the "blue" nanoparticles (Fig.(4.7)), these were carried out at 532 nm, despite it appearing that it would favour occurring at 633 nm. As can be gathered from the below spectra, it appears to be sufficient. This might however explain why, compared to the above "yellow" nanoparticles, that for R6G, it is not very sensitive up to about an initial concentration of 10^{-11} M. From the concentrations 10^{-11} M and 10^{-12} M, the sensitivity is significantly degraded due to the signal-to-noise and the appearance

of d/g bands.

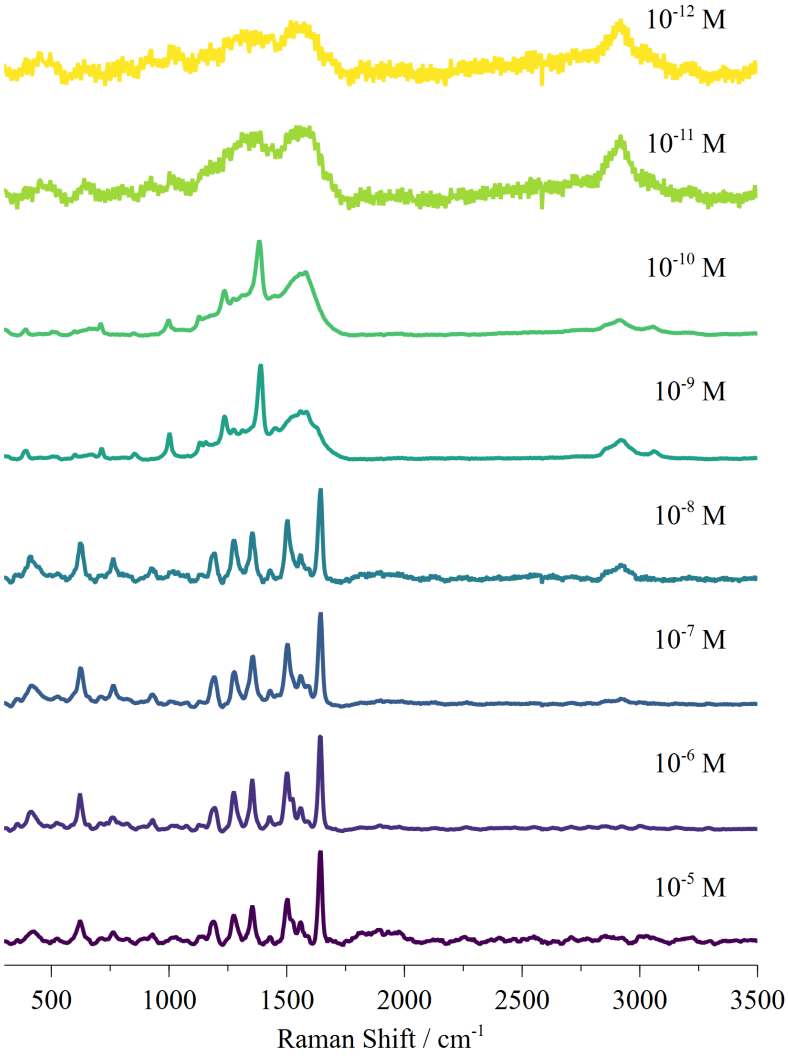

Figure 4.7: Stacked spectra showing the range of initial concentrations of R6G to evaluate the sensitivity of the silver nanoprisms. Excitation wavelength: 532 nm. Excitation wavelength: 532 nm.

The silica capped 'blue@SiO_2' nanoparticles and their corresponding spectra in Fig.(4.8), show a very low signal-to-noise ratio which exaggerates the 'dead' pixel at around 2592 cm^{-}1, however, it does appear to show some signals up to an initial concentration of 10^{-8} M. The "dead" pixel is simply a region on the detector (which is a CCD detector) that no longer is able to detect any radiation coming from that specific wavelength. A pixel in a detect can "die" for any number of reasons; it could simply be dust obscuring the "pixel", or the capacitor has stopped working. However, there does appear to be a C-H stretching band appearing in the 10^{-9} M to 10^{-12} M spectra, in a similar trend to the previous Figs. (4.5), (4.6), and Fig.(4.7).

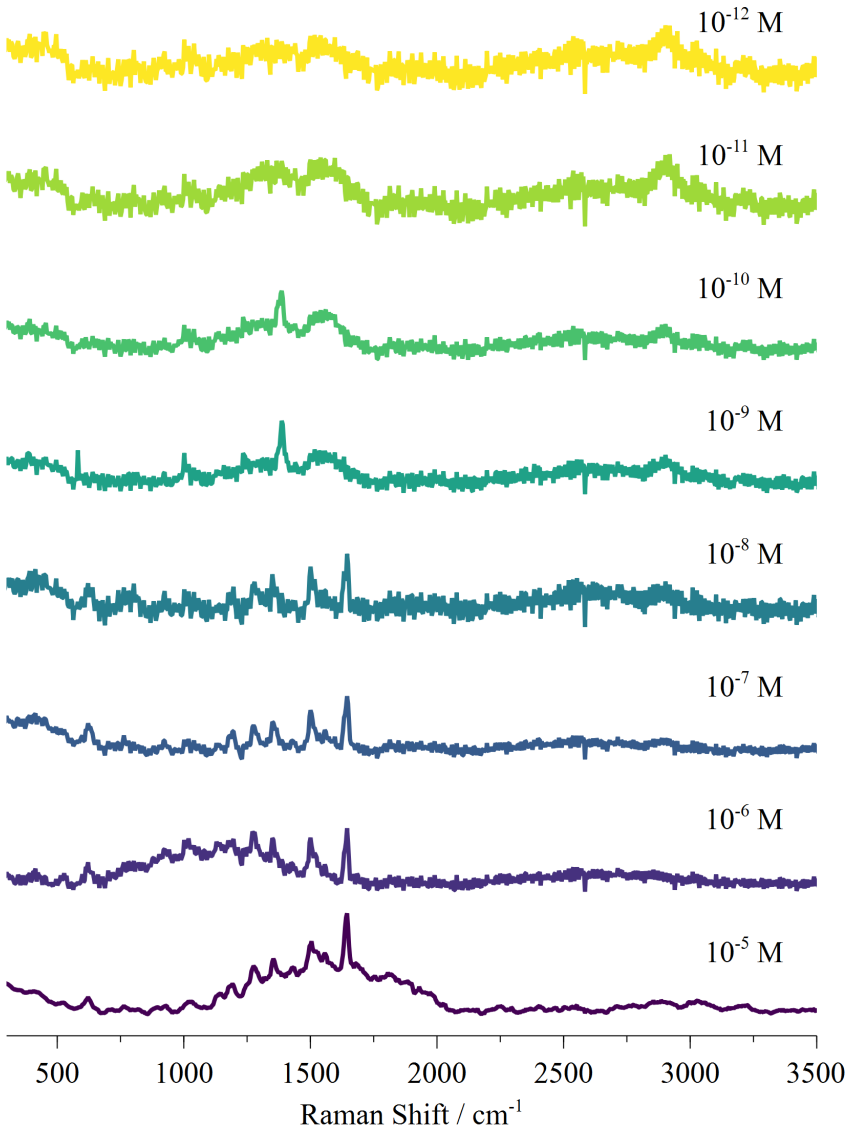

Figure 4.8: Stacked spectra showing the range of initial concentrations of R6G to evaluate the sensitivity of the blue@SiO_2 nanoparticles. Note that the 'dead' pixel at around 2592 cm-1 is exaggerated at the low signal-to-noise. Excitation wavelength: 532 nm.

4.1.1.3 Nanocubes

The silver nanocubes (Fig.(4.9)), show fluorescence at 10^{-6} M, 10^{-7} and 10^{-8} M spectra, resulting in what appears as low signal-to-noise when baselined. However, these do appear to show signals similar to those found in previous figures. In addition, much like Figs.(4.5), (4.6), (4.7) and Fig.(4.8), a C-H peak appears at an initial concentration of 10^{-9} M and subsequent lower initial concentrations.

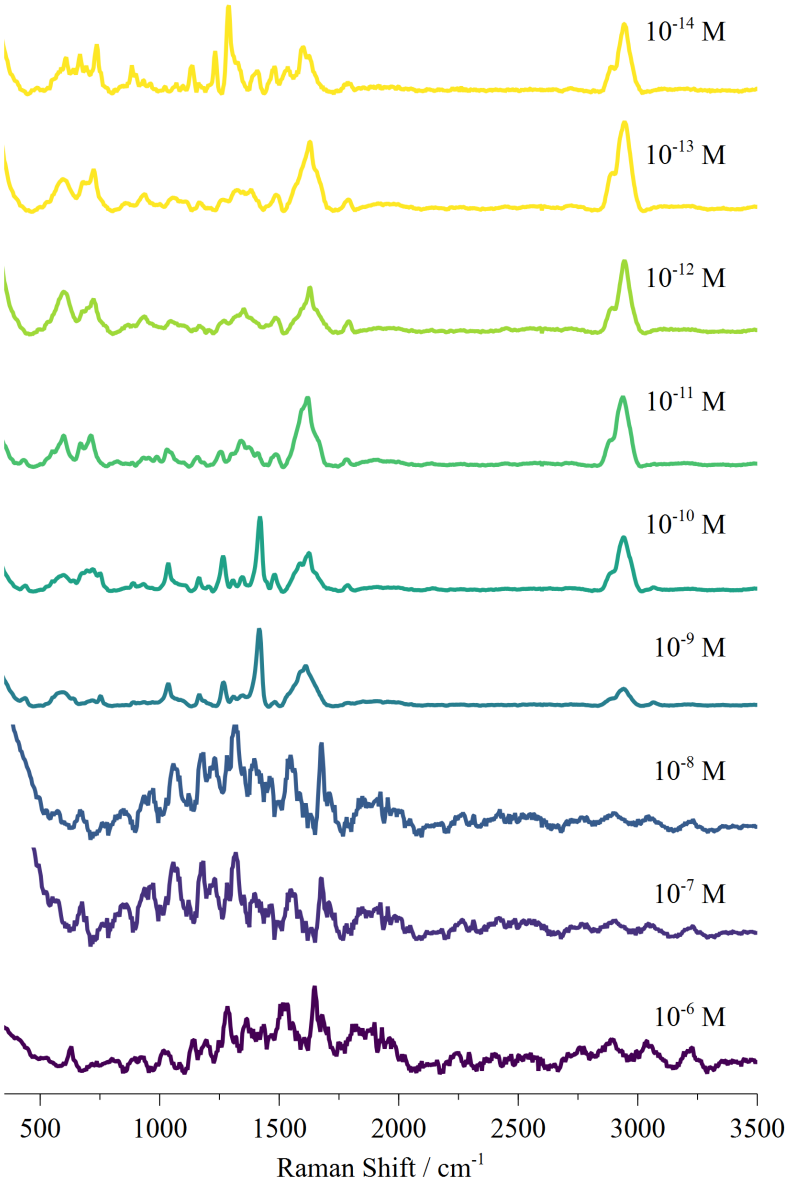

Figure 4.9: Stacked spectra showing the range of initial concentrations of R6G to evaluate the sensitivity of the silver nanocubes. Excitation wavelength: 532 nm.

4.1.1.4 Spherical Nanoparticles

The spectra in Fig.(4.10) have clear R6G signals up to about a concentration of 10^{-7} M, after which the signals become difficult to distinguish. In addition, as the concentration increases, the relative intensity of the peak at around 2995 cm^{-1} appears to get stronger.

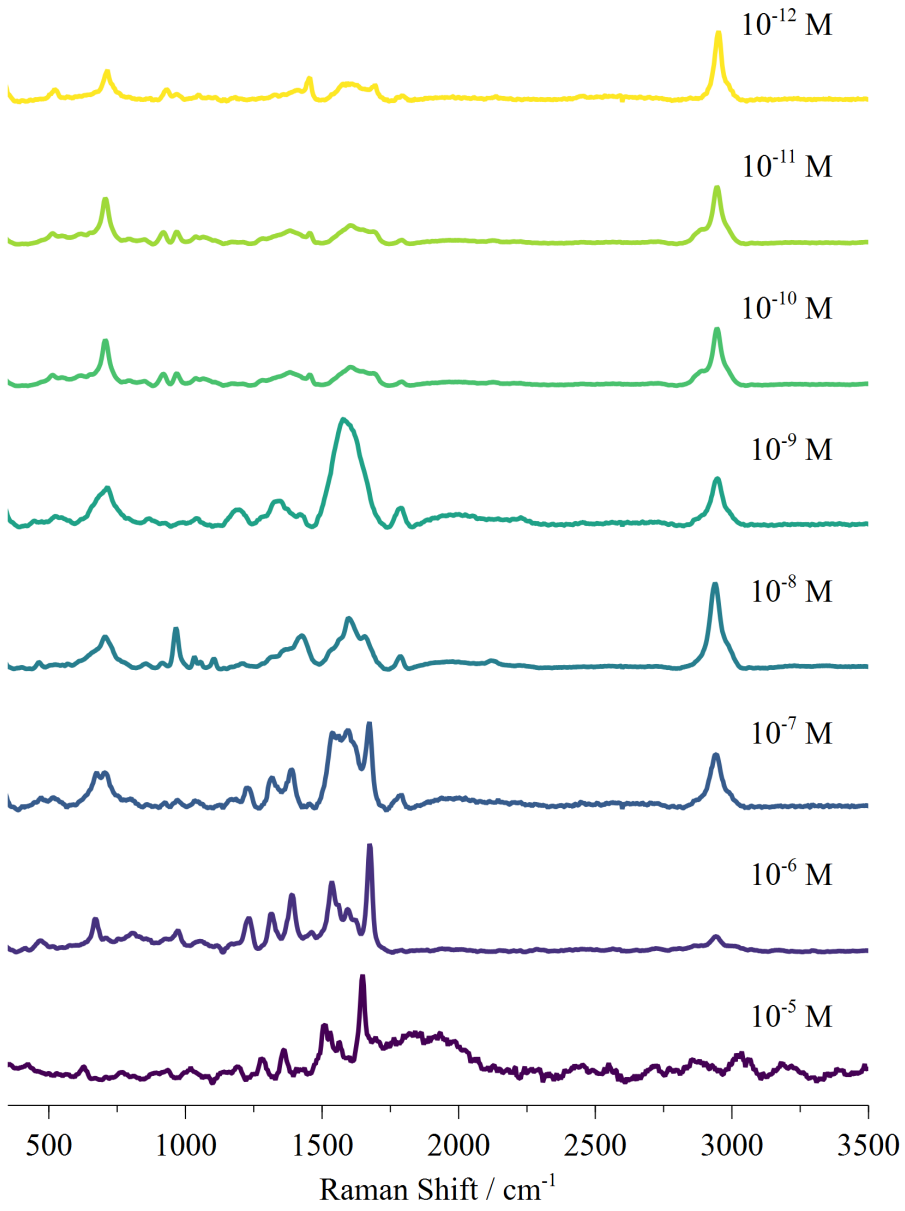

Figure 4.10: Stacked spectra showing the range of initial concentrations of R6G to evaluate the sensitivity of the spherical nanoparticles. Excitation wavelength: 532 nm.

The 'spheres@SiO_2' in Fig.(4.11) show that R6G signals are apparent until a concentration of about 10^{-6} M. As the concentration decreases, the signals become less distingushable. And, as he concentration approaches 10^{-8} M, characteristic d/g bands cause signals to be difficult to distinguish. A comparison of a d/g band spectra in Fig.(4.12b) shows that the spectrum with the most d/g bands is at an initial concentration of 10^{-10} M.

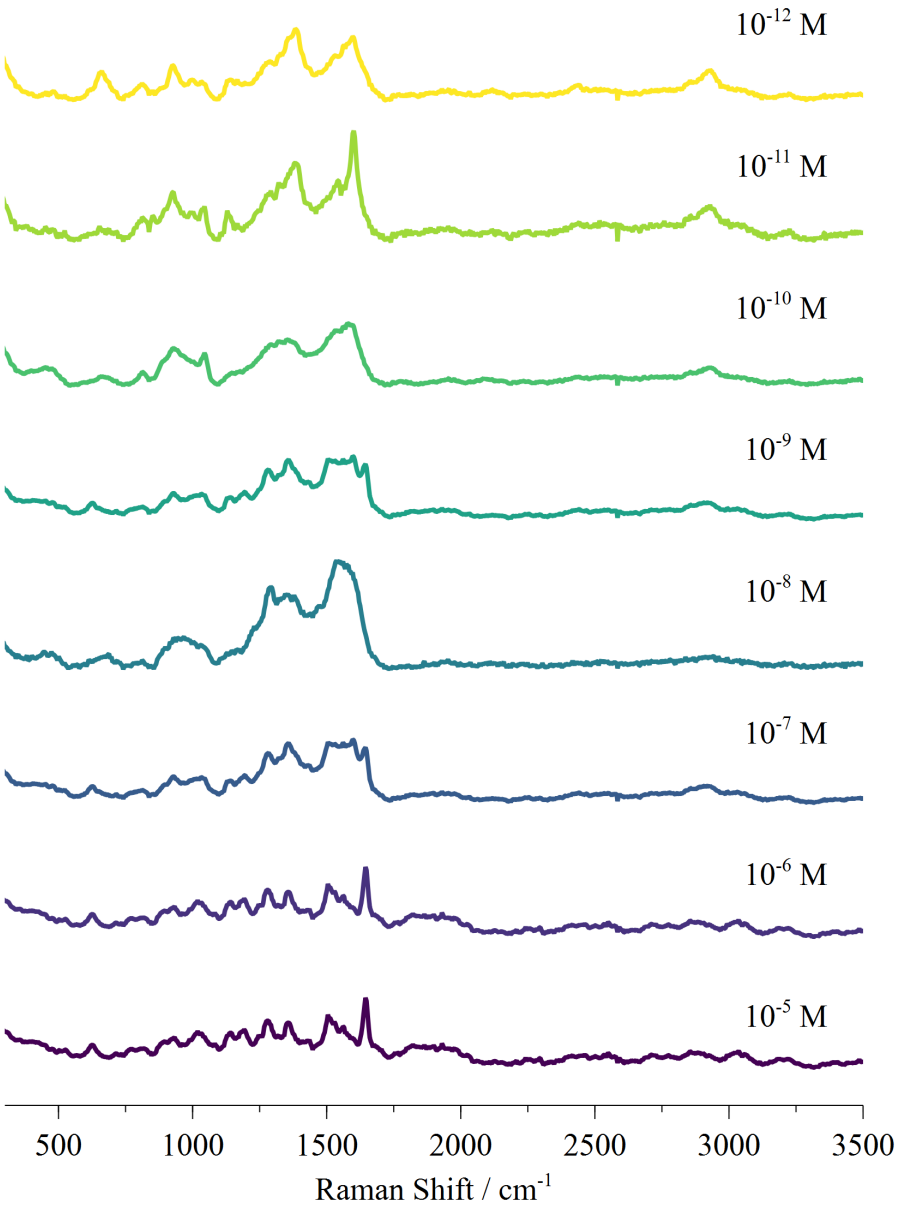

Figure 4.11: Stacked spectra showing the range of initial concentrations of R6G to evaluate the sensitivity of the Spheres@SiO_2 nanoparticles. Excitation wavelength: 532 nm.

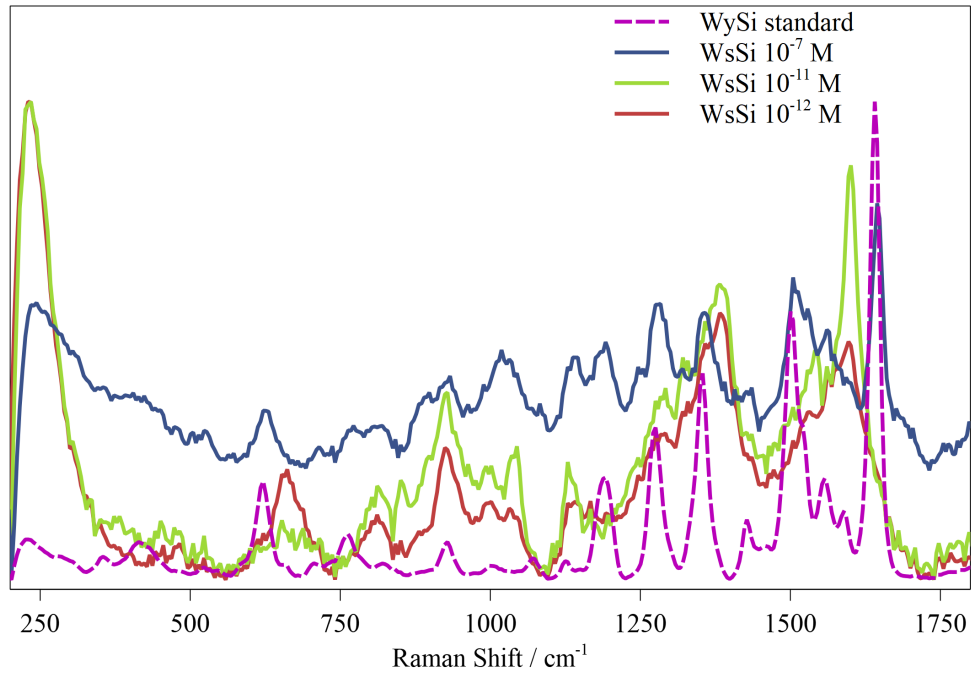

(a)

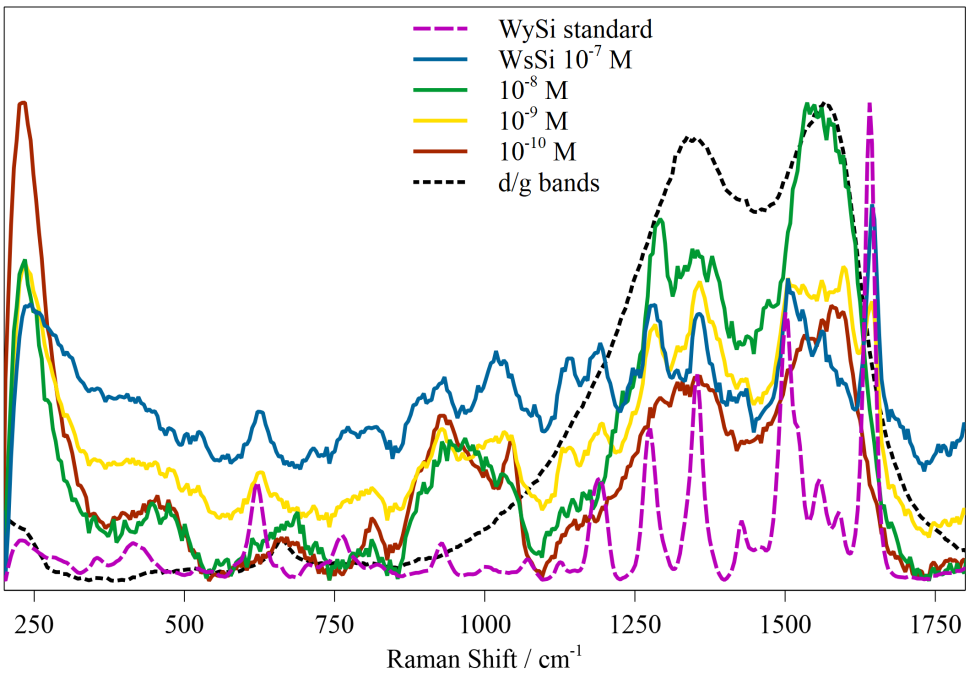

(b)

Figure 4.12: (a) The silica capped spherical nanoparticles at an initial concentration of 10^{-7} M, 10^{-11} M, 10^{-12} M R6G compared to the SERS standard using the silica capped yellow nanoparticles; (b) the silica capped spherical nanoparticles at an initial concentration of 10^{-9} M, 10^{-10} M, 10^{-10} M R6G compared to the SERS standard using the silica capped yellow nanoparticles and a spectra to show how the spectra are forming d/g bands (dotted line). Excitation wavelength: 532 nm.

The 'Spheres@SiO_2-Sat' nanoparticles in Fig.(4.11) show fluorescence from concentrations 10^{-6} M to 10^{-9} M. Then, at an initial concentration of 10^{-9} M, the bands typical of R6G become apparent. However, this appears to be the limit of these nanoparticles, as from the lower concentrations of 10^{-10} M, the low signal-to-noise makes it difficult to distinguish bands from one another.

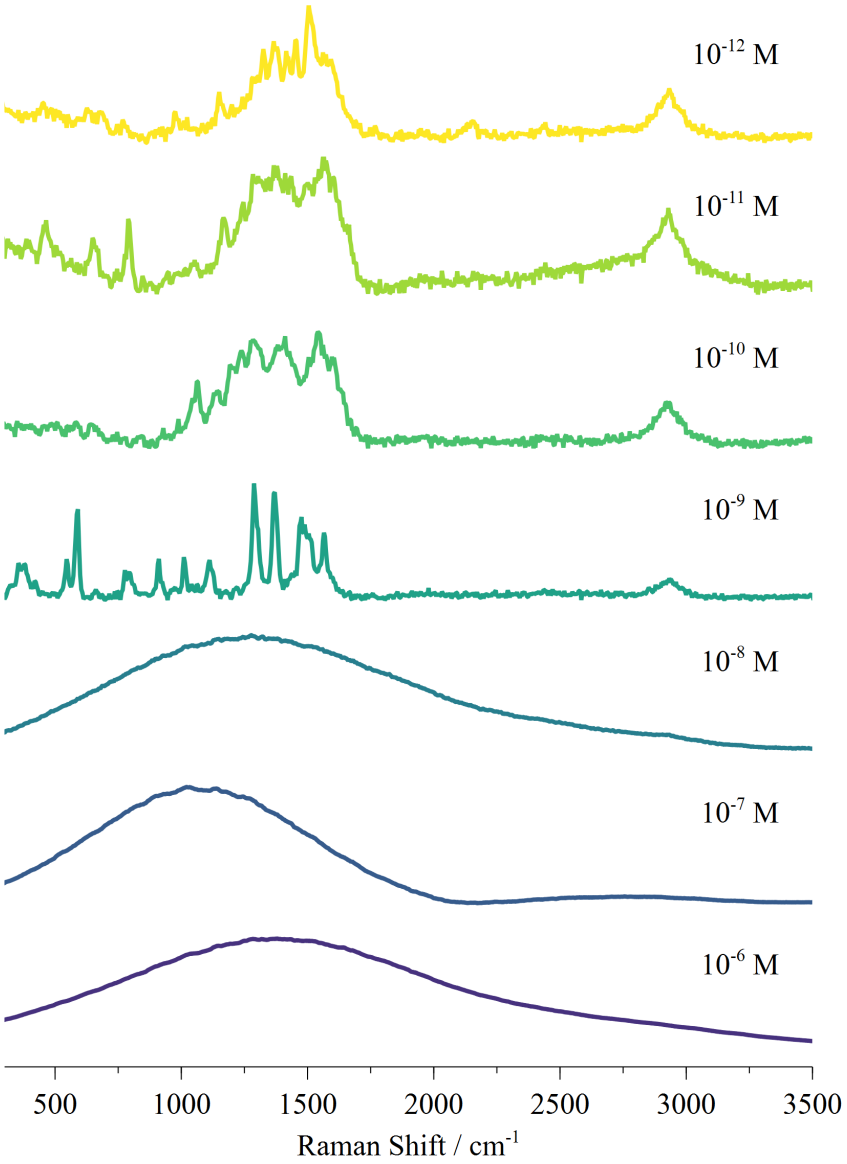

Figure 4.13: Stacked spectra showing the range of initial concentrations of R6G to evaluate the sensitivity of the 'Spheres@SiO2-Sat' nanoparticles. Excitation wavelength: 532 nm.

However, at the lower concentrations, it appears d/g character dominates (Fig.4.14b). Despite the d/g character, it appears that there is at least R6G being detected at a concentration of 10^{-9} M. the fluorescence seen at concentrations higher than 10^{-8} M may be due to the introduction of additional smaller satellite silver nanoparticles. Closer inspection of the bands at the lower concentrations in Fig.(4.12b) show that

at 10^{-11} M d/g bands interfere with the signals the most, which could explain why there are no noticeable R6G signals.

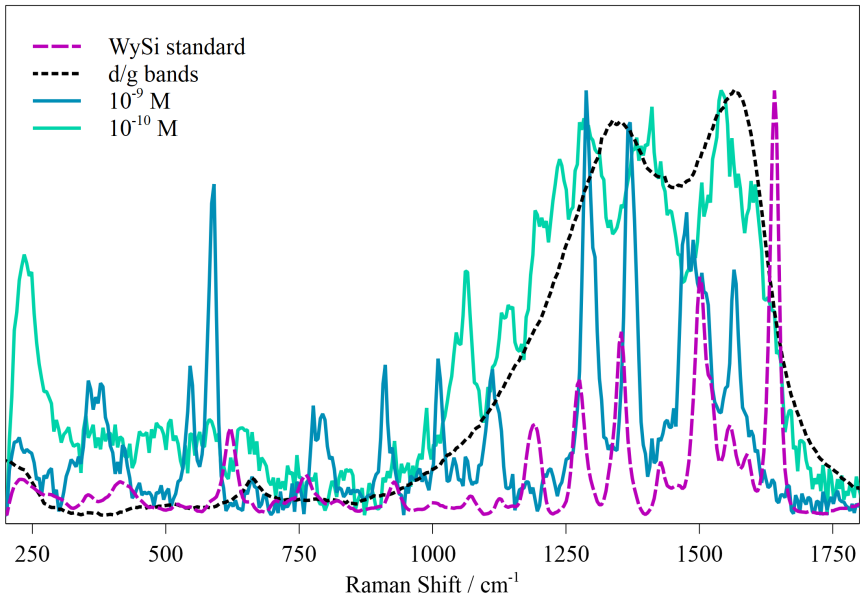

(a)

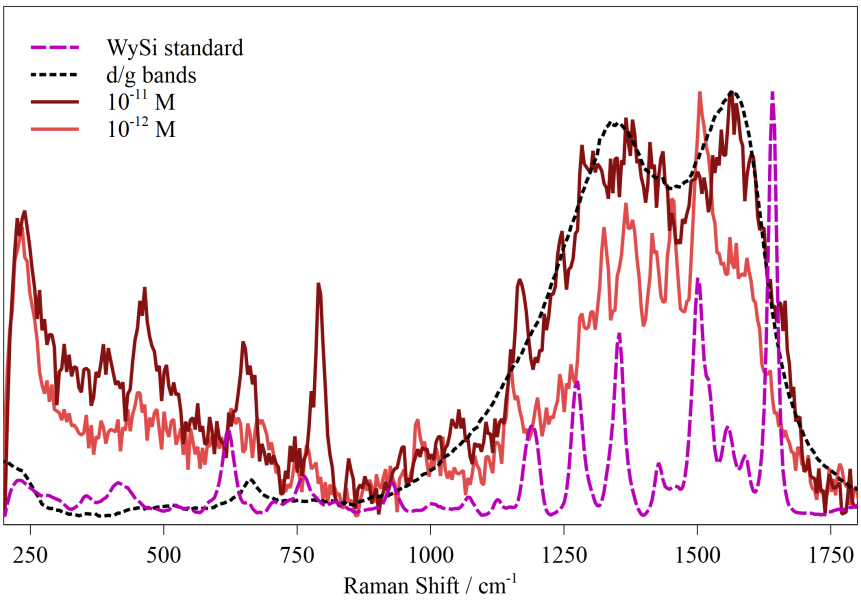

(b)

Figure 4.14: (a) The silica capped spherical nanoparticles with Ag satellites at an initial concentration of, 10^{-9} M, 10^{-10} M R6G compared to the SERS standard using the silica capped yellow nanoparticles and a d/g band spectra. Excitation wavelength: 532 nm. (b) The silica capped spherical nanoparticles with Ag satellites at initial concentrations of 10^{-11} M, 10^{-12} M R6G compared to the SERS standard using the silica capped yellow nanoparticles and a d/g band spectra. Excitation wavelength: 532 nm.

4.1.1.5 Comparison of all nanoparticle types for R6G

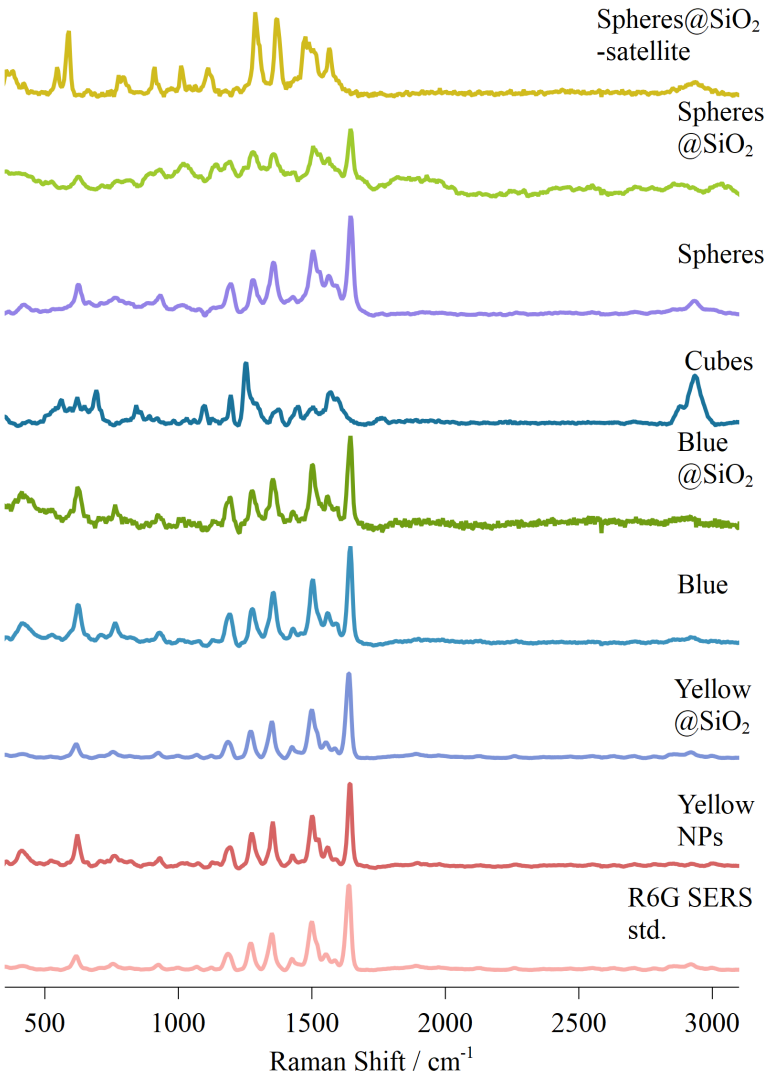

Figure 4.15: Stacked SLIPSERS spectra for all nanoparticle types for Rhodamine 6G. Excitation wavelength: 532 nm.

Comparing all the nanoparticle types in Fig.(4.15), it can be seen that the nanoparticle type with the worst signal-to-noise ratio is the Blue@SiO_2 nanoparticles, then Spheres@SiO_2, followed by Spheres@SiO_2-satellite nanoparticles. This is likely due to the fact the nanoparticles scatter too much of the incident beam due to the silica shells being too thick. The nanocubes, are able to get R6G signals up to about 10^{-14} M. The "yellow"@SiO2 dispersion appears to be one of the more sensitive nanoparticle substrates. This is likely due to the heterogeneity of the dispersion, where more than one type of shape exists. This same dispersion (without the silica shell) has been used previously for this same purpose.[95] In addition, the spherical nanoparticles and the 'blue' nanoprisms appear to be very similar in performance to each other.

4.1.2 Ponceau 4R (P4R)

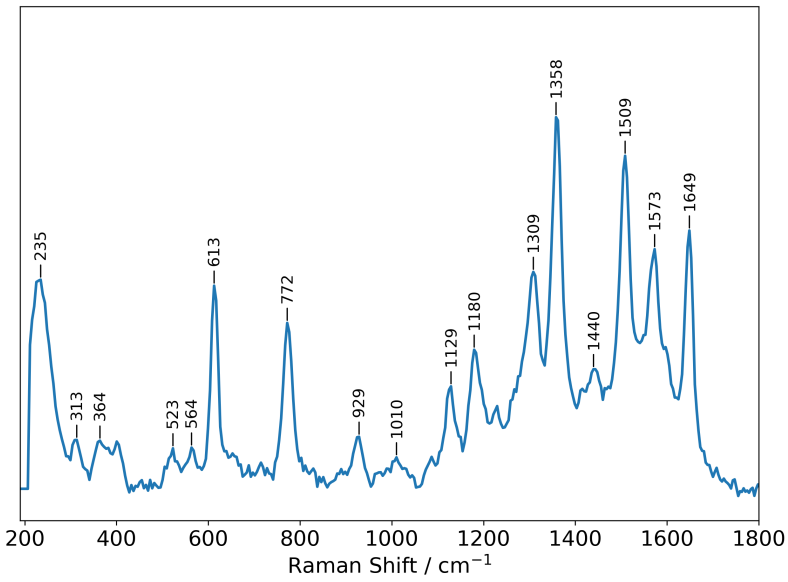

Figure 4.16: SLIPSERS spectra of P4R and the "yellow" nanoparticle dispersion at an initial concentration of 10^{-7} M. Excitation wavelength: 532 nm.

Ponceau 4R is a food dye and is prone to fluorescence at higher concentrations much like R6G. From Fig.4.16, there are some key peaks: 235 cm^{-1} from the nanoparticles (this appears in the R6G spectra). The key factors to consider in the P4R SLIPSERS spectrum are the extremely common ring vibration modes, such as at 613 cm^{-1}, 772 cm^{-1}, 1356 cm^{-1} and 1502 cm^{-1}. These, along with the important modes found in the literature are shown in Table 4.2.

Mode(s)	**Raman Shift (cm^{-1})**	
	Literature	Experimental
Crystal vibration	–	235
C-H out of plane bend	–	772
C-C-C in plane ring bend	–	613
		929
	1030	–
	1236	–
	–	1309
Aromatic C-C stretch	1356	1358
Aromatic C-C stretch	1502	1509
		1440
		1649

Table 4.2: Summary table of key concentration Raman active modes in the literature values[220] and collected experimental SLIP-SERS spectra of P4R. Excitation wavelength: 532 nm.

4.1.2.1 'Yellow' and 'Yellow'@SiO2 Nanoparticles

The 'yellow' nanoparticles Fig.(4.17) show significant fluorescence at an initial concentration of 10^{-6}, resulting in what appears to be a noisy spectrum when baselined. At an initial concentration of 10^{-7} M, peaks are more defined.

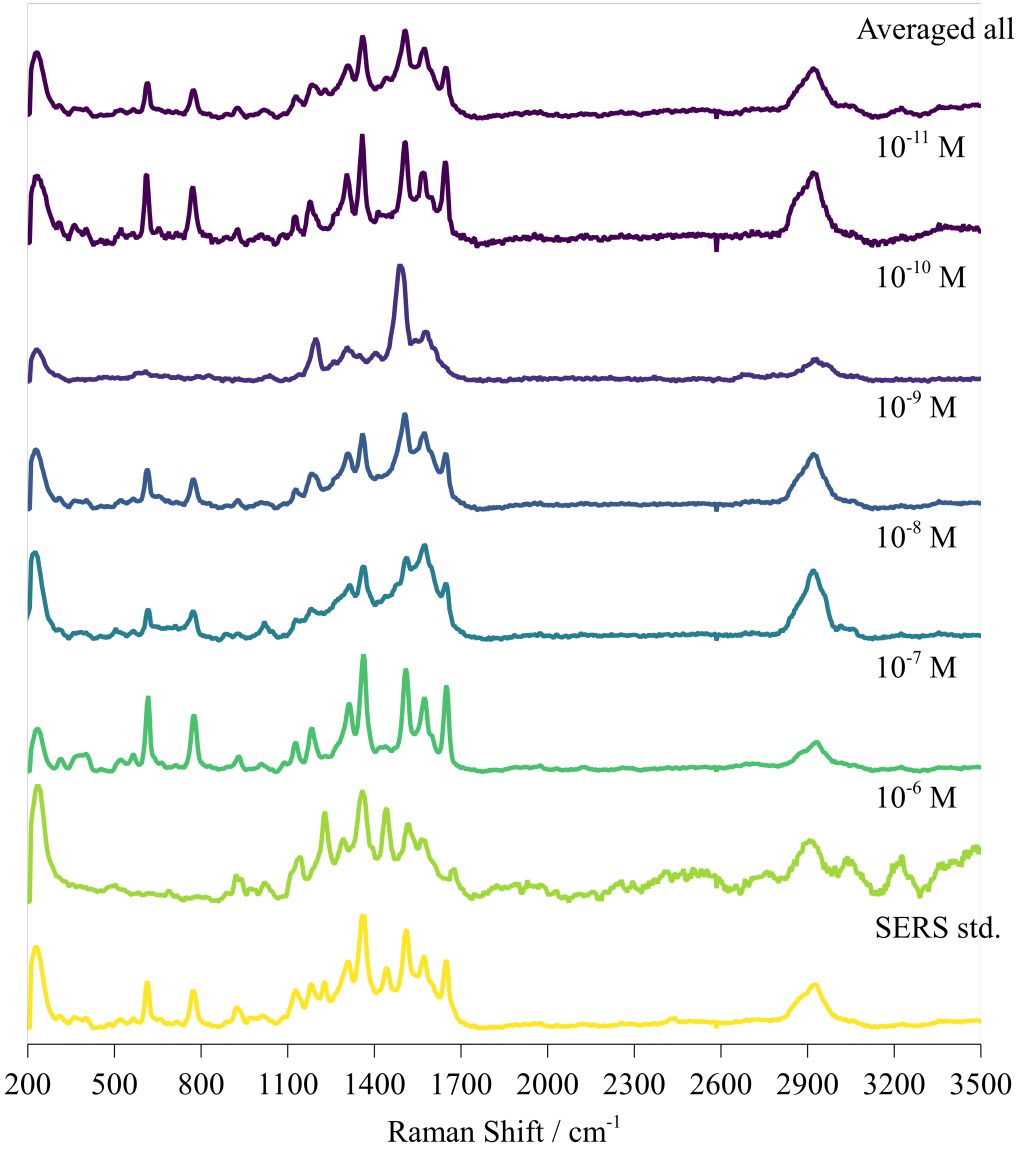

Figure 4.17: Stacked SLIPSERS spectra showing the initial concentration of added P4R in aqueous mixture (50μL) to 50μL of concentrated "yellow" nanoparticle dispersion. Arbitrary intensity. Excitation wavelength: 532 nm.

Investigating further at 500 cm^{-1} - 1900 cm^{-1} in Fig.(4.18) shows that many signals appear in most of the spectra, and that peaks at 614 and 772 cm^{-1} appear at all initial concentrations except at an initial concentration of $10^{-}6$ M. Signal to noise does not seem to degrade much at the lower concentrations.

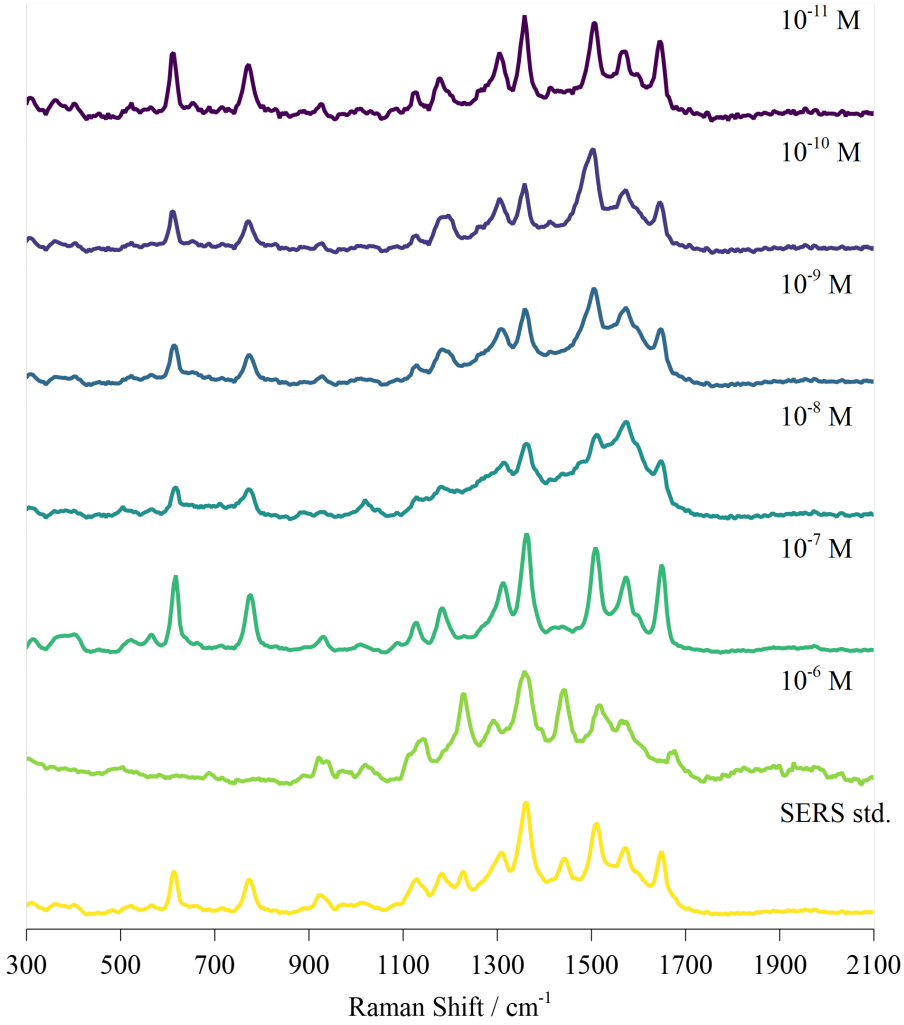

Figure 4.18: Zoomed in detail on the 'yellow' nanoparticle Raman spectra from Fig.(4.17), for the ranges 500-1900 cm^{-1}. Excitation wavelength: 532 nm.

The silica capped 'yellow' nanoparticles (Fig.(4.19)), show signals up to an initial concentration of 10^{-11} M. In addition, a C-H peak appears in all spectra at around 2929 cm^{-1}. Unlike most of the spectra in this range of analytes the spectra with the most d/g band character is at an initial concentration of 10^{-8} M, however, the peak that usually appears at around 1440 cm^{-1} is still apparent, despite losing most peak information between 1100 cm^{-1} and 1800 cm^{-1}.

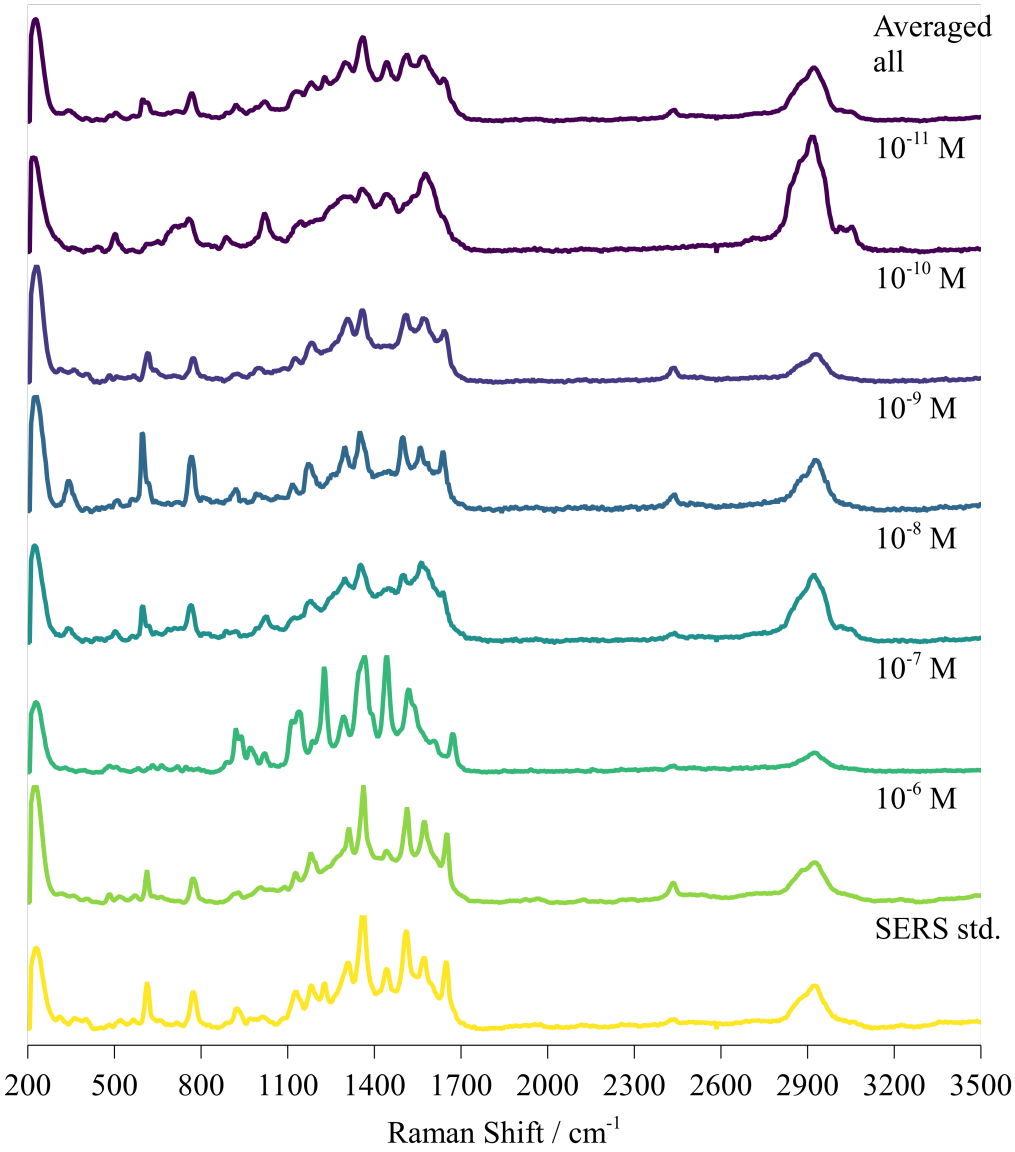

Figure 4.19: Stacked SLIPSERS spectra showing the initial concentration of added P4R in aqueous mixture (50μL) to 50μL of concentrated "yellow@SiO_2" nanoparticle dispersion. Arbitrary intensity. Excitation wavelength: 532 nm.

4.1.2.2 'Blue' Nanoprisms

In Fig.(4.20), the silver nanoprisms show a sensitivity of up to an initial concentration of 10^{-10} M. In addition, are an initial concentration of 10^{-6} M there is a significant amount of fluorescence, which is responsible for the uneven peak-like "bumps" from 3000 cm^{-1} and higher. However the C-H peak at around 2929 cm^{-1} is present in all of the spectra, indicating that at the very least an organic molecule is being detected. The presence of very apparent peaks at around 1350 cm^{-1} and 1561 cm^{-1} in the spectrum with an in initial concentration of 10^{-8}M shows that there is at least some P4R being detected with these nanoparticles. Compared to the "yellow" nanoparticles, however, there is significantly more signal-to-noise in these spectra.

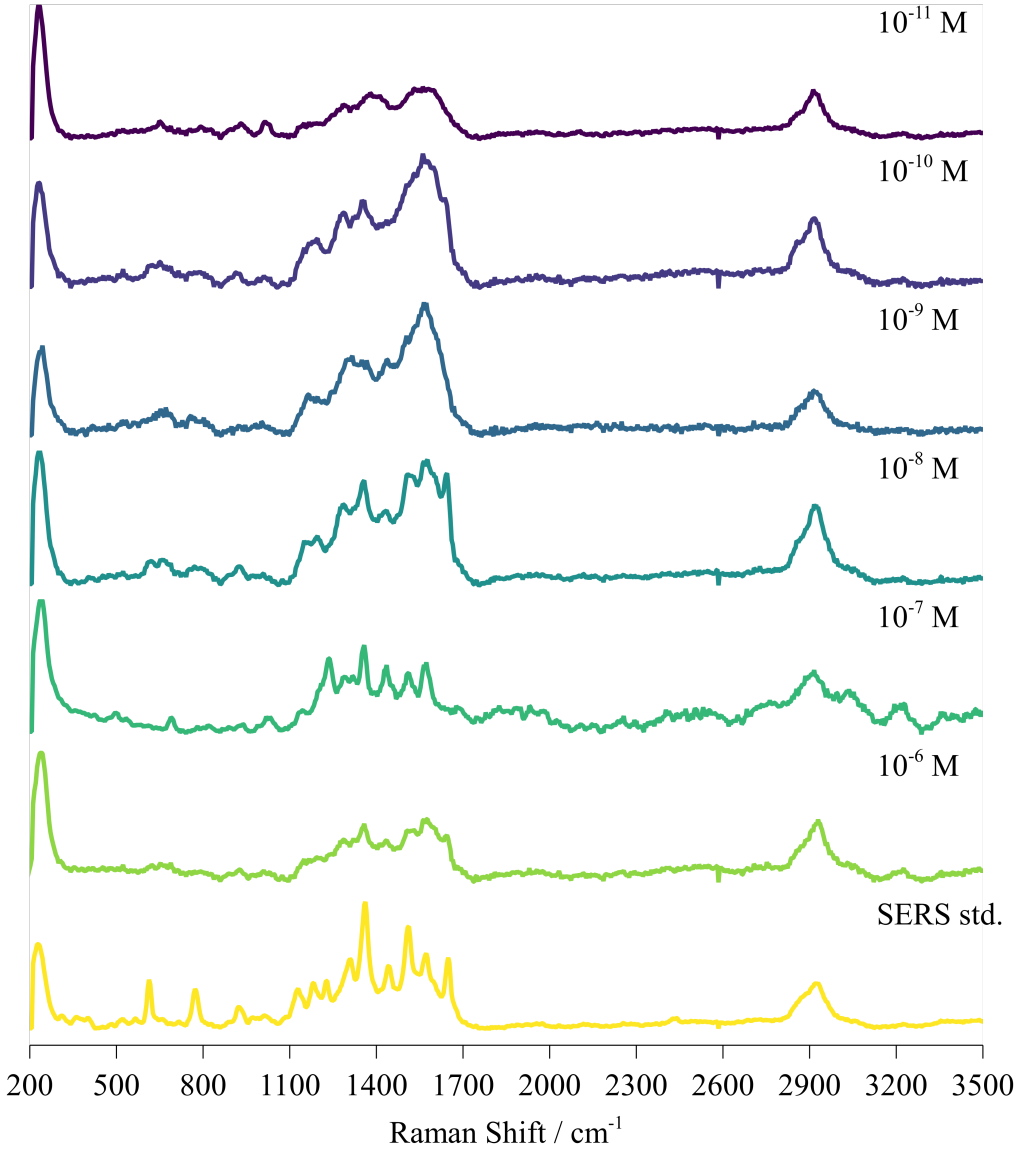

Figure 4.20: Stacked SLIPSERS spectra showing the initial concentration of added P4R in aqueous mixture (50μL) to 50μL of concentrated "blue" nanoprisms. Arbitrary intensity. Excitation wavelength: 532 nm.

The silica capped nanoprisms in Fig.(4.21), show similar behaviour as they did in the previous section with R6G, and do not display many signals relating to P4R. As with Figs.(4.17) and (4.19), C-H bands at around 2929 cm^{-1} appear at all initial concentrations. At the initial two concentrations of 10^{-6} M and 10^{-7} M, 10^{-9} M, and 10^{-10} M the raw spectrum is very fluorescent, which is responsible for the uneven peak-like "bumps" from 2300 cm^{-1} and higher. However, based on the rest of the spectra present for this nanoparticle type, they have low signal-to-noise. At the initial concentrations of 10^{-7} M, 10^{-8}, 10^{-9}, d/g bands appear to affect the spectra significantly, which is concerning. Compared to the nanoprisms in Fig.(4.20), the spectra here are significantly noisier, and have no perceptible P4R signals.

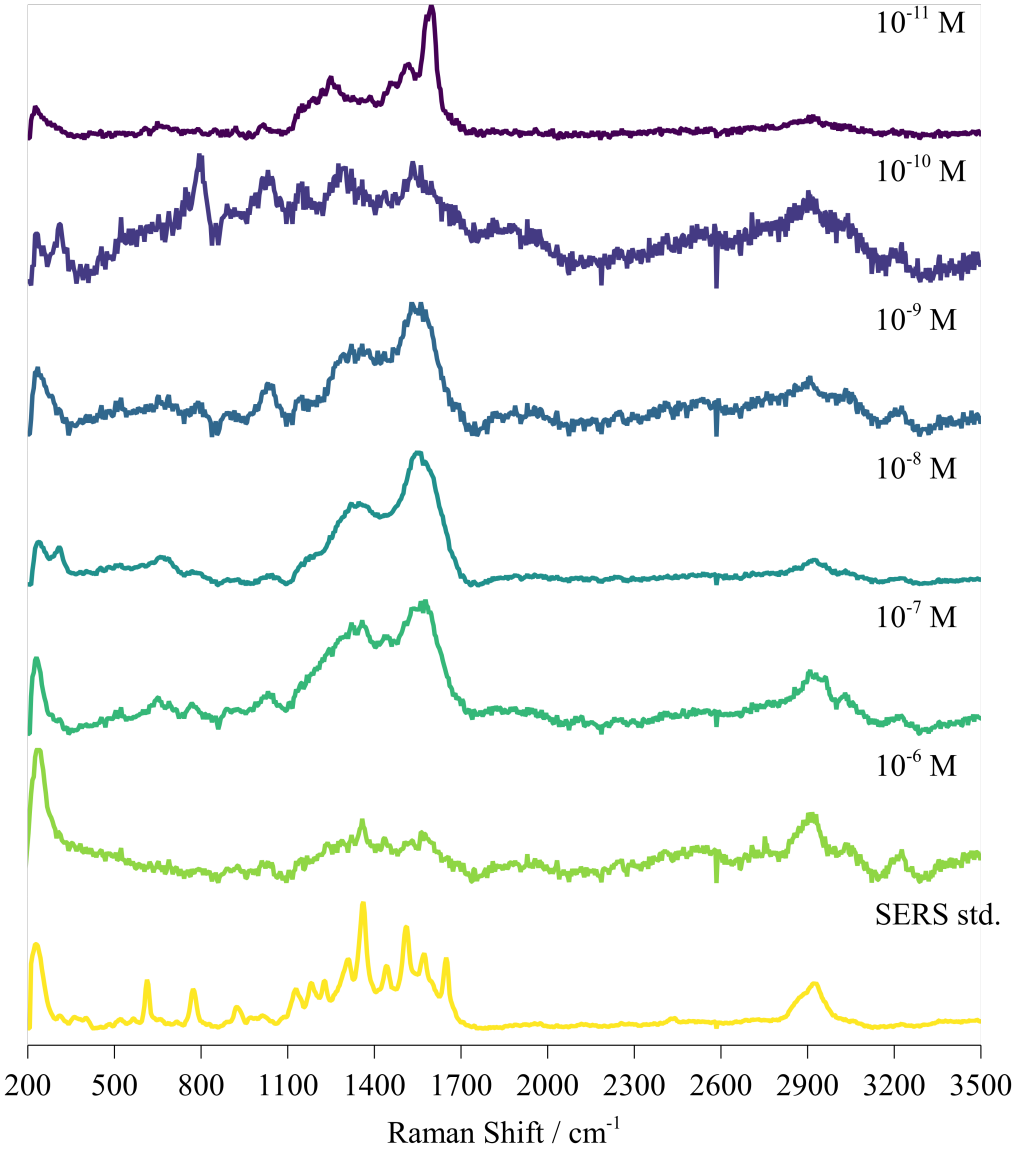

Figure 4.21: Using the silver nanoprisms capped with silica as a SERS substrate, stacked SLIPSERS spectra showing the initial concentration of added P4R in aqueous mixture (50μL) to 50μL of concentrated "blue@sio2" nanoprisms. Arbitrary intensity. Excitation wavelength: 532 nm.

4.1.2.3 Nanocubes

The Silver nanocube spectra in Fig.(4.22) show quite a lot of fluorescence from initial concentrations of 10^{-6} M to 10^{-8} M, which is responsible for the uneven peak-like "bumps" from 2300 cm^{-1} and higher. Starting at an initial concentration of 10^{-8} M, the C-H peak at around 2929 cm^{-1} appears in the SLIPSERS spectra; in addition, there also appears to be some d/g influence starting at this concentration, however, it appears as if some P4R peaks come through. In terms of signal-to-noise, there appears to be a better signal-to-noise as the initial concentration decreases. Unlike previously with R6G, the sensitivity appears to be limited with P4R, this may be

due to how P4R adsorbs differently onto the nanoparticle compared to R6G, and it not being as emissive as R6G.

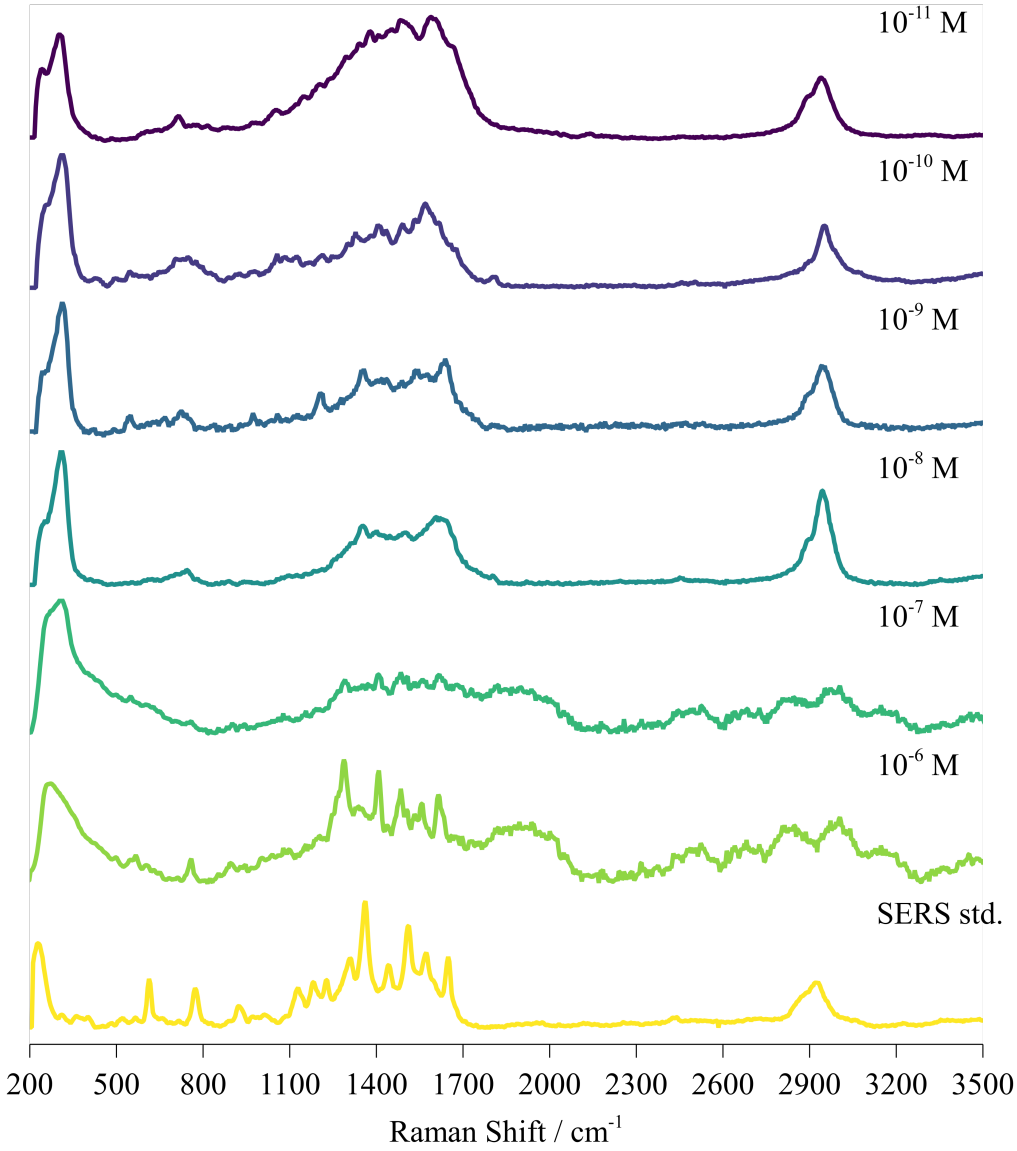

Figure 4.22: Using the silver nanocubes as a SERS substrate, stacked SLIPSERS spectra showing the initial concentration of added P4R in aqueous mixture (50μL) to 50μL of nanocubes. Arbitrary intensity. Excitation wavelength: 532 nm.

4.1.2.4 Spherical Nanoparticles

The spherical nanoparticles in Fig.(4.23) show less activity than SLIPSERS standard at an initial concentration of 10^{-6} M, however, there does appear to be significant activity at an initial concentration of 10^{-11} M. The spherical nanoparticles do appear to be capable SLIPSERS substrates, at least for P4R and R6G.

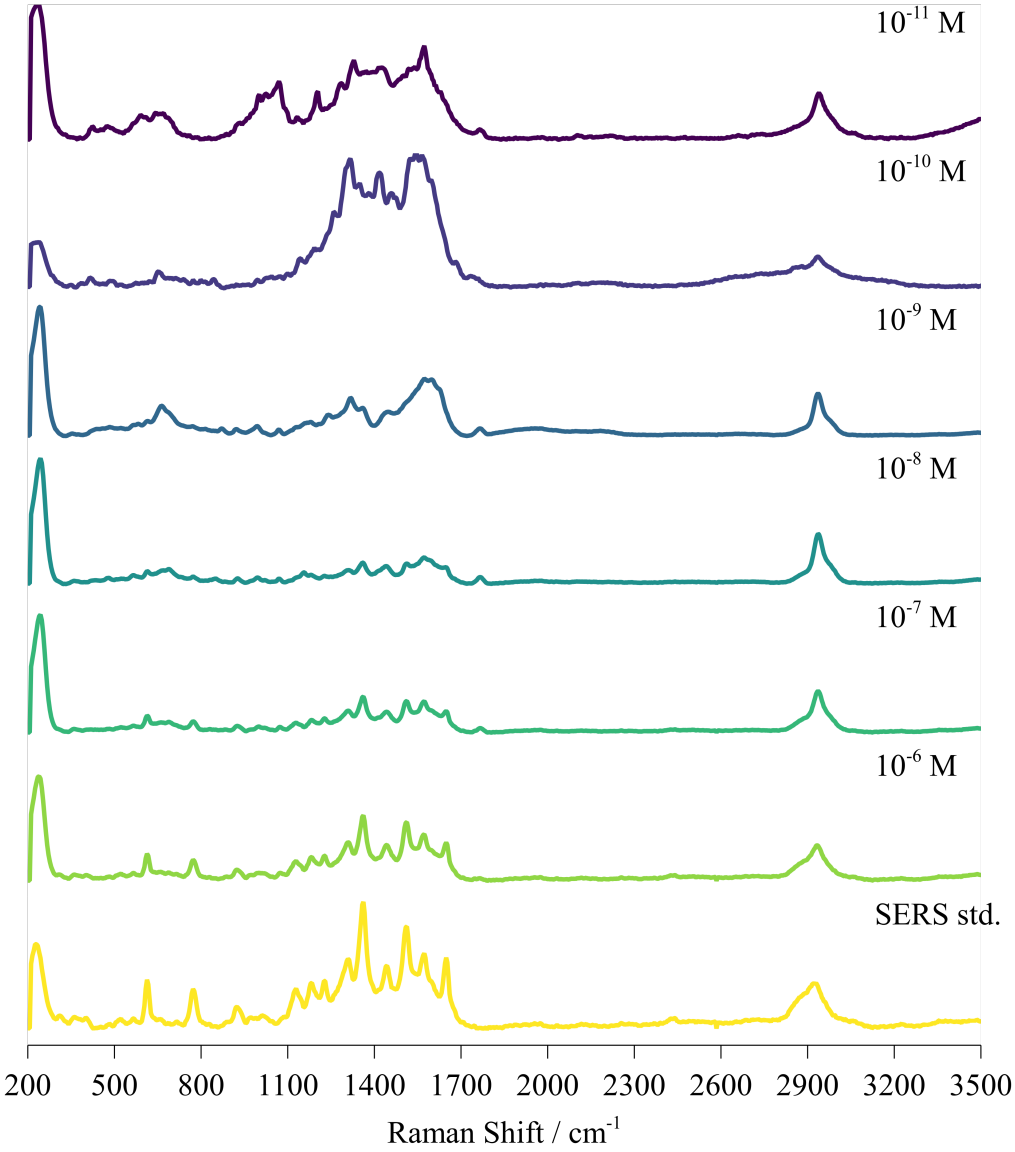

Figure 4.23: Stacked SLIPSERS spectra showing the initial concentration of added P4R in aqueous mixture (50μL) to 50μL of concentrated nanospheres. Arbitrary intensity. Excitation wavelength: 532 nm.

In Fig.(4.24), there are not many significant signals at initial concentrations of 10^{-6} M and 10^{-6} M. However, at the initial concentration of 10^{-10} M, there is the most activity that is closest to the SLIPSERS standard in similarity. This spectra with peak labels is available in Fig.(A.5). Despite this, there does appear to be some signals at around 613 m^{-1} even at an initial concentration of 10^{-11} M.

In Fig.(4.25), at an initial concentration of 10^{-6} M, there are not many high-intensity signals, however at an initial concentration of 10^{-9} M, there are strong signals, most notably at about at 1403 cm^{-1}. Despite the lack of intensity at initial concentrations of 10^{-7} M, 10^{-8} M, 10^{-10} M and 10^{-10} M, there do appear to be some signals at an initial concentration of 10^{-11} M. They appear to be a broadening of

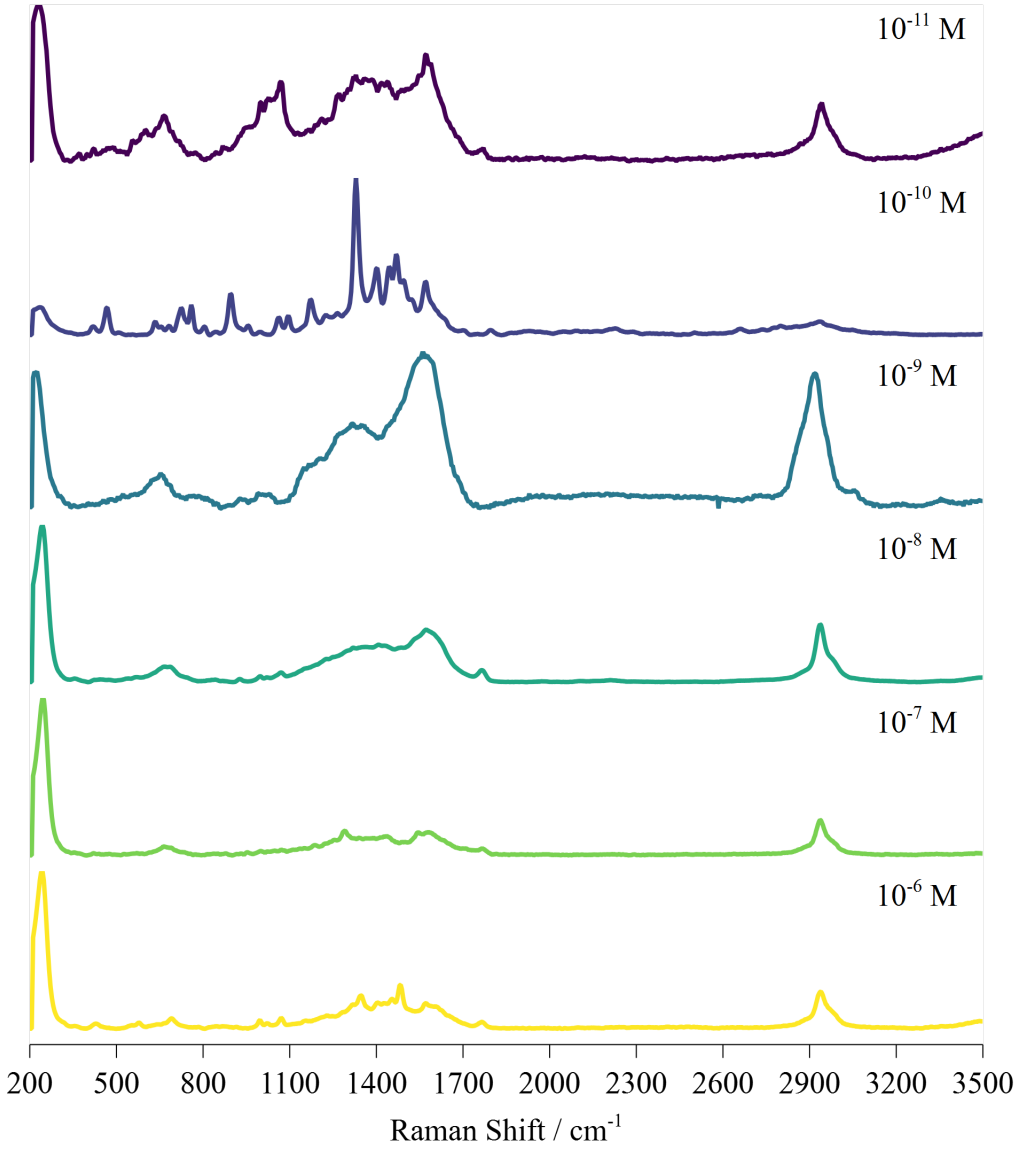

Figure 4.24: Stacked SLIPSERS spectra showing the initial concentration of added P4R in aqueous mixture (50μL) to 50μL of concentrated spheres@SiO_2. Arbitrary intensity. Excitation wavelength: 532 nm.

the modes found in 10^{-9} M and the SLIPSERS standard. A labelled spectra of the spectra an initial concentration of 10^{-9} M is found in Fig.(A.1).

4.1.2.5 Comparison of All Nanoparticle Types

Based on the comparison of selected spectra from each nanoparticle type in Fig.(4.26), it appears that the spectra with the best signal to noise are the "yellow" nanoparticle dispersion, while the noisiest spectra are from both of the nanoprisms types ("blue"). The yellow nanoparticles have the closest to the SERS standard spectra due to the yellow nanoparticles being used to create the SERS standard.

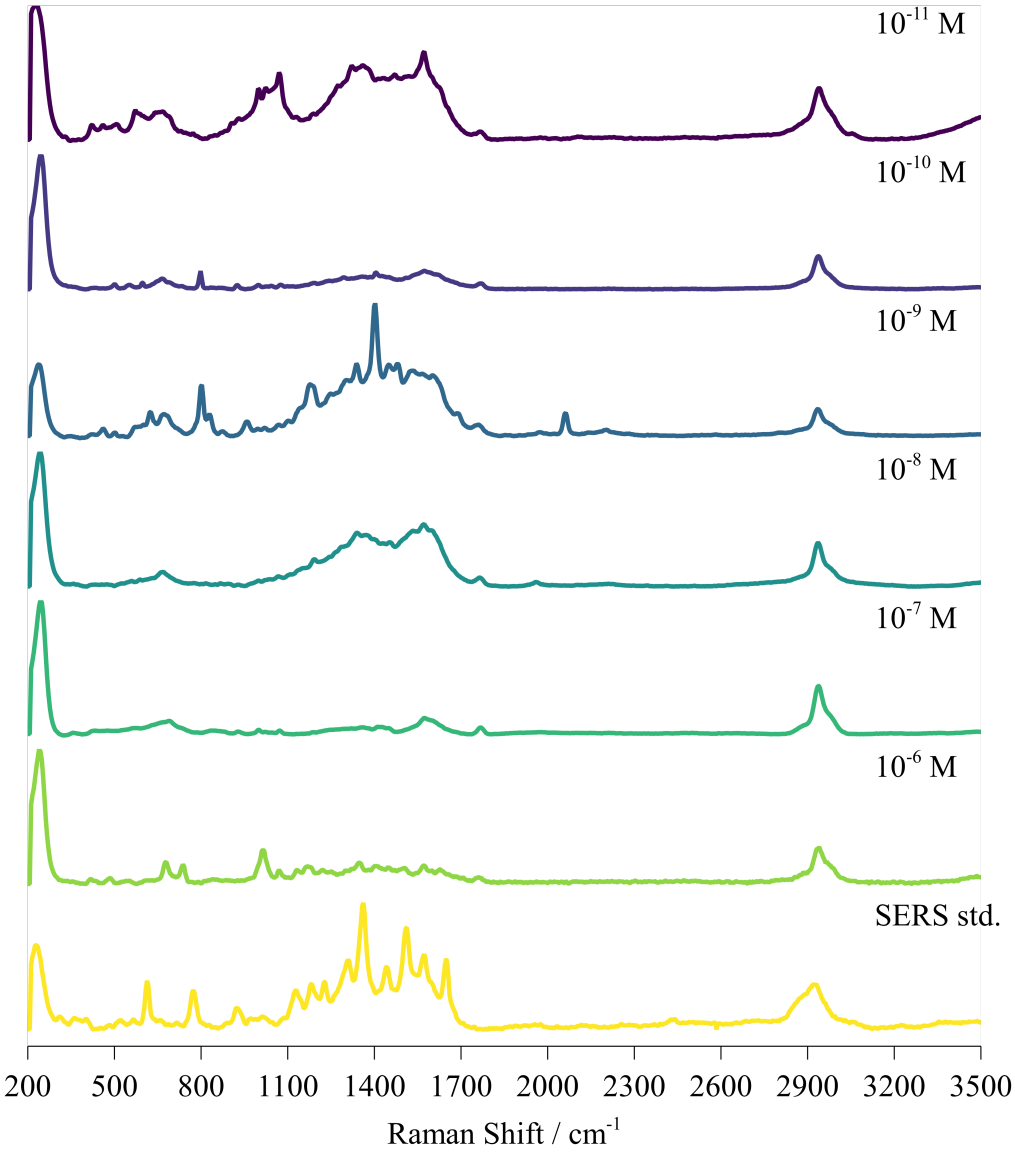

Figure 4.25: Stacked SLIPSERS spectra showing the initial concentration of added P4R in aqueous mixture (50μL) to 50μL of concentrated spheres@sio2 with Ag Satellites. Arbitrary intensity. Excitation wavelength: 532 nm.

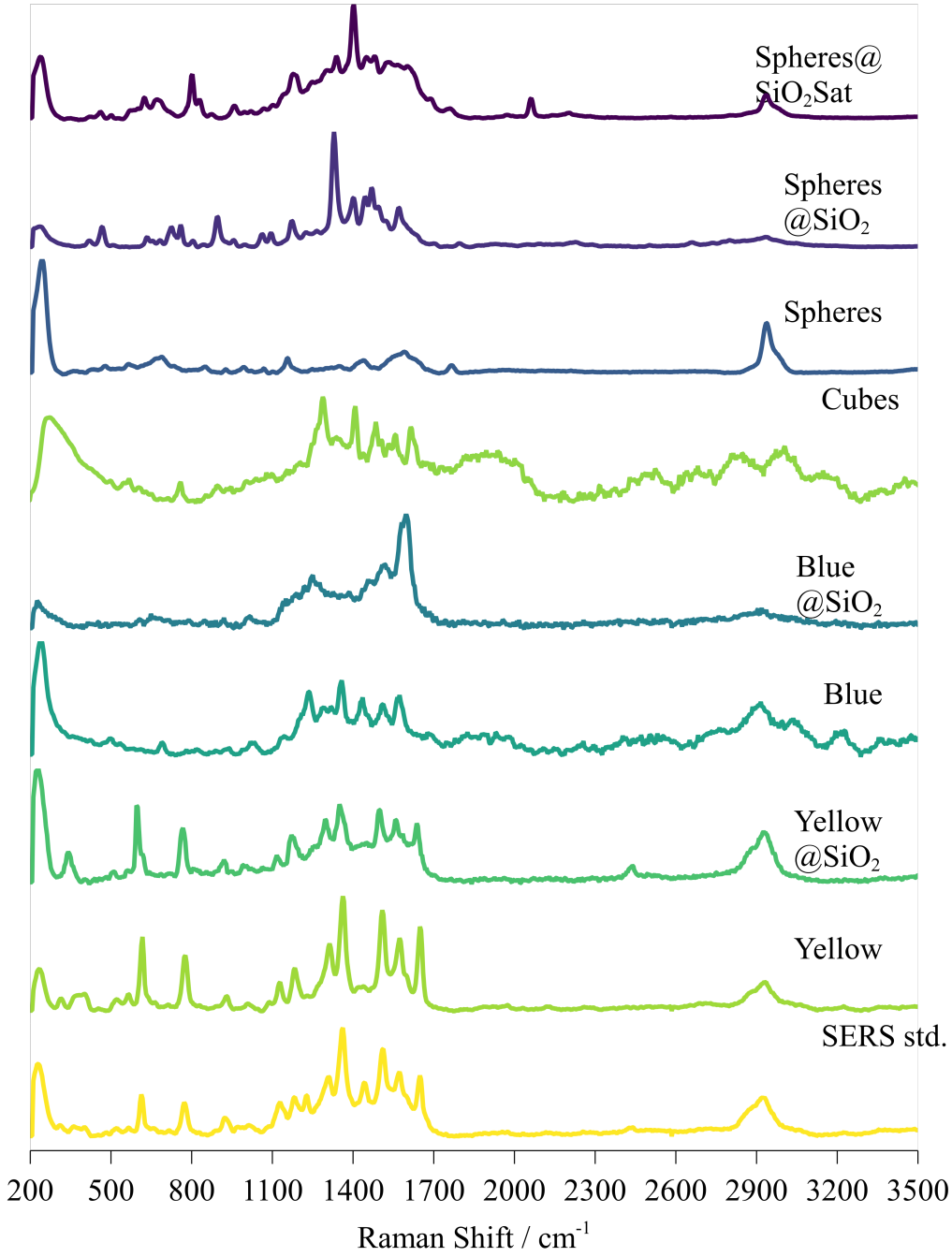

Figure 4.26: Summary of selected SERS spectra based on their nanoparticle substrate type for P4R. Excitation wavelength: 532 nm.

4.2 Linear Discriminant Analysis of the dye spectra

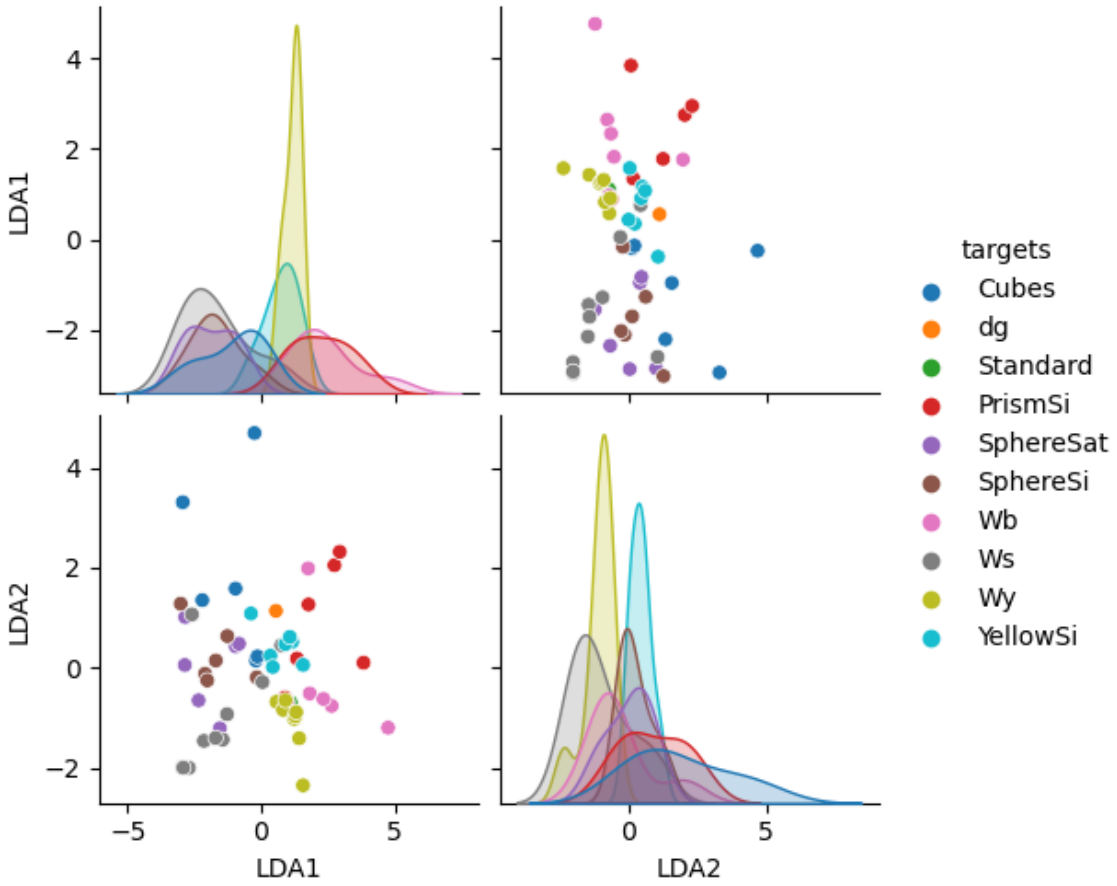

Figure 4.27: Linear Discriminant Analysis of all of the P4R SLIPSERS spectra, organised by their nanoparticle type.

In Fig.(4.28), the LDA analysis of only the SHIN substrates for P4R shows that the nanoparticles are forming independent groups. However, based on the previous spectra, much of this appears to be due to either a fluorescent background or the d/g background.

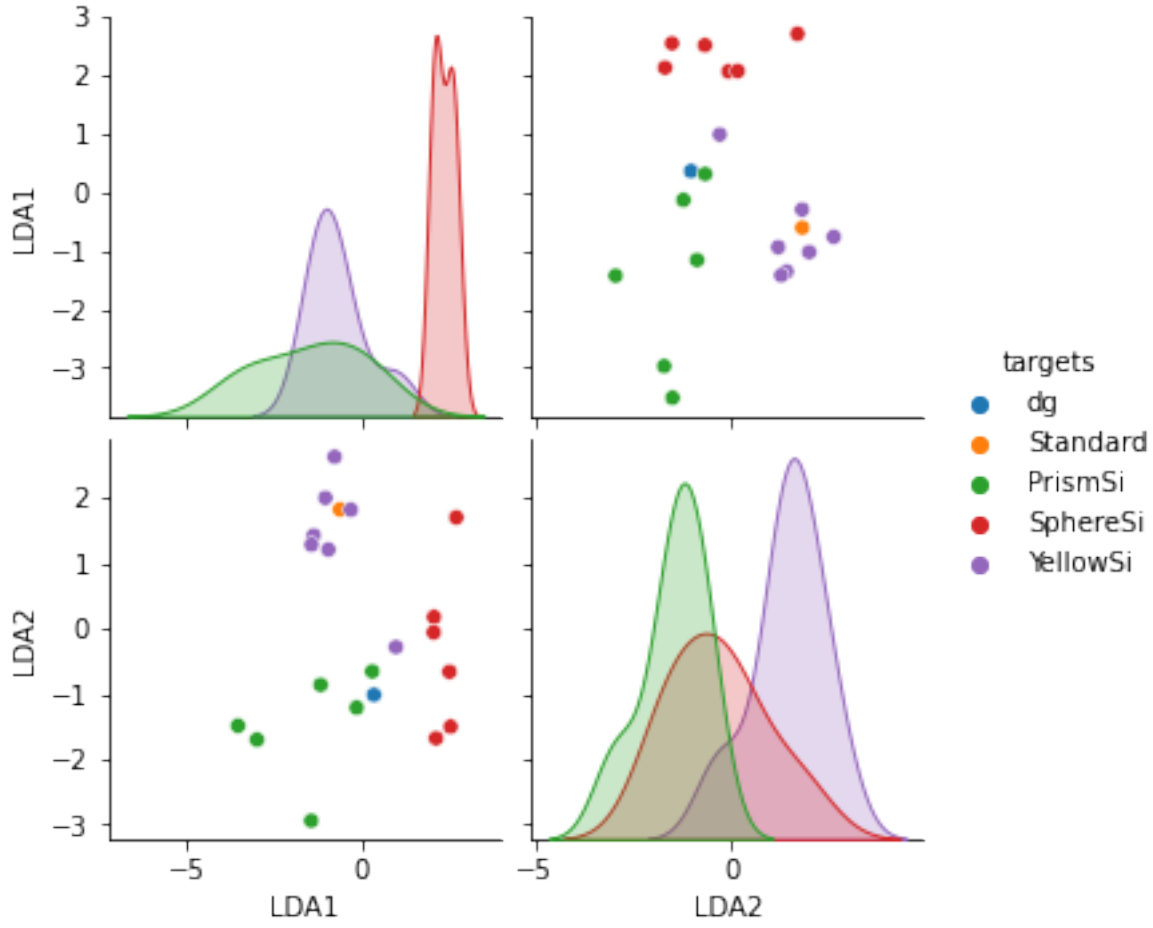

Figure 4.28: Linear Discriminant Analysis of all of the P4R SLIPSERS spectra which use SHINs as their substrate, organised by their nanoparticle type.

In contrast, comparing the spectra by nanoparticle type for R6G, it appears that there are similar amounts of grouping to the previous LDA plot. However, it appears more consistent based on the distribution plots. This might either indicate that, because R6G is more emissive, more vibrations appear, further increasing the chances of differences between the spectra, or that in the P4R experiments, there is more user error.

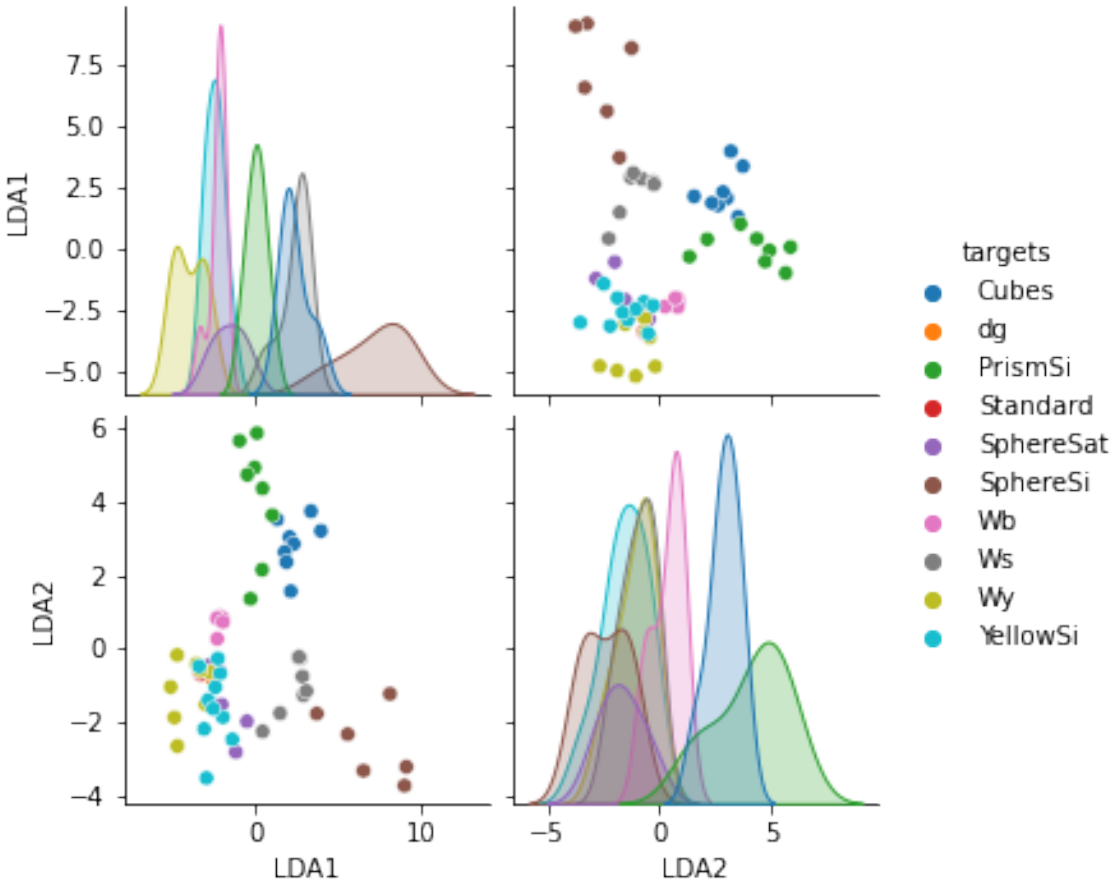

Figure 4.29: Linear Discriminant Analysis of all of the R6G SLIPSERS spectra, by their nanoparticle type.

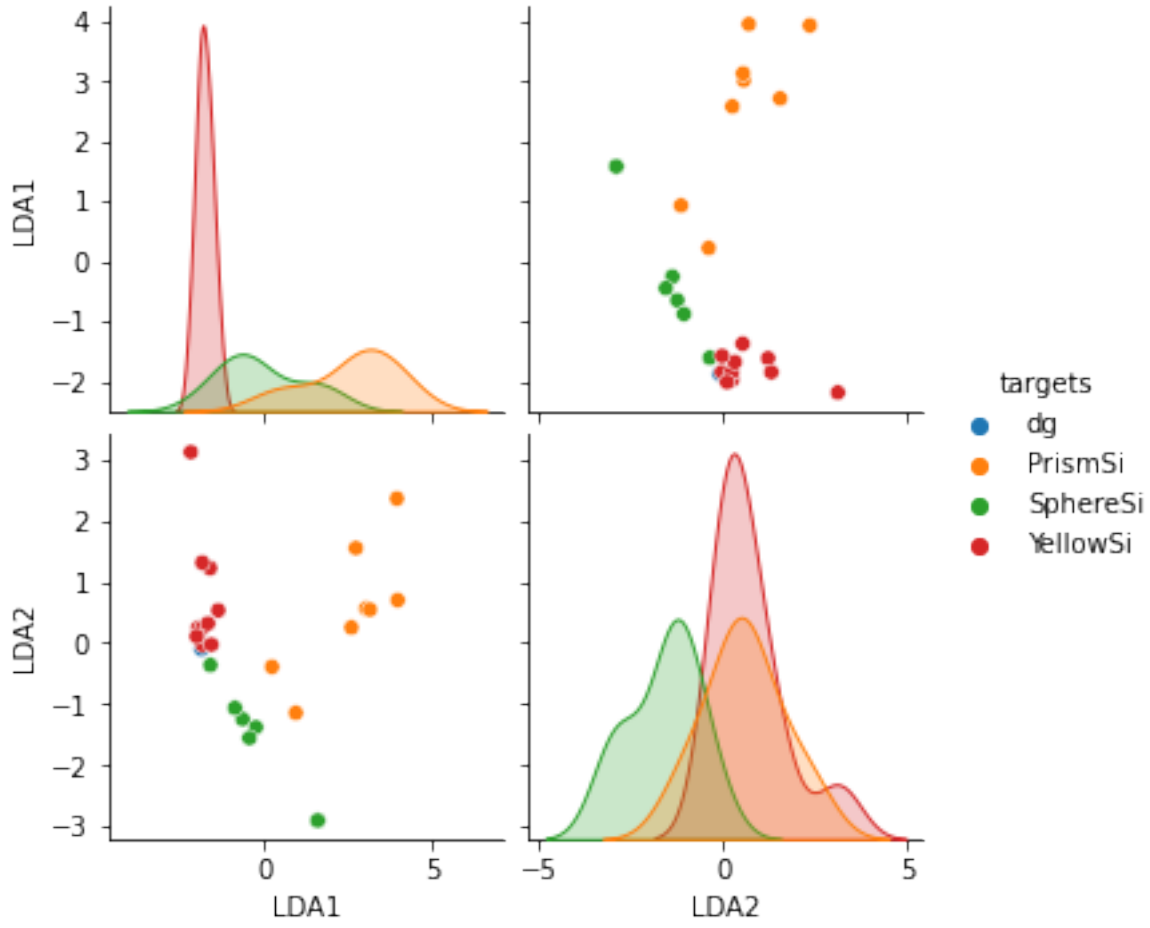

Figure 4.30: Linear Discriminant Analysis of all of the R6G SLIPSERS spectra which use SHINs as their substrate, organised by their nanoparticle type.

Finally, comparing all of the spectra for both dyes in Fig.(4.31) there is a very clear separation between both types of dye with very little overlap between the two classes of dye. In addition, there is little to no clustering of the analyte clusters with the d/g reference spectra (green dot). This suggests that the spectra collected via SLIPSERS are statistically different from one another, potentially ruling out significant issues related to user error, or the presence of similar capping agents that were not removed sufficiently, which can increase the similarity between the spectra.

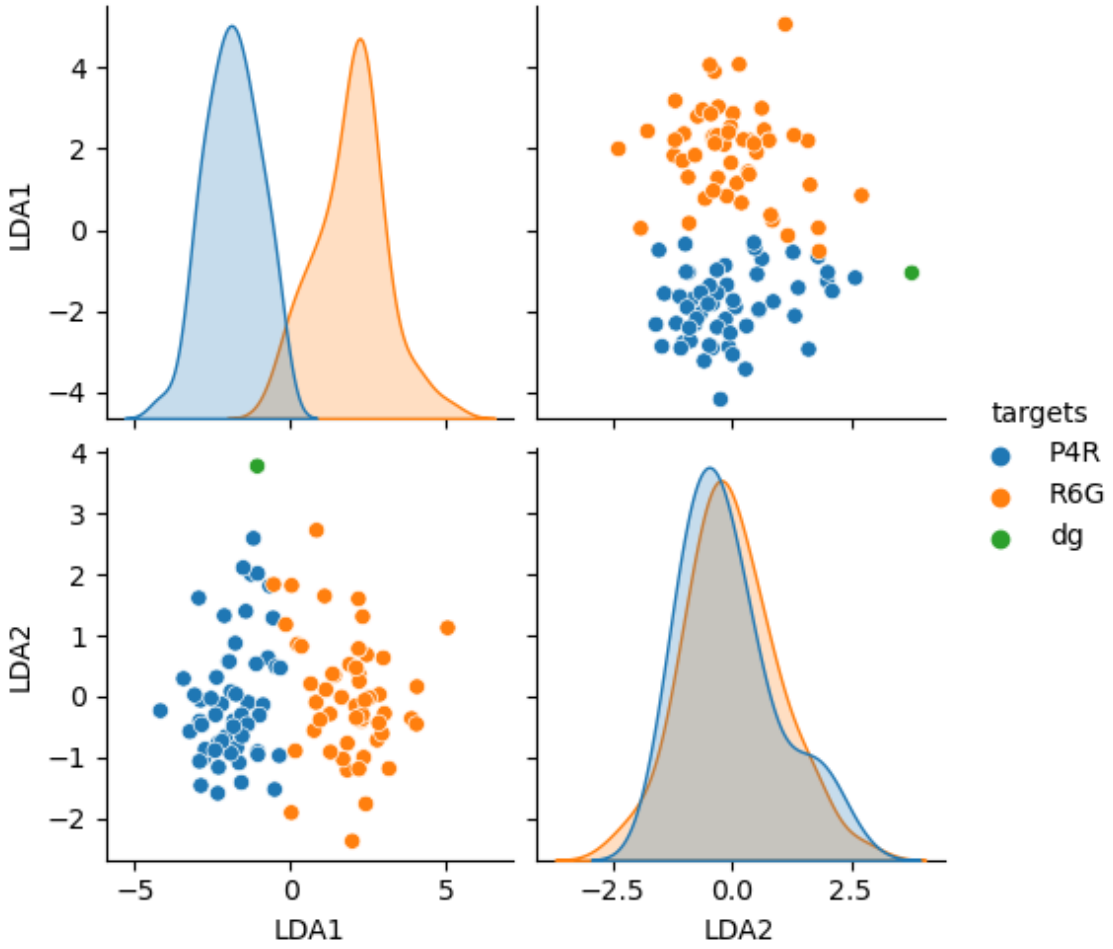

Figure 4.31: Linear Discriminant Analysis comparing of all of the P4R and R6G SLIPSERS spectra, by the type of dye.

Next, comparing all of the dyes, but only using the SHIN substrates used in Fig.(4.32), shows that there is a clear separation between the three kinds of SHINs, indicating that the nanoparticles do produce very different spectra from each other. There is some overlap with the silica capped "yellow" nanoparticles, however, this is because the standard spectra for both P4R and R6G were made using silica capped "yellow" nanoparticles.

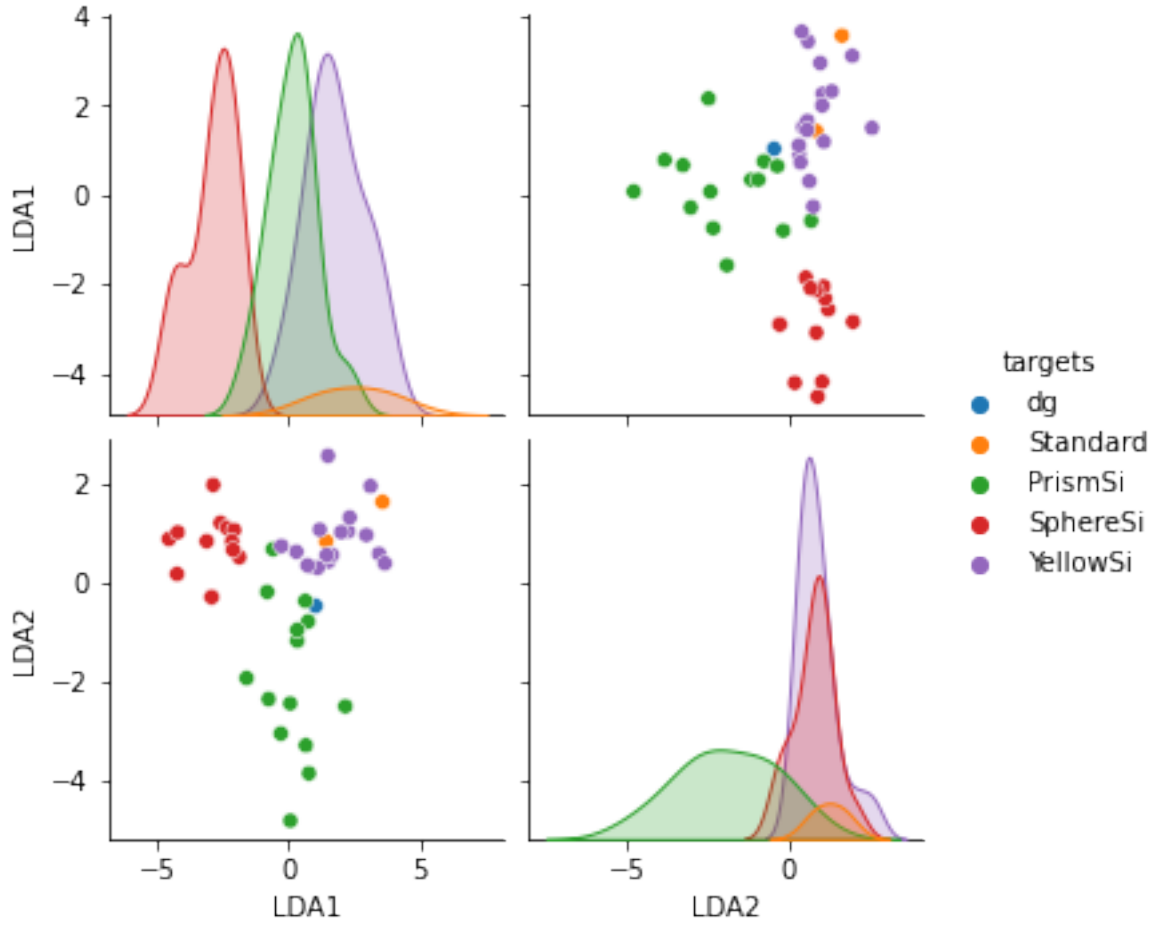

Figure 4.32: Linear Discriminant Analysis of all of the dye SLIPSERS spectra which use SHINs as their substrate, organised by their nanoparticle type.

Conversely, when comparing the separation between the two dye types, there is not as much separation observed as when all of the nanoparticle types are included in Fig.(4.31), this can be explained by the LDA algorithm finding more variation between the two spectra when all of the other nanoparticle types are included, so the model can identify more of the features in the spectra. The loadings plot in Fig.(A.21) shows how each peak contributes to the observed variations in the SHIN spectra for both dyes; in particular, PC1 is very noisy, indicating that this principal component has to do with intensities of the SERS signals. In addition, there is most of the variation in the ranges 400 cm^{-1} to 2000 cm^{-1}.

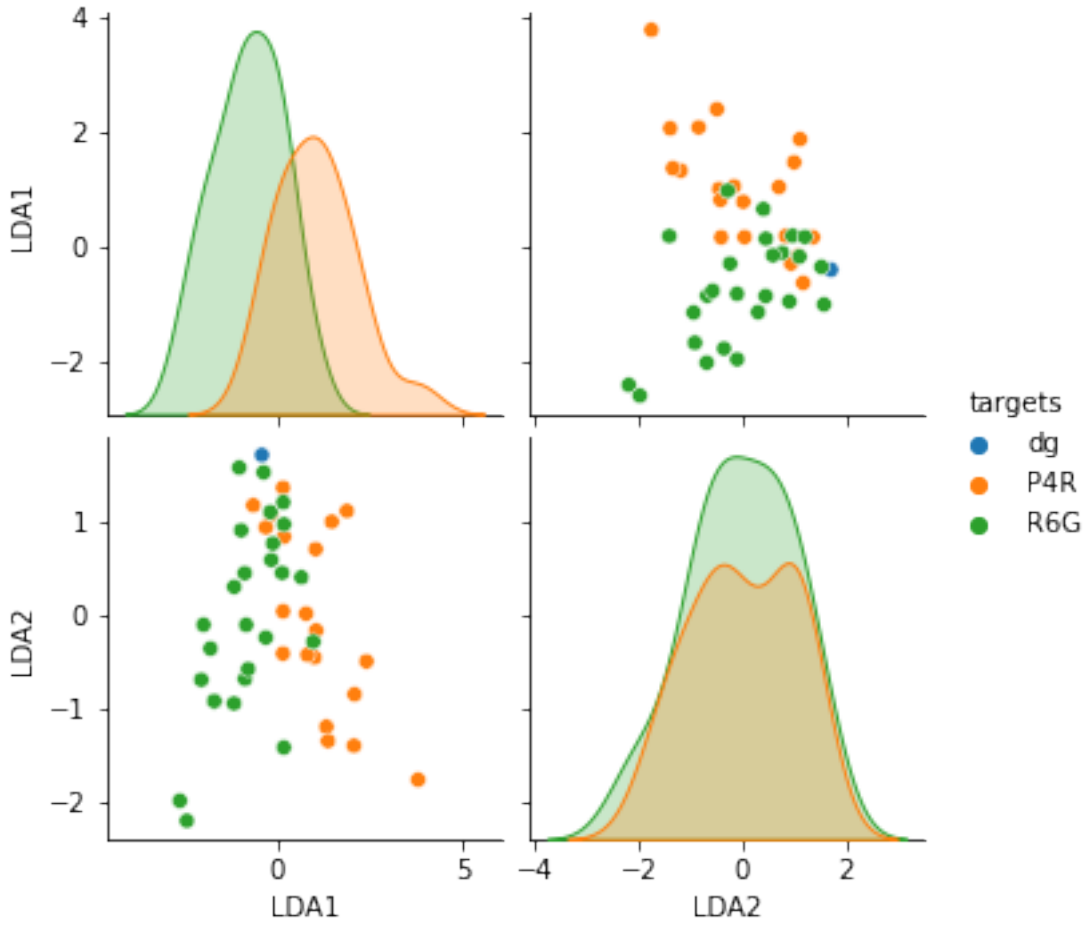

Figure 4.33: Linear Discriminant Analysis of all of the dye SLIPSERS spectra which use SHINs as their substrate, organised by the analyte.

5. SLIP-SERS Detection of Glyphosate

5.1 Raman spectrum

In order to understand the fundamental modes occurring in the SERS spectra, it would be important to understand the Raman spectrum of glyphosate. In Fig.(5.1) important, but generic modes such as the C-H vibrations can be seen at 2900-3000 cm^{-1}. This is also compared to the calculated spectra using B3LYP with basis set of 6-311++G(3d,2p) in Fig.(5.2), where it exists in the same region, although shifted a bit more towards 3100-3200 cm^{-1}. Given that glyphosate is a polyprotic compound, its SERS spectra will change depending on the chemical environment, in the case of the Raman spectra, it is taken in powdered form and free of solvents. This will mean that it is in its neutral form.

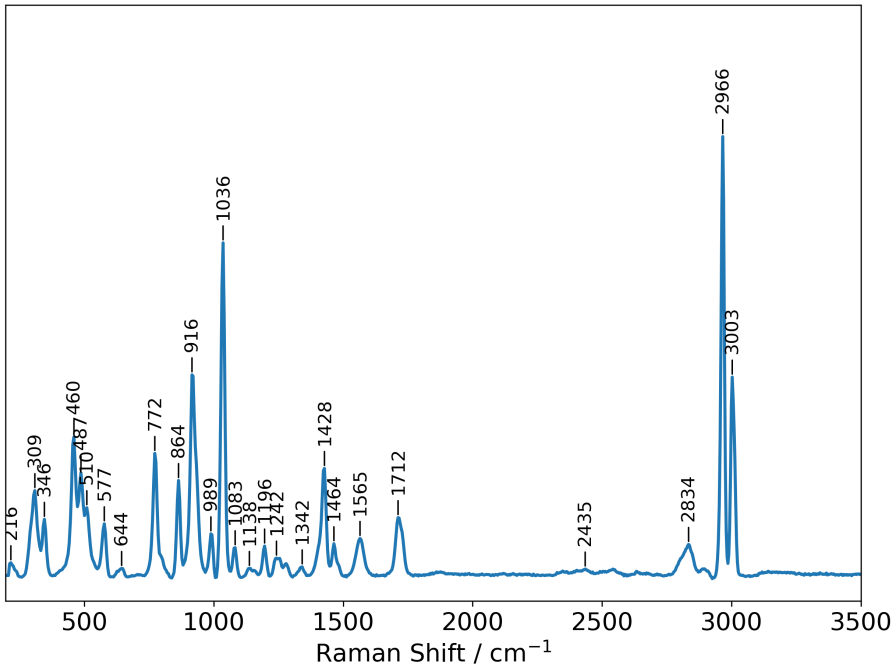

Figure 5.1: Peak labelled Raman spectra of a sample of PESTANAL analytical grade (99%) Glyphosate sandwiched between two cover slips. Collected at 532 nm.

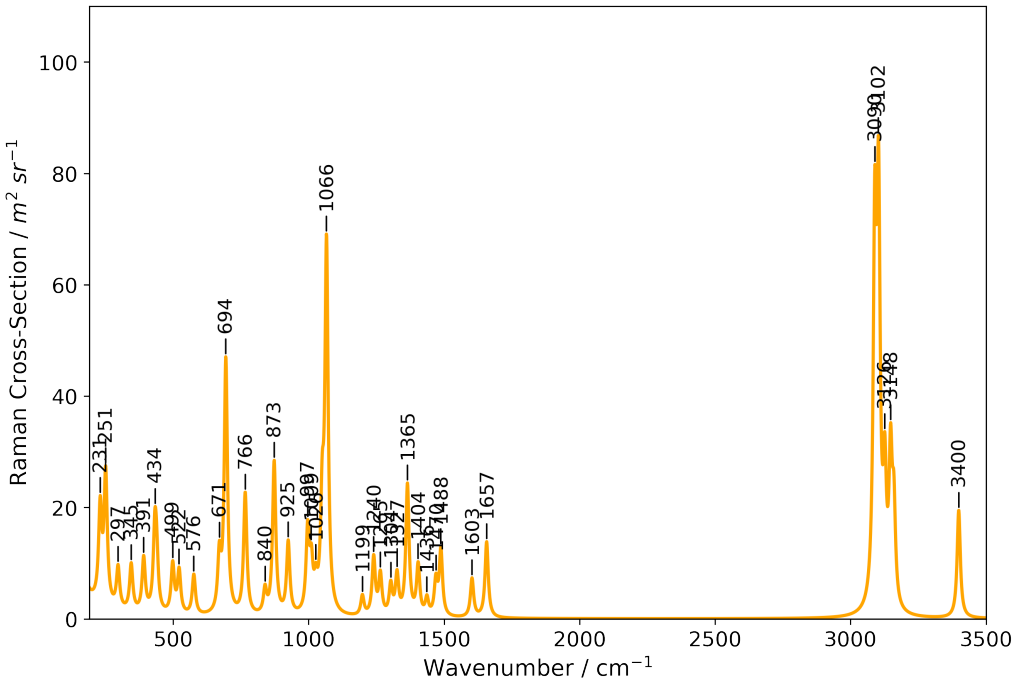

Figure 5.2: Calculated Raman spectra of the glyphosate anion using B3LYP and 6-311++G(3d,2p) basis set.

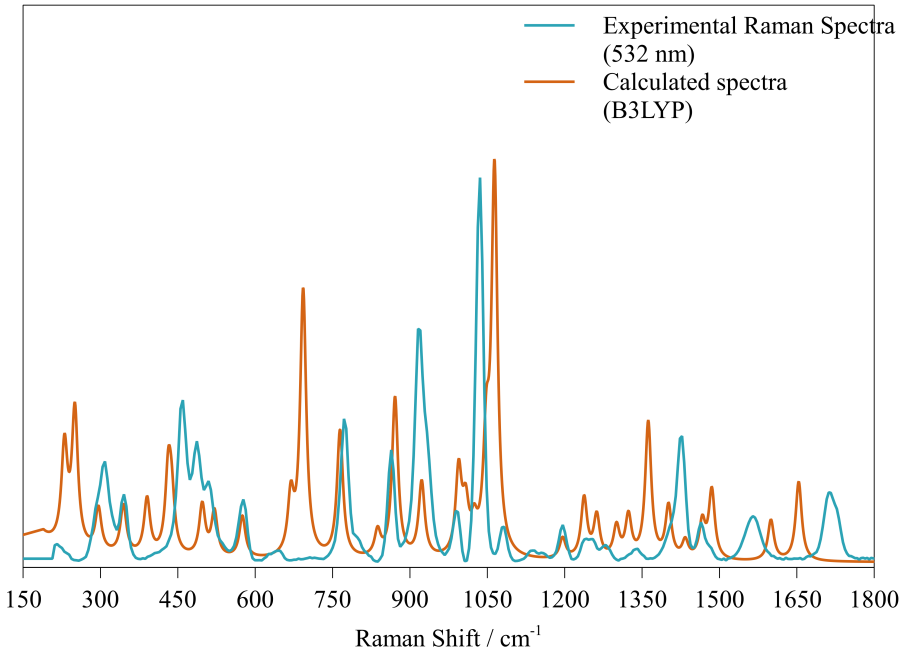

Figure 5.3: Overlayed comparison of the calculated Raman spectra (B3LYP 6-311++G(3d,2p)) (orange) and the experimental Raman spectra (teal) collected at 532 nm. Frequencies are scaled.

Comparing the Raman spectrum and the calculated Raman spectrum in Fig.(5.3)

there appears to be minimal agreement with the collected spectra, the reason for this could be the

	Wavenumber (cm^{-1})	
Mode(s)	Calculated	Experimental
v_s C-H	3090	2966
v_{as} C-H	3148	3003
v_{as} -CO_2, bend -NH_2	1657	1712
bend NH_2	1565	1603
wag -CH_2, -NH_2 wag	1365	1364
-CH_2 twist	1199	1196
torsion C-N, P-O	1066	1033
torsion -CH_2	766	772
torsion -NH_2	671	—
P-OH wag	297	309
torsion -O-H, -CH_2	345	346
lattice, -CH_2 torsion	216	231

Table 5.1: Summary table of the important Raman active modes in the experimental and calculated spectra (B3LYP and B3LYP and 6-311++G(3d,2p) basis set. of glyphosate. Collected at 532 nm.

5.2 SLIPSERS Spectra

Glyphosate is a polyprotic compound, and the electronic structure will affect its observed spectrum due to the changes in polarizability; this will also affect how it adsorbs onto the nanoparticle surface. In these experiments, glyphosate is initially exposed to water with a pH of about 7 (MilliQ filtered water). However, 50 μL of this solution is exposed to a 50 μL solution containing the silver nanoparticles, and then it is subsequently dried during the SLIPS preparation (which ideally would remove most if not all of the water from the system). To establish an understanding of the SERS spectrum, an exploration with silica capped nanoparticles and an excess amount of glyphosate (0.1 M initial concentration, using 50μL concentrated nanoparticles and 50μL glyphosate in water) was done to avoid any complications with organic capping agents like PVP or citrate. Three spectra were collected in order to capture a larger set of data (each spectrum contains about 120 "frames" which are individual spectra in and of themselves).

	Wavenumber (cm^{-1})		
Mode(s)	SERS	Raman	Calculated Raman
v_s -CH_2 stretch	2939	2966	3090
asym -CH_2 stretch	2973	3003	3158
-NH_2 bend, v_s -CO_2	1629	1657	1712
v_s C=O	1629		1657
	1576		
-CH_2 wag	1362	—	1365
	733		
torsion -O-H, -CH_2	345	346	345
lattice	211, 235	216	231

Table 5.2: Summary table of the observed SERS modes present in the average of the three spectra containing excess glyphosate with silica capped nanoparticles compared with the experimental Raman spectra and calculated Raman spectra of glyphosate. Collected at 532 nm.

In Fig.(5.4), there are common motifs with the three spectra collected: there is a prominent -CH_2 stretching band at around 2939 cm^{-1}, and what appears to be a combination of modes around the 235 cm^{-1} area. This most likely corresponds to a combination of lattice modes from the silver nanoparticles themselves, the lattice from Ag@SiO_2 and possibly enhanced modes that appear weak in the Raman spectra of glyphosate at 216 cm^{-1}, which also appear in the calculated spectra at 231 and 251 cm^{-1}.

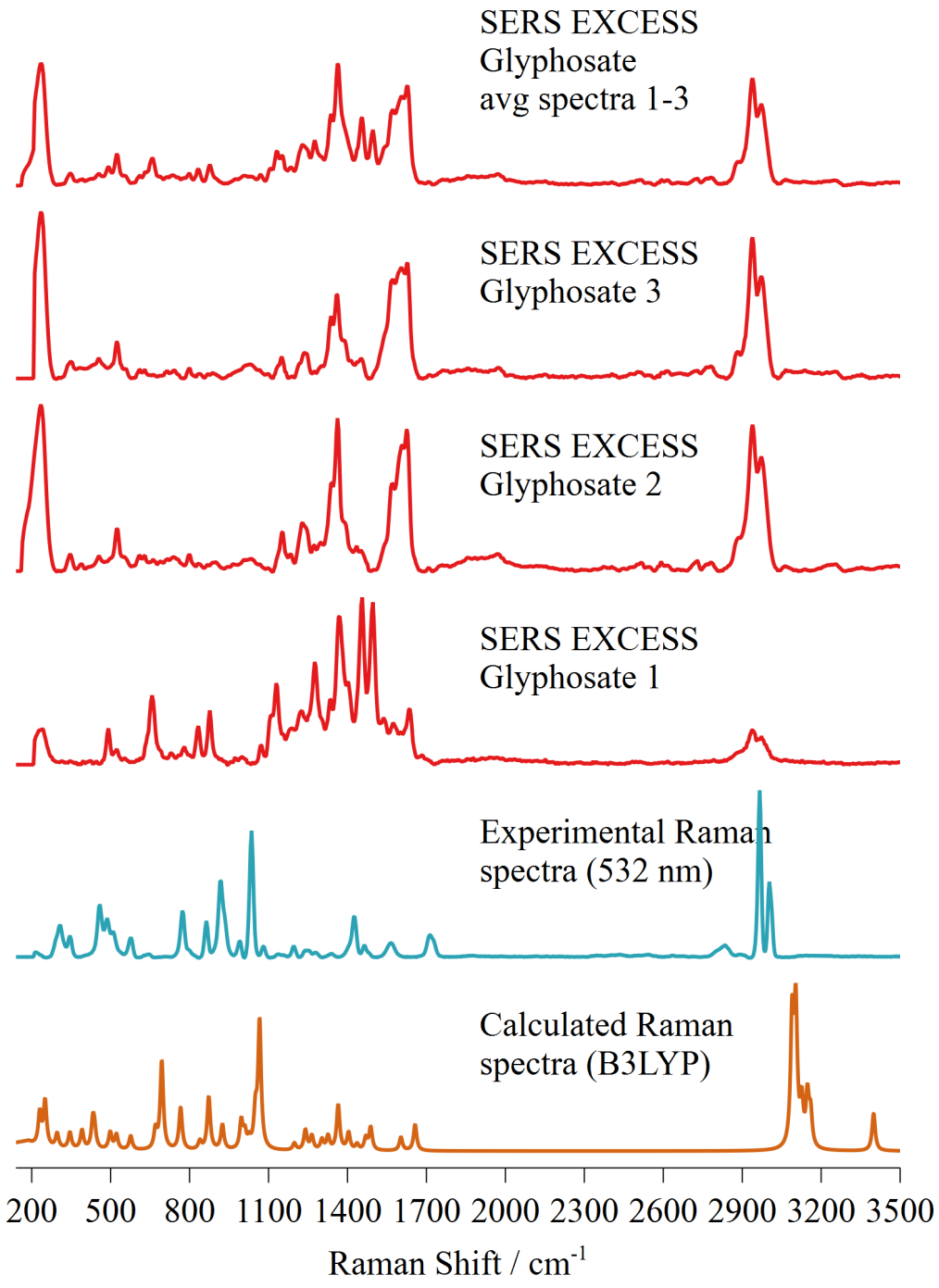

Figure 5.4: Comparison of glyphosate calculated and experimental Raman spectra with SERS spectra containing an excess of glyphosate, and an average of the three collected spectra (top). Collected at 532 nm.

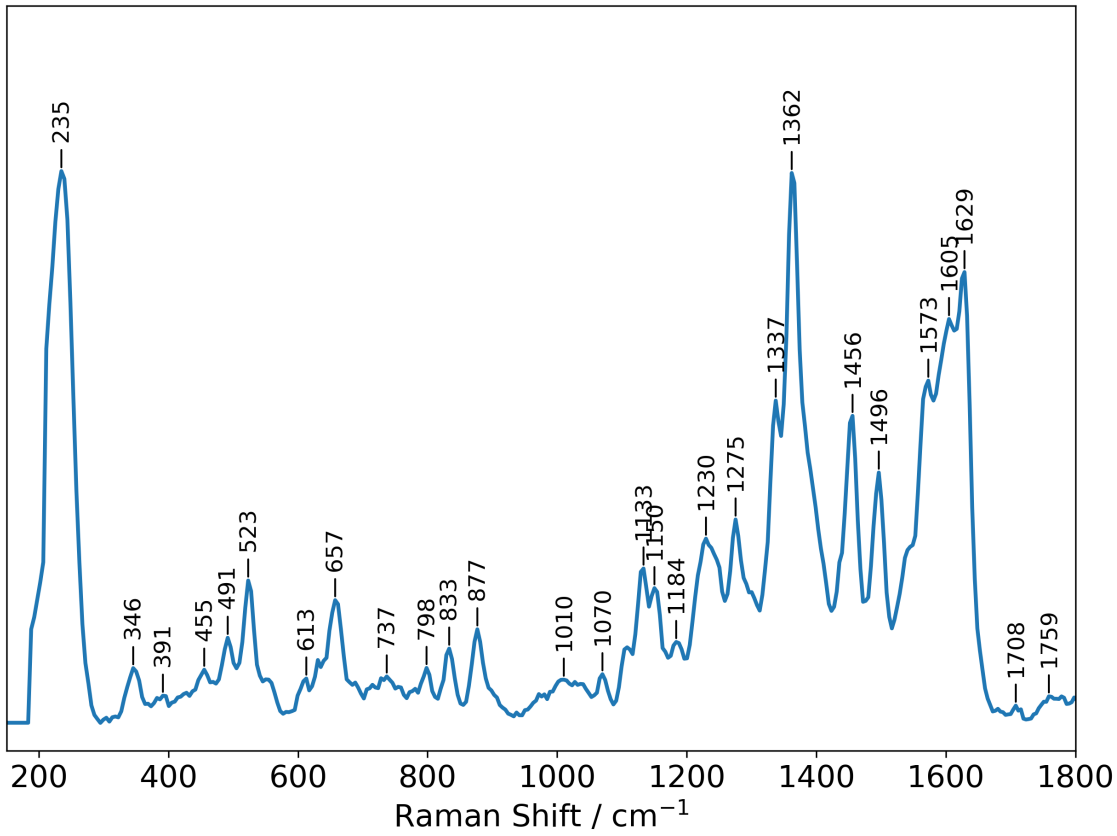

Figure 5.5: Averaged spectra of the three spectra collected of excess glyphosate with the yellow Ag@SiO_2 substrate. Collected at 532 nm.

Note that the flat line after 180 cm^{-1} is due to binning some data because of the limits of the detector causing issues with the peak at 235 cm^{-1} that would exaggerate it after data processing. The environmental conditions (such as pH), and resonance can affect how the polarizability of glyphosate changes with respect to the Raman intensity of the C=O bands.

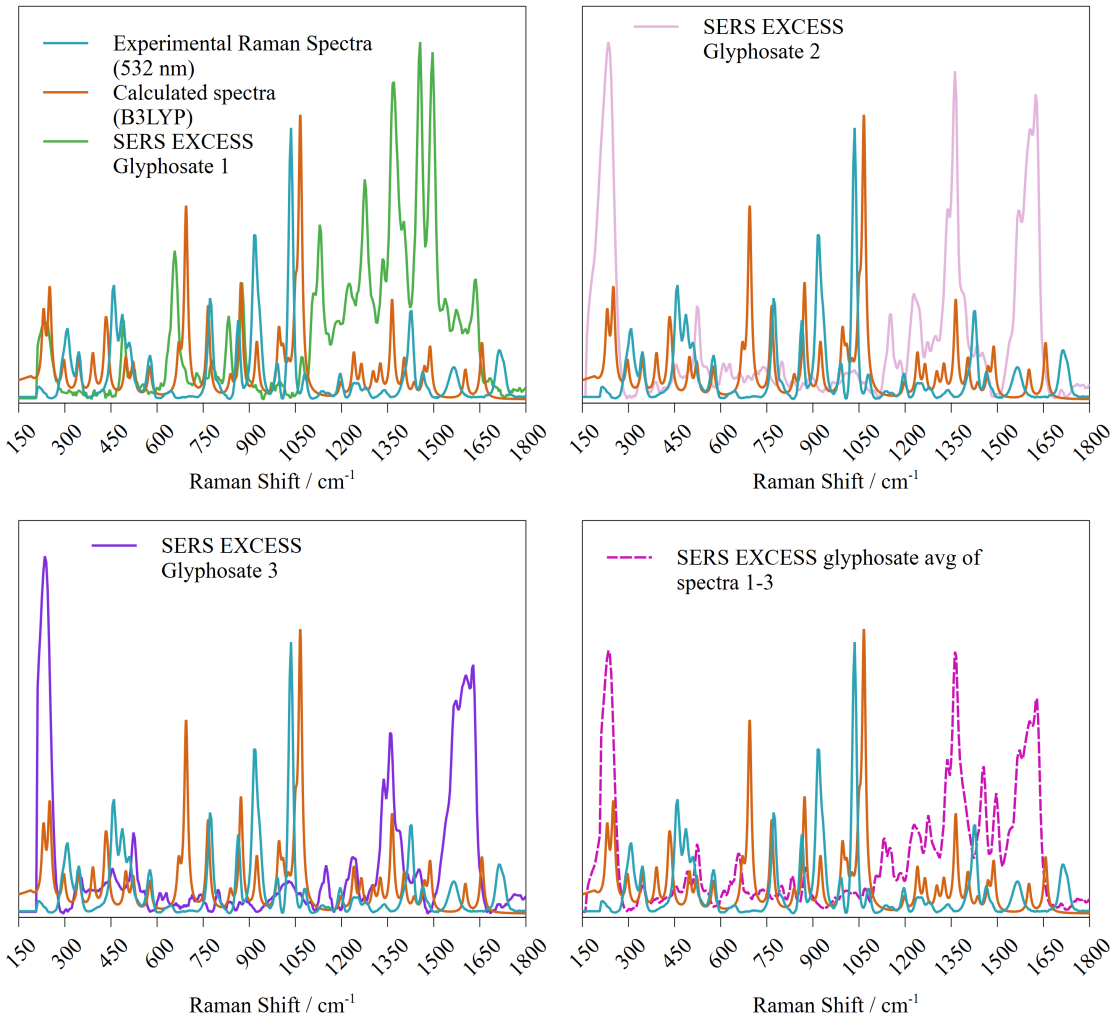

Figure 5.6: Comparison of collected glyphosate SERS spectra and the average of these spectra with the calculated and experimental Raman spectra. Collected at 532 nm.

5.2.0.1 'Yellow' and 'Yellow'@SiO2 Nanoparticles

In order to evaluate the sensitivity of the individual nanoparticle shapes with glyphosate, a range of initial concentrations was prepared in an aqueous environment. In Fig.(5.7), there is a significant amount of activity up to initial concentrations of 10^{-11} M. With the most activity that appears like the SLIPSERS standard being that at 10^{-9} M. This is promising as a SLIPSERS substrate, and has previously been used by this research group for similar contaminant analysis.[95]. A spectra with labelled peaks at an initial concentration of 10^{-9} M is in Fig.(A.4).

In Fig.(5.8), there is a decrease in overall intensity is seen for the given initial concentration until an initial concentration of 10^{-10} M, possibly due to the single molecule regime, which ignores concentration dependence.

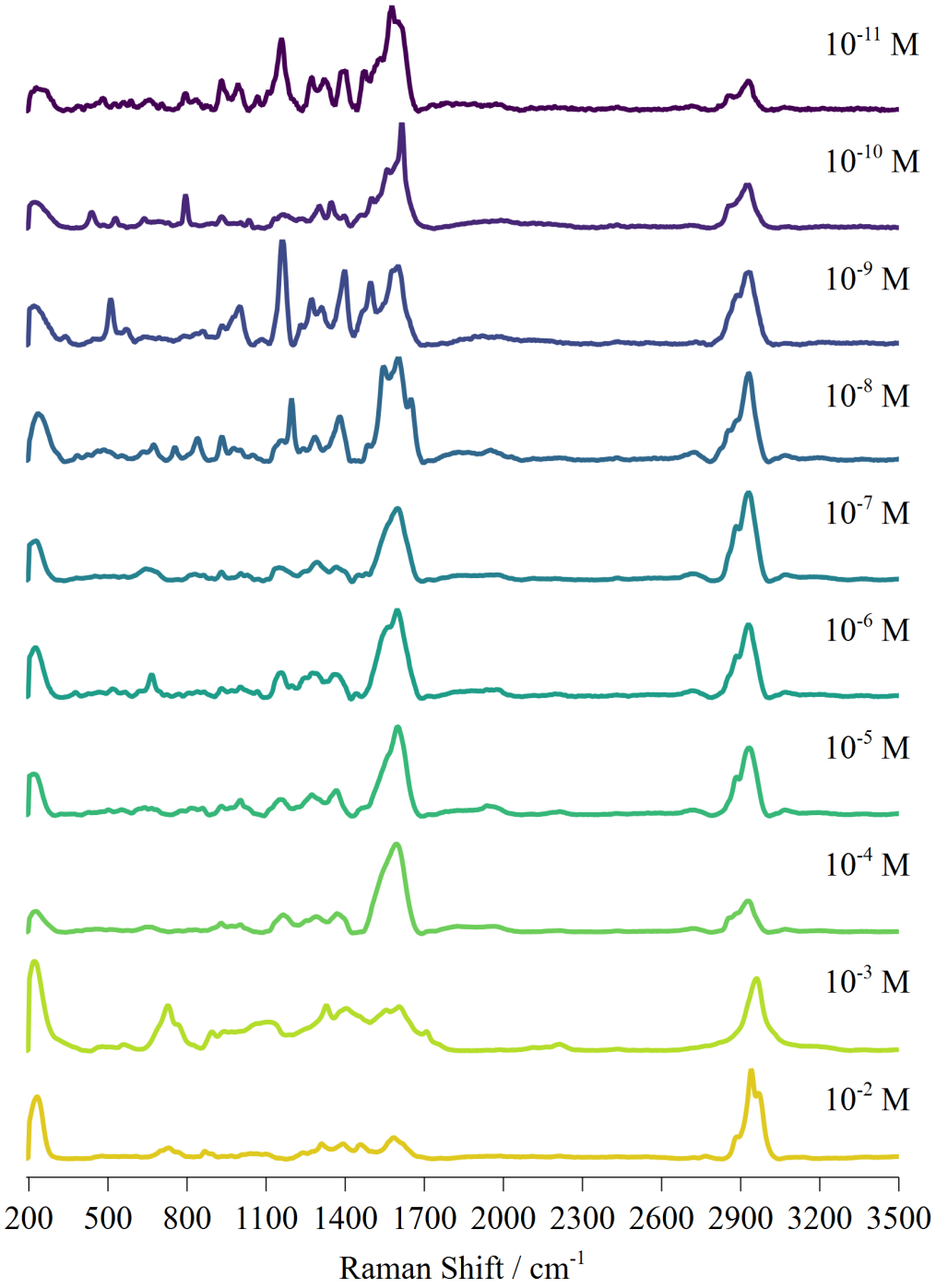

Figure 5.7: Stacked SERS spectra using the 'yellow' substrate over a range of initial concentrations of glyphosate. Collected at 532 nm.

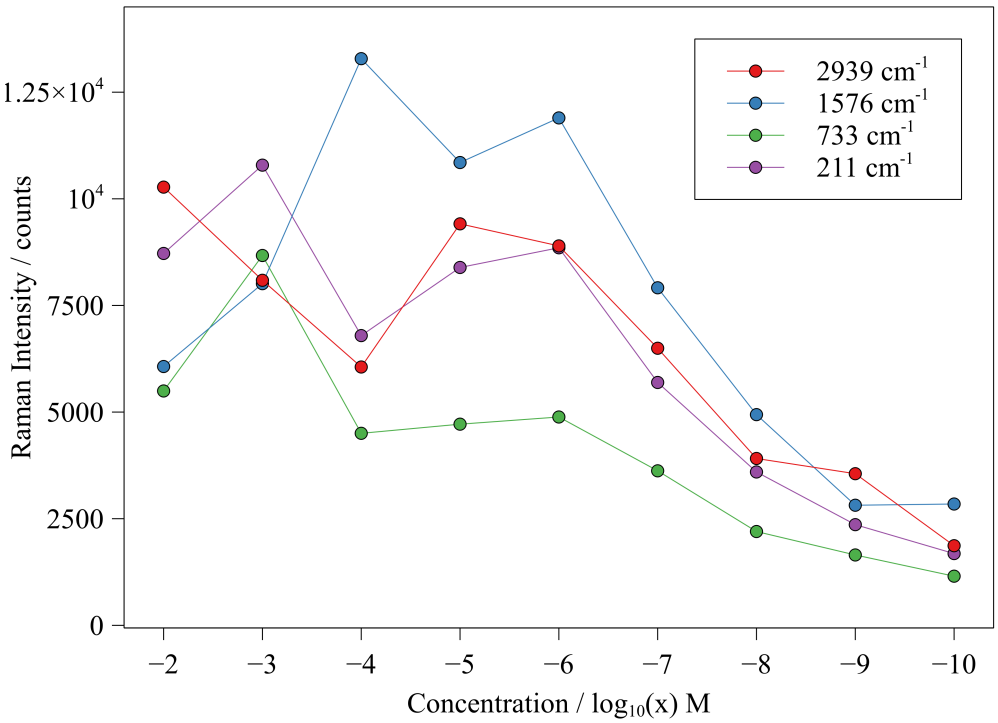

Figure 5.8: Initial concentration dependence of glyphosate at 211, 733, 1576, and 2939 cm^{-1} for the 'yellow' substrate for the average spectra shown in Fig.(5.7). Collected at 532 nm.

As with the excess glyphosate SERS spectra in Fig. (5.6), there are some similar peaks in Fig.(5.9: there is the peak in the lower end at around 235 cm^{-1}, this corresponds to lattice vibrations and -CH2 torsion, and the -CH2 asymmetric and symmetric stretch peaks at around 2990-3100 cm^{-1}. There are signals observed up until an initial concentration of 10^{-11} M.

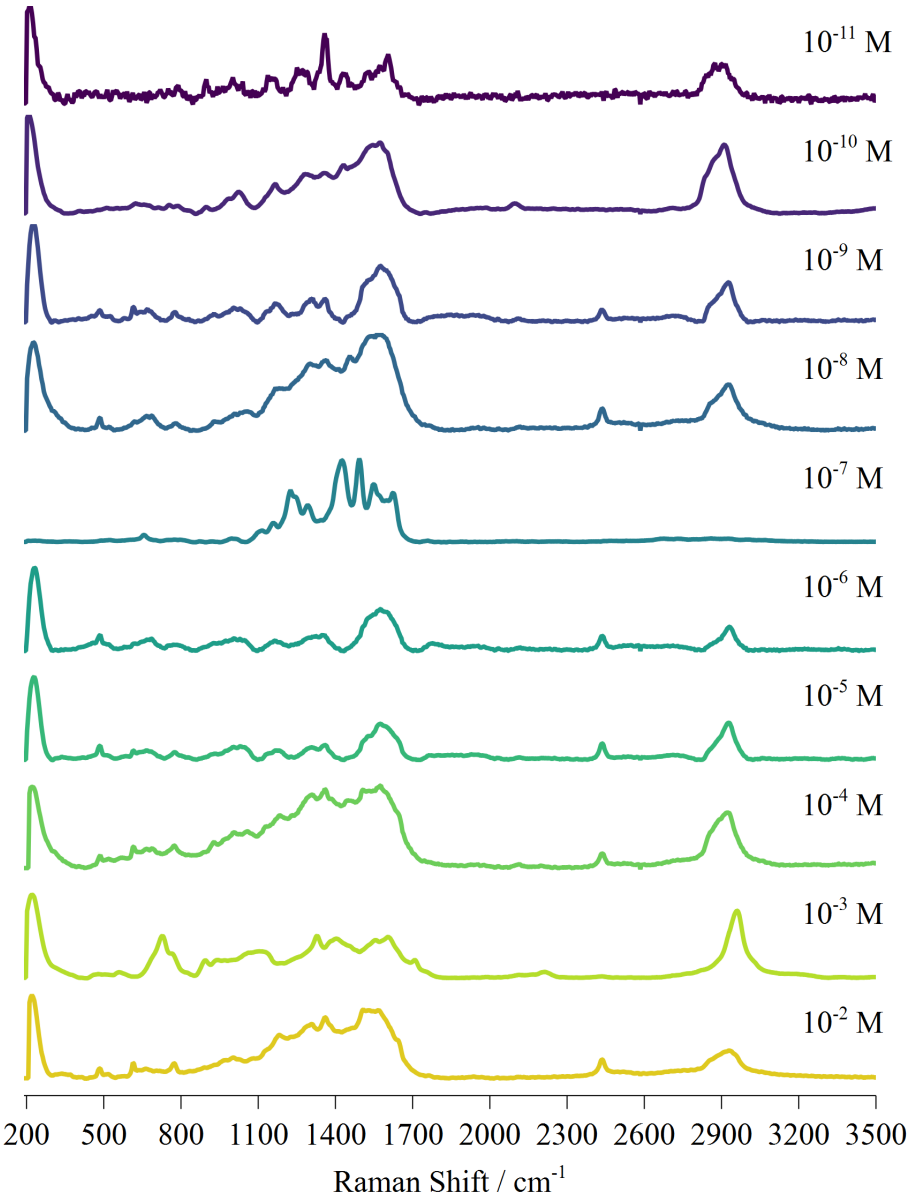

Figure 5.9: Stacked SERS spectra using the Yellow@SiO_2 substrate over a range of initial concentrations of glyphosate. Collected at 532 nm.

5.2.0.2 'Blue' Nanoprisms

In Fig.(5.10), there is significantly more activity than the silica capped "yellow" nanoparticles in Fig.(5.9). Especially at an initial concentration of 10^{-9} M and

10^{-10} M. Labelled spectra at 10^{-3} M and 10^{-10} M is found in Figs.(A.2) and (A.3), respectively.

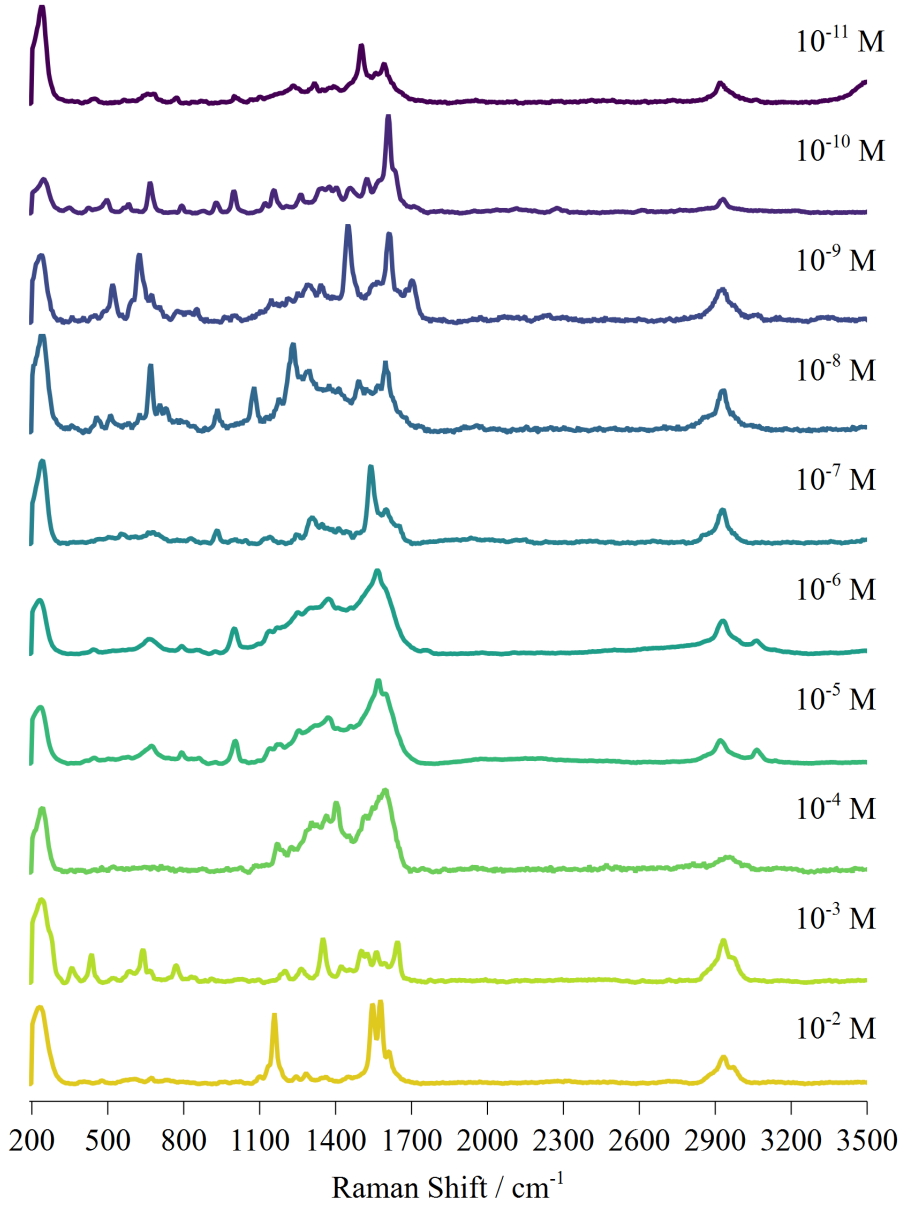

Figure 5.10: Stacked SERS spectra using the 'blue' silver nanoprism substrate over a range of initial concentrations of glyphosate. Collected at 532 nm.

In Fig.(5.11), a decrease in overall intensity is seen for the given initial concentrations up until a concentration of 10^{-10} M, due to the single molecule regime.

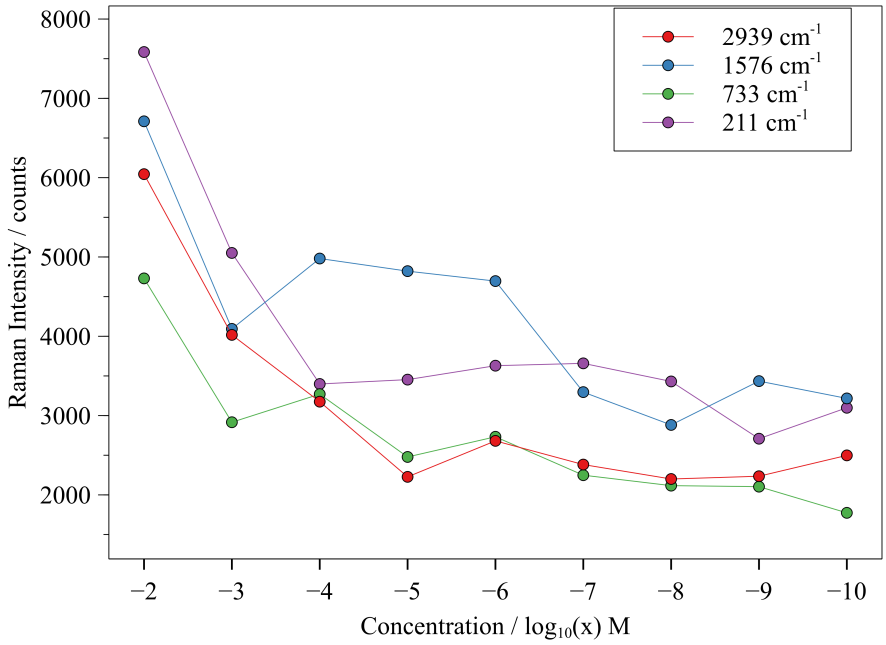

Figure 5.11: Initial concentration dependence of glyphosate at 211 cm^{-1}, 733 cm^{-1}, 1576 cm^{-1}, and 2939 cm^{-1} for the 'blue' silver nanoprism substrate.

In Fig.(5.12), much like in the dye spectra, there is low signal to noise. However, there are still significant peaks up to a concentration of 10^{-10} M. At this point, signal-to-noise suffers. In the majority of the spectra shown here, there does not seem to be any significant peaks related to glyphosate.

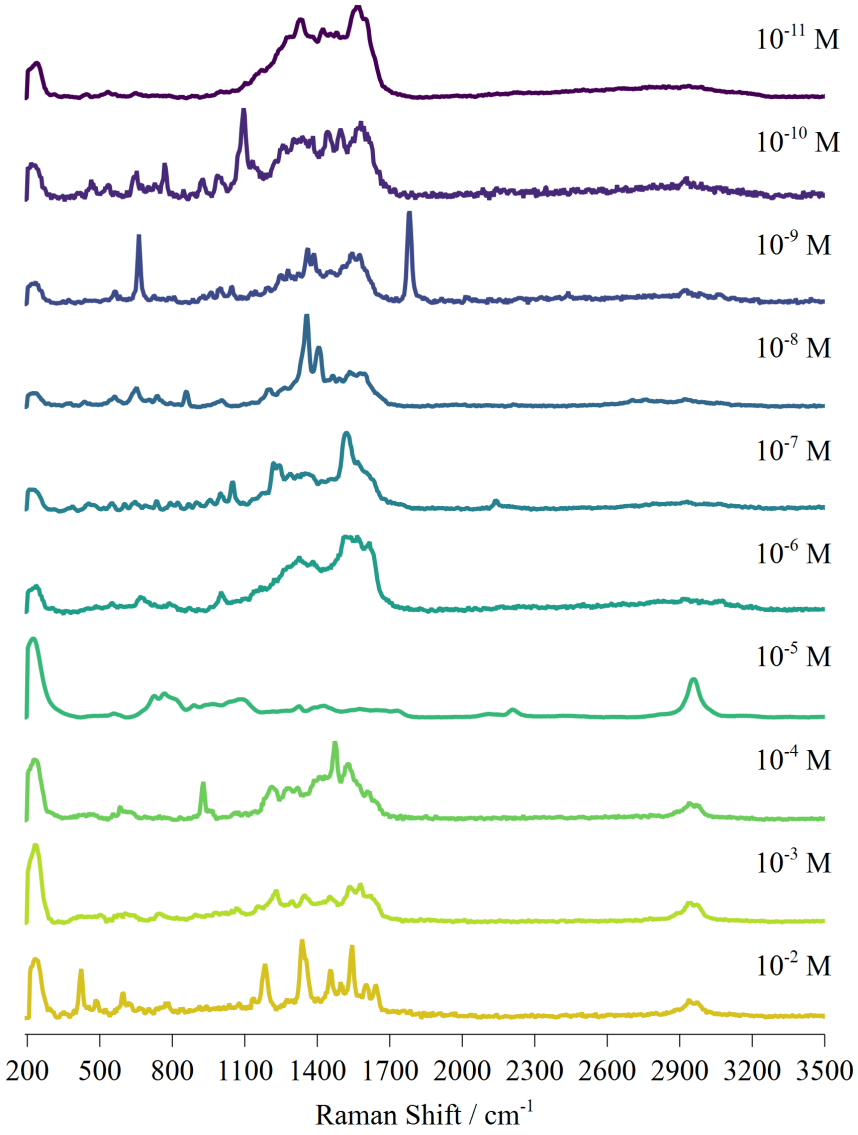

Figure 5.12: Stacked SERS spectra using the Blue@SiO_2 nanoprism substrate over a range of initial concentrations of glyphosate. Collected at 532 nm.

5.2.0.3 Spherical Nanoparticles

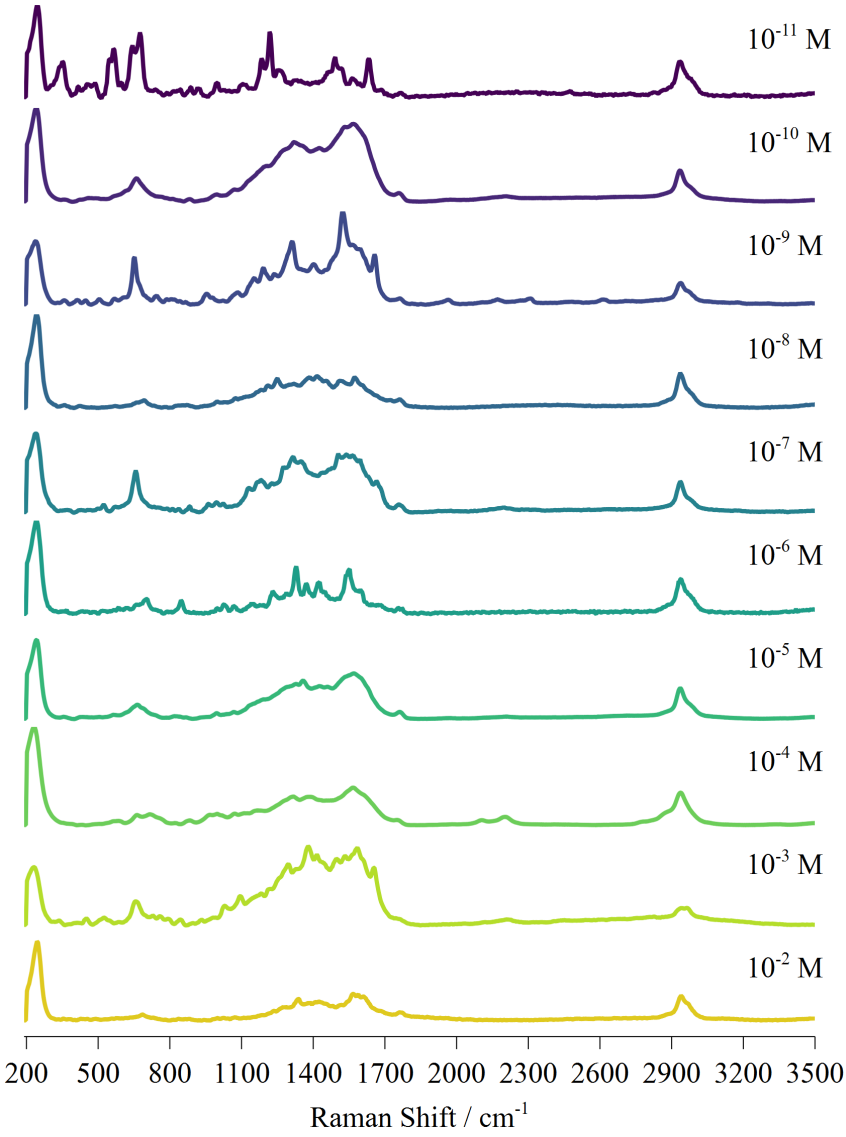

Figure 5.13: Stacked SERS spectra using the silver nanospheres substrate over a range of initial concentrations of glyphosate. Excitation wavelength: 532 nm.

In Fig.(5.13), it appears that there are signals observed up to an initial concentration of 10^{-11} M. In addition, there appear to be d/g bands affecting the spectra at initial concentrations of 10^{-4} M, 10^{-5} M, and 10^{-10} M. However, the spectra at 10^{-11} M appears to have high SERS activity compared to the rest of the spectra, despite the low signal to noise, this is likely due to the single molecule regime mentioned in Section 1.2.6. Despite the influence of d/g bands in several of the spectra here, it is promising that there are signals at the lower concentrations, in particular at 10^{-6} M, 10^{-9} M and 10^{-11} M. In all of the spectra there are C-H peaks at around 2929 cm^{-1}. There is a labelled spectra of 10^{-6} M and 10^{-11} M in Figs.(A.6),(A.7) showing

modes such as 1533 cm^{-1}, 1329 cm^{-1}, 846 cm^{-1} and 702 cm^{-1}.

The silica capped silver nanospheres in Fig.(5.14) show that there is detection sensitivity of glyphosate up until an initial concentration of 10^{-10} M. There does appear to be some influence of d/g bands starting at an initial concentration of 10^{-8} M. Overall, apart from some modes appearing in the spectra at 10^{-8} M and 10^{-9} M, it does not appear that this substrate is a good SERs substrate for this molecule; though there does appear to be peaks at an initial concentration of 10^{-11} M. Compared to the silver nanospheres in 6.10, this substrate has significantly less sensitivity and worse signal to noise, particularly at the lower concentrations. As a reference, a fully labelled spectrum of the spectrum at an initial concentration of 10^{-4} M is in Fig.(A.8).

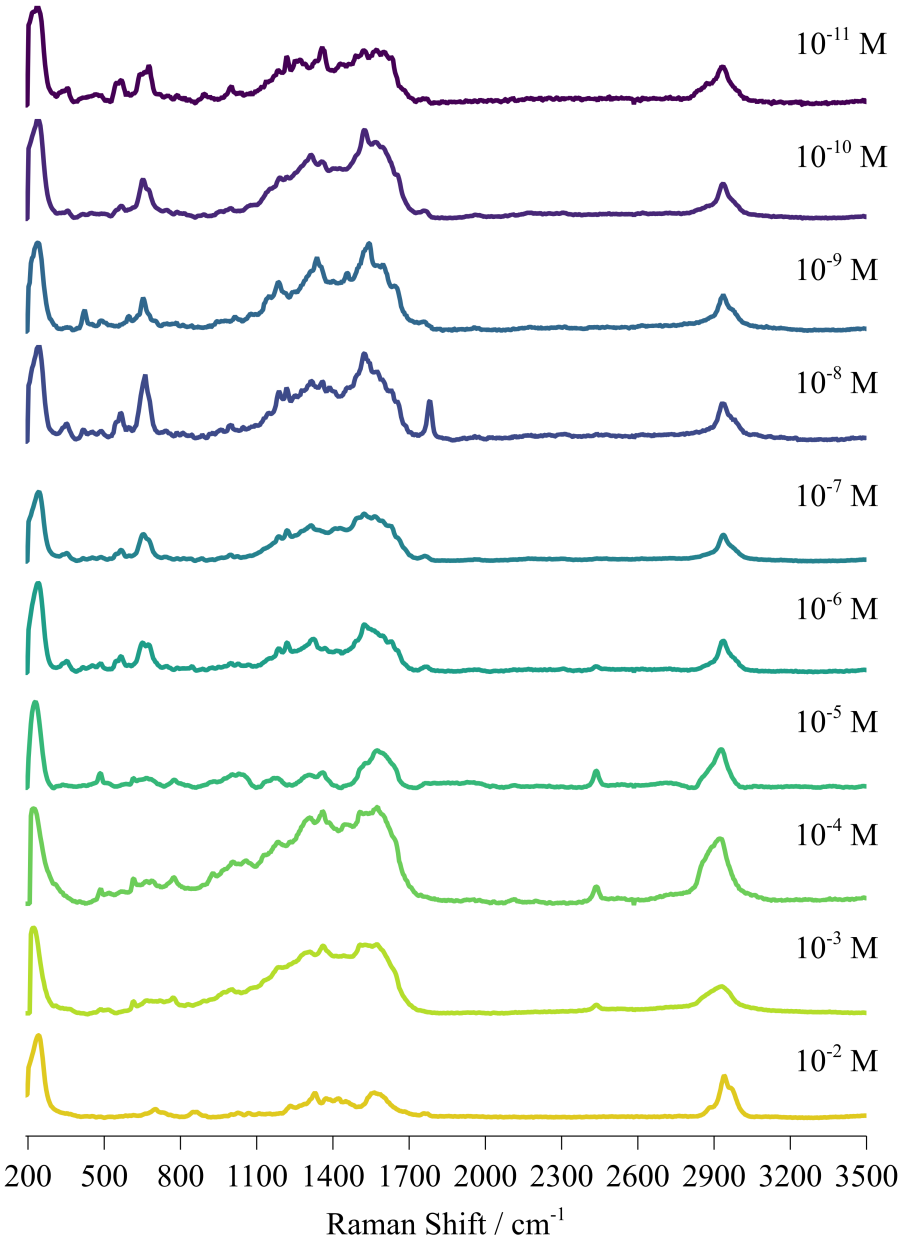

Figure 5.14: Stacked SERS spectra of the the silica capped silver nanosphere substrate over a range of initial concentrations of glyphosate. Excitation wavelength: 532 nm.

5.2.0.4 Nanocubes

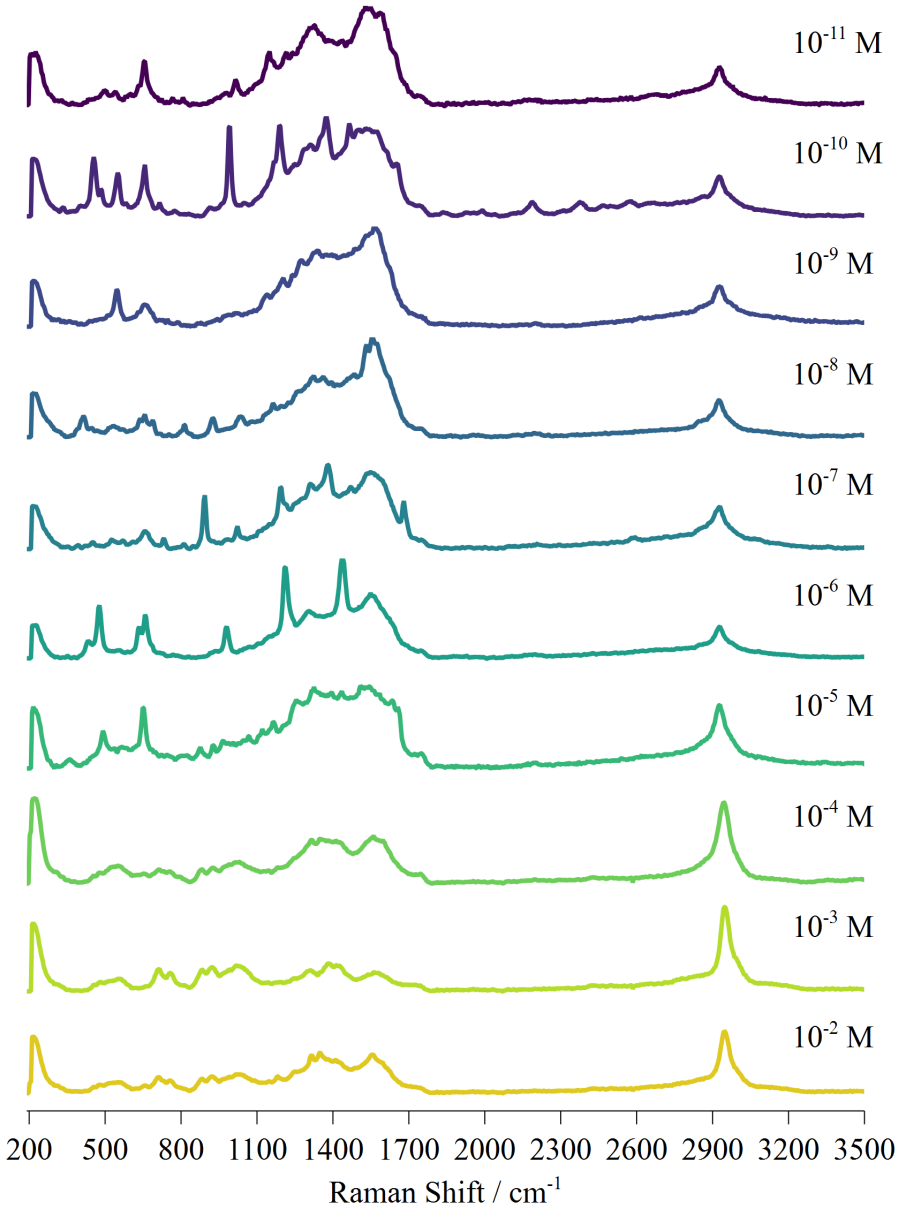

Figure 5.15: Stacked SERS spectra using the silver nanocube substrate over a range of initial concentrations of glyphosate. Excitation wavelength: 532 nm.

The silver nanocubes in Fig.(5.15) show surprisingly less enhancement than the equivalent experiments with the nanoparticle dispersion in Fig.(5.7), however, it still shows detection of glyphosate signals up until an initial concentration of 10^{-11} M. In particular at this concentration, the peak at around 670 cm^{-1}, is prominent in most of the initial concentrations. In particular is the spectra at an initial concentration of 10^{-11} M. At an initial concentration of 10^{-10} M there appears to be significant peak activity, with signature peaks at 658 cm^{-1}, 993 cm^{-1}, 1188 cm^{-1} and 1374 cm^{-1}; these appear to be similar to the modes in Fig.(5.5), where there are peaks at 657

cm^{-1}, 1184 cm^{-1}, and 1362 cm^{-1}. A fully labelled spectrum of the spectra at an initial concentration of 10^{-10} M is found in Fig.(A.9).

5.2.0.5 Comparison of All Nanoparticle Types

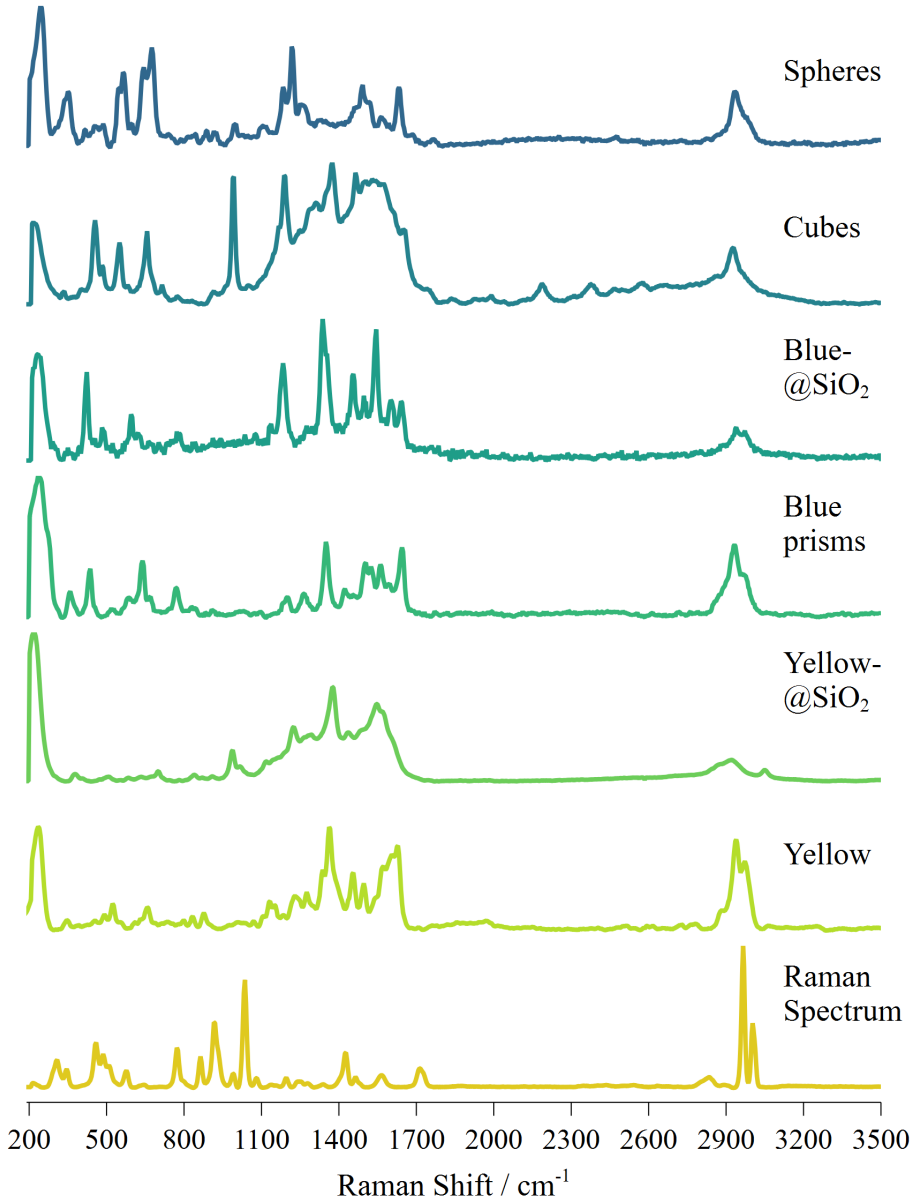

Figure 5.16: Stacked SERS spectra the different silver substrates over a range of initial concentrations of glyphosate compared to the Raman spectrum. Excitation wavelength: 532 nm.

Based on the observed "quality" of the signals obtained with each nanoparticle type, it appears that the majority of nanoparticle types can produce SERS signals that correspond to glyphosate up until an initial (before drying) concentration of 10^{-11} M. However, signal-to-noise suffers more with the silica capped substrates. This

can be explained by the silica coating creating more distance between the plasmonic surface and the analyte, indicating that the silica shell was not controlled to an appropriately thin thickness. In addition, there is significant d/g bands affecting some of the spectra, which can obscure other peaks.

5.3 Linear Discriminant Analysis of Glyphosate SLIPSERS spectra

From the LDA classification of the data in Fig.(5.17), that there is some grouping of the data, indicating that the nanoparticle type has an effect on the observed spectra.

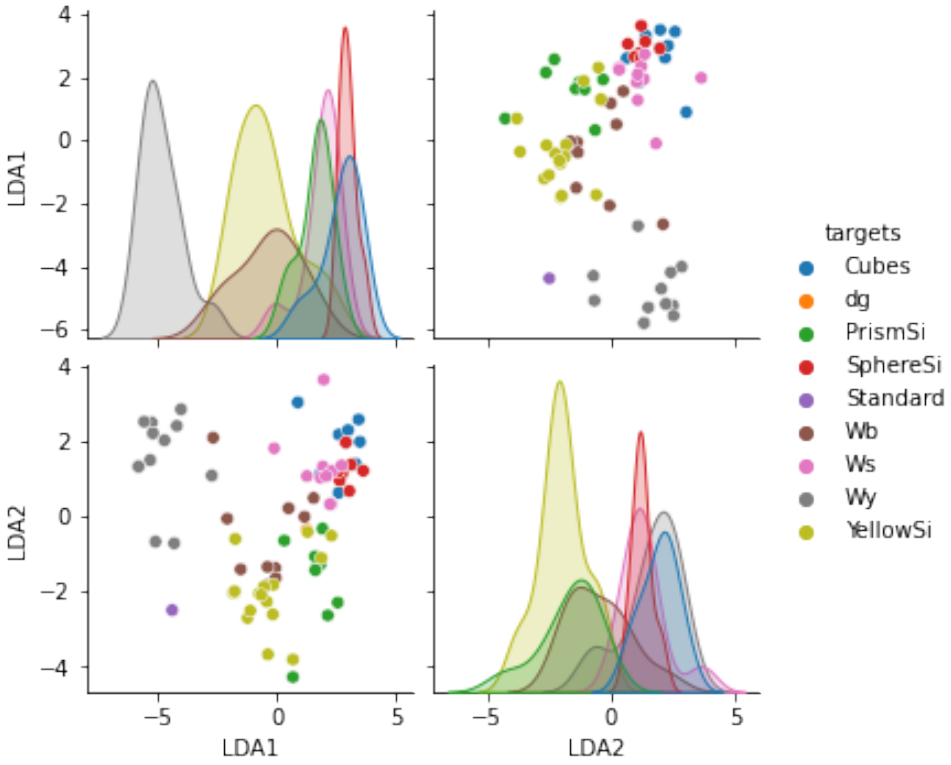

Figure 5.17: LDA plot of all of the glyphosate SLIPSERS spectra separated by the nanoparticle type.

In Fig.(5.17) there are two distinct groups, one from the 'yellow' nanoparticles (in grey) and the nanocubes. Whilst there is some overlap between the other nanoparticle types. One thing to note from this figure is that the Raman spectra (marked in red) are extremely far from the main grouping of the SLIPSERS spectra and that the d/g band spectrum is buried in the grouping of the SLIPSERS spectra. The loadings plot in Fig.(A.22), shows that there is a lot of contribution to the variation of all of the spectra in the 200 cm^{-1} to 2000 cm^{-1} region, with some variation in the C-H peaks at around 2800 cm^{-1} to 3100 cm^{-1}.

In Fig.(5.18), it appears that there is some distinctive grouping of the SHIN classes. There is some overlap with the silica capped "yellow" nanoparticles (YellowSi, purple)

and the silica capped "spherical" nanoparticles (SphereSi, green). As mentioned previously in Section 5.2, some spectra had d/g influence, this can be seen where silica capped nanoprisms (PrismSi, orange) are close to the d/g spectrum (blue). It does however appear that the d/g influence is minimal on the distinctive grouping of the SHIN classes.

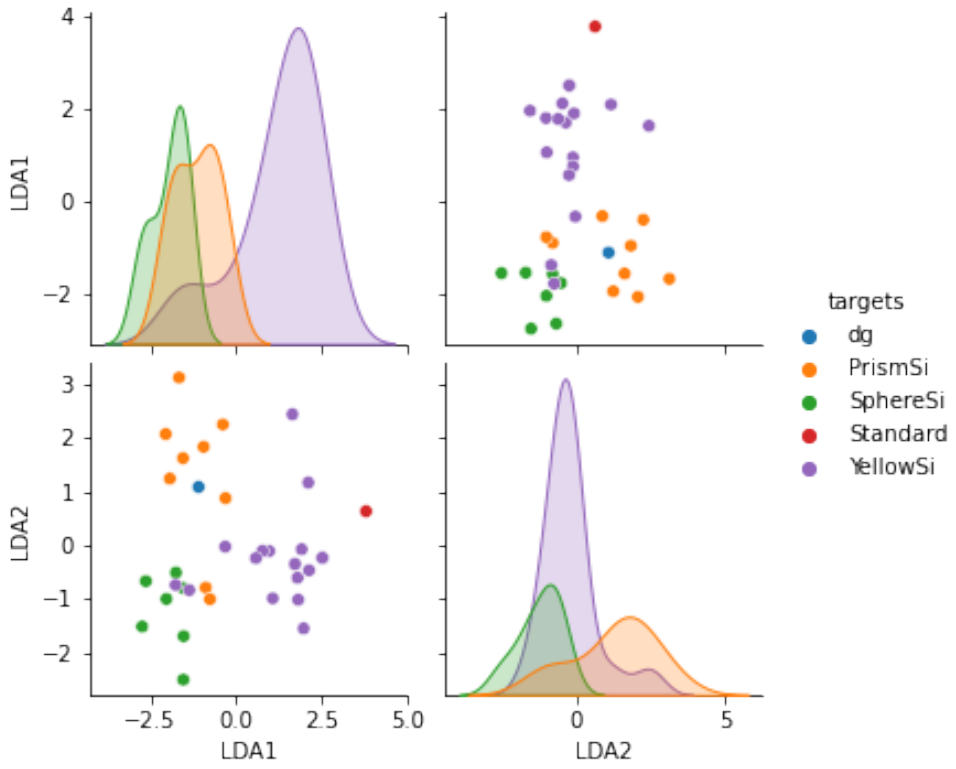

Figure 5.18: Linear Discriminant Analysis of all of the glyphosate SLIPSERS spectra which use SHINs as their substrate, organised by their nanoparticle type.

6. SLIP-SERS Detection of Diazinon

6.1 Raman spectrum

Even under ideal conditions, it appears that diazinon would not be a good Raman scatterer (see A.10 for a good example of one of the drastically different Raman spectra acquired of diazinon in liquid form). As a result, this required increasing the laser power beyond 10 mW (in comparison, SLIPSERS spectra recorded here are typically sub 1 mW). However, it is possible to gather the Raman spectrum (see Figs.(6.1) and (6.2).

	Wavenumber (cm^{-1})		
Mode(s)	Lit. Raman	Experimental Raman	Notes
$v(CH_3)$	3026-2844	2872, 2929, 2973	–
v_s(P-O-CH_2-CH_3)	1450-1439	1452	CH_3 symm.
semicircle	1375-1410,	1379	ring
	1400-1480	1452	stretch
quadrant	1555-1590,	1585,	ring
	1520-1565	1561	stretch
v(P-CH_2)	1440-1405	1452	
v(P-O-CH_2-CH_3)	1008-1042,	1019	–
	920-928		
v(P-O-Ar)	1130-1090	1100	ring mode
			+PO-C
v(C-H)	1050-1040	1019, 1066	rocking
			of P-O-C
Radial	980-1005	989, 950	in phase
v(P=S)	600-670	635	–

Table 6.1: Summary of the observed modes for diazinon of the literature values for modes and the experimental Raman modes[221] collected in a 532 nm setup as described in Sec.(2.6).

From these spectra, it becomes apparent that unlike in the previous section,

the peaks are broader and less well defined. The broad baseline might have to do with the Raman spectrum being collected on a liquid sample (a better medium for Rayleigh scattering than Raman scattering), and/or diazinon not being an ideal Raman scatterer *and* due to the sample being collected on a glass cover-slip. Despite this, Figs.(6.1) the expected strong C-H band exists at the the 2930-3000 cm^{-1}. Compared to glyphosate, this mode seems stronger, likely due to the total of C-H bonds in diazinon (twenty-one) compared to those of glyphosate (four). The summary of all the important modes in diazinon is in Table 6.2. The literature also describes a strong band in the ranges 1081-1100 cm^{-1}. In similar Raman and SERS comparison studies using *p*-mercaptobenzoic acid (PMBA), similar modes were observed in a solid state at 1588 cm^{-1}, 1080 cm^{-1} and 635 cm^{-1}.[68] Many of these, such as at 1578 cm^{-1} are six-membered ring modes, so it assists in establishing that these modes are from the diazinon itself and not from any contamination.

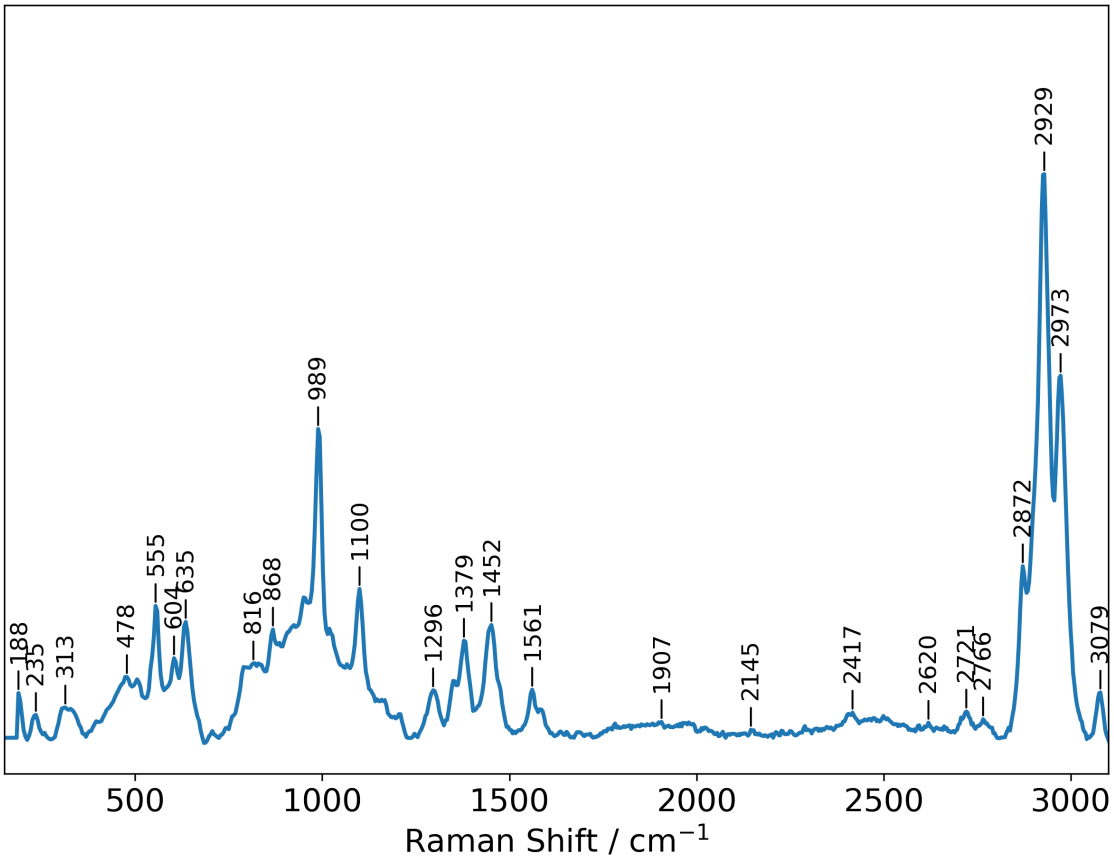

Figure 6.1: A Raman spectrum of an analytical grade sample (Pestanal, 99%) of diazinon on a 532 nm incident beam, captured by using a small drop on a welled microscope slide.

From the Raman spectrum in Fig.(6.2), this appears to be the case. However, there is supposed to be a very strong band in the ranges 686-758 cm^{-1}; instead a band at 989 cm^{-1} is very strong. However, in monosubstituted diazines (pyridines) there is supposed to be a very strong Raman band at the ranges 985-1030 cm^{-1} due

to a Radial vibration;[221] this falls within this region, so this may be the peak being observed here. Listed modes are in Table 6.1.

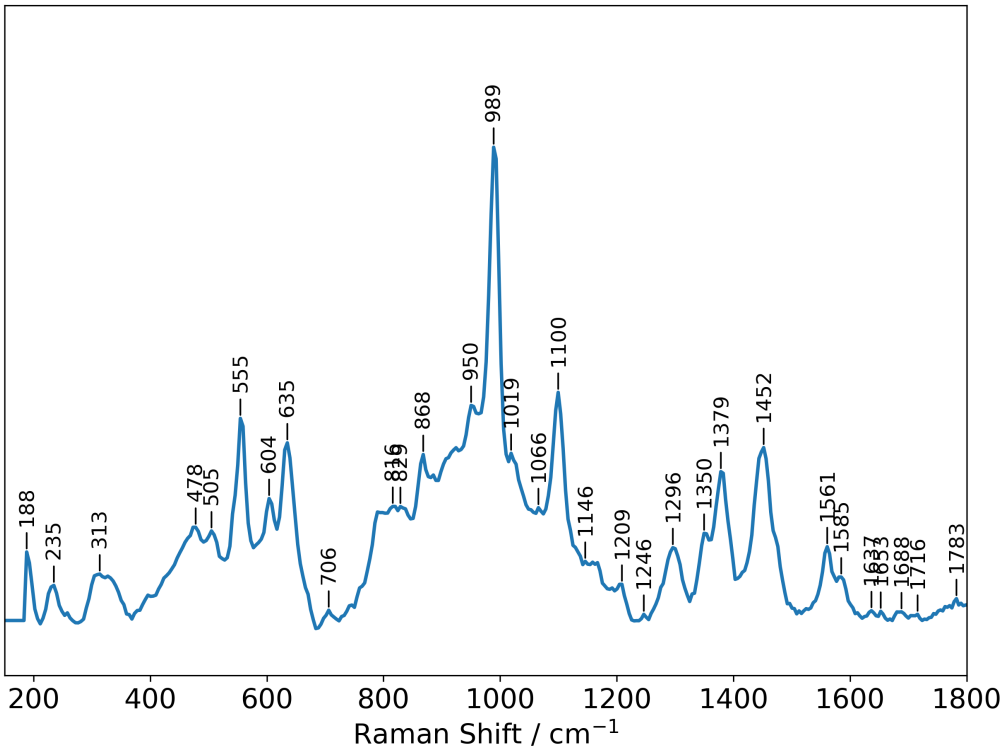

Figure 6.2: The Raman spectra for Diazinon in the 150-1800 cm^{-1} range. 532 nm excitation wavelength.

6.2 SLIPSERS Spectra

To avoid competitive binding or the nanoparticles being destabilised by the R-P=S bond, the amount of diazinon as 'excess' was controlled to 0.01 M. Analysis of the SERS spectrum of diazinon becomes complicated due to the R-P=S group, as it can form a R-P=S-Ag bond with the silver surface. This will introduce However, unlike the Raman spectrum, the SLIPSERS spectra of diazinon in Figs.(6.3)(6.4) is much more well defined with less broadening. Granted, these SERS spectra are done under SLIP conditions, however, several modes have been enhanced while others are harder to notice. For example, the 989 cm^{-1} peak from the Raman spectrum has been shifted to about 985 cm^{-1}, but it remains the second most prominent peak (if the C-H peak is not ignored) in the SLIPSERS spectrum that is being used as a standard. The literature also describes a strong band in the ranges 1081-1100 cm^{-1}. In similar SERS studies using *p*-mercaptobenzoic acid (PMBA), similar modes were observed in a neutral pH in aqueous environment at 1575 cm^{-1}, 1378 cm^{-1} 1070 cm^{-1}, 1020 cm^{-1} and 998 cm^{-1}.[68] Many of these, such as at 1578 cm^{-1} are six-membered ring modes, so, along with the textbook examples, it assists in establishing that these

modes observed in the SERS spectra are likely from diazinon itself interacting with the silver substrate.

	Wavenumber (cm^{-1})			**Wavenumber (cm^{-1})**	
Mode(s)	Raman	SERS	Mode(s)	Raman	SERS
v_a(C-H)	2973	–		1100	1129,1192
v_s(C-H)	2929	2919	Radial	989	985
quadrant	1561	1513,1565		816-868	890
	1452	–		635	648
	1379	1370		555	559
	1296	1271,1300	–	313	300-430

Table 6.2: Summary of the observed modes for diazinon in the experimental Raman modes for the standard Raman spectrum and SERS spectrum.

One thing that seems to align with what was hypothesised about the SERS spectra in Section 1.7 was that the P=S bond will change from the Raman spectra to the SERS spectra as the P=S-Ag bond with the nanoparticles would form. This can be seen from the fact that the modes that correspond to a "radial" pyrimidine stretch are enhanced much more than in the Raman spectrum. In addition, in the pyrimidine "quadrant" mode Fig.(6.4) it appears that peaks at 1513 and 1565 cm^{-1} are enhanced and shifted compared to its Raman counterpart which corresponded to two broad peaks at 1561 and 1585 cm^{-1}. The literature describes these as characteristic bands of 2,3-disubstituted pyrazines (pyrimidines), which should have a peak at 1558-1580 cm^{-1} and another peak at 1525-1570 cm^{-1}. There appears to be some agreement with these values, however, it is described as a "medium" intensity band; in the collected spectra here, it is relatively weak. This is likely due to the influence of the other substituents attached to the pyrimidine ring.

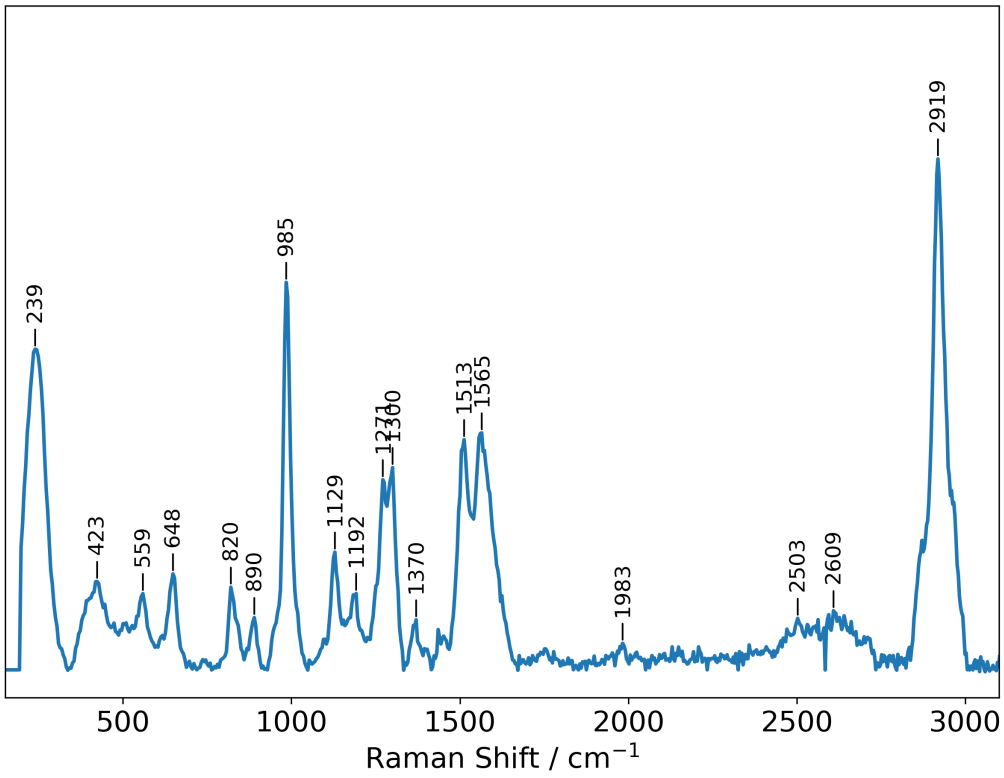

Figure 6.3: The SERS spectrum for diazinon using an Ag@SiO_2 substrate and excess diazinon (about 0.01 M initial concentration).

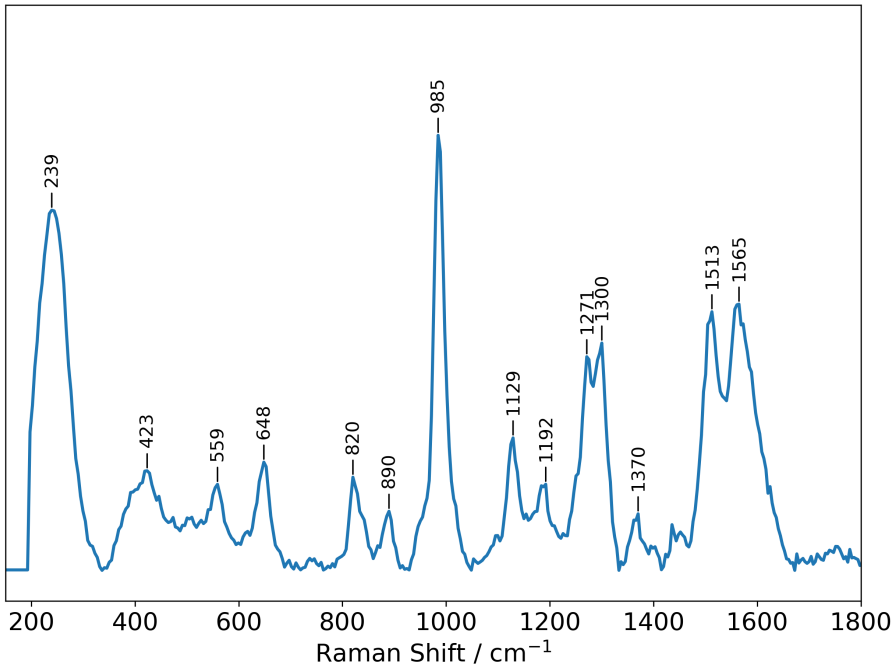

Figure 6.4: The SERS spectrum of diazinon using an Ag@SiO_2 substrate and excess diazinon (about 0.01 M), in the range 150cm-1 to 1800cm-1.

6.2.0.1 'Yellow' and 'Yellow'@SiO2 Nanoparticles

The SLIPSERS spectra using the yellow nanoparticles as a substrate in Fig.(6.5) based on the SLIPSERS spectra before it, that there are diazinon peaks up to about an initial concentration of 10^{-9} M. These are the peaks at 1234 cm^{-1} and 1428 cm^{-1}, just before the broad peak from 1494 cm^{-1} to 1649 cm^{-1}. This broad peak appears to be a broadening of the double peaks in the Excess (SERS) spectrum. Peaks at 1234 cm^{-1} and 1585 cm^{-1} still appear up until an initial concentration of 10^{-9} M (see Fig.(A.11).

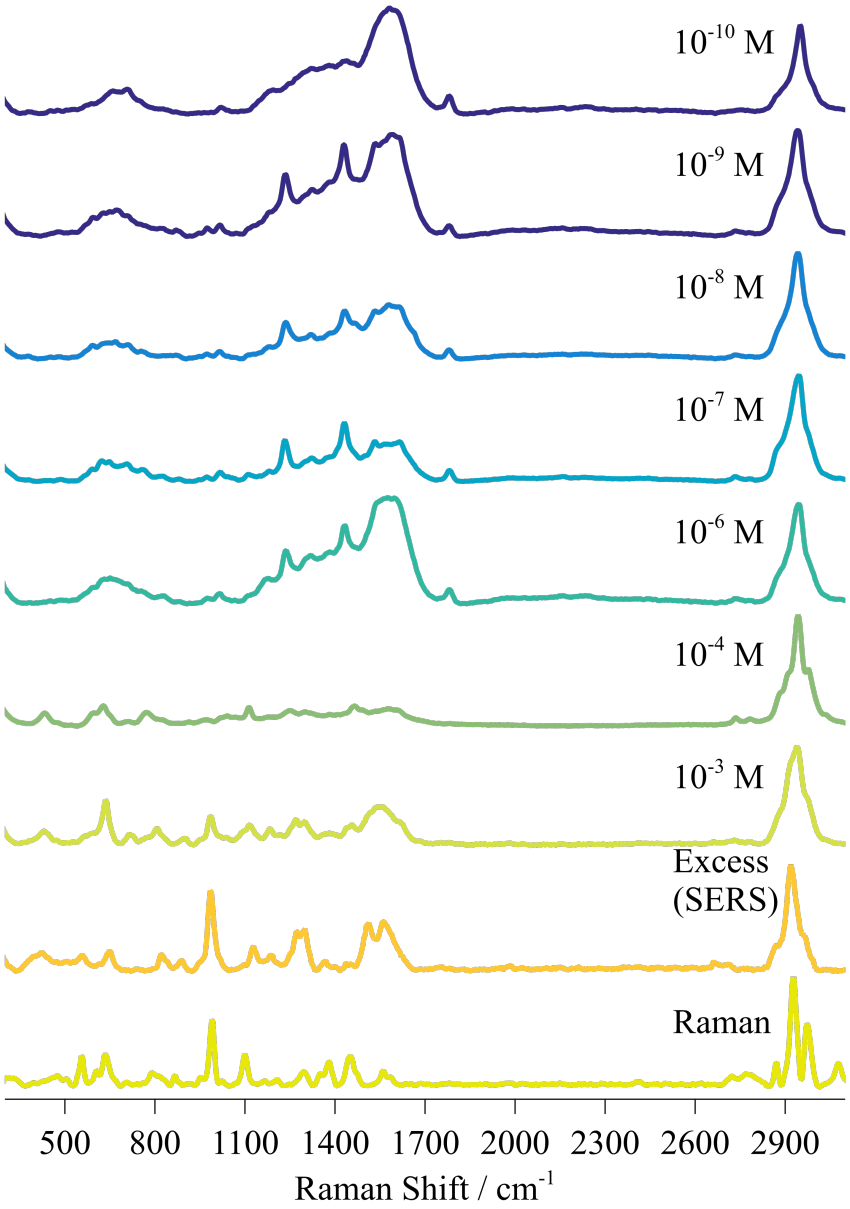

Figure 6.5: Stacked spectra comparing the Raman spectra of diazinon, a SERS spectra containing excess diazinon with the "yellow" nanoparticles, and SLIPSERS spectra collected at various initial concentrations of diazinon with silver nanoparticle dispersion ("yellow") as a SERS substrate.

The silica capped yellow nanoparticle dispersion in Fig.(6.6) shows a sensitivity up until an initial concentration of 10^{-10} M. This is promising as even the signal to noise does not suffer too much in this spectra. At initial concentrations of 10^{-7} and 10^{-8}, there appears to be some loss of some SERS activity, however, at the lower initial concentrations, there is more SERS activity. As mentioned in Section 1.2.6, this is likely due to the single molecule regime, at this point concentration dependence has less of an effect on the observed SERS spectra. In addition, the spectrum at an initial concentration of 10^{-9} M is similar to the reference spectrum, which was done using the same type of substrate.

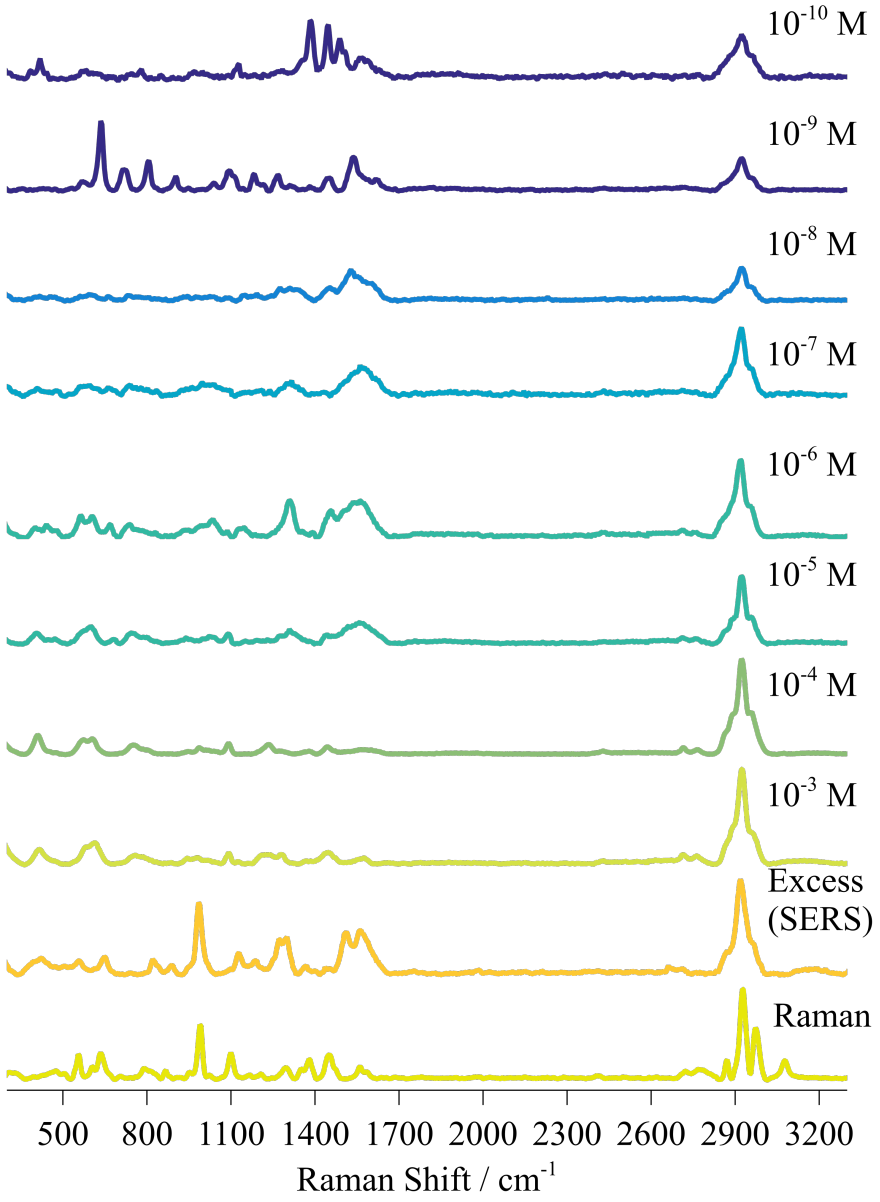

Figure 6.6: Stacked spectra using the silica capped "yellow" nanoparticle dispersion, and comparing the Raman spectra of diazinon, a SERS spectra containing excess diazinon and various initial concentrations of diazinon.

6.2.0.2 'Blue' Nanoprisms

The silver nanoprisms in Fig.(6.7), it is observed that there are what appear to be diazinon modes up until an initial concentration of 10^{-10} M. Starting at an initial concentration of 10^{-5} M, then again from 10^{-7} M onward, there appears to be broadening of a band at 1533 cm^{-1}, however, this broad band does not appear to be related to d/g bands, as only one broad band appears. By an initial concentration of 10^{-10} M, there appears to be a sharpening of this band again, possibly due to reaching a single molecule regime (see Fig.(A.12) for a peak picked spectra at 10^{-10} M).

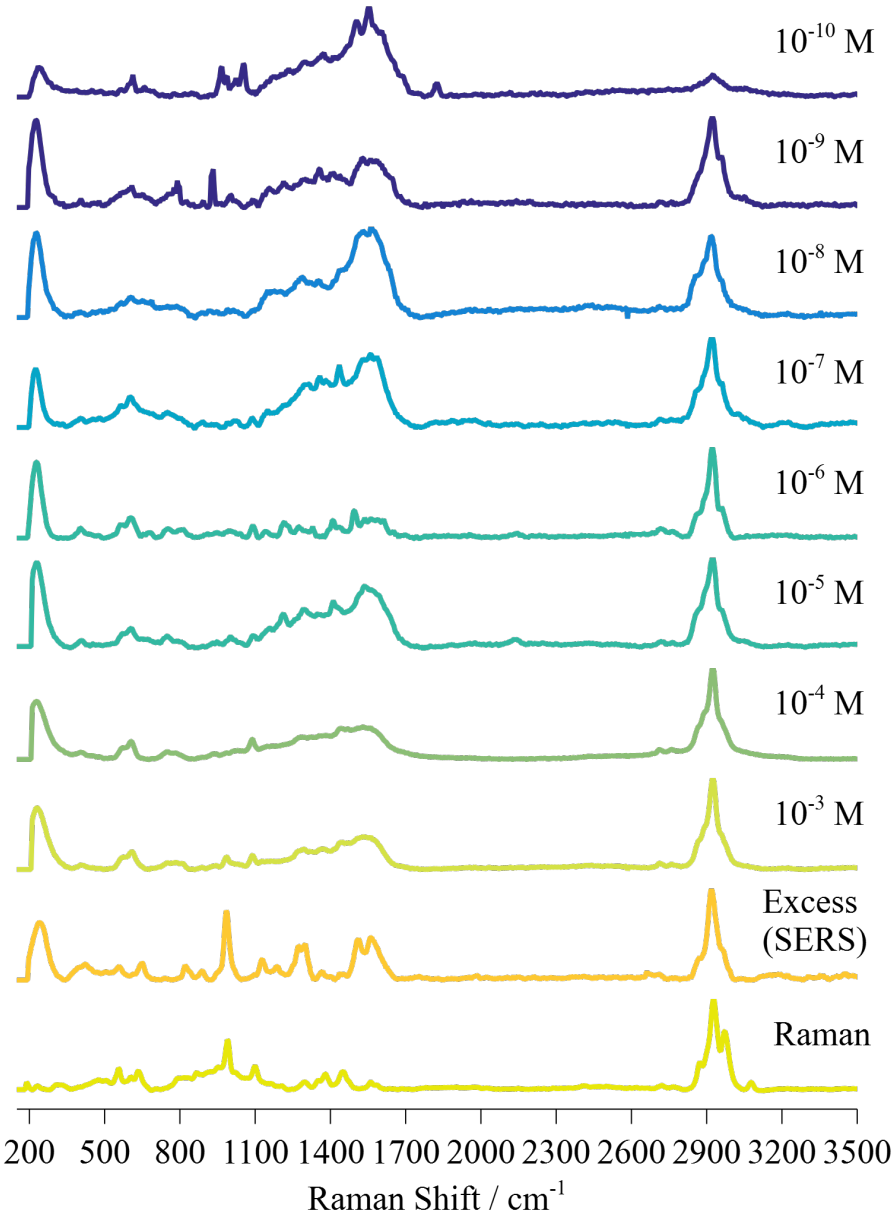

Figure 6.7: Stacked spectra comparing the Raman spectra of diazinon, a standard SLIPSERS spectra containing excess diazinon and various initial concentrations of diazinon with silver nanoprisms as a SERS substrate.

In Fig.(6.8), it appears that despite signal to noise not suffering too much, diazinon is only detectable to about an initial concentration of 10^{-5} M, by an initial concentration of 10^{-6} M or lower, there are no significant peaks of diazinon appearing in these spectra. It is unclear what is causing this, but it seems to be due to the nanoparticle not picking up any modes, and as there are no d/g bands, it is not due to user error where the diazinon is broken down.

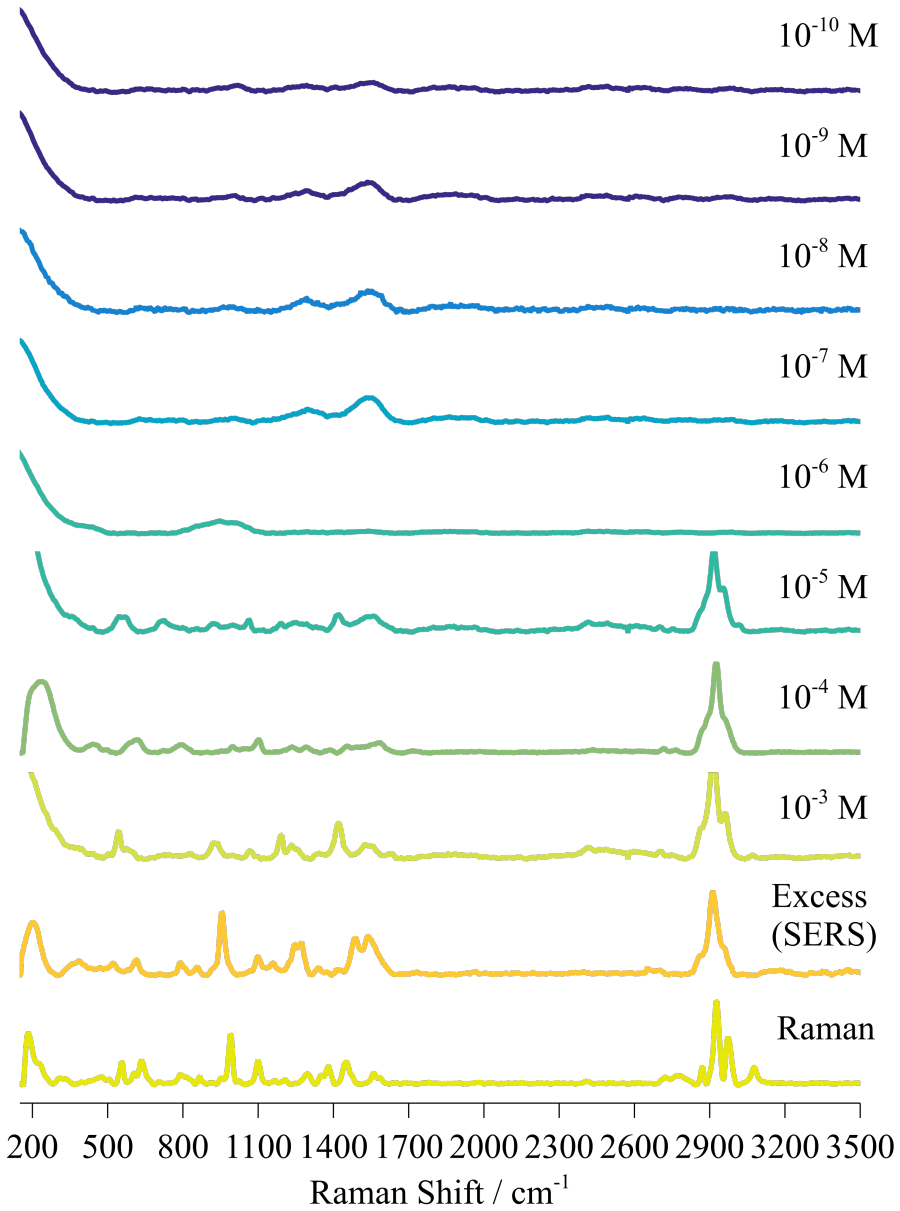

Figure 6.8: Stacked spectra with the silica capped nanoprism substrate, comparing the Raman spectra of diazinon, a standard SLIPSERS spectra containing excess diazinon and various initial concentrations of diazinon with the silica capped prisms as the SERS substrate.

6.2.0.3 Nanocubes

The silver nanocubes in Fig.(6.9) appear to show diazinon peaks up until an initial concentration of 10^{-10} M, which is promising. However in the spectra at initial concentrations of 10^{-6} M and 10^{-7} M, and slightly in 10^{-8} M, some d/g bands are forming, which is affecting the spectra. However, even at these concentrations, the peak at around 653 cm^{-1} still appears even with the d/g influence. The signal to noise does get worse at the lower concentrations, however, it does not appear to affect

the identification of peaks. The a labelled spectrum at an initial concentration of 10^{-10} M is found in Fig.(A.13).

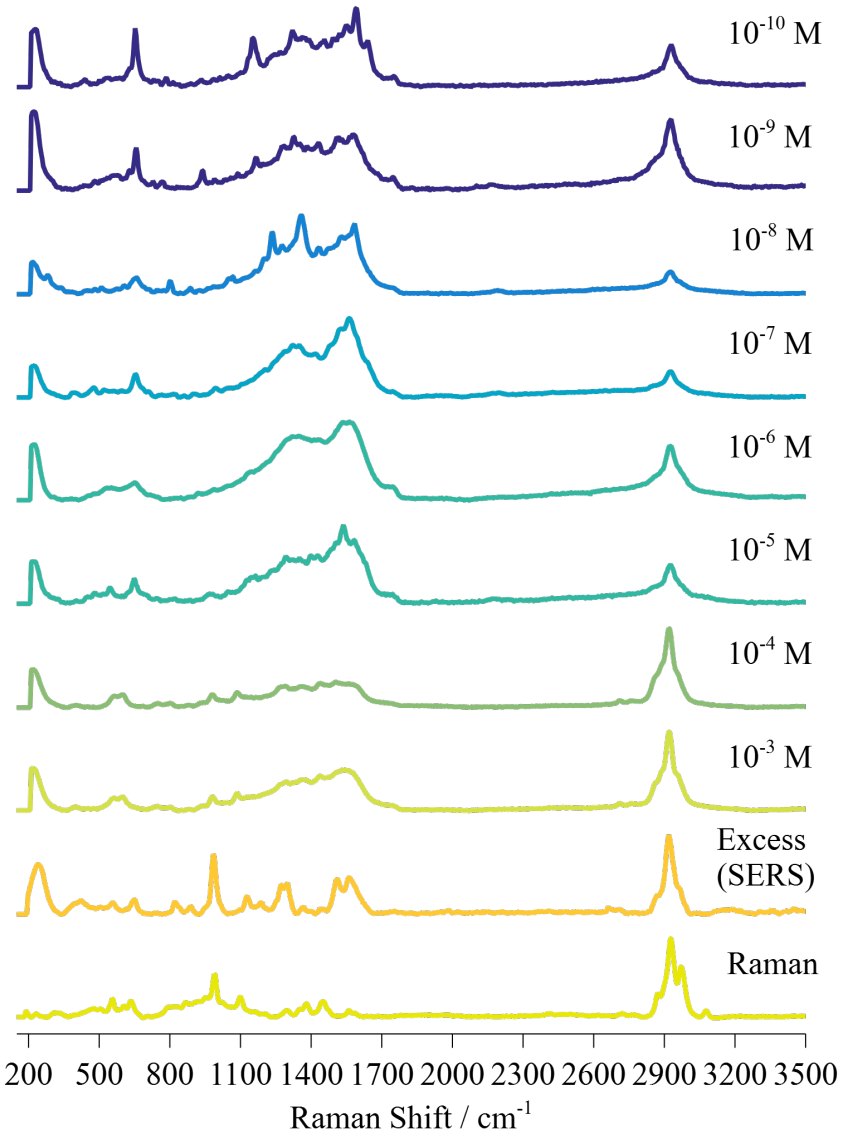

Figure 6.9: Stacked spectra with the nanocube substrate, comparing the Raman spectra of diazinon, a standard SLIPSERS spectrum containing excess diazinon and various initial concentrations of diazinon with the silver nanocubes as a SERS substrate.

6.2.0.4 Spherical Nanoparticles

The peaks present in Fig.(6.10) at initial concentrations of 10^{-3} M and 10^{-4} M appear small due to the scaling factor caused the abnormally large peak around 200 cm^{-1}. At closer inspection, in Fig.(6.11) this appears to not be the case. However, it does appear that there is increased activity at the initial concentrations of 10^{-9} M and 10^{-7} M. This could be due to the competitive binding at the nanoparticle surface;

such as a large layer of analyte blocking contact to the plasmonic surface. However, the activity observed at an initial concentration of 10^{-7} M is unlike anything observed for diazinon, so it is unclear why this is occurring.

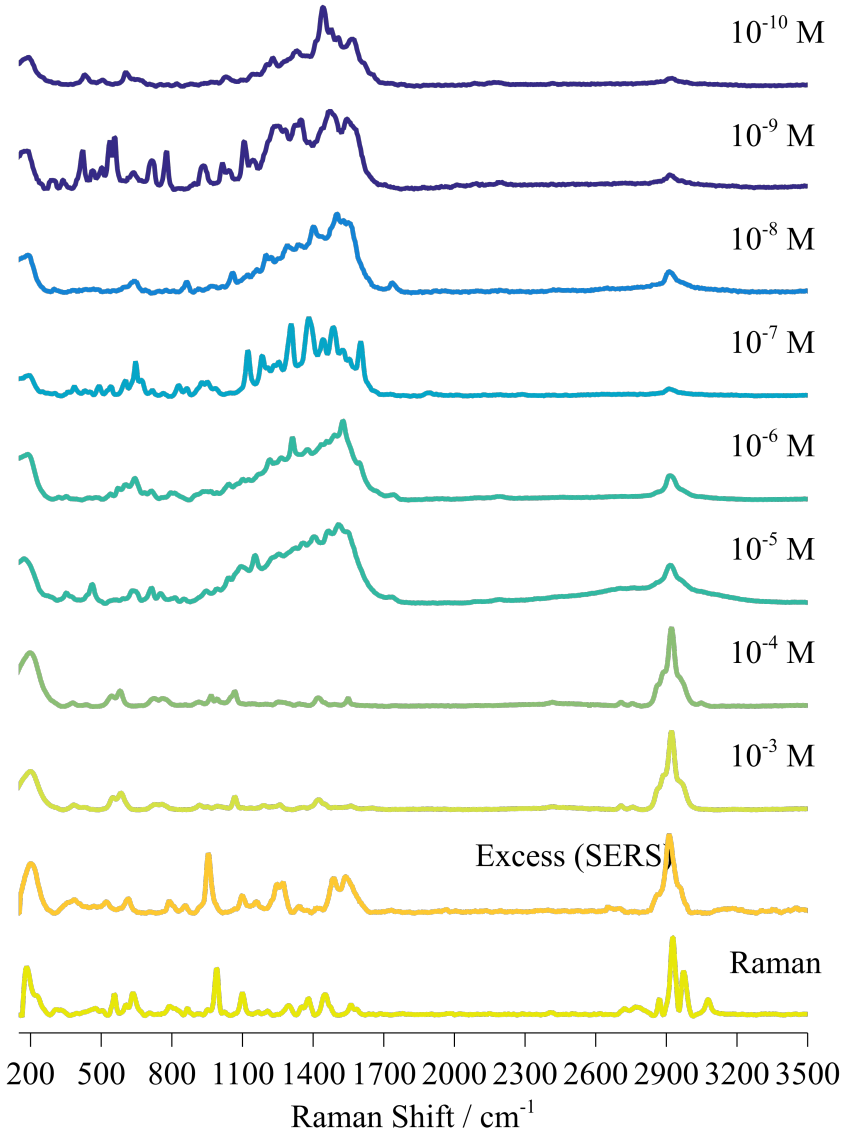

Figure 6.10: Stacked spectra with the nanospheres substrate, compared with the Raman spectra of diazinon, a standard SLIPSERS spectra containing excess diazinon and various initial concentrations of diazinon with the nanospheres as the SERS substrate. Incident beam at 532 nm.

Further investigation in Fig.(6.11), confuses matters further, however, it does appear that at the previously mentioned unusual spectra, there are at least some shared modes between these spectra.

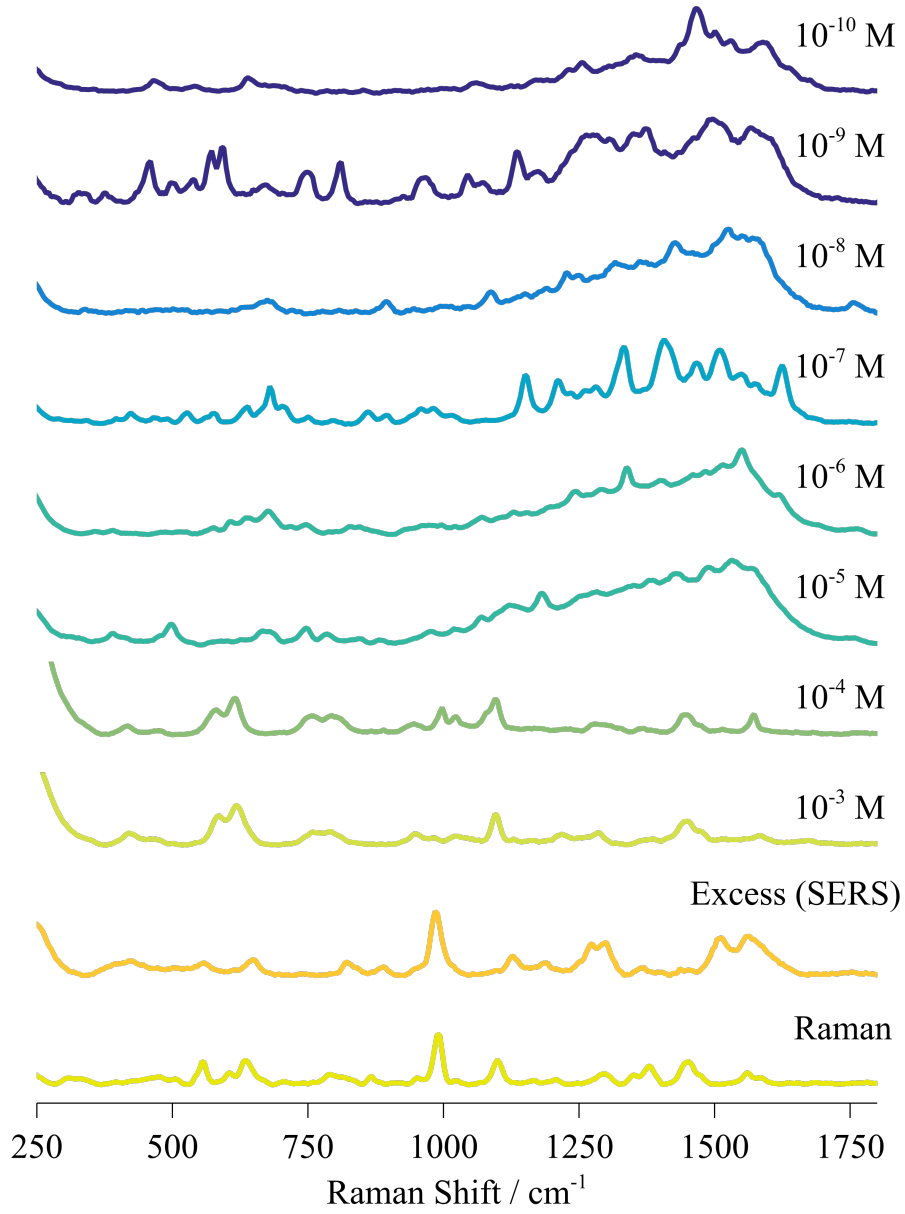

Figure 6.11: Stacked spectra with the nanospheres substrate, compared with the Raman spectra of diazinon, a standard SLIPSERS spectrum containing excess diazinon and various initial concentrations of diazinon with the nanospheres as the SERS substrate. Zoomed in to 250 cm^{-1} to 1800 cm^{-1}. Incident beam at 532 nm.

On the other hand, for the silica-capped nanospheres, there appears to be less sensitivity at least with respect to how many modes are being observed in the SERS spectrum; in particular, there is a very low signal-to-noise at an initial concentration of 10^{-3}. This might be due to either an over-saturated surface and the silica shell that is making it difficult for the diazinon molecules to interact with the plasmonic core. This could explain why at an initial concentration of 10^{-5} M there is an increase in sensitivity and peaks begin appearing, likely due to the aforementioned

single-molecule regime. At this point concentration dependence has less an effect on the observed SERS spectra and is now dependent on a molecule interacting with a hotspot.

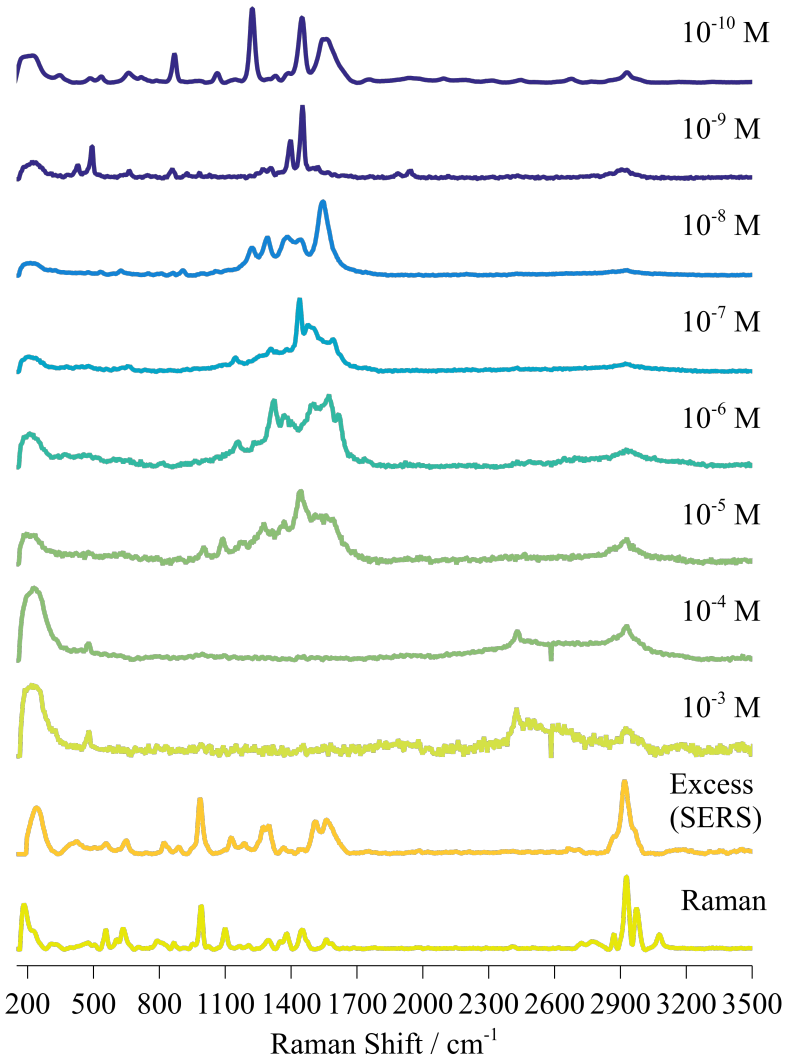

Figure 6.12: Stacked spectra with the silica capped nanospheres substrate, compared with the Raman spectra of diazinon, a standard SLIPSERS spectrum containing excess diazinon and various initial concentrations of diazinon with the silica capped nanospheres as the SERS substrate. Incident beam at 532 nm.

6.2.0.5 Comparison of All Nanoparticle Types

A comparison of all of the "best" spectra collected for each nanoparticle type in Fig.(6.13) shows that there are some modes that are shared between the SERS standard and the Raman spectrum (also in Table 6.2), and the other nanoparticle types. Strangely, unlike for the spectrum of glyphosate or the dyes for the "yellow" nanoparticle dispersion. However, for the other nanoparticle types, there is less overlap.

Of note is that the spherical nanoparticles and the nanocubes are characteristically unique at least compared to the other spectra.

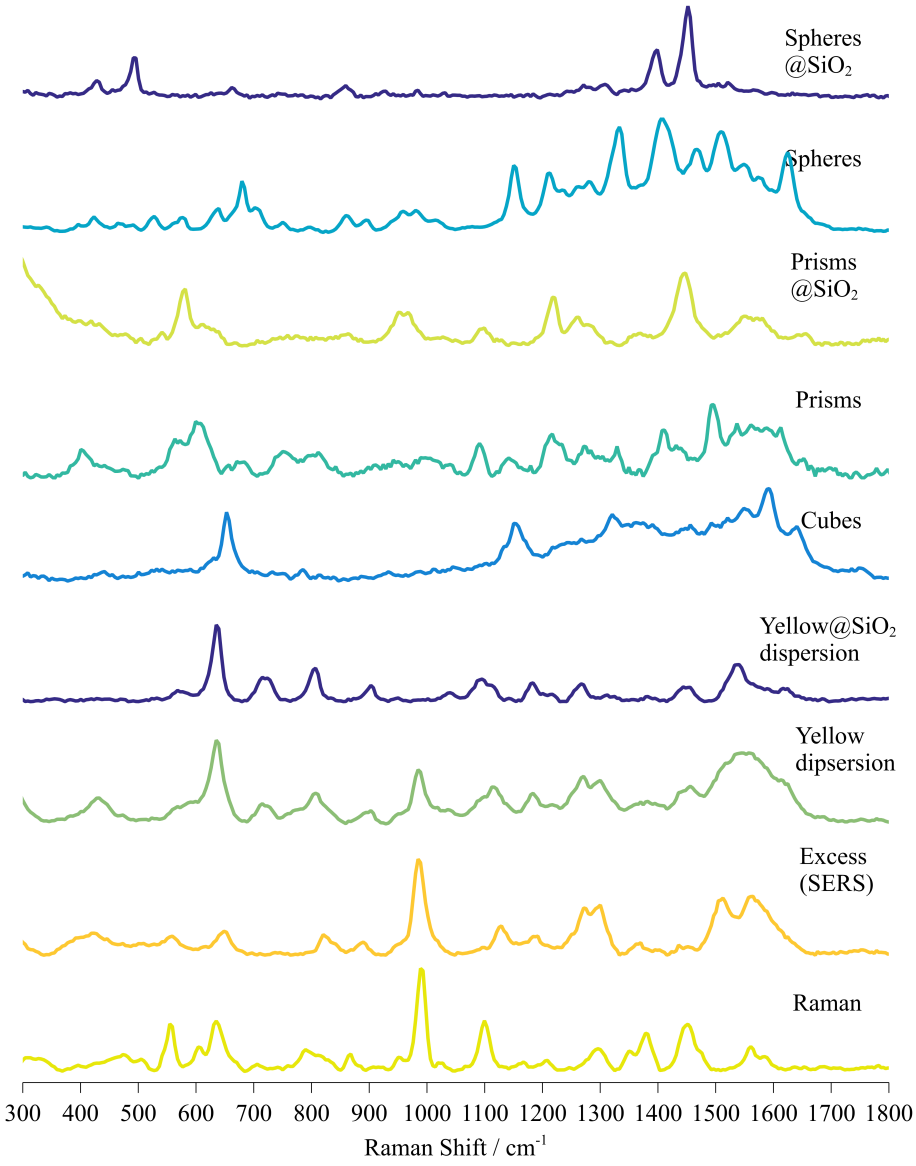

Figure 6.13: A comparison of all of the "best" SLIPSERS spectra of diazinon for each of the silver nanoparticle types, compared to the SERS standard and its Raman spectrum. As most of the variation between the spectra occurs at the 300 cm^{-1} to 1800 cm^{-1}, the rest of the wavenumbers will be omitted from this figure.

6.3 Linear discriminant analysis and comparison of the diazinon and glyphosate SLIPSERS spectra

From Fig.(6.14), there is a clear grouping of the "yellow" nanoparticles, the silica capped "yellow" nanoparticles and the nanoprisms. In addition, as the SLIPSERS standard was conducted on the silica capped "yellow" nanoparticles they appear in this grouping too. It also appears that much of the overlap occurs between the nanocubes, prisms, silica-capped spheres, and the nanospheres. Initially, it appears that it is due to the edges of the nanoparticles; for instance, both the nanocubes and the nanoprisms have sharp edges, however, the fact that the spheres and silica capped spheres exist in this overlap too. Based on the presence of the d/g band spot, however, it seems likely that the reason for this is due to user error, as the d/g bands are influencing the spectra to such a degree that they are over. However, many of the 'yellow' dispersion SLIPSERS spectra also contain some d/g influence, so it is unclear why these are not overlapping with this group of spectra; it might be due to them having less d/g character, making them statistically not as similar as the other spectra. Loadings plots for these spectra can be found in Fig.(A.25), it can be seen that the majority of variation contribution comes from the 400 cm^{-1} to 2000 cm^{-1} range, particularly in principal component 6.

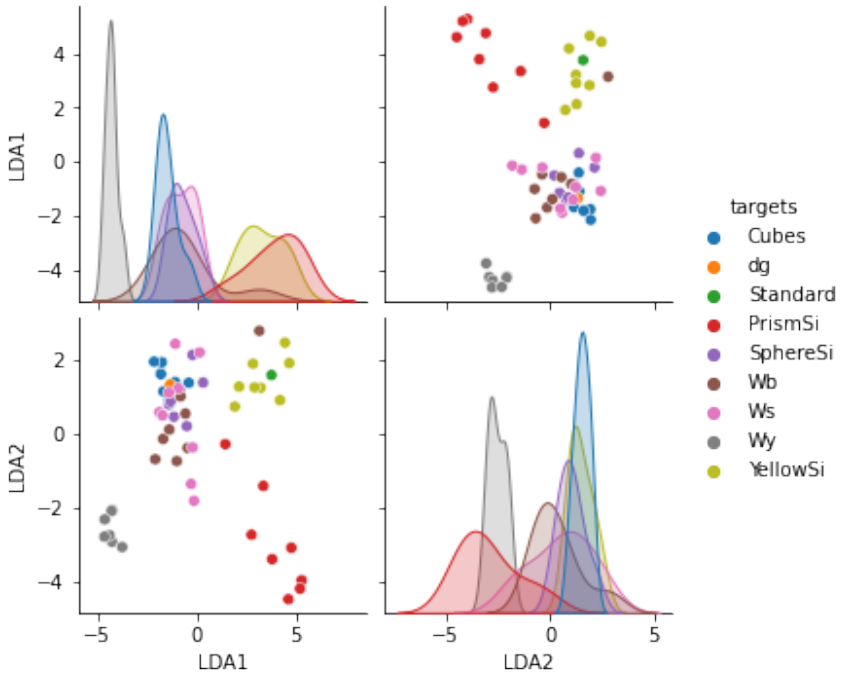

Figure 6.14: Linear Discriminant Analysis of all of the diazinon spectra according to the types of nanoparticles used.

As the main goal of this thesis is to see if SHINs are capable of detecting organophosphorus compounds, a Linear Discriminant Analysis of the SHINs and how well their

SLIPSERS spectra compare to one another. From Fig.(6.15) it can be seen that there is a clear grouping of the nanoparticles, with a small amount of overlap of the silica capped nanoprisms with the nanoparticles from the silica capped "yellow" nanoparticles. It is unclear why this overlap exists, however, considering the standard SLIPSERS spectra use the silica capped "yellow" nanoparticles as a substrate, it might explain why this overlap exists, as, due to the nature of SERS, produced similar spectra to those found in the silica capped "yellow" nanoparticles SLIPSERS spectra.

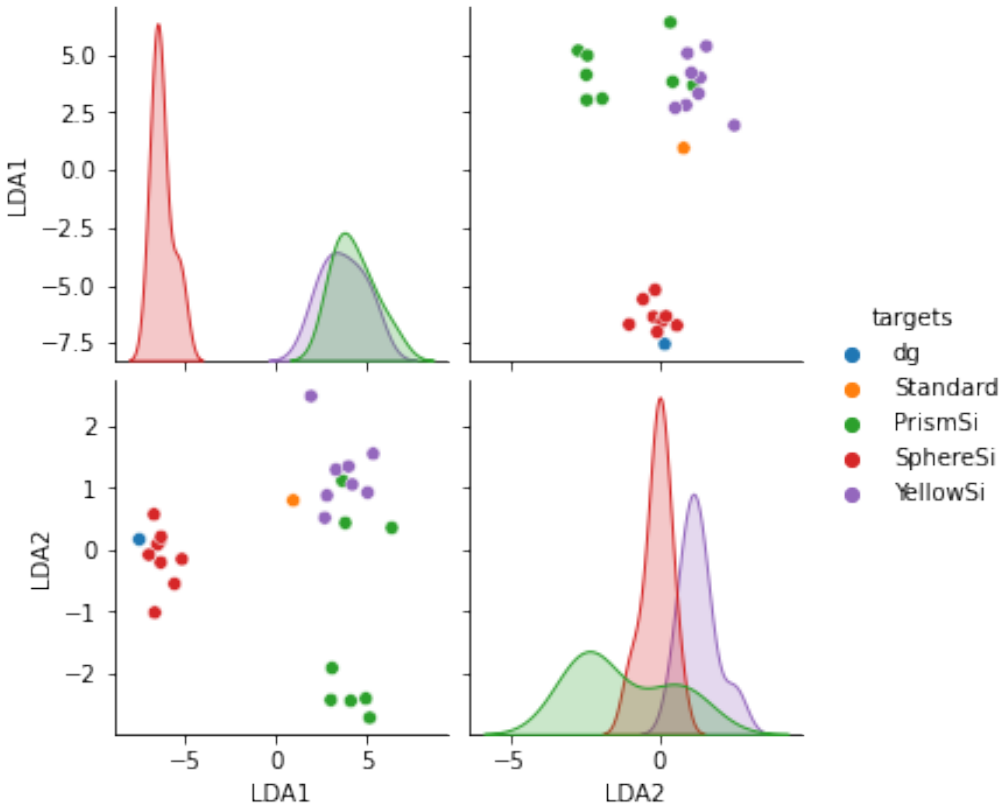

Figure 6.15: Linear Discriminant Analysis of all of the diazinon SLIPSERS spectra which use SHINs as their substrate, organised by their nanoparticle type.

Conducting a Linear Discriminant analysis of all of the glyphosate and diazinon spectra shows a grouping of the spectra, (this section would not have been appropriate in the previous chapter as the diazinon spectra were not introduced yet) indicating that the collected spectra are not of capping agents or some other compound in the samples. There is some overlap between the two groups, though it appears somewhat minimal; this might be due to shared modes between the two compounds being enhanced in a similar fashion, or the influence of d/g bands. However, if this were the case, it would be likely to see that there would be more silica-capped nanoparticles grouping in this region.

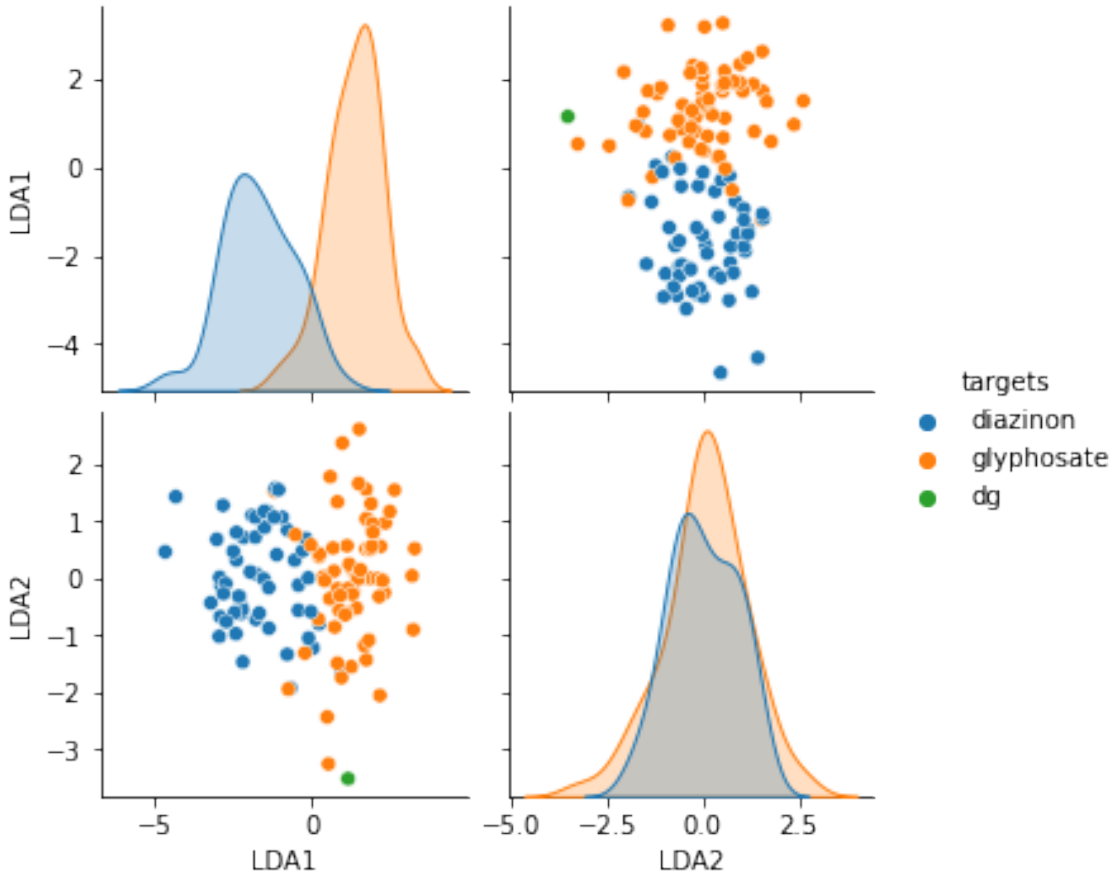

Figure 6.16: Linear Discriminant Analysis comparing all of the diazinon and glyphosate spectra.

As mentioned already, analysis of the effectiveness of the SHINs is one of the main goals of this thesis, therefore an LDA comparison of the glyphosate and diazinon spectra as in Fig.(6.16) should reveal some insights into how well these spectra are differentiated. In Fig.(6.17), the LDA is carried out under the nanoparticle type as classes ('targets'). Here it can be observed that there is a clear separation between the nanoparticle SHIN type and their spectra. It is unclear why this is happening. However, the other visualisations of the data appear to show that the diazinon SERS spectra are at least somewhat different by nanoparticle type (in Fig.(6.14)). It is likely that making one class from two (the glyphosate and diazinon) causes issues with the dimensionality of the data.

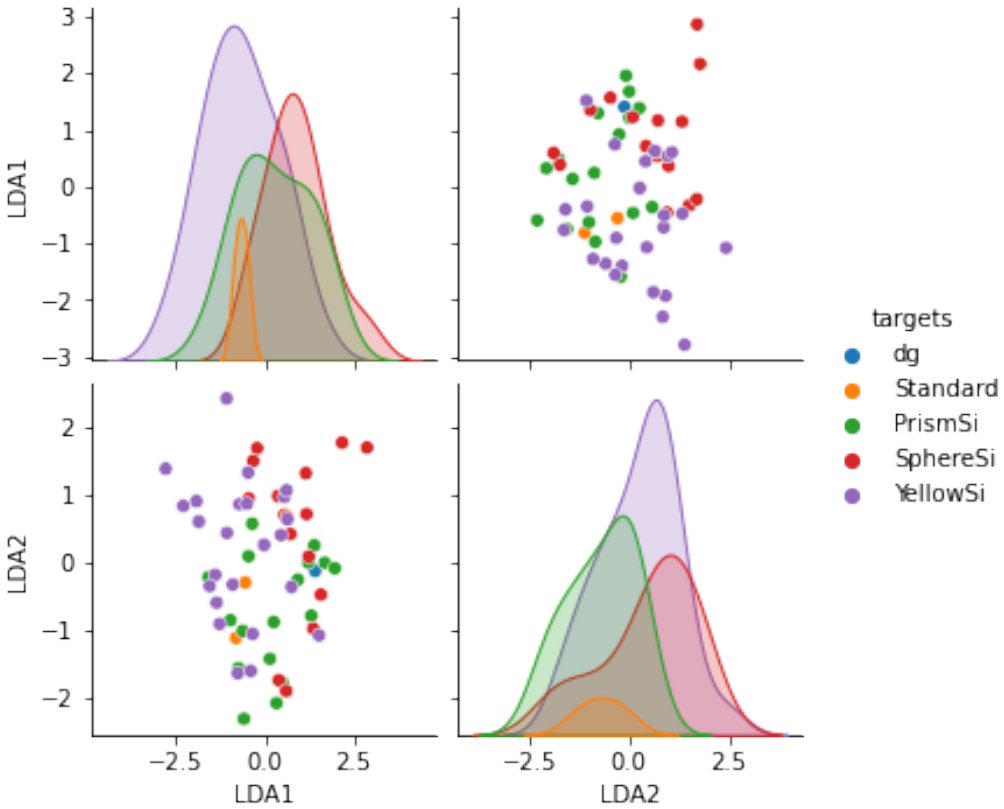

Figure 6.17: Linear Discriminant Analysis of all of the diazinon and glyphosate SLIPSERS spectra which use SHINs as their substrate, organised by their nanoparticle type.

In Fig.(6.18), it can be seen that unlike in the previous figure, there is a clear difference between the different spectra when sorting out the SHINs by their analyte, however, some outliers make it difficult to make a good estimation of what is going on. It was difficult to pinpoint these with the code written at the time. Loadings plots for these analytes by their SHIN substrates can be found in Fig.(A.25).

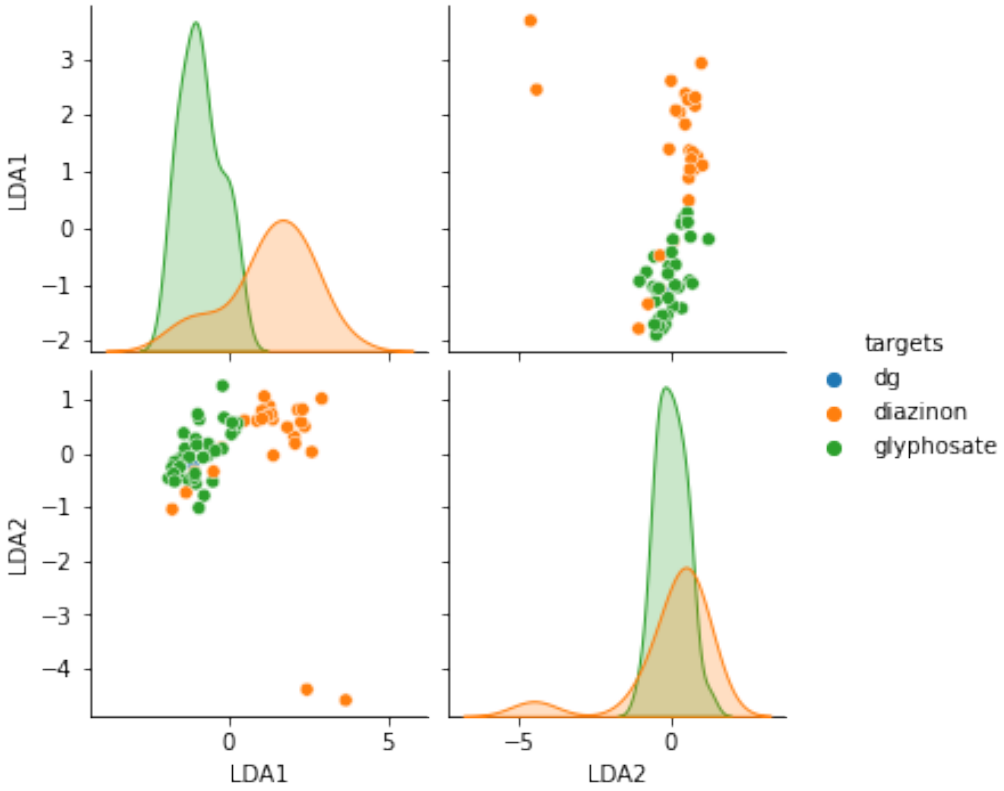

Figure 6.18: Linear Discriminant Analysis of all of the diazinon and glyphosate SLIPSERS spectra which use SHINs as their substrate, organised by their analyte type.

7. Conclusions

7.1 Linear Discriminant Analysis of all of the collected SLIPSERS spectra

Using LDA classification on all of the collected data will help formulate some conclusions with respect to similar LDA classification in Sections A.2.2 and A.2.4 A.2.3. For instance, in Fig.(7.1), there is at least some grouping between the types of analytes, with most of the overlap between analytes occurring due to P4R. Although not required to understand how this variation occurs, the figures in Fig.(A.14) and Fig.(A.17) show that for the analytes, the majority of the variation between the samples occurs within the 400 cm^{-1} to 2000 cm^{-1} range. Though this is not surprising, a lot of important modes in organic molecules occur here.

This overlap could indicate is that either; the spectra are shown in Section 4.1.2 were collected with major errors; or, that P4R shares many similar modes with the spectra that it overlaps with. Another possibility is because of the limitations of LDA explained in Section 2.9. Namely, the assumption of equal covariance matrices; this may not hold if the classes have different variances or if the relationship between the features is different for each class. This can occur if the data is collected from different sources or if the underlying processes generating the data are different for each class. In the case of this thesis, this is why Figs.(4.31) and (6.16) show much more distinct groups than the other LDA plots. In addition, using LDA classification in Fig.(7.2), there also appears to be some grouping, although significantly more overlap, this is likely due to the d/g bands in some spectra causing more similarity as expected however, the Raman spectra all appear as outliers. However, based on all of the LDA plots in Figures (7.2), (4.27), (4.29), and (4.31), (6.14), (5.17) it appears that in the case of the yellow nanoparticles, they consistently produce an easily identifiable cluster in the Linear Discriminant Analysis. This indicates that they are much more easily reproducible, or that the quality of the other nanoparticles isn't as consistent. However, considering the yellow nanoparticles are very inhomogeneous; this is known to decrease SERS signal intensity,[222–224]. As these spectra were done under SLIPS conditions, this effect will be minimised due to the concentration of the nanoparticles and the analytes in the SLIPs samples.

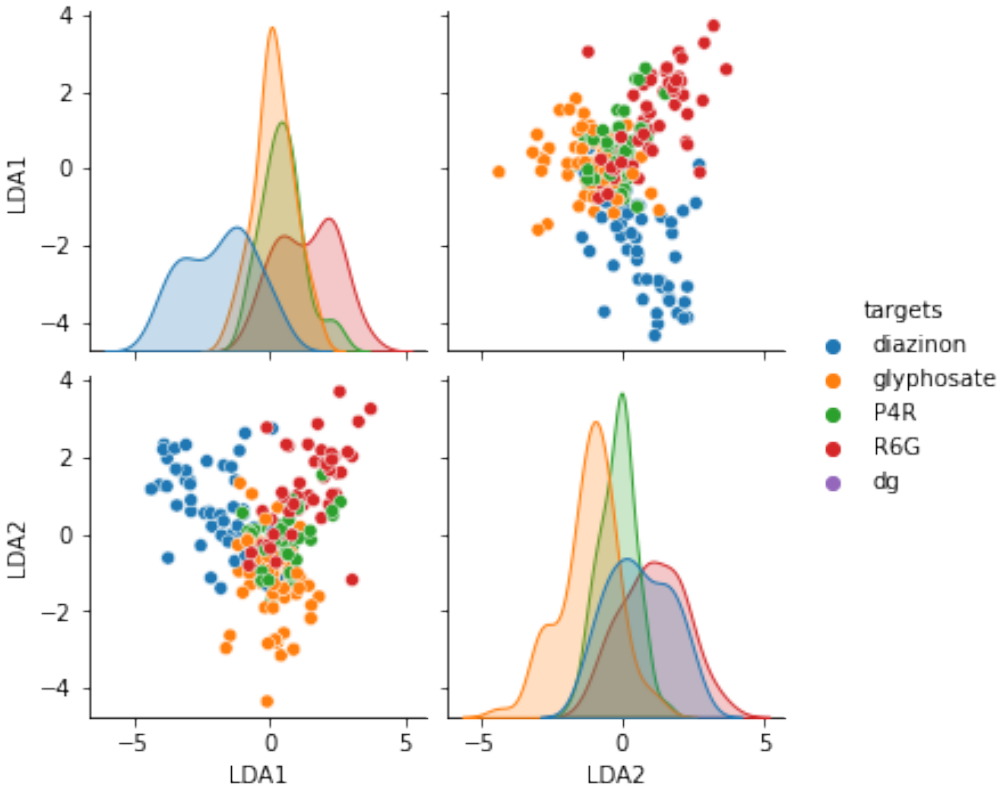

Figure 7.1: Linear Discriminant Analysis of all of the SLIPSERS spectra according to the analytes in the sample.

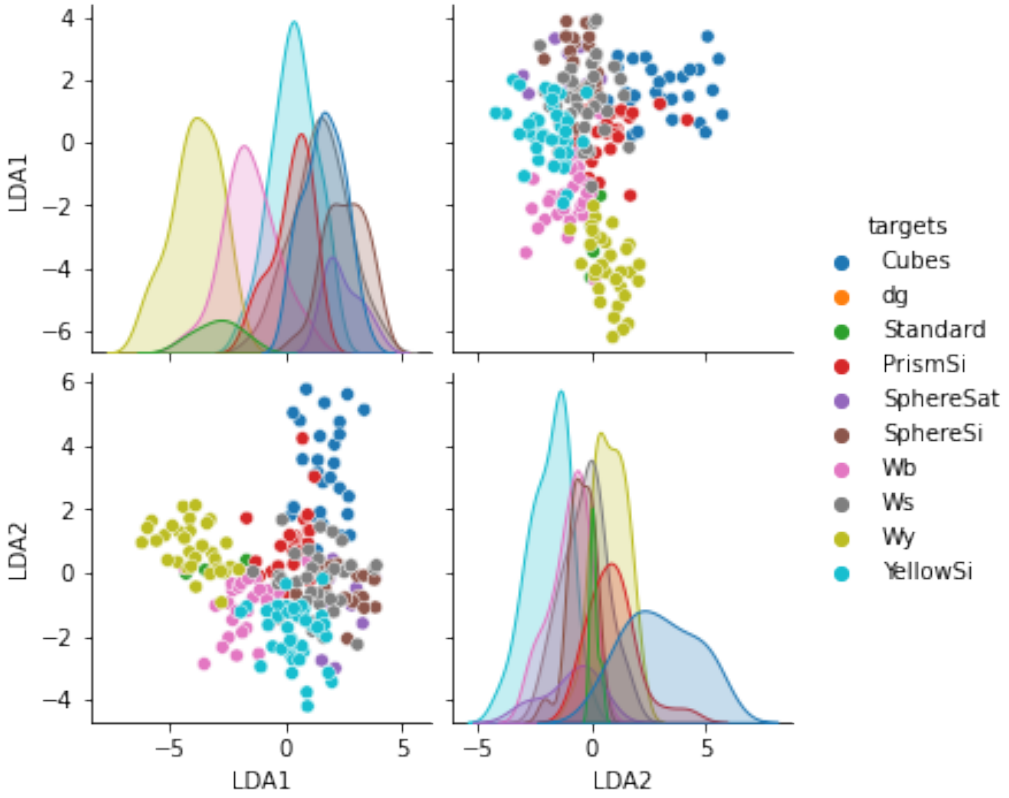

Figure 7.2: Linear Discriminant Analysis of all of the SLIPSERS spectra according to the types of nanoparticle substrates in the sample.

Fig.(7.2) also shows that there is three distinct groups; the yellow nanoparticles, the nanocubes, and the silica capped yellow nanoparticles. The other nanoparticle classes show significant overlap. As this dataset combines all of the analytes, the overlap can be explained by both spectral similarity and the limitations of the LDA. Overall, given the observed separation between the nanoparticle type and analyte types in the above LDA plots and LDA plots in previous chapters, clear differences were observed between the types of substrates used and the analyte type (with respect to comparing dyes or organophosphorus compounds).

7.2 SLIPSERS detection of Dyes

From Section4.2, we see that there is a clear separation between the P4R and R6G SLIPSERS spectra. This indicates that the spectra collected are significantly different from each other. There also does appear to be some separation in terms of the nanoparticle type in Figures (4.27) and (4.29), indicating the nanoparticle type plays a key role in the observed Raman spectra. In addition, the observed sudden increase in sensitivity in many spectra at low concentrations in, for example, Fig.(4.17) shows that there are strong P4R peaks at an initial concentration of 10^{-11} M, despite relatively the low signal to noise. Therefore, SLIPSERS for both P4R and R6G is a good platform for the detection of these dyes using the nanoparticle types in this

thesis.

7.2.1 Efficacy of SHIN-SLIPSERS for the detection of dyes

However, for the SHIN substrates, it appears that in Section 4.1, that the silica capping agents prevent some of the SERS enhancement from the plasmonic core. This can be explained due to the silica shell separating the plasmonic surface from the adsorbed dyes. This indicates that the nanoparticle silica shell produced was not sufficiently thin, and the silica capping experiments need to be repeated to obtain a better tuned SHIN system. However it appears that for R6G and P4R, the SHIN-SLIPSERS system produced using the silica capped nanospheres is an improvement over the silica capped nanoparticles of any other type. It therefore appears that the SHINs and their ability to detect the dyes are also dependent on their shell thickness, and likely the homogeneity of the nanoparticle morphology in the SLIP aggregate; this would have to be explored further. In addition, the addition of more Ag-nanospheres improved the performance of silica capped silver nanospheres in the detection of dyes. This is likely due to the introduction of the satellites as explained in 2.1.2, which introduces more plasmonic material into the SLIP surface. It is clear that it will be required to improve the quality (shell thickness in particular) of the silica capped nanoparticles for further study. A major disadvantage with the Ag-Satellite SHIN-SLIPSERS method, appears to be a question of long-term storage and stability, as the Ag satellites are bare silver nanoparticles and are prone to destabilising if the conditions of the mixture change significantly. For example, it was observed that the SHIN-satellite lose stability after about eight weeks (observed by the colour change to a black solution of oxidised nanoparticles). If the Ag-satellite nanoparticles are stored in a fridge they are stable for at least two months. So, at the benefit of better SERS performance, the advantage of a stable central core, this method (in this thesis at least) comes at the cost of an unstable nanoparticle dispersion. This nanoparticle composite (SHIN-Satellites) would be an ideal candidate for further research in SLIPSERS, and SERS in general.

7.3 SLIPSERS detection of glyphosate

Glyphosate is a small molecule, which makes it difficult to determine how well it will Raman scatter, and, unlike the dyes in the previous sections, it is not fluorophore. However, the data in Section 5.2 shows that glyphosate is detected well by all of the nanoparticle substrates, and, unlike the dyes, there was a minimal amount of spectra with low signal-to-noise or many highly fluorescent spectra. As shown by Section 5.3, there is some grouping of the SLIPSERS spectra by their nanoparticle type. This indicates that the nanoparticle type might play a role in how different the SLIPSERS spectra will be observed.

7.3.1 Efficacy of SHIN-SLIPSERS for the detection of glyphosate

In comparison to the dyes using the SHIN substrate, the SHINs were somewhat more capable of detecting glyphosate. As shown in Section 5.3, each SHIN has a more distinct glyphosate spectrum. Comparing the LDA of the SHINs and the differences between the glyphosate and diazinon spectra, there is distinct grouping of the spectra with some overlap (likely due to common modes). Based on the SHIN performance for detecting glyphosate, the SHINs are a potentially good substrate for the detection of organophosphorus compounds, for example in the case of all of the SHINs used, they all picked up some SERS signals in their spectra to 10^{-11} M, in Figs.(5.9), (5.12) (5.14). These are promising results that could be expanded upon further in more experiments; or by choosing another organophosphorus compound with an improved Raman or SERS cross section. A recommendation for further study is to perhaps use surface modifications on the silica shell in combination with SLIPSERS, as it should improve analyte specificity.

7.4 SLIPSERS detection of diazinon

For diazinon, the spectra are consistent between each nanoparticle type. However, in the case of the silica capped nanoprisms, there was a very low detection limit of only up to 10^{-6} M, likely due to a incorrectly controlled silica shell. This consistency, was hypothesised in Section 1.7. What was not significantly observed were strong P=S bond vibrations. which is unusual as these should be the strongest, being directly parallel to the plasmon modes coming from the surface of the silver nanoparticles. This could be due to diazinon being unstable and prone to degradation, and the drying method accelerating this process; it is possible that what was being observed was a diazinon-related compound and not diazinon itself.

7.4.1 Efficacy of SHIN-SLIPSERS for the detection of diazinon

In the LDA plot in Fig.(6.14) it was found that there was some grouping of the nanoparticles, with much of the overlap occurring between the nanocubes, prisms, silica capped spheres and the nanospheres. Based on the presence of the d/g band spot, however, it appears that the reason for this is the d/g bands are influencing the spectra. Many of the 'yellow' dispersion SLIPSERS spectra also contain some d/g influence, so it is likely that this overlap is due to similarity in the observed modes in the spectra. In addition, an LDA analysis *just* using the SHINs as targets in Fig.(6.15) showed that there is a more obvious separation between all three of the SHIN substrates, indicating that each shape and their silica shell plays an important role in the spectra observed in Section 6.2. More distinct groups were observed for the silica capped 'yellow' dispersion, the 'yellow' nanoparticles and the silica capped nanoprisms. In the case of the silica capped nanoprisms, this is likely due to the fact the spectra with an initial concentration lower than 10^{-6} M do not have any significant modes showing up, making them different from the other spectra. Therefore, of all

of the SHIN nanoparticles that were analysed, the silica capped "yellow" dispersion showed the best significant improvement over the other SHIN substrates used in this thesis. This could be observed due to errors with data collection, and/or the capping of the silica on the nanoparticle substrates resulting in separation from the plasmonic core. Regardless, it is promising that these substrates can be used to detect diazinon up to an initial concentration of 10^{-10} M in most cases; likely due to the single molecule regime being enhanced by the concentrative effect of the SLIPS spot.

7.5 Future Work

The most important aspect that was missed would be to appropriately verify the concentrations of all of the analytes using mass spectrometry - an aspect of SERS studies that is often overlooked, and is yet another overlooked aspect in this thesis. This would be important as the limits of detection are effectively determined by the presence (or lack thereof) of contaminants at the lower concentration (such as pico- and subpicomolar) regions; if the contaminants are present, bands that do not belong to the chosen analyte in the SERS spectra will be observed, and the practical limit of detection has been reached. A full, accurate characterisation of the vibrational modes is almost impossible with the current hardware due to the SERS effect, however, a more in-depth study into how the organophosphorus compounds specifically bind to the silver nanoparticles would be interesting, as the orientation is an important factor in understanding the modes observed in the SERS spectra.[66] One key factor that was missed was more characterisation of the nanoparticle systems. For example, it was not explored *how* crystalline the silica capped nanoparticles (SHINs) were, so powdered X-ray diffraction (pXRD) could have been useful, as the prominent 111 modes would be easily seen and therefore easily verified. One other important avenue to explore is the absorption spectrum of the aggregate on the SLIPS samples (a solid UV-vis), as it is assumed that the absorption spectrum of the colloidal solution is the same as the aggregate; this could be done using the current detector setup in the Raman lab, but using a broader light source such as a white lamp. In addition, more optimisation could have been done on the silicon capped nanoparticles, in particular, the prisms and nanocubes (which weren't attempted in this thesis), as molecules such as mercaptohexadecanoic acid and Another missed opportunity was what the specific nanoparticle size distribution and surface charges were. This, while not crucial to the understanding of the SERS spectra, might bring more insight into how the systems used would be affected by the changes in the environment and how the analytes would bind to the nanoparticle surface. A comparison of the SERS spectra where glyphosate was under different pH conditions would also have been an interesting set of experiments that were not thought of; as the differing electronic structure could likely change how the spectra are observed.

In addition, including some SEM images of the SLIP nanoparticle aggregate, and Atomic Force Microscopy (AFM) images of the nanoparticle 'spot' on the SLIPs slides would be useful (though a very small nanoparticle aggregate would be required for the AFM due to the physical constraints). In particular, the AFM would provide some insight into the general morphology of the agglomerated nanoparticle spot produced

as a result of no contact line pinning, and therefore help to predict (partly because the nanoparticles will never dry in the same agglomerated spot every time) how the hotspots are forming within the SLIPS spot.
In addition, it would likely be prudent to analyse the prisms under the 633 nm laser, as this is a bit closer to the observed LSPR of Fig.(3.2). For much of the spectra, it appeared to not be necessary due to the broad absorption observed by the nanoparticles; an addition that was recently added to this laser line also allows the use of a motorised stage that can collect a spectrum of a sample at each coordinate that is given to it. This can then be used to create what is essentially a heat map, allowing us to map an entire nanoparticle aggregate and identify any points of interest (such as areas of hotspot activity). Combined with the AFM, this could gain some insight into how exactly the aggregate is interacting with the incident beam based on its surface structure.

Bibliography

[1] I. van der Veen, J. de Boer, "Phosphorus flame retardants: Properties, production, environmental occurrence, toxicity and analysis", *Chemosphere* **2012**, *88*, 1119–1153.

[2] G.-L. Wei, D.-Q. Li, M.-N. Zhuo, Y.-S. Liao, Z.-Y. Xie, T.-L. Guo, J.-J. Li, S.-Y. Zhang, Z.-Q. Liang, "Organophosphorus flame retardants and plasticizers: Sources, occurrence, toxicity and human exposure", *Environ. Pollut.* **2015**, *196*, 29–46.

[3] X. Wang, Q. Zhu, X. Yan, Y. Wang, C. Liao, G. Jiang, "A review of organophosphate flame retardants and plasticizers in the environment: Analysis, occurrence and risk assessment", *Sci. Total Environ.* **2020**, *731*, 139071.

[4] C. Fest, K.-J. Schmidt in *The Chemistry of Organophosphorus Pesticides*, Springer Science & Business Media, **2012**.

[5] I. Pantelaki, D. Voutsa, "Organophosphate flame retardants (OPFRs): A review on analytical methods and occurrence in wastewater and aquatic environment", *Sci. Total Environ.* **2019**, *649*, 247–263.

[6] J. Li, N. Yu, B. Zhang, L. Jin, M. Li, M. Hu, X. Zhang, S. Wei, H. Yu, "Occurrence of organophosphate flame retardants in drinking water from China", *Water Research* **2014**, *54*, 53–61.

[7] H. M. Stapleton, S. Klosterhaus, S. Eagle, J. Fuh, J. D. Meeker, A. Blum, T. F. Webster, "Detection of Organophosphate Flame Retardants in Furniture Foam and U.S. House Dust", *Environ. Sci. Technol.* **2009**, *43*, 7490–7495.

[8] N. Ali, A. C. Dirtu, N. V. d. Eede, E. Goosey, S. Harrad, H. Neels, A. 't Mannetje, J. Coakley, J. Douwes, A. Covaci, "Occurrence of alternative flame retardants in indoor dust from New Zealand: Indoor sources and human exposure assessment", *Chemosphere* **2012**, *88*, 1276–1282.

[9] J. A. WILSON, A. C. G. HEATH, "Resistance to two organophosphorus insecticides in New Zealand populations of the Australian sheep blowfly, Lucilia cuprina", *Med. Vet. Entomol.* **1994**, *8*, 231–237.

[10] J. Wilson, A. Heath, L. Stringfellow, N. Haack, A. Clark, "Relative efficacy of organophosphorus insecticides against susceptible and resistant strains of the strike blowfly Lucilia cuprina (Calliphoridae) in New Zealand sheep", *N. Z. Vet. J.* **1996**, *44*, 185–187.

[11] R. D. Newcomb, D. M. Gleeson, C. G. Yong, R. J. Russell, J. G. Oakeshott, "Multiple Mutations and Gene Duplications Conferring Organophosphorus Insecticide Resistance Have Been Selected at the Rop-1 Locus of the Sheep Blowfly, Lucilia cuprina", *J. Mol. Evol.* **2005**, *60*, 207–220.

[12] D. M. Suckling, R. B. Chapman, D. R. Penman, "Insecticide Resistance in the Light Brown Apple Moth, Epiphyas postvittana (Walker) (Lepidoptera: Tortricidae): Larval Response to Azinphosnlethyl", *J. Econ. Entomol.* **1984**, *77*, 579–582.

[13] R. P. Hide, D. M. Suckling, "Decision analysis of insecticide resistance in light-brown apple moth", *N. Z. J. Crop Hortic. Sci.* **1988**, *16*, 219–224.

[14] D. M. Suckling, J. G. I. Khoo, "Cross-resistance in the lightbrown apple moth Epiphyas postvittana (Lepidoptera: Tortricidae)", *N. Z. J. Crop Hortic. Sci.* **1990**, *18*, 173–180.

[15] D. M. Suckling, P. W. Shaw, "Large-scale trials of mating disruption of lightbrown apple moth in Nelson, New Zealand", *N. Z. J. Crop Hortic. Sci.* **1995**, *23*, 127–137.

[16] D. M. Suckling, E. G. Brockerhoff, "Invasion biology, ecology, and management of the light brown apple moth (Tortricidae)", *Annu. Rev. Entomol.* **2010**, *55*, 285–306.

[17] L. G. Varela, J. T. Walker, P. L. Lo, D. J. Rogers, "New Zealand lessons may aid efforts to control light brown apple moth in California", *Calif. Agr.* **2010**, *64*, 6–12.

[18] Y. Al Naggar, G. Codling, A. Vogt, E. Naiem, M. Mona, A. Seif, J. P. Giesy, "Organophosphorus insecticides in honey, pollen and bees (Apis mellifera L.) and their potential hazard to bee colonies in Egypt", *Ecotoxicol. Environ. Saf.* **2015**, *114*, 1–8.

[19] M. Fernández, Y. Picó, J. Mañes, "Rapid screening of organophosphorus pesticides in honey and bees by liquid chromatography—Mass spectrometry", *Chromatographia* **2002**, *56*, 577–583.

[20] A. L. Dorneles, A. de Souza Rosa, B. Blochtein, "Toxicity of organophosphorus pesticides to the stingless bees Scaptotrigona bipunctata and Tetragonisca fiebrigi", *Apidologie* **2017**, *48*, 612–620.

[21] A. O. Affum, S. O. Acquaah, S. D. Osae, E. E. Kwaansa-Ansah, "Distribution and risk assessment of banned and other current-use pesticides in surface and groundwaters consumed in an agricultural catchment dominated by cocoa crops in the Ankobra Basin, Ghana", *Sci. Total Environ.* **2018**, *633*, 630–640.

[22] A. Martine 't Mannetje, "The carcinogenicity of pesticides used in New Zealand", *N. Z. Med. J.* **2020**, *133*, 76–88.

[23] M. C. Keifer, J. Firestone, "Neurotoxicity of Pesticides", *J. Agromedicine* **2007**, *12*, 17–25.

[24] D. Sharma, A. Nagpal, Y. B. Pakade, J. K. Katnoria, "Analytical methods for estimation of organophosphorus pesticide residues in fruits and vegetables: A review", *Talanta* **2010**, *82*, 1077–1089.

[25] A. I. García-Valcárcel, J. L. Tadeo, "A combination of ultrasonic assisted extraction with LC–MS/MS for the determination of organophosphorus pesticides in sludge", *Anal. Chim. Acta* **2009**, *641*, 117–123.

[26] A. Cappiello, G. Famiglini, P. Palma, F. Mangani, "Trace Level Determination of Organophosphorus Pesticides in Water with the New Direct-Electron Ionization LC/MS Interface", *Anal. Chem.* **2002**, *74*, 3547–3554.

[27] S. Inoue, T. Saito, H. Mase, Y. Suzuki, K. Takazawa, I. Yamamoto, S. Inokuchi, "Rapid simultaneous determination for organophosphorus pesticides in human serum by LC–MS", *J. Pharm. Biomed* **2007**, *44*, 258–264.

[28] Z.-L. Xu, H. Deng, X.-F. Deng, J.-Y. Yang, Y.-M. Jiang, D.-P. Zeng, F. Huang, Y.-D. Shen, H.-T. Lei, H. Wang, Y.-M. Sun, "Monitoring of organophosphorus pesticides in vegetables using monoclonal antibody-based direct competitive ELISA followed by HPLC–MS/MS", *Food Chem.* **2012**, *131*, 1569–1576.

[29] H. John, F. Worek, H. Thiermann, "LC-MS-based procedures for monitoring of toxic organophosphorus compounds and verification of pesticide and nerve agent poisoning", *Anal. Bioanal. Chem.* **2008**, *391*, 97–116.

[30] J. Ma, R. Xiao, J. Li, X. Zhao, B. Shi, S. Li, "Determination of Organophosphorus Pesticides in Underground Water by SPE-GC-MS", *J. Chromatogr. Sci.* **2009**, *47*, 110–115.

[31] M. Jain, P. Yadav, A. Joshi, P. Kodgire, "Advances in detection of hazardous organophosphorus compounds using organophosphorus hydrolase based biosensors", *Crit. Rev. Toxicol.* **2019**, *49*, 387–410.

[32] C. Pundir, A. Malik, Preety, "Bio-sensing of organophosphorus pesticides: A review", *Biosens. Bioelectron.* **2019**, *140*, 111348.

[33] H. Hu, L. Yang, "Development of enzymatic electrochemical biosensors for organophosphorus pesticide detection", *J. Environ. Sci. Health C* **2021**, *56*, 168–180.

[34] J. Dong, H. Yang, Y. Li, A. Liu, W. Wei, S. Liu, "Fluorescence sensor for organophosphorus pesticide detection based on the alkaline phosphatase-triggered reaction", *Anal. Chim. Acta* **2020**, *1131*, 102–108.

[35] R. J. H. Clark, T. J. Dines, "Resonance Raman Spectroscopy, and Its Application to Inorganic Chemistry. New Analytical Methods (27)", *Angew. Chem. Int. Ed.* **1986**, *25*, 131–158.

[36] D. Pines, "Electron Interaction in Solids", *Can. J. Phys.* **1956**, *34*, 1379–1394.

[37] In *Principles of Surface-Enhanced Raman Spectroscopy*, (Eds.: E. C. Le Ru, P. G. Etchegoin), Elsevier, Amsterdam, **2009**, pp. 523–528.

[38] Z. T. Solutions, Types of Waves Quiz - PPB, **2014**, `https://www.flickr.com/photos/102642344@N02/15278413843/` (visited on 07/11/2022).

[39] W. Li, P. H. C. Camargo, X. Lu, Y. Xia, "Dimers of Silver Nanospheres: Facile Synthesis and Their Use as Hot Spots for Surface-Enhanced Raman Scattering", *Nano Lett.* **2009**, *9*, 485–490.

[40] M. Rycenga, P. H. C. Camargo, W. Li, C. H. Moran, Y. Xia, "Understanding the SERS Effects of Single Silver Nanoparticles and Their Dimers, One at a Time", *J. Phys. Chem. Lett.* **2010**, *1*, 696–703.

[41] B. Pietrobon, M. McEachran, V. Kitaev, "Synthesis of Size-Controlled Faceted Pentagonal Silver Nanorods with Tunable Plasmonic Properties and Self-Assembly of These Nanorods", *ACS Nano* **2009**, *3*, 21–26.

[42] J. Jiu, K. Murai, D. Kim, K. Kim, K. Suganuma, "Preparation of Ag nanorods with high yield by polyol process", *Mater. Chem. Phys.* **2009**, *114*, 333–338.

[43] S.-B. Li, L.-M. Li, J. R. Anema, B. Ren, J.-J. Sun, Z.-Q. Tian, "Shell-Isolated Nanoparticle-Enhanced Raman Spectroscopy (SHINERS) Based on Gold-Core Silica-Shell Nanorods", *Z. Phys. Chem.* **2011**, *225*, 775–784.

[44] Y. Wang, Y. Zheng, C. Z. Huang, Y. Xia, "Synthesis of Ag Nanocubes 18–32 nm in Edge Length: The Effects of Polyol on Reduction Kinetics, Size Control, and Reproducibility", *J. Am. Chem. Soc.* **2013**, *135*, 1941–1951.

[45] W. A. Tegegne, W.-N. Su, M.-C. Tsai, A. B. Beyene, B.-J. Hwang, "Ag nanocubes decorated 1T-MoS2 nanosheets SERS substrate for reliable and ultrasensitive detection of pesticides", *Appl. Mater. Today* **2020**, *21*, 100871.

[46] S. H. Im, Y. T. Lee, B. Wiley, Y. Xia, "Large-Scale Synthesis of Silver Nanocubes: The Role of HCl in Promoting Cube Perfection and Monodispersity", *Angew. Chem. Int. Ed.* **2005**, *44*, 2154–2157.

[47] J. Zhu, C. Kan, X. Zhu, J.-g. Wan, M. Han, Y. Zhao, B. Wang, G. Wang, "Synthesis of perfect silver nanocubes by a simple polyol process", *J. Mater. Res.* **2007**, *22*, 1479–1485.

[48] C. Xue, C. A. Mirkin, "pH-Switchable Silver Nanoprism Growth Pathways", *Angew. Chem. Int. Ed.* **2007**, *46*, 2036–2038.

[49] C. Xue, X. Chen, S. J. Hurst, C. A. Mirkin, "Self-Assembled Monolayer Mediated Silica Coating of Silver Triangular Nanoprisms", *Adv. Mater.* **2007**, *19*, 4071–4074.

[50] X. Dong, X. Ji, J. Jing, M. Li, J. Li, W. Yang, "Synthesis of Triangular Silver Nanoprisms by Stepwise Reduction of Sodium Borohydride and Trisodium Citrate", *J. Phys. Chem. C* **2010**, *114*, 2070–2074.

[51] B. Xue, D. Wang, J. Zuo, X. Kong, Y. Zhang, X. Liu, L. Tu, Y. Chang, C. Li, F. Wu, Q. Zeng, H. Zhao, H. Zhao, H. Zhang, "Towards high quality triangular silver nanoprisms: improved synthesis, six-tip based hot spots and ultra-high local surface plasmon resonance sensitivity", *Nanoscale* **2015**, *7*, 8048–8057.

[52] A. J. Frank, N. Cathcart, K. E. Maly, V. Kitaev, "Synthesis of Silver Nanoprisms with Variable Size and Investigation of Their Optical Properties: A First-Year Undergraduate Experiment Exploring Plasmonic Nanoparticles", *J. Chem. Educ.* **2010**, *87*, 1098–1101.

[53] B. J. Wiley, Y. Xiong, Z.-Y. Li, Y. Yin, Y. Xia, "Right Bipyramids of Silver: A New Shape Derived from Single Twinned Seeds", *Nano Lett.* **2006**, *6*, 765–768.

[54] A. Garcia-Leis, J. V. Garcia-Ramos, S. Sanchez-Cortes, "Silver Nanostars with High SERS Performance", *J. Phys. Chem. C* **2013**, *117*, 7791–7795.

[55] M. A. C., F. K. P., S. Singh, S. Baik, "Hierarchically-structured silver nanoflowers for highly conductive metallic inks with dramatically reduced filler concentration", *Sci. Rep.* **2016**, *6*, 34894.

[56] J. Chen, J. M. McLellan, A. Siekkinen, Y. Xiong, Z.-Y. Li, Y. Xia, "Facile Synthesis of Gold-Silver Nanocages with Controllable Pores on the Surface", *J. Am. Chem. Soc.* **2006**, *128*, 14776–14777.

[57] F. Huang, G. Ma, J. Liu, J. Lin, X. Wang, L. Guo, "High-Yield Synthesis of Hollow Octahedral Silver Nanocages with Controllable Pack Density and Their High-Performance Sers Application", *Small* **2016**, *12*, 5442–5448.

[58] J. Chen, F. Saeki, B. J. Wiley, H. Cang, M. J. Cobb, Z.-Y. Li, L. Au, H. Zhang, M. B. Kimmey, X. Li, Y. Xia, "Gold Nanocages: Bioconjugation and Their Potential Use as Optical Imaging Contrast Agents", *Nano Lett.* **2005**, *5*, 473–477.

[59] M. W. Knight, N. S. King, L. Liu, H. O. Everitt, P. Nordlander, N. J. Halas, "Aluminum for Plasmonics", *ACS Nano* **2014**, *8*, 834–840.

[60] D. Gérard, S. K. Gray, "Aluminium plasmonics", *J. Phys* **2014**, *48*, 184001.

[61] C. R. Jacobson, D. Solti, D. Renard, L. Yuan, M. Lou, N. J. Halas, "Shining Light on Aluminum Nanoparticle Synthesis", *Acc. Chem. Res.* **2020**, *53*, 2020–2030.

[62] Jianwen Xu, Kyoung-Sik Moon, C. Tison, C. P. Wong, "A novel aluminum-filled composite dielectric for embedded passive applications", *IEEE Trans. Adv. Packag.* **2006**, *29*, 295–306.

[63] E. C. Le Ru, P. G. Etchegoin in *Principles of Surface-Enhanced Raman Spectroscopy*, (Eds.: E. C. Le Ru, P. G. Etchegoin), Elsevier, Amsterdam, **2009**, pp. 185–264.

[64] E. C. Le Ru, P. G. Etchegoin in *Principles of Surface-Enhanced Raman Spectroscopy*, (Eds.: E. C. Le Ru, P. G. Etchegoin), Elsevier, Amsterdam, **2009**, pp. 1–27.

[65] E. C. Le Ru, P. G. Etchegoin, J. Grand, N. Félidj, J. Aubard, G. Lévi, "Mechanisms of Spectral Profile Modification in Surface-Enhanced Fluorescence", *J. Phys. Chem. C* **2007**, *111*, 16076–16079.

[66] J. Creighton, "Surface raman electromagnetic enhancement factors for molecules at the surface of small isolated metal spheres: The determination of adsorbate orientation from sers relative intensities", *Surf. Sci.* **1983**, *124*, 209–219.

[67] D. V. Chulhai, L. Jensen, "Determining Molecular Orientation With Surface-Enhanced Raman Scattering Using Inhomogenous Electric Fields", *J. Phys. Chem. C* **2013**, *117*, 19622–19631.

[68] A. Michota, J. Bukowska, "Surface-enhanced Raman scattering (SERS) of 4-mercaptobenzoic acid on silver and gold substrates", *J. Raman Spectrosc.* **2003**, *34*, 21–25.

[69] M. Dendisová-Vyškovská, A. Kokaislová, M. Ončák, P. Matějka, "SERS and in situ SERS spectroscopy of riboflavin adsorbed on silver, gold and copper substrates. Elucidation of variability of surface orientation based on both experimental and theoretical approach", *J. Mol. Struct.* **2013**, *1038*, 19–28.

[70] C. Sun, T. Chen, W. Ruan, B. Zhao, Q. Cong, "Controlling the orientation of probe molecules on surface-enhanced Raman scattering substrates: A novel strategy to improve sensitivity", *Anal. Chim. Acta* **2017**, *994*, 65–72.

[71] R. C. Maher in *Raman spectroscopy for nanomaterials characterization*, Springer, **2012**, pp. 215–260.

[72] D. Radziuk, H. Moehwald, "Prospects for plasmonic hot spots in single molecule SERS towards the chemical imaging of live cells", *Phys. Chem. Chem. Phys.* **2015**, *17*, 21072–21093.

[73] E. Le Ru, P. Etchegoin, "Sub-wavelength localization of hot-spots in SERS", *Chem. Phys. Lett.* **2004**, *396*, 393–397.

[74] M. Futamata, "Single molecule sensitivity in SERS: importance of junction of adjacent Ag nanoparticles", *Faraday Discuss.* **2006**, *132*, 45–61.

[75] Jiang, K. Bosnick, M. Maillard, L. Brus, "Single Molecule Raman Spectroscopy at the Junctions of Large Ag Nanocrystals", *J. Phys. Chem. B* **2003**, *107*, 9964–9972.

[76] A. M. Michaels, Jiang, L. Brus, "Ag Nanocrystal Junctions as the Site for Surface-Enhanced Raman Scattering of Single Rhodamine 6G Molecules", *J. Phys. Chem. B* **2000**, *104*, 11965–11971.

[77] H. Xu, J. Aizpurua, M. Käll, P. Apell, "Electromagnetic contributions to single-molecule sensitivity in surface-enhanced Raman scattering", *Phys. Rev. E* **2000**, *62*, 4318–4324.

[78] D. J. Anderson, M. Moskovits, "A SERS-Active System Based on Silver Nanoparticles Tethered to a Deposited Silver Film", *J. Phys. Chem. B* **2006**, *110*, 13722–13727.

[79] P. G. Etchegoin, M. Meyer, E. Blackie, E. C. Le Ru, "Statistics of Single-Molecule Surface Enhanced Raman Scattering Signals: Fluctuation Analysis with Multiple Analyte Techniques", *Anal. Chem.* **2007**, *79*, 8411–8415.

[80] P. G. Etchegoin, M. Meyer, E. C. Le Ru, "Statistics of single molecule SERS signals: is there a Poisson distribution of intensities?", *Phys. Chem. Chem. Phys.* **2007**, *9*, 3006–3010.

[81] E. C. Le Ru, P. G. Etchegoin, "Quantifying SERS enhancements", *MRS Bulletin* **2013**, *38*, 631–640.

[82] P. G. Etchegoin, E. C. Le Ru, "A perspective on single molecule SERS: current status and future challenges", *Phys. Chem. Chem. Phys.* **2008**, *10*, 6079–6089.

[83] J. Gersten, A. Nitzan, "Electromagnetic theory of enhanced Raman scattering by molecules adsorbed on rough surfaces", *J. Chem. Phys.* **1980**, *73*, 3023–3037.

[84] M. Moskovits, D. P. Dilellla, "Enhanced raman spectra of ethylene and propylene adsorbed on silver", *Chemical Physics Letters* **1980**, *73*, 500–505.

[85] H. Metiu, P. Das, "The Electromagnetic Theory of Surface Enhanced Spectroscopy", *Annu. Rev. Phys. Chem.* **1984**, *35*, 507–536.

[86] G. C. Schatz, "Theoretical studies of surface enhanced Raman scattering", *Acc. Chem. Res.* **1984**, *17*, 370–376.

[87] M. Philpott, R., "THEORY OF SURFACE ENHANCED RAMAN SCATTERING : A PROSPECTIVE VIEW", *J. Phys. Colloques* **1983**, *44*, C10–295.

[88] A. Wokaun, "Surface-Enhanced Electromagnetic Processes", *Solid State Phys.*, Solid State Physics **1984**, *38*, (Eds.: H. Ehrenreich, D. Turnbull, F. Seitz), 223–294.

[89] A. Wokaun, "Surface enhancement of optical fields", *Mol. Phys.* **1985**, *56*, 1–33.

[90] W.-H. Park, Z. H. Kim, "Charge Transfer Enhancement in the SERS of a Single Molecule", *Nano Lett.* **2010**, *10*, 4040–4048.

[91] G. C. Schatz, M. A. Young, R. P. Van Duyne in *Surface-Enhanced Raman Scattering: Physics and Applications*, (Eds.: K. Kneipp, M. Moskovits, H. Kneipp), Springer Berlin Heidelberg, Berlin, Heidelberg, **2006**, pp. 19–45.

[92] K. L. Kelly, E. Coronado, L. L. Zhao, G. C. Schatz, "The Optical Properties of Metal Nanoparticles: The Influence of Size, Shape, and Dielectric Environment", *J. Phys. Chem. B* **2003**, *107*, 668–677.

[93] T. Neuman, R. Esteban, G. Giedke, M. K. Schmidt, J. Aizpurua, "Quantum description of surface-enhanced resonant Raman scattering within a hybrid-optomechanical model", *Phys. Rev. A* **2019**, *100*, 043422.

[94] J. H. Guan, G. G. Wells, B. Xu, G. McHale, D. Wood, J. Martin, S. Stuart-Cole, "Evaporation of Sessile Droplets on Slippery Liquid-Infused Porous Surfaces (SLIPS)", *Langmuir* **2015**, *31*, 11781–11789.

[95] M. Mehta, M. Waterland, "Ultrasensitive surface-enhanced Raman scattering detection of biological pollutants by controlled evaporation on omniphobic substrates", *Heliyon* **2020**, *6*, e04317.

[96] D. Zhang, H. You, L. Yuan, R. Hao, T. Li, J. Fang, "Hydrophobic Slippery Surface-Based Surface-Enhanced Raman Spectroscopy Platform for Ultrasensitive Detection in Food Safety Applications", *Anal. Chem.* **2019**, *91*, 4687–4695.

[97] Yang Shikuan, Dai Xianming, Stogin Birgitt Boschitsch, Wong Tak-Sing, "Ultrasensitive surface-enhanced Raman scattering detection in common fluids", *Proc. Natl. Acad. Sci. U.S.A.* **2016**, *113*, 268–273.

[98] J. Yang, L. Zhou, X.-Y. Wang, G. Song, L.-J. You, J.-M. Li, "Core-satellite Ag/TiO2/Ag composite nanospheres for multiple SERS applications in solution by a portable Raman spectrometer", *Colloids and Surfaces A: Physicochemical and Engineering Aspects* **2020**, *584*, 124013.

[99] M. Meng, F.-L. Zhang, J. Yi, L.-H. Lin, C.-L. Zhang, N. Bodappa, C.-Y. Li, S.-J. Zhang, R. F. Aroca, Z.-Q. Tian, J.-F. Li, "Shell-Isolated Nanoparticle-Enhanced Phosphorescence", *Anal. Chem.* **2018**, *90*, 10837–10842.

[100] R. Harding, "Stability of silica dispersions", *Journal of Colloid and Interface Science* **1971**, *35*, 172–174.

[101] R. K. Iler in *The Colloid Chemistry of Silica and Silicates*, UMI, **1989**.

[102] M. S. Azam, C. Cai, J. M. Gibbs, E. Tyrode, D. K. Hore, "Silica Surface Charge Enhancement at Elevated Temperatures Revealed by Interfacial Water Signals", *J. Am. Chem. Soc.* **2020**, *142*, 669–673.

[103] N. N. Vlasova, L. P. Golovkova, "The adsorption of amino acids on the surface of highly dispersed silica", *Colloid Journal* **2004**, *66*, 657–662.

[104] K. Kołątaj, J. Krajczewski, A. Kudelski, "Silver Nanoparticles with Many Sharp Apexes and Edges as Efficient Nanoresonators for Shell-Isolated Nanoparticle-Enhanced Raman Spectroscopy", *J. Phys. Chem. C* **2017**, *121*, 12383–12391.

[105] Y.-J. Kim, S.-W. Ha, S.-M. Jeon, D. W. Yoo, S.-H. Chun, B.-H. Sohn, J.-K. Lee, "Fabrication of Triacetylcellulose-SiO2 Nanocomposites by Surface Modification of Silica Nanoparticles", *Langmuir* **2010**, *26*, 7555–7560.

[106] J.-F. Li, J. R. Anema, T. Wandlowski, Z.-Q. Tian, "Dielectric shell isolated and graphene shell isolated nanoparticle enhanced Raman spectroscopies and their applications", *Chem. Soc. Rev.* **2015**, *44*, 8399–8409.

[107] G. Barbillon, "Applications of Shell-Isolated Nanoparticle-Enhanced Raman Spectroscopy", *Photonics* **2021**, *8*, DOI `10.3390/photonics8020046`.

[108] X.-D. Lin, J.-F. Li, Y.-F. Huang, X.-D. Tian, V. Uzayisenga, S.-B. Li, B. Ren, Z.-Q. Tian, "Shell-isolated nanoparticle-enhanced Raman spectroscopy: Nanoparticle synthesis, characterization and applications in electrochemistry", *J. Electroanal. Chem.* **2013**, *688*, 5–11.

[109] H. Zhang, C. Wang, H.-L. Sun, G. Fu, S. Chen, Y.-J. Zhang, B.-H. Chen, J. R. Anema, Z.-L. Yang, J.-F. Li, Z.-Q. Tian, "In situ dynamic tracking of heterogeneous nanocatalytic processes by shell-isolated nanoparticle-enhanced Raman spectroscopy", *Nat. Commun.* **2017**, *8*, 15447.

[110] V. Uzayisenga, X.-D. Lin, L.-M. Li, J. R. Anema, Z.-L. Yang, Y.-F. Huang, H.-X. Lin, S.-B. Li, J.-F. Li, Z.-Q. Tian, "Synthesis, Characterization, and 3D-FDTD Simulation of Ag@SiO2 Nanoparticles for Shell-Isolated Nanoparticle-Enhanced Raman Spectroscopy", *Langmuir* **2012**, *28*, 9140–9146.

[111] J. Krajczewski, A. Kudelski, "Shell-Isolated Nanoparticle-Enhanced Raman Spectroscopy", *Front. Chem.* **2019**, *7*.

[112] H. Zhang, S. Duan, P. M. Radjenovic, Z.-Q. Tian, J.-F. Li, "Core–Shell Nanostructure-Enhanced Raman Spectroscopy for Surface Catalysis", *Acc. Chem. Res.* **2020**, *53*, 729–739.

[113] J. E. Q. Quinsaat, M. Alexandru, F. A. Nüesch, H. Hofmann, A. Borgschulte, D. M. Opris, "Highly stretchable dielectric elastomer composites containing high volume fractions of silver nanoparticles", *J. Mater. Chem. A* **2015**, *3*, 14675–14685.

[114] K. Bourzac, "Quantum dots go on display", *Nature* **2013**, *493*, 283–283.

[115] V. Privman in *Complex-Shaped Metal Nanoparticles: Bottom-Up Syntheses and Applications*, John Wiley & Sons, Ltd, **2012**, pp. 239–268.

[116] I. J. Kim, K. Y. Cho, E. Kim, Y. J. Kwon, M. Y. Shon, B.-I. Park, S. Yu, J. H. Lee, "Development of High Dielectric Electrostrictive PVDF Terpolymer Blends for Enhanced Electromechanical Properties", *Nanomaterials* **2020**, *11*, 6.

[117] Z. Li, K. S. Moon, S. Kim, C. P. Wong in 2011 IEEE 61st Electronic Components and Technology Conference (ECTC), 2011 IEEE 61st Electronic Components and Technology Conference (ECTC), **2011**, pp. 2073–2078.

[118] Y. Lee, J.-r. Choi, K. J. Lee, N. E. Stott, D. Kim, "Large-scale synthesis of copper nanoparticles by chemically controlled reduction for applications of inkjet-printed electronics", *Nanotechnology* **2008**, *19*, 415604.

[119] J. Reszczyńska, A. Jurek, I. Łącka, E. Skwarek, A. Zaleska, "Preparation of Silver Nanoparticles in Reverse Micelles and Antibacterial Activity of Silver Modified-Paints", *Prog. Mater. Sci.* **2011**, *10*, 12–20.

[120] V. K. Sharma, R. A. Yngard, Y. Lin, "Silver nanoparticles: Green synthesis and their antimicrobial activities", *Adv. Colloid Interface Sci.* **2009**, *145*, 83–96.

[121] A. Goyal, A. Kumar, P. K. Patra, S. Mahendra, S. Tabatabaei, P. J. J. Alvarez, G. John, P. M. Ajayan, "In situ Synthesis of Metal Nanoparticle Embedded Free Standing Multifunctional PDMS Films", *Macromol. Rapid Commun.* **2009**, *30*, 1116–1122.

[122] M. K. Yu, Y. Y. Jeong, J. Park, S. Park, J. W. Kim, J. J. Min, K. Kim, S. Jon, "Drug-Loaded Superparamagnetic Iron Oxide Nanoparticles for Combined Cancer Imaging and Therapy In Vivo", *Angew. Chem. Int. Ed.* **2008**, *47*, 5362–5365.

[123] H. Lee, M. K. Yu, S. Park, S. Moon, J. J. Min, Y. Y. Jeong, H.-W. Kang, S. Jon, "Thermally Cross-Linked Superparamagnetic Iron Oxide Nanoparticles: Synthesis and Application as a Dual Imaging Probe for Cancer in Vivo", *J. Am. Chem. Soc.* **2007**, *129*, 12739–12745.

[124] M. Hu, J. Chen, Z.-Y. Li, L. Au, G. V. Hartland, X. Li, M. Marquez, Y. Xia, "Gold nanostructures: engineering their plasmonic properties for biomedical applications", *Chem. Soc. Rev.* **2006**, *35*, 1084–1094.

[125] R. Xu, D. Wang, J. Zhang, Y. Li, "Shape-Dependent Catalytic Activity of Silver Nanoparticles for the Oxidation of Styrene", *Chem. Asian J.* **2006**, *1*, 888–893.

[126] C. Burda, X. Chen, R. Narayanan, M. A. El-Sayed, "Chemistry and Properties of Nanocrystals of Different Shapes", *Chem. Rev.* **2005**, *105*, 1025–1102.

[127] J. Lu, F. Su, Z. Huang, C. Zhang, Y. Liu, X. Ma, J. Gong, "N-doped Ag/TiO2 hollow spheres for highly efficient photocatalysis under visible-light irradiation", *RSC Adv.* **2013**, *3*, 720–724.

[128] H. A. Atwater, A. Polman, "Plasmonics for improved photovoltaic devices", *Nat. Mater.* **2010**, *9*, 205–213.

[129] J. Qi, X. Dang, P. T. Hammond, A. M. Belcher, "Highly Efficient Plasmon-Enhanced Dye-Sensitized Solar Cells through Metal@Oxide Core-Shell Nanostructure", *ACS Nano* **2011**, *5*, 7108–7116.

[130] A. Tavakoli, M. Sohrabi, A. Kargari, "A review of methods for synthesis of nanostructured metals with emphasis on iron compounds", *Chem. Pap.* **2007**, *61*, 151–170.

[131] C.-H. Cui, S.-H. Yu in *Complex-Shaped Metal Nanoparticles: Bottom-Up Syntheses and Applications*, John Wiley & Sons, Ltd, **2012**, pp. 91–116.

[132] H. Huo, C. Wang, H. Ren, M. Johnson, M. Shen, "Surface Enhanced Raman Scattering Sensing with Nanostructures Fabricated by Soft Nanolithography", *J. Macromol. Sci. A* **2009**, *46*, 1182–1184.

[133] X. Liu, L. Fu, S. Hong, V. Dravid, C. Mirkin, "Arrays of Magnetic Nanoparticles Patterned via "Dip-Pen" Nanolithography", *Adv. Mater.* **2002**, *14*, 231–234.

[134] M. Fedoruk, M. Meixner, S. Carretero-Palacios, T. Lohmüller, J. Feldmann, "Nanolithography by Plasmonic Heating and Optical Manipulation of Gold Nanoparticles", *ACS Nano* **2013**, *7*, 7648–7653.

[135] R. Maoz, E. Frydman, S. R. Cohen, J. Sagiv, "Constructive Nanolithography: Site-Defined Silver Self-Assembly on Nanoelectrochemically Patterned Monolayer Templates", *Adv. Mater.* **2000**, *12*, 424–429.

[136] M. L. Coluccio, G. Das, F. Mecarini, F. Gentile, A. Pujia, L. Bava, R. Tallerico, P. Candeloro, C. Liberale, F. De Angelis, E. Di Fabrizio, "Silver-based surface enhanced Raman scattering (SERS) substrate fabrication using nanolithography and site selective electroless deposition", *Microelectron. Eng.* **2009**, *86*, 1085–1088.

[137] E. Le Ru, P. Etchegoin, J. Grand, N. Félidj, J. Aubard, G. Lévi, A. Hohenau, J. Krenn, "Surface enhanced Raman spectroscopy on nanolithography-prepared substrates", *Curr. Appl. Phys.* **2008**, *8*, 467–470.

[138] W. Yue, Z. Wang, Y. Yang, L. Chen, A. Syed, K. Wong, X. Wang, "Electron-beam lithography of gold nanostructures for surface-enhanced Raman scattering", *J. Micromech. Microeng.* **2012**, *22*, 125007.

[139] L. Petti, R. Capasso, M. Rippa, M. Pannico, P. La Manna, G. Peluso, A. Calarco, E. Bobeico, P. Musto, "A plasmonic nanostructure fabricated by electron beam lithography as a sensitive and highly homogeneous SERS substrate for bio-sensing applications", *Vib. Spectrosc.* **2016**, *82*, 22–30.

[140] T. Wu, Y.-W. Lin, "Surface-enhanced Raman scattering active gold nanoparticle/nanohole arrays fabricated through electron beam lithography", *Appl. Surf. Sci.* **2018**, *435*, 1143–1149.

[141] M. Kahl, E. Voges, S. Kostrewa, C. Viets, W. Hill, "Periodically structured metallic substrates for SERS", *Sens. Actuators B Chem.* **1998**, *51*, 285–291.

[142] N. Toshima, T. Yonezawa, "Bimetallic nanoparticles-novel materials for chemical and physical applications", *New J. Chem.* **1998**, *22*, 1179–1201.

[143] N. R. Jana, L. Gearheart, C. J. Murphy, "Seeding Growth for Size Control of 5-40 nm Diameter Gold Nanoparticles", *Langmuir* **2001**, *17*, 6782–6786.

[144] J. Park, J. Joo, S. G. Kwon, Y. Jang, T. Hyeon, "Synthesis of Monodisperse Spherical Nanocrystals", *Angew. Chem. Int. Ed.* **2007**, *46*, 4630–4660.

[145] M.-C. Daniel, D. Astruc, "Gold Nanoparticles: Assembly, Supramolecular Chemistry, Quantum-Size-Related Properties, and Applications toward Biology, Catalysis, and Nanotechnology", *Chem. Rev.* **2004**, *104*, 293–346.

[146] A. Guiet, T. Reier, N. Heidary, D. Felkel, B. Johnson, U. Vainio, H. Schlaad, Y. Aksu, M. Driess, P. Strasser, A. Thomas, J. Polte, A. Fischer, "A One-Pot Approach to Mesoporous Metal Oxide Ultrathin Film Electrodes Bearing One Metal Nanoparticle per Pore with Enhanced Electrocatalytic Properties", *Chem. Mater.* **2013**, *25*, 4645–4652.

[147] N. R. Jana, L. Gearheart, C. J. Murphy, "Seed-Mediated Growth Approach for Shape-Controlled Synthesis of Spheroidal and Rod-like Gold Nanoparticles Using a Surfactant Template", *Adv. Mater.* **2001**, *13*, 1389–1393.

[148] S. D. Perrault, W. C. W. Chan, "Synthesis and Surface Modification of Highly Monodispersed, Spherical Gold Nanoparticles of 50-200 nm", *J. Am. Chem. Soc.* **2009**, *131*, 17042–17043.

[149] K. R. Brown, D. G. Walter, M. J. Natan, "Seeding of Colloidal Au Nanoparticle Solutions. 2. Improved Control of Particle Size and Shape", *Chem. Mater.* **2000**, *12*, 306–313.

[150] N. R. Jana, L. Gearheart, C. J. Murphy, "Evidence for Seed-Mediated Nucleation in the Chemical Reduction of Gold Salts to Gold Nanoparticles", *Chem. Mater.* **2001**, *13*, 2313–2322.

[151] X. Ji, X. Song, J. Li, Y. Bai, W. Yang, X. Peng, "Size Control of Gold Nanocrystals in Citrate Reduction: The Third Role of Citrate", *J. Am. Chem. Soc.* **2007**, *129*, 13939–13948.

[152] J. Niu, T. Zhu, Z. Liu, "One-step seed-mediated growth of 30–150 nm quasi-spherical gold nanoparticles with 2-mercaptosuccinic acid as a new reducing agent", *Nanotechnology* **2007**, *18*, 325607.

[153] J. Rodríguez-Fernández, J. Pérez-Juste, F. J. García de Abajo, L. M. Liz-Marzán, "Seeded Growth of Submicron Au Colloids with Quadrupole Plasmon Resonance Modes", *Langmuir* **2006**, *22*, 7007–7010.

[154] T. Zhu, K. Vasilev, M. Kreiter, S. Mittler, W. Knoll, "Surface Modification of Citrate-Reduced Colloidal Gold Nanoparticles with 2-Mercaptosuccinic Acid", *Langmuir* **2003**, *19*, 9518–9525.

[155] K. J. Klabunde, *Nanoscale Materials in Chemistry*, 1st ed., John Wiley & Sons, Ltd, **2001**, 285 pp.

[156] N. T. K. Thanh, N. Maclean, S. Mahiddine, "Mechanisms of Nucleation and Growth of Nanoparticles in Solution", *Chem. Rev.* **2014**, *114*, 7610–7630.

[157] V. K. LaMer, R. H. Dinegar, "Theory, Production and Mechanism of Formation of Monodispersed Hydrosols", *J. Am. Chem. Soc.* **1950**, *72*, 4847–4854.

[158] R. Becker, W. Döring, "Kinetic treatment of germ formation in supersaturated vapour", *Annalen der Physik* **1935**, *416*, 719–752.

[159] C. C. Yec, H. C. Zeng, "Synthesis of complex nanomaterials via Ostwald ripening", *J. Mater. Chem. A* **2014**, *2*, 4843–4851.

[160] M. A. Watzky, R. G. Finke, "Nanocluster Size-Control and "Magic Number" Investigations. Experimental Tests of the "Living-Metal Polymer" Concept and of Mechanism-Based Size-Control Predictions Leading to the Syntheses of Iridium(0) Nanoclusters Centering about Four Sequential Magic Numbers", *Chem. Mater.* **1997**, *9*, 3083–3095.

[161] Zheng Haimei, Smith Rachel K., Jun Young-wook, Kisielowski Christian, Dahmen Ulrich, Alivisatos A. Paul, "Observation of Single Colloidal Platinum Nanocrystal Growth Trajectories", *Science* **2009**, *324*, 1309–1312.

[162] Z. A. Peng, X. Peng, "Mechanisms of the Shape Evolution of CdSe Nanocrystals", *J. Am. Chem. Soc.* **2001**, *123*, 1389–1395.

[163] X. Peng, L. Manna, W. Yang, J. Wickham, E. Scher, A. Kadavanich, A. P. Alivisatos, "Shape control of CdSe nanocrystals", *Nature* **2000**, *404*, 59–61.

[164] M. A. Watzky, E. E. Finney, R. G. Finke, "Transition-Metal Nanocluster Size vs Formation Time and the Catalytically Effective Nucleus Number: A Mechanism-Based Treatment", *J. Am. Chem. Soc.* **2008**, *130*, 11959–11969.

[165] C. Besson, E. E. Finney, R. G. Finke, "A Mechanism for Transition-Metal Nanoparticle Self-Assembly", *J. Am. Chem. Soc.* **2005**, *127*, 8179–8184.

[166] S. Yao, Y. Yuan, C. Xiao, W. Li, Y. Kou, P. J. Dyson, N. Yan, H. Asakura, K. Teramura, T. Tanaka, "Insights into the Formation Mechanism of Rhodium Nanocubes", *J. Phys. Chem. C* **2012**, *116*, 15076–15086.

[167] C. Ribeiro, E. J. H. Lee, E. Longo, E. R. Leite, "A Kinetic Model to Describe Nanocrystal Growth by the Oriented Attachment Mechanism", *ChemPhysChem* **2005**, *6*, 690–696.

[168] J. W. Mullin, H.-M. Ang, "Nucleation characteristics of aqueous nickel ammonium sulphate solutions", *Faraday Discuss. Chem. Soc.* **1976**, *61*, 141–148.

[169] J. Garside, R. Ristić, "Growth rate dispersion among ADP crystals formed by primary nucleation", *J. Cryst. Growth* **1983**, *61*, 215–220.

[170] J. Liu, Å. C. Rasmuson, "Influence of Agitation and Fluid Shear on Primary Nucleation in Solution", *Cryst. Growth Des.* **2013**, *13*, 4385–4394.

[171] W. J. E. M. Habraken, J. Tao, L. J. Brylka, H. Friedrich, L. Bertinetti, A. S. Schenk, A. Verch, V. Dmitrovic, P. H. H. Bomans, P. M. Frederik, J. Laven, P. van der Schoot, B. Aichmayer, G. de With, J. J. DeYoreo, N. A. J. M. Sommerdijk, "Ion-association complexes unite classical and non-classical theories for the biomimetic nucleation of calcium phosphate", *Nat. Commun.* **2013**, *4*, 1507.

[172] X. C. Zeng, D. W. Oxtoby, "Gas-liquid nucleation in Lennard-Jones fluids", *J. Chem. Phys.* **1991**, *94*, 4472–4478.

[173] D. B. Dickens, J. J. Sloan, "The Nucleation and Freezing of Dilute Nitric Acid Aerosols", *J. Phys. Chem. A* **2002**, *106*, 10543–10549.

[174] G. W. Turner, L. S. Bartell, "On the Probability of Nucleation at the Surface of Freezing Drops", *J. Phys. Chem. A* **2005**, *109*, 6877–6879.

[175] J. Y. Rempel, M. G. Bawendi, K. F. Jensen, "Insights into the Kinetics of Semiconductor Nanocrystal Nucleation and Growth", *J. Am. Chem. Soc.* **2009**, *131*, 4479–4489.

[176] T. Hiemstra, W. Van Riemsdijk, G. Bolt, "Multisite proton adsorption modeling at the solid/solution interface of (hydr)oxides: A new approach: I. Model description and evaluation of intrinsic reaction constants", *J. Colloid Interface Sci.* **1989**, *133*, 91–104.

[177] D. E. Yates, T. W. Healy, "The structure of the silica/electrolyte interface", *J. Colloid Interface Sci.* **1976**, *55*, 9–19.

[178] D. Grolimund, M. Elimelech, M. Borkovec, "Aggregation and deposition kinetics of mobile colloidal particles in natural porous media", *Colloids. Surf. Sci.* **2001**, *191*, 179–188.

[179] L. H. Allen, E. Matijević, "Stability of colloidal silica: I. Effect of simple electrolytes", *J. Colloid Interface Sci.* **1969**, *31*, 287–296.

[180] J. Depasse, A. Watillon, "The stability of amorphous colloidal silica", *J. Colloid Interface Sci.* **1970**, *33*, 430–438.

[181] J. Depasse, "Simple Experiments to Emphasize the Main Characteristics of the Coagulation of Silica Hydrosols by Alkaline Cations: Application to the Analysis of the Model of Colic et al.", *Journal of Colloid and Interface Science* **1999**, *220*, 174–176.

[182] S. K. Milonjić, "A relation between the amounts of sorbed alkali cations and the stability of colloidal silica", *Colloids Surf.* **1992**, *63*, 113–119.

[183] M. Kobayashi, F. Juillerat, P. Galletto, P. Bowen, M. Borkovec, "Aggregation and Charging of Colloidal Silica Particles: Effect of Particle Size", *Langmuir* **2005**, *21*, 5761–5769.

[184] J. Wang, H. F. M. Boelens, M. B. Thathagar, G. Rothenberg, "In Situ Spectroscopic Analysis of Nanocluster Formation", *ChemPhysChem* **2004**, *5*, 93–98.

[185] A. Henglein, M. Giersig, "Formation of Colloidal Silver Nanoparticles: Capping Action of Citrate", *J. Phys. Chem. B* **1999**, *103*, 9533–9539.

[186] M. Harada, E. Katagiri, "Mechanism of Silver Particle Formation during Photoreduction Using In Situ Time-Resolved SAXS Analysis", *Langmuir* **2010**, *26*, 17896–17905.

[187] U. Nickel, K. Mansyreff, S. Schneider, "Production of monodisperse silver colloids by reduction with hydrazine: the effect of chloride and aggregation on SER(R)S signal intensity", *J. Raman Spectrosc.* **2004**, *35*, 101–110.

[188] A. A. Ádám, M. Szabados, G. Varga, Á. Papp, K. Musza, Z. Kónya, Á. Kukovecz, P. Sipos, I. Pálinkó, "Ultrasound-Assisted Hydrazine Reduction Method for the Preparation of Nickel Nanoparticles, Physicochemical Characterization and Catalytic Application in Suzuki-Miyaura Cross-Coupling Reaction", *Nanomaterials* **2020**, *10*, 632.

[189] J. Turkevich, P. C. Stevenson, J. Hillier, "A study of the nucleation and growth processes in the synthesis of colloidal gold", *Discuss. Faraday Soc.* **1951**, *11*, 55–75.

[190] Q. Zhang, N. Li, J. Goebl, Z. Lu, Y. Yin, "A Systematic Study of the Synthesis of Silver Nanoplates: Is Citrate a "Magic" Reagent?", *J. Am. Chem. Soc.* **2011**, *133*, 18931–18939.

[191] J. E. Q. Quinsaat, F. A. Nüesch, H. Hofmann, D. M. Opris, "Dielectric properties of silver nanoparticles coated with silica shells of different thicknesses", *RSC Adv.* **2013**, *3*, 6964–6971.

[192] W. Li, P. H. C. Camargo, L. Au, Q. Zhang, M. Rycenga, Y. Xia, "Etching and Dimerization: A Simple and Versatile Route to Dimers of Silver Nanospheres with a Range of Sizes", *Angew. Chem. Int. Ed.* **2010**, *49*, 164–168.

[193] Z. Chen, T. Balankura, K. A. Fichthorn, R. M. Rioux, "Revisiting the Polyol Synthesis of Silver Nanostructures: Role of Chloride in Nanocube Formation", *ACS Nano* **2019**, *13*, 1849–1860.

[194] A. R. Siekkinen, J. M. McLellan, J. Chen, Y. Xia, "Rapid synthesis of small silver nanocubes by mediating polyol reduction with a trace amount of sodium sulfide or sodium hydrosulfide", *Chemical Physics Letters* **2006**, *432*, 491–496.

[195] Y. Sun, B. Mayers, T. Herricks, Y. Xia, "Polyol Synthesis of Uniform Silver Nanowires: A Plausible Growth Mechanism and the Supporting Evidence", *Nano Lett.* **2003**, *3*, 955–960.

[196] S. Coskun, B. Aksoy, H. E. Unalan, "Polyol Synthesis of Silver Nanowires: An Extensive Parametric Study", *Cryst. Growth Des.* **2011**, *11*, 4963–4969.

[197] F. Fiévet, S. Ammar-Merah, R. Brayner, F. Chau, M. Giraud, F. Mammeri, J. Peron, J.-Y. Piquemal, L. Sicard, G. Viau, "The polyol process: a unique method for easy access to metal nanoparticles with tailored sizes, shapes and compositions", *Chem. Soc. Rev.* **2018**, *47*, 5187–5233.

[198] M. Eddleston, F. R. Chowdhury, "Pharmacological treatment of organophosphorus insecticide poisoning: the old and the (possible) new", *Br. J. Clin. Pharmacol.* **2016**, *81*, 462–470.

[199] S. Pang, T. Yang, L. He, "Review of surface enhanced Raman spectroscopic (SERS) detection of synthetic chemical pesticides", *Trends Anal. Chem.* **2016**, *85*, 73–82.

[200] Q. Zhao, G. Liu, H. Zhang, F. Zhou, Y. Li, W. Cai, "SERS-based ultrasensitive detection of organophosphorus nerve agents via substrate's surface modification", *J. Hazard. Mater.* **2017**, *324*, 194–202.

[201] T. Wang, S. Wang, Z. Cheng, J. Wei, L. Yang, Z. Zhong, H. Hu, Y. Wang, B. Zhou, P. Li, "Emerging core–shell nanostructures for surface-enhanced Raman scattering (SERS) detection of pesticide residues", *Chem. Eng. J.* **2021**, *424*, 130323.

[202] G. Aragay, F. Pino, A. Merkoçi, "Nanomaterials for Sensing and Destroying Pesticides", *Chem. Rev.* **2012**, *112*, 5317–5338.

[203] Y. Nie, Y. Teng, P. Li, W. Liu, Q. Shi, Y. Zhang, "Label-free aptamer-based sensor for specific detection of malathion residues by surface-enhanced Raman scattering", *Spectrochim. Acta A Mol. Biomol. Spectrosc.* **2018**, *191*, 271–276.

[204] S. E. J. Bell, M. R. McCourt, "SERS enhancement by aggregated Au colloids: effect of particle size", *Phys. Chem. Chem. Phys.* **2009**, *11*, 7455–7462.

[205] M. D. Porter, R. J. Lipert, L. M. Siperko, G. Wang, R. Narayanan, "SERS as a bioassay platform: fundamentals, design, and applications", *Chem. Soc. Rev.* **2008**, *37*, 1001–1011.

[206] T. Stanborough, F. M. Given, B. Koch, C. R. Sheen, A. B. Stowers-Hull, M. R. Waterland, D. L. Crittenden, "Optical Detection of CoV-SARS-2 Viral Proteins to Sub-Picomolar Concentrations", *ACS Omega* **2021**, *6*, 6404–6413.

[207] P. Hildebrandt, M. Stockburger, "Surface-enhanced resonance Raman spectroscopy of Rhodamine 6G adsorbed on colloidal silver", *J. Phys. Chem.* **1984**, *88*, 5935–5944.

[208] K. J. Hageman, C. H. Aebig, K. H. Luong, S. L. Kaserzon, C. S. Wong, T. Reeks, M. Greenwood, S. Macaulay, C. D. Matthaei, "Current-use pesticides in New Zealand streams: Comparing results from grab samples and three types of passive samplers", *Environ. Pollut.* **2019**, *254*, 112973.

[209] V. Aggarwal, X. Deng, A. Tuli, K. S. Goh in *Reviews of Environmental Contamination and Toxicology Volume 223*, (Ed.: D. M. Whitacre), Springer New York, New York, NY, **2013**, pp. 107–140.

[210] Q. Zhou, X. Sun, R. Gao, J. Hu, "Mechanism and kinetic properties for OH-initiated atmospheric degradation of the organophosphorus pesticide diazinon", *Atmos. Environ.* **2011**, *45*, 3141–3148.

[211] C. Zhang, S. Z. Jiang, C. Yang, C. H. Li, Y. Y. Huo, X. Y. Liu, A. H. Liu, Q. Wei, S. S. Gao, X. G. Gao, B. Y. Man, "Gold@silver bimetal nanoparticles/pyramidal silicon 3D substrate with high reproducibility for high-performance SERS", *Sci. Rep.* **2016**, *6*, 25243.

[212] B. Tim, P. Błaszkiewicz, A. B. Nowicka, M. Kotkowiak, "Optimizing SERS performance through aggregation of gold nanorods in Langmuir-Blodgett films", *Appl. Surf. Sci.* **2022**, *573*, 151518.

[213] M. Tahghighi, D. Janner, J. Ignés-Mullol, "Optimizing Gold Nanoparticle Size and Shape for the Fabrication of SERS Substrates by Means of the Langmuir–Blodgett Technique", *Nanomaterials* **2020**, *10*, DOI 10.3390/nano10112264.

[214] N. Li, Z. Han, Y. Huang, K. Liang, X. Wang, F. Wu, X. Qi, Y. Shang, L. Yu, B. Ding, "Strong plasmon–exciton coupling in bimetallic nanorings and nanocuboids", *J. Mater. Chem. C* **2020**, *8*, 7672–7678.

[215] Silver, dispersion nanoparticles, 10 nm particle size (TEM), 0.02 mg/mL in aqueous buffer, contains sodium citrate as stabilizer | Sigma-Aldrich, Silver, dispersion nanoparticles, 10 nm particle size (TEM), 0.02 mg/mL in aqueous buffer, contains sodium citrate as stabilizer, https://www.sigmaaldrich.com/NZ/en/product/aldrich/730785 (visited on 07/24/2022).

[216] O. Pandoli, R. D. S. Martins, E. C. Romani, S. Paciornik, M. H. D. P. Maurício, H. D. L. Alves, F. V. Pereira-Meirelles, E. L. Luz, S. M. L. Koller, H. Valiente, K. Ghavami, "Colloidal silver nanoparticles: an effective nano-filler material to prevent fungal proliferation in bamboo", *RSC Adv.* **2016**, *6*, 98325–98336.

[217] L. Wu, W. Wu, X. Jing, J. Huang, D. Sun, T. Odoom-Wubah, H. Liu, H. Wang, Q. Li, "Trisodium Citrate-Assisted Biosynthesis of Silver Nanoflowers by Canarium album Foliar Broths as a Platform for SERS Detection", *Ind. Eng. Chem. Res.* **2013**, *52*, 5085–5094.

[218] E. C. Le Ru, E. Blackie, M. Meyer, P. G. Etchegoin, "Surface Enhanced Raman Scattering Enhancement Factors: A Comprehensive Study", *J. Phys. Chem. C* **2007**, *111*, 13794–13803.

[219] H. Watanabe, N. Hayazawa, Y. Inouye, S. Kawata, "DFT Vibrational Calculations of Rhodamine 6G Adsorbed on Silver: Analysis of Tip-Enhanced Raman Spectroscopy", *J. Phys. Chem. B* **2005**, *109*, 5012–5020.

[220] Y. Xie, Y. Li, Y. Sun, H. Wang, H. Qian, W. Yao, "Theoretical calculation (DFT), Raman and surface-enhanced Raman scattering (SERS) study of ponceau 4R", *Spectrochimica Acta Part A: Molecular and Biomolecular Spectroscopy* **2012**, *96*, 600–604.

[221] D. Lin-Vien, N. B. Colthup, W. G. Fateley, J. G. Grasselli in *The Handbook of Infrared and Raman Characteristic Frequencies of Organic Molecules*, (Eds.: D. Lin-Vien, N. B. Colthup, W. G. Fateley, J. G. Grasselli), Academic Press, San Diego, **1991**, pp. 263–276.

[222] W. Xie, P. Qiu, C. Mao, "Bio-imaging, detection and analysis by using nanostructures as SERS substrates", *J. Mater. Chem.* **2011**, *21*, 5190–5202.

[223] F. Zhao, W. Wang, H. Zhong, F. Yang, W. Fu, Y. Ling, Z. Zhang, "Robust quantitative SERS analysis with Relative Raman scattering intensities", *Talanta* **2021**, *221*, 121465.

[224] M. Baia, F. Toderas, L. Baia, J. Popp, S. Astilean, "Probing the enhancement mechanisms of SERS with p-aminothiophenol molecules adsorbed on self-assembled gold colloidal nanoparticles", *Chem. Phys. Lett.* **2006**, *422*, 127–132.

A. Appendix

A.1 Miscellaneous Spectra

A.1.1 Ponceau 4R

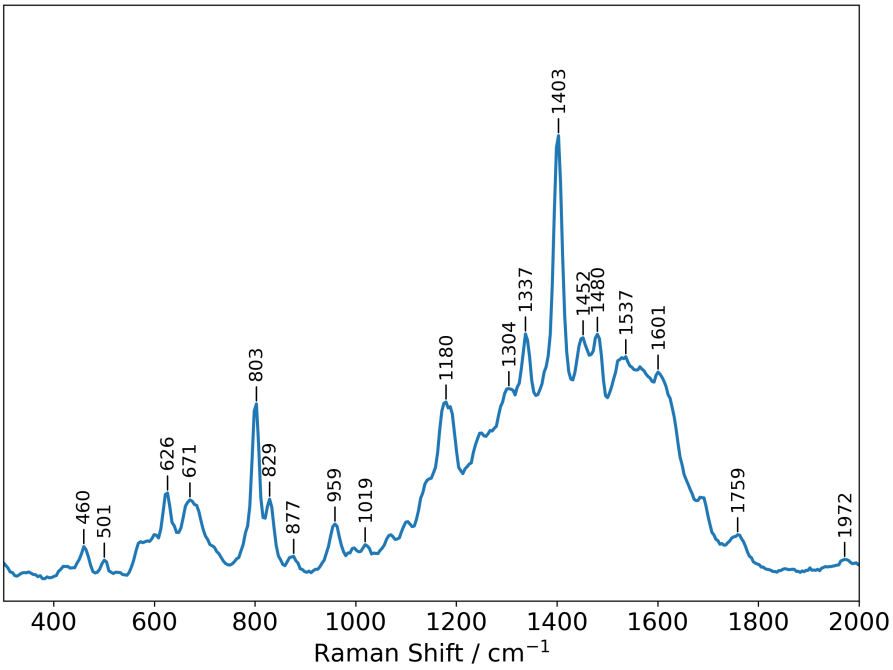

Figure A.1: Ponceau-4R absorbed onto the silica capped silver nanosphere substrate with silver nanosphere satellites at an initial concentration of 10^{-9} M. Excitation wavelength: 532 nm.

A.1.2 Glyphosate

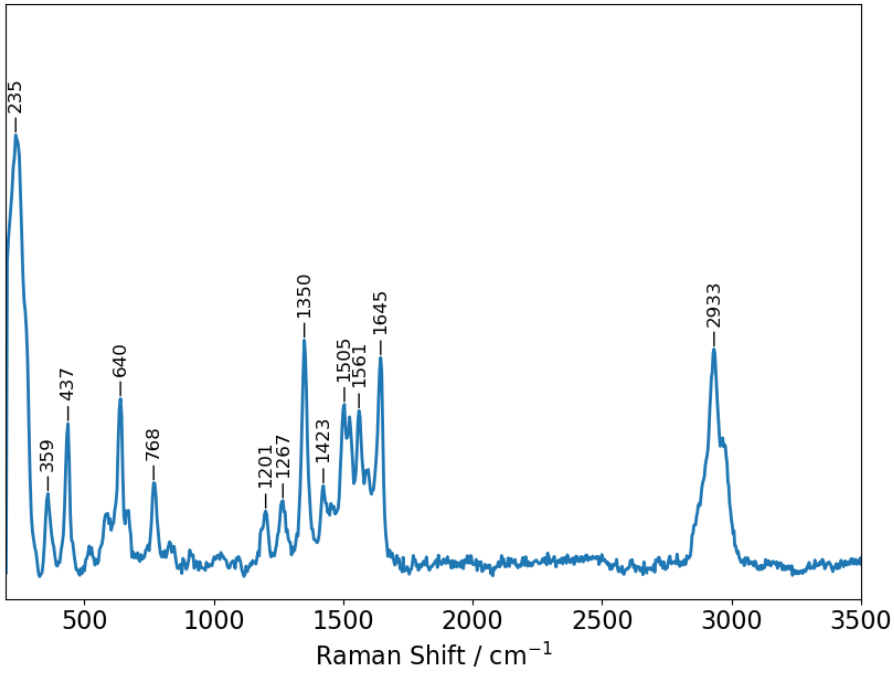

Figure A.2: Glyphosate absorbed onto the silica capped silver nanoparticle dispersion "yellow" substrate satellites at an initial concentration of 10^{-3} M. Excitation wavelength: 532 nm.

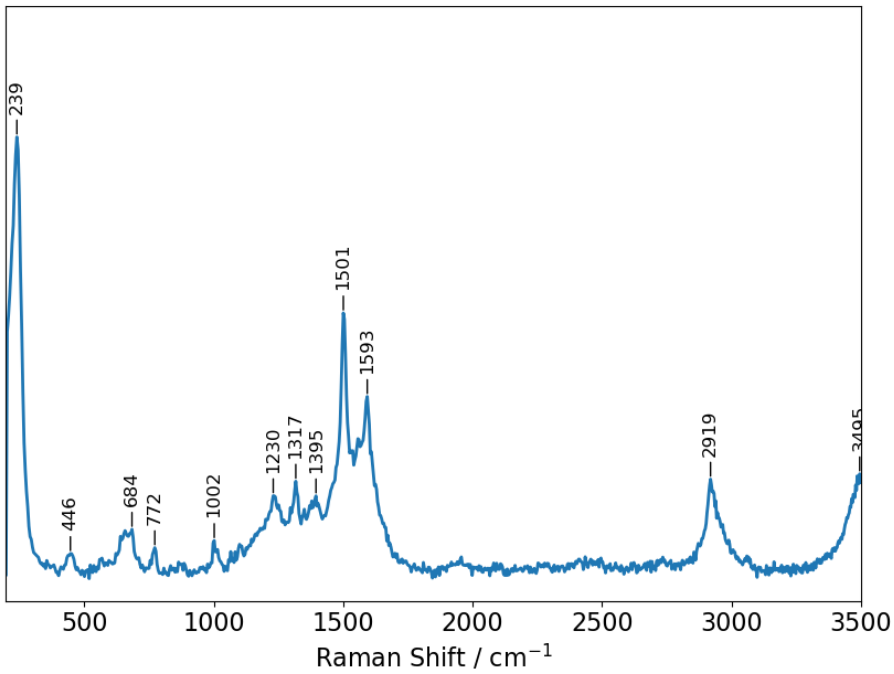

Figure A.3: Glyphosate absorbed onto the silica capped silver nanoparticle dispersion "yellow" substrate satellites at an initial concentration of 10^{-10} M. Excitation wavelength: 532 nm.

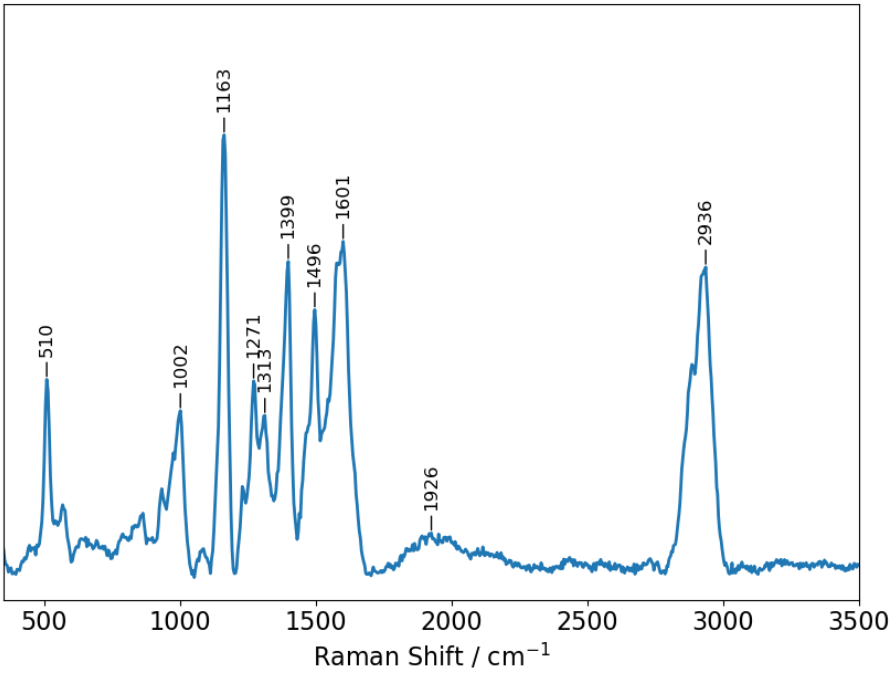

Figure A.4: Glyphosate absorbed onto the silica capped silver nanoparticle dispersion "yellow" substrate satellites at an initial concentration of 10^{-9} M. Excitation wavelength: 532 nm.

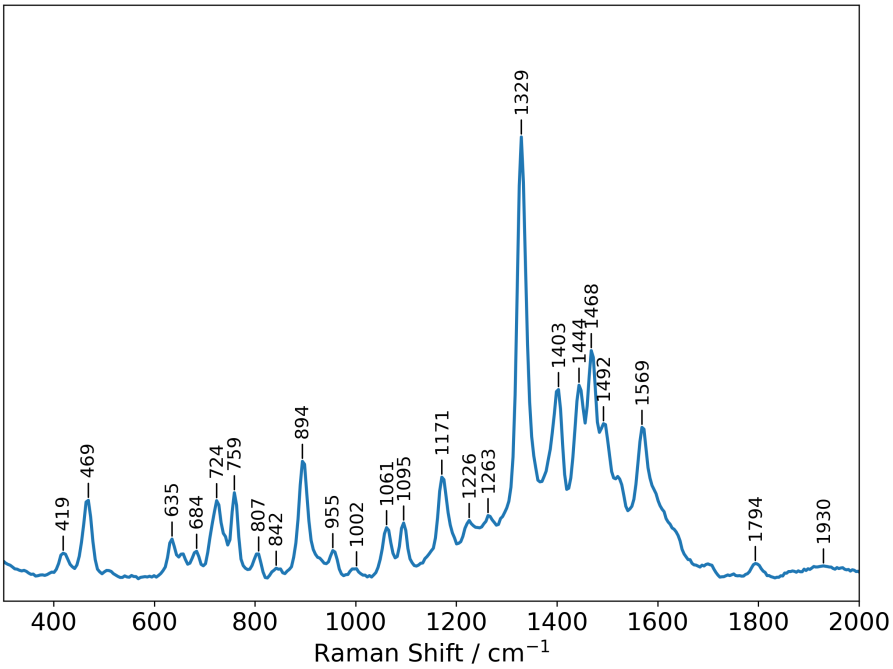

Figure A.5: Glyphosate absorbed onto the silica capped silver nanosphere substrate satellites at an initial concentration of 10^{-10} M. Excitation wavelength: 532 nm.

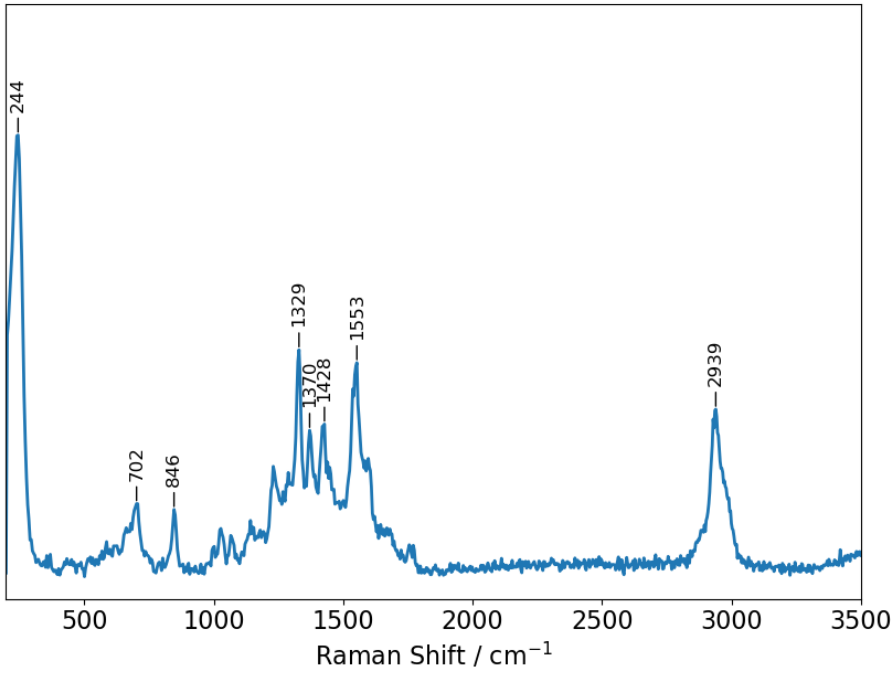

Figure A.6: Glyphosate absorbed onto the silver nanospheres substrate at an initial concentration of 10^{-6} M. Excitation wavelength: 532 nm.

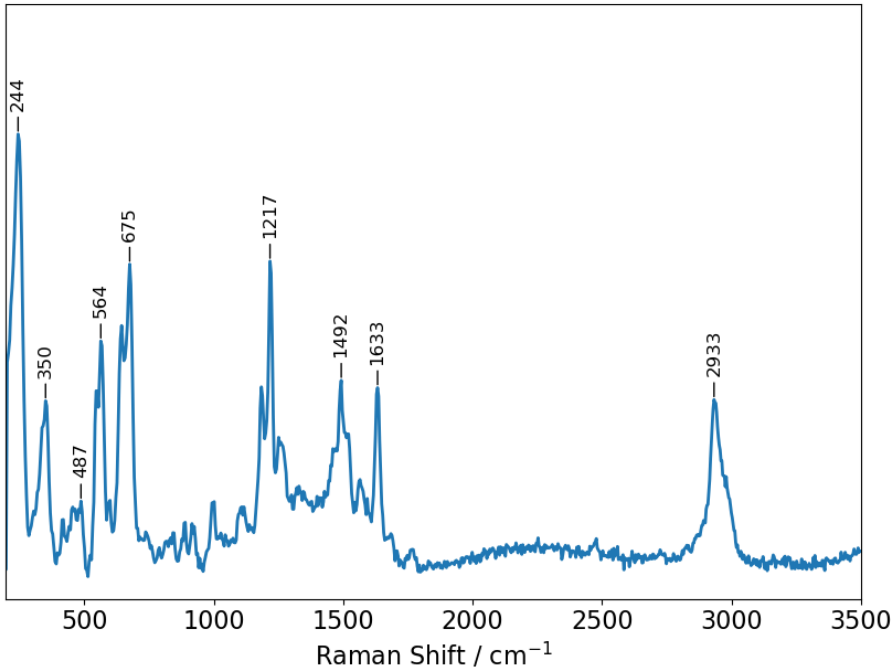

Figure A.7: Glyphosate absorbed onto the silver nanospheres substrate at an initial concentration of 10^{-11} M. Excitation wavelength: 532 nm.

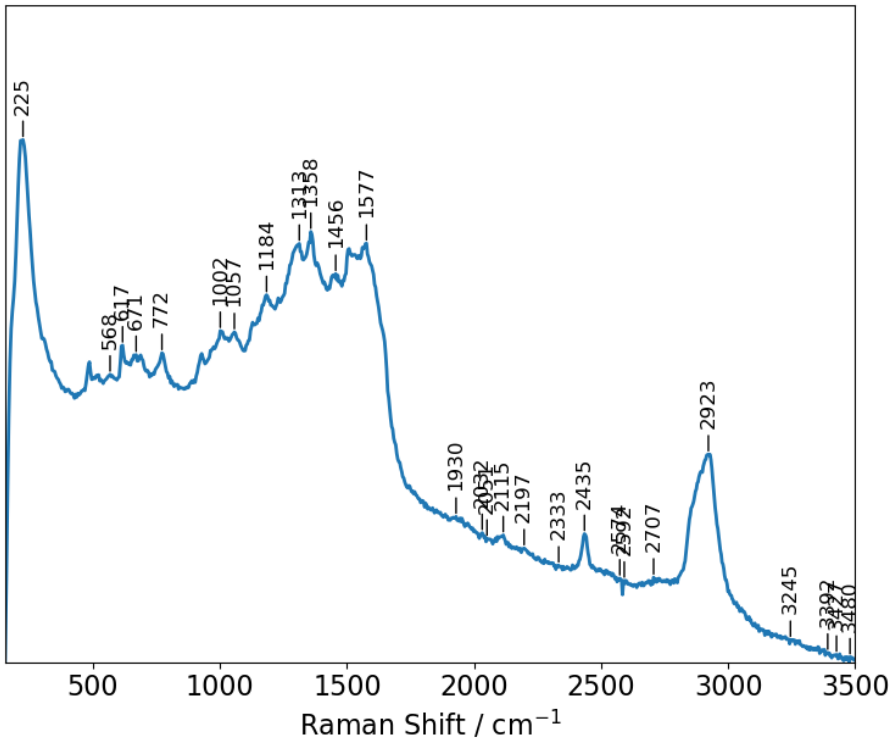

Figure A.8: Glyphosate absorbed onto the silica capped silver nanospheres substrate at an initial concentration of 10^{-10} M. Excitation wavelength: 532 nm.

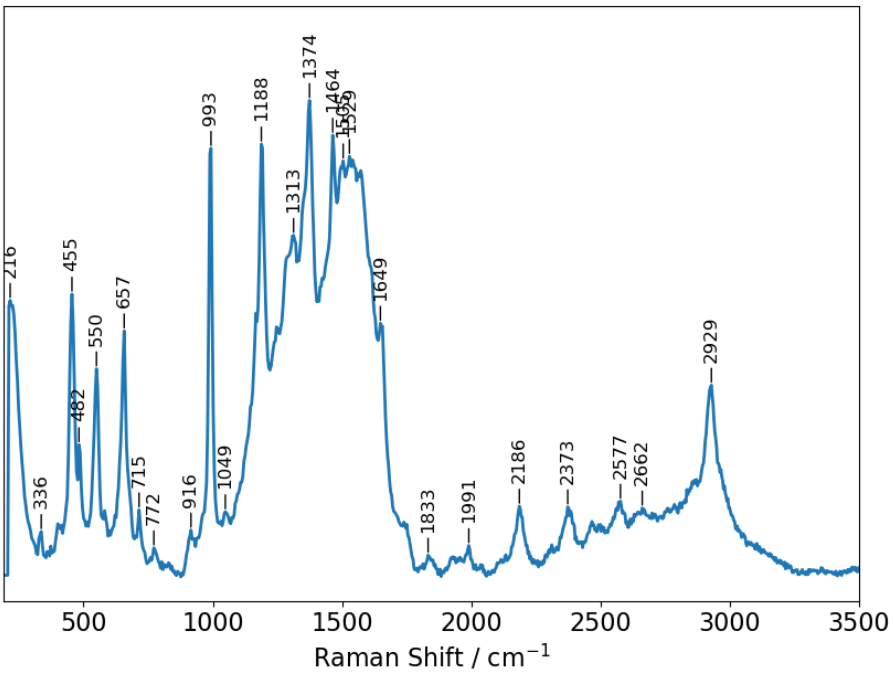

Figure A.9: Glyphosate absorbed onto the silver nanocube substrate at an initial concentration of 10^{-10} M. Excitation wavelength: 532 nm.

A.1.3 Diazinon

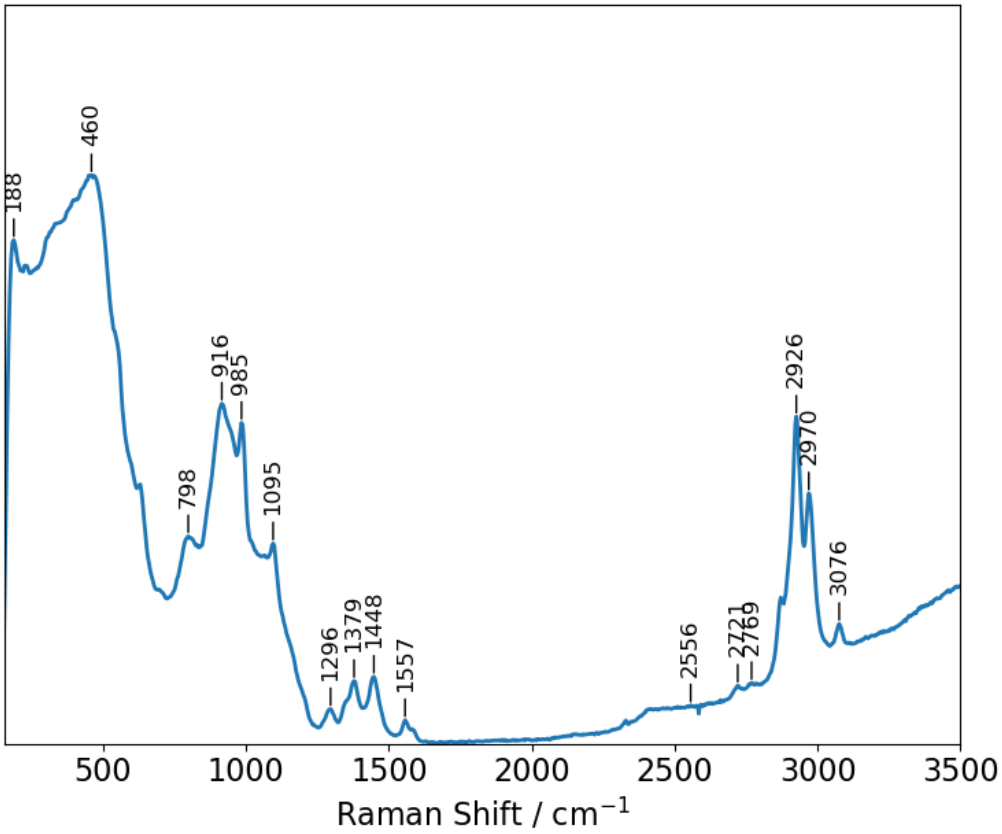

Figure A.10: A Raman spectrum of diazinon on a 532 nm incident beam, captured by using a small drop on a microcope slide.

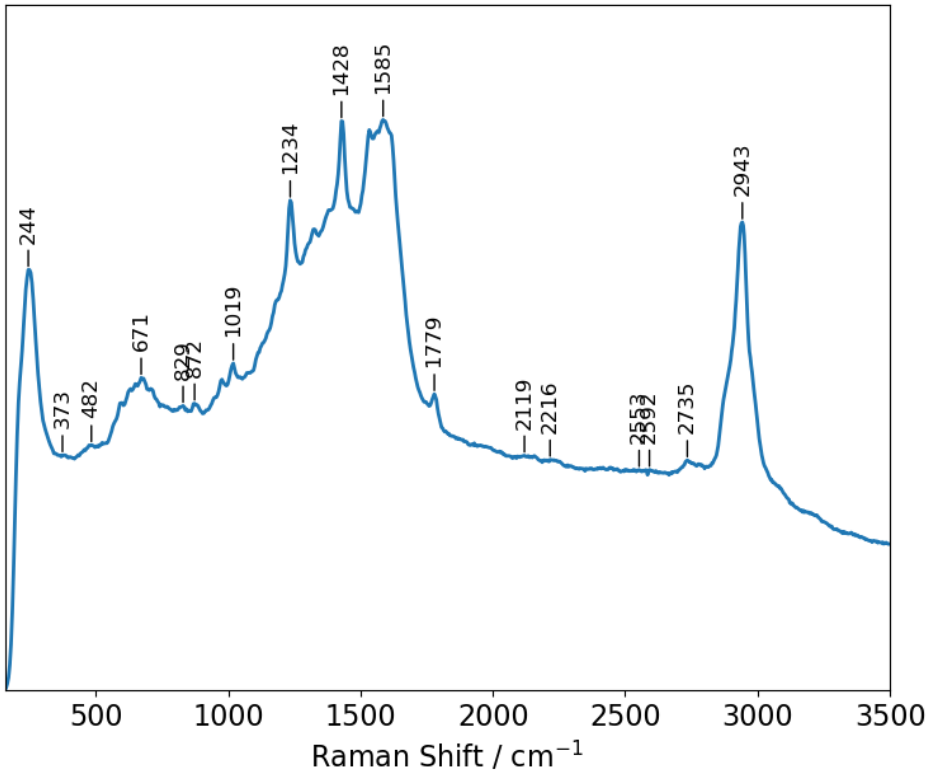

Figure A.11: Diazinon absorbed onto a "yellow" substrate at an initial concentration of 10^{-9} M. Excitation wavelength: 532 nm.

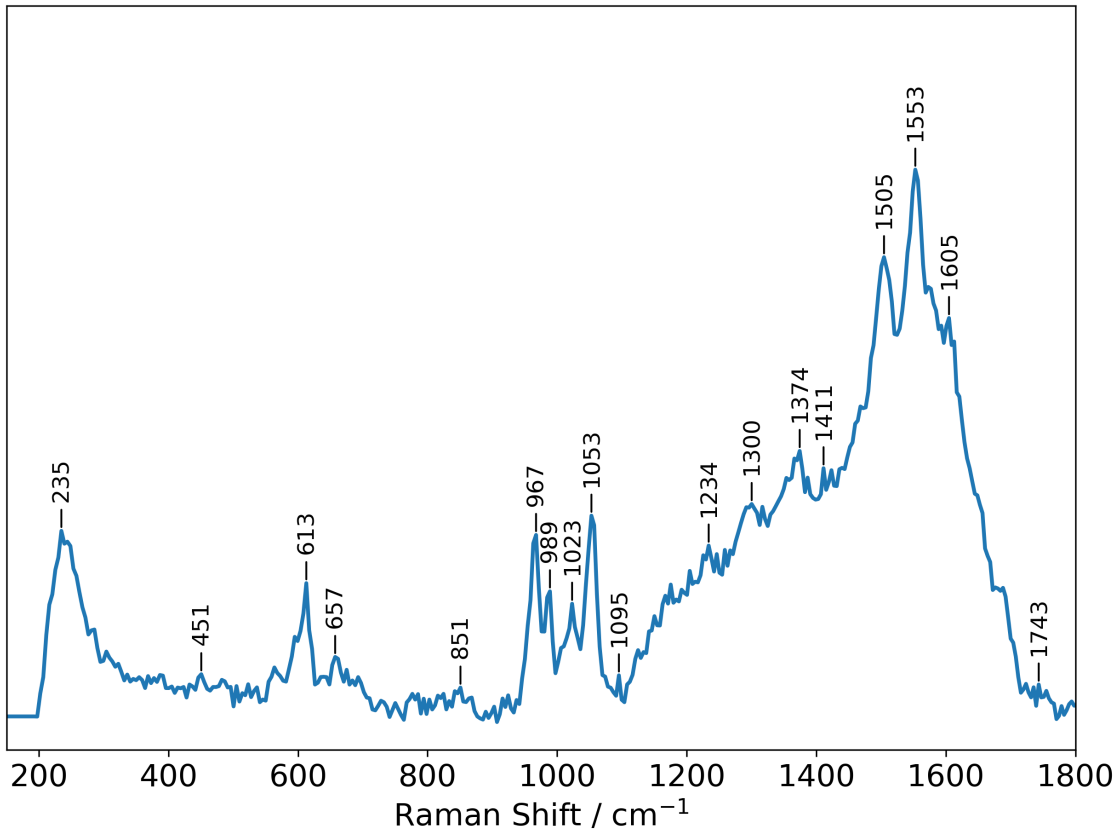

Figure A.12: Diazinon absorbed onto the silver nanoprism substrate at an initial concentration of 10^{-10} M. Excitation wavelength: 532 nm.

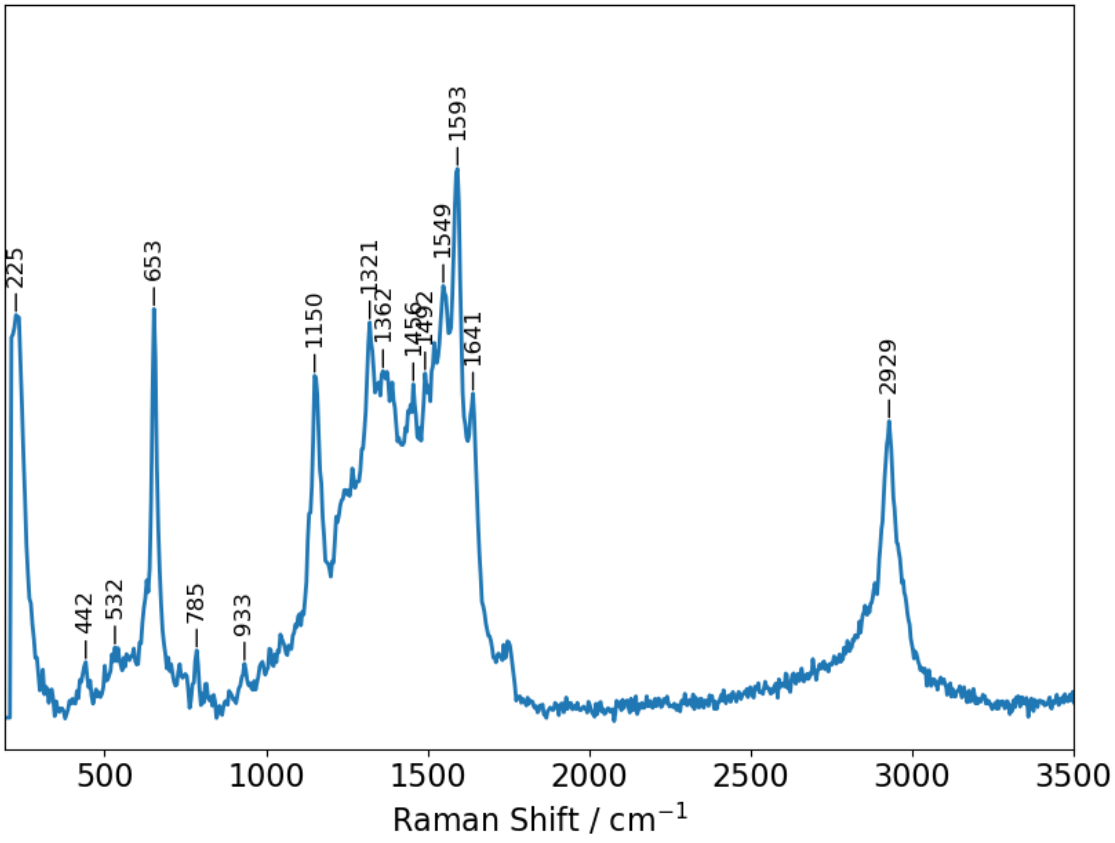

Figure A.13: Diazinon absorbed onto the silver nanocube substrate at an initial concentration of 10^{-10} M. Excitation wavelength: 532 nm.

A.2 Nanoparticle Distributions

A.2.1 All Analytes

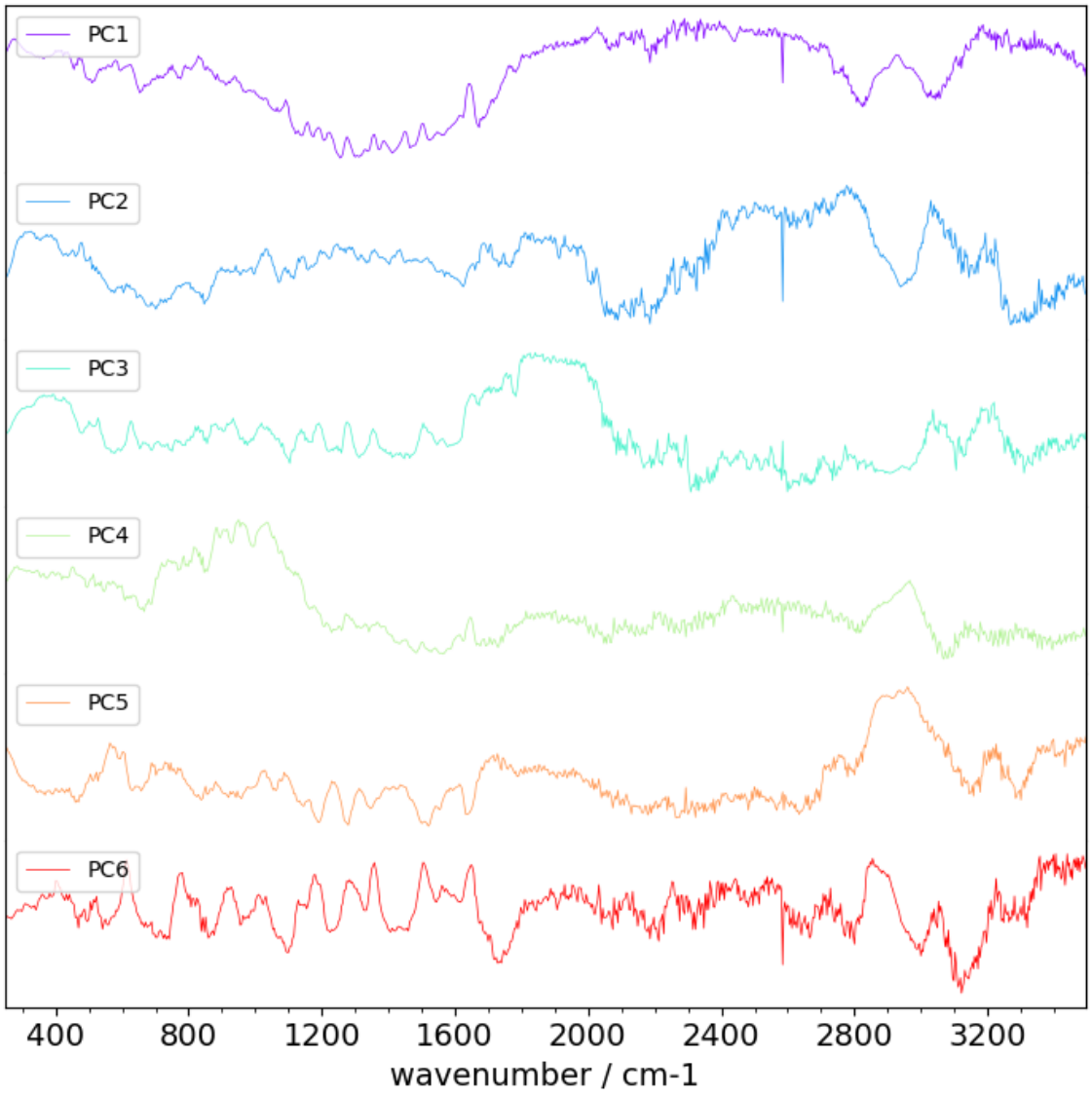

Figure A.14: Loadings plot of the SLIPSERS spectra for all analytes for each of the principle components.

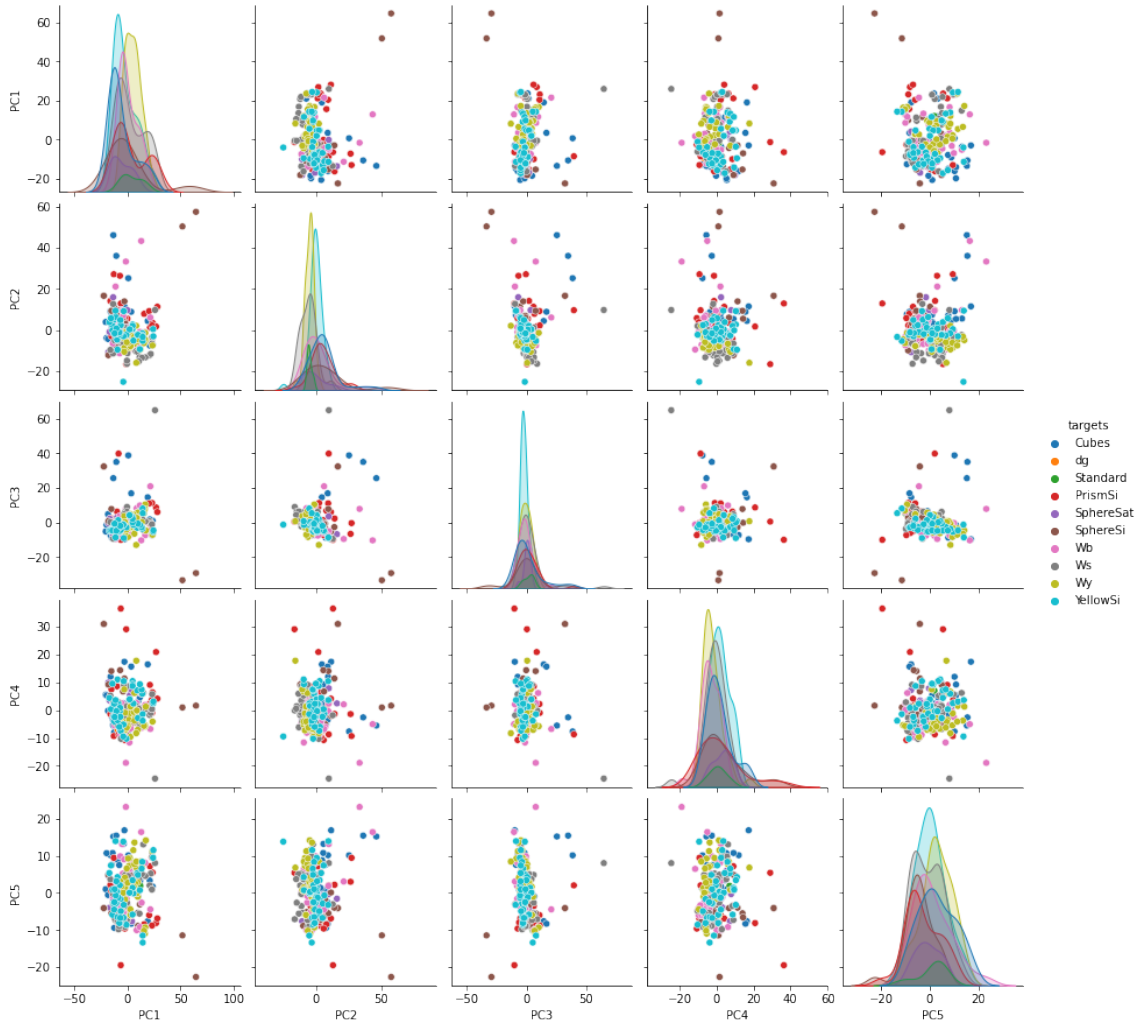

Figure A.15: For the all of the spectra, a scattermatrix plot with distribution curves and scatterplots showing the distribution of spectra by the nanoparticle type using their principle components

A.2.2 Dyes

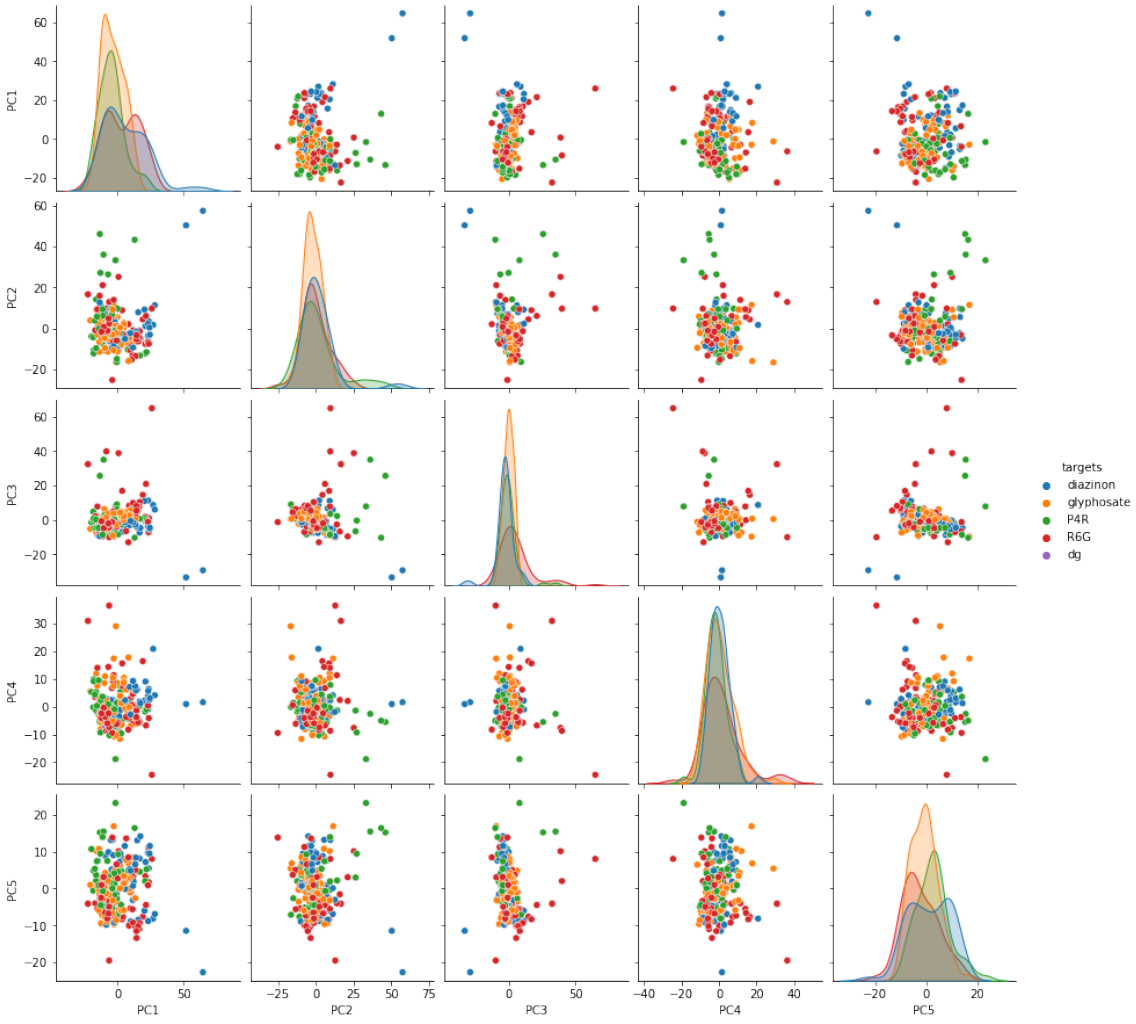

Figure A.16: For the all of the spectra, a collection of PCA scattermatrix plots with distribution curves and scatterplots showing the distribution of spectra by the analyte type by the first five principle components.

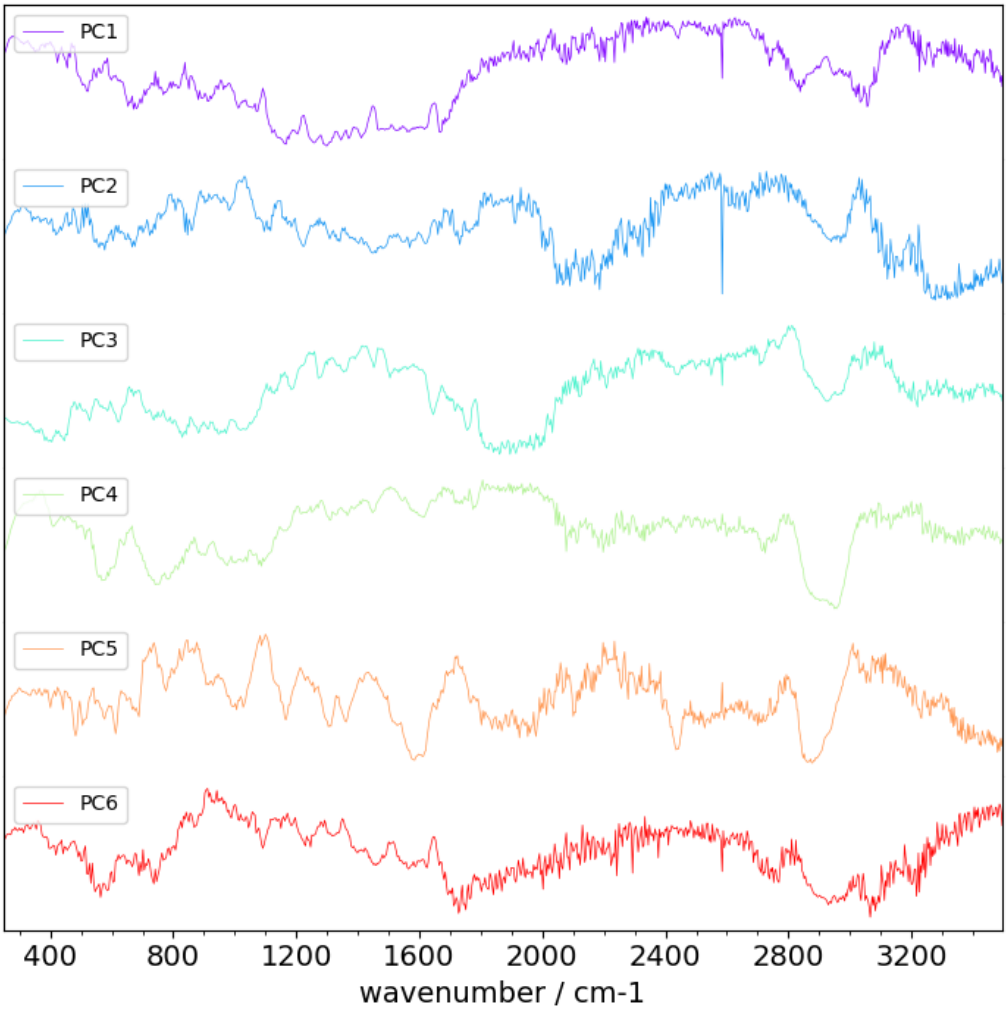

Figure A.17: For the all of the SLIPSERS spectra containing SHINs as nanoparticles, and all of the analytes a collection of loadings plots for principle components 1-5 showing which modes contribute more variation between the samples.

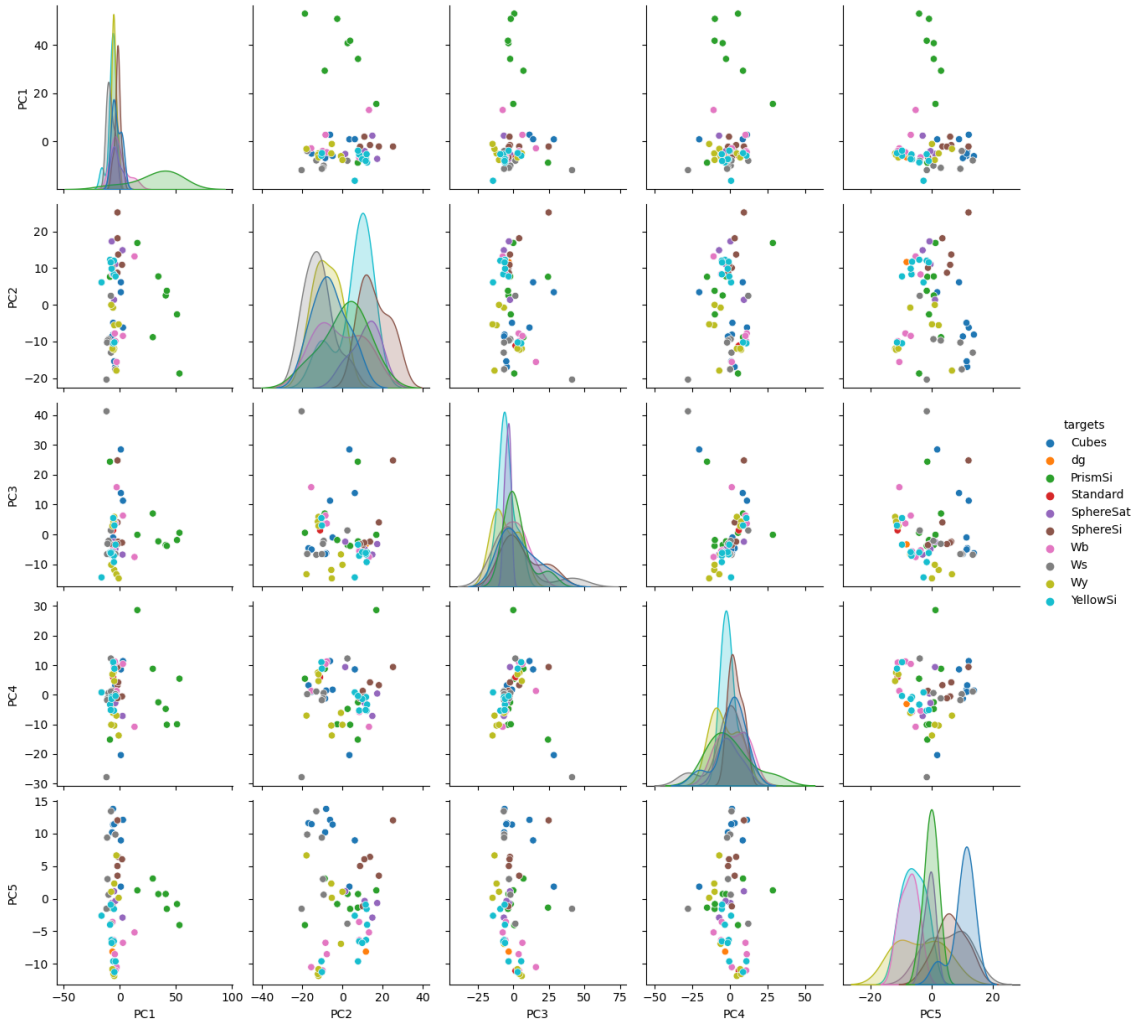

Figure A.18: For the all of the R6G spectra, a collection of PCA scattermatrix plots with distribution curves and scatterplots showing the distribution of spectra by the nanoparticle type by the first five principle components.

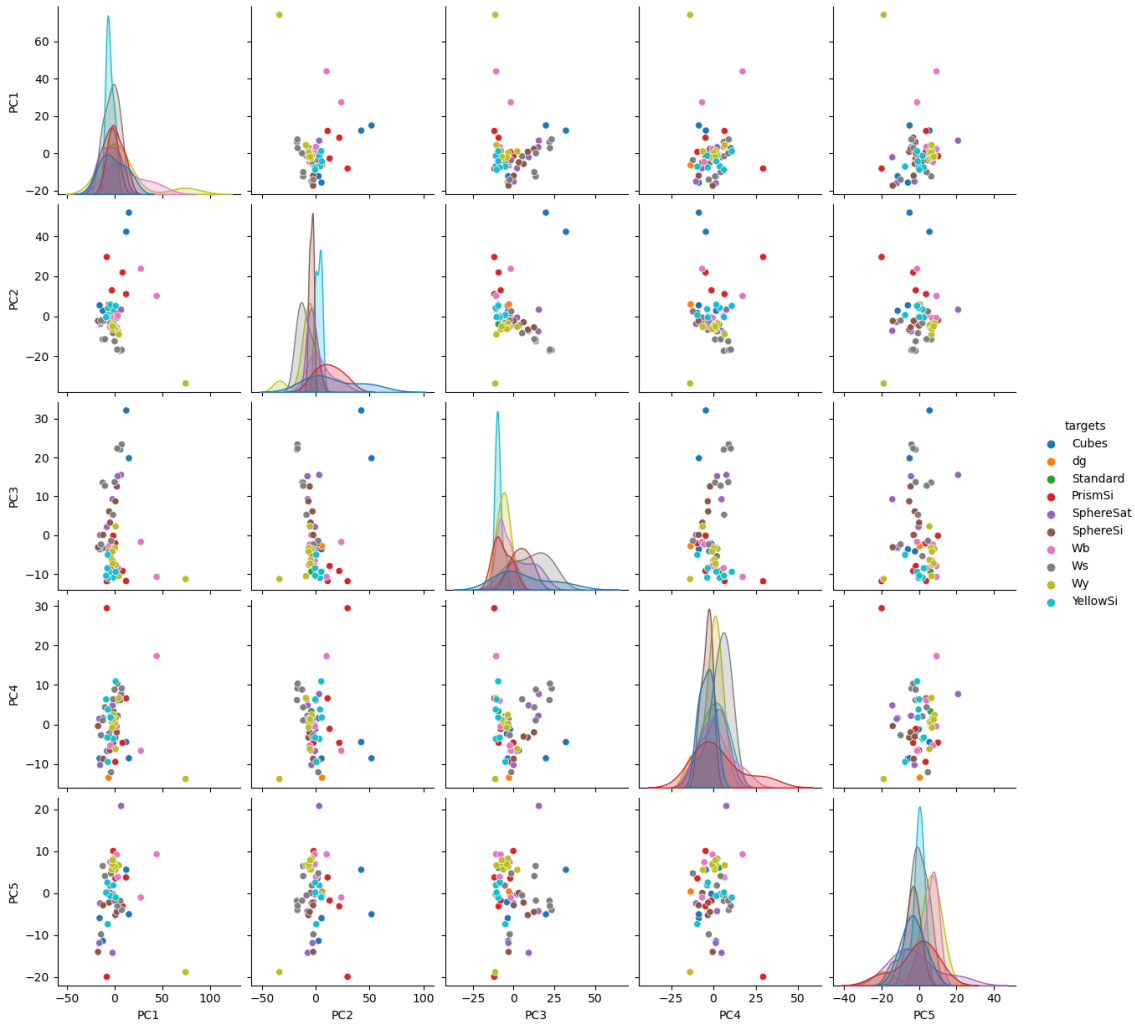

Figure A.19: For the all of the P4R spectra, a collection of PCA scattermatrix plots with distribution curves and scatterplots showing the distribution of spectra by the nanoparticle type by the first five principle components.

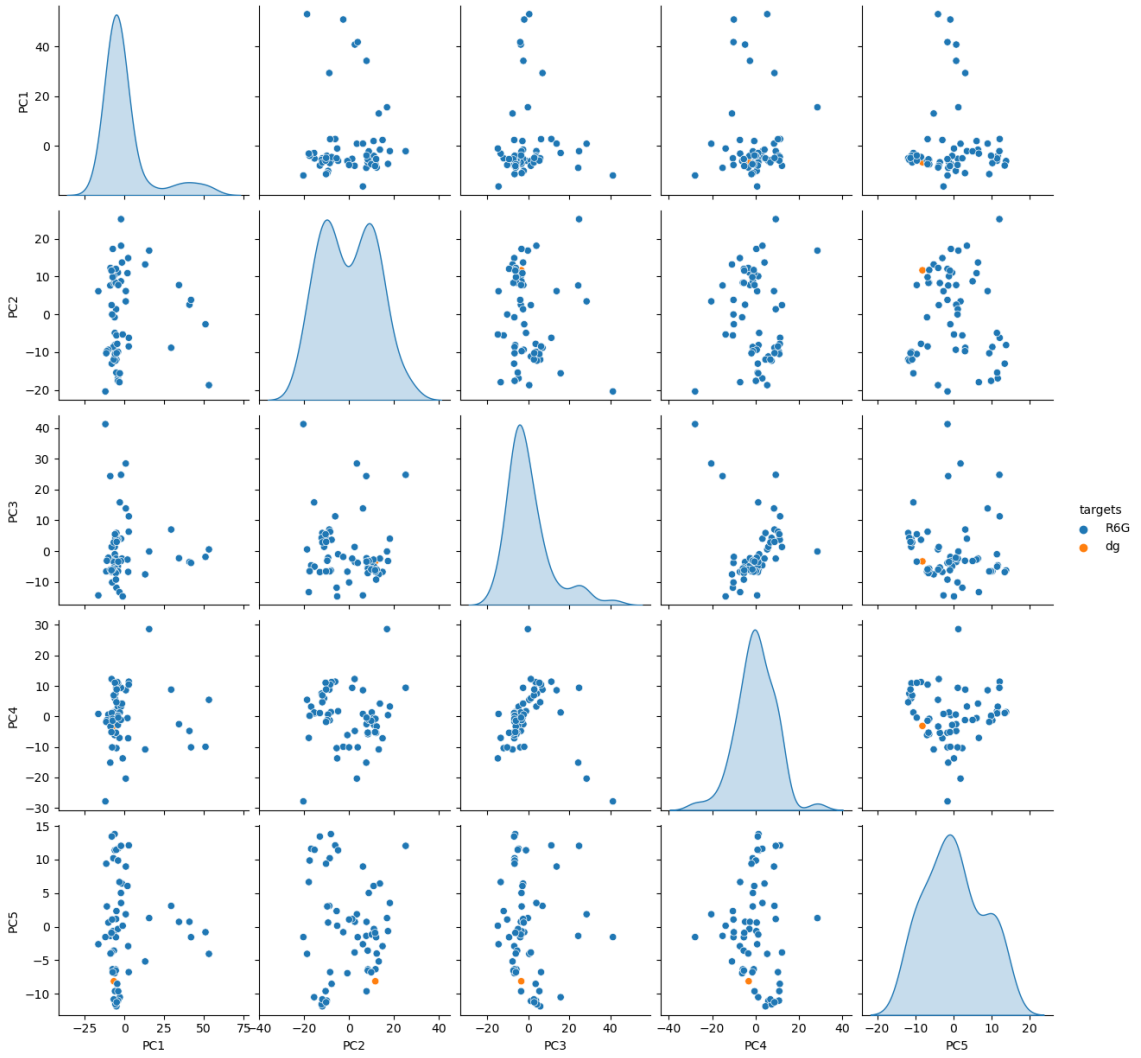

Figure A.20: For the R6G, a scattermatrix plot with distribution curves and scatterplots showing the distribution of spectra by the analyte type using their principle components.

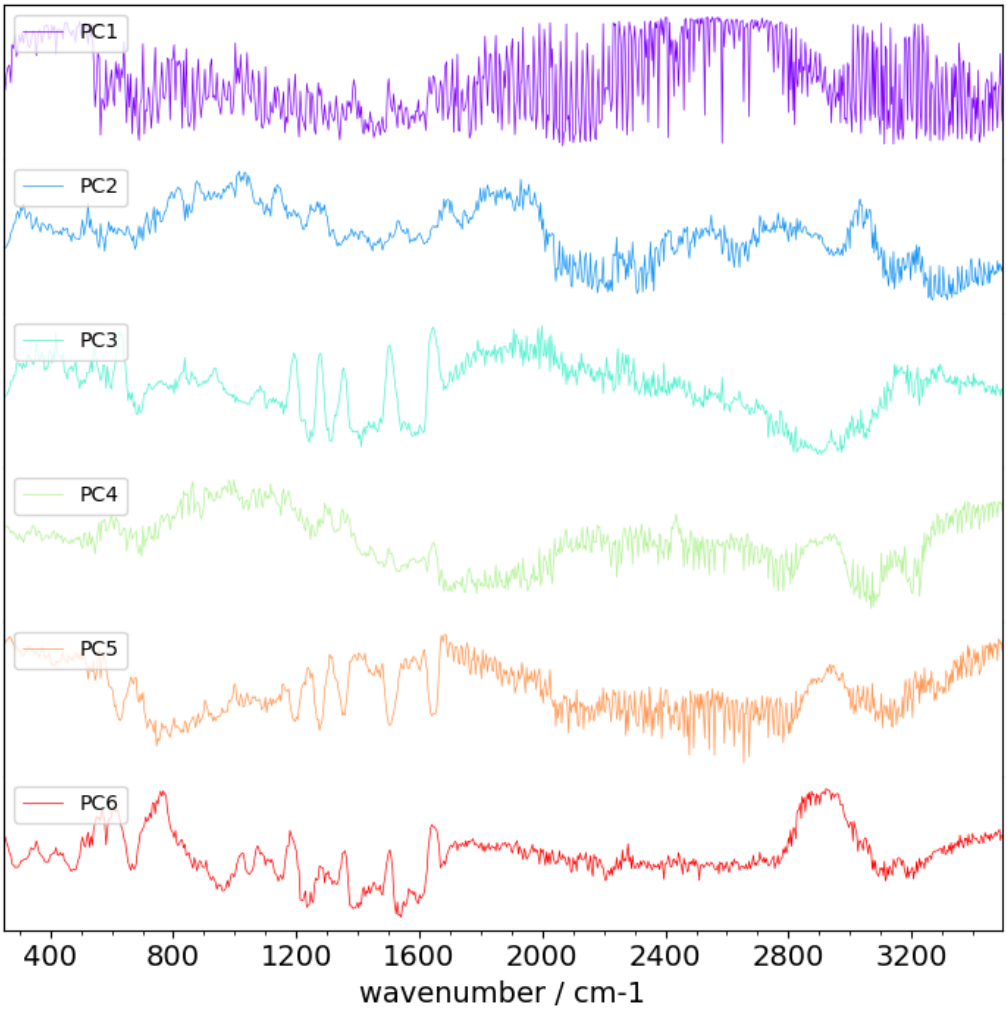

Figure A.21: For the all of the SLIPSERS spectra containing SHINs as nanoparticles, and all of the dyes as analytes, a collection of loadings plots for principle components 1-5 showing which modes contribute more variation between the samples.

A.2.3 Glyphosate

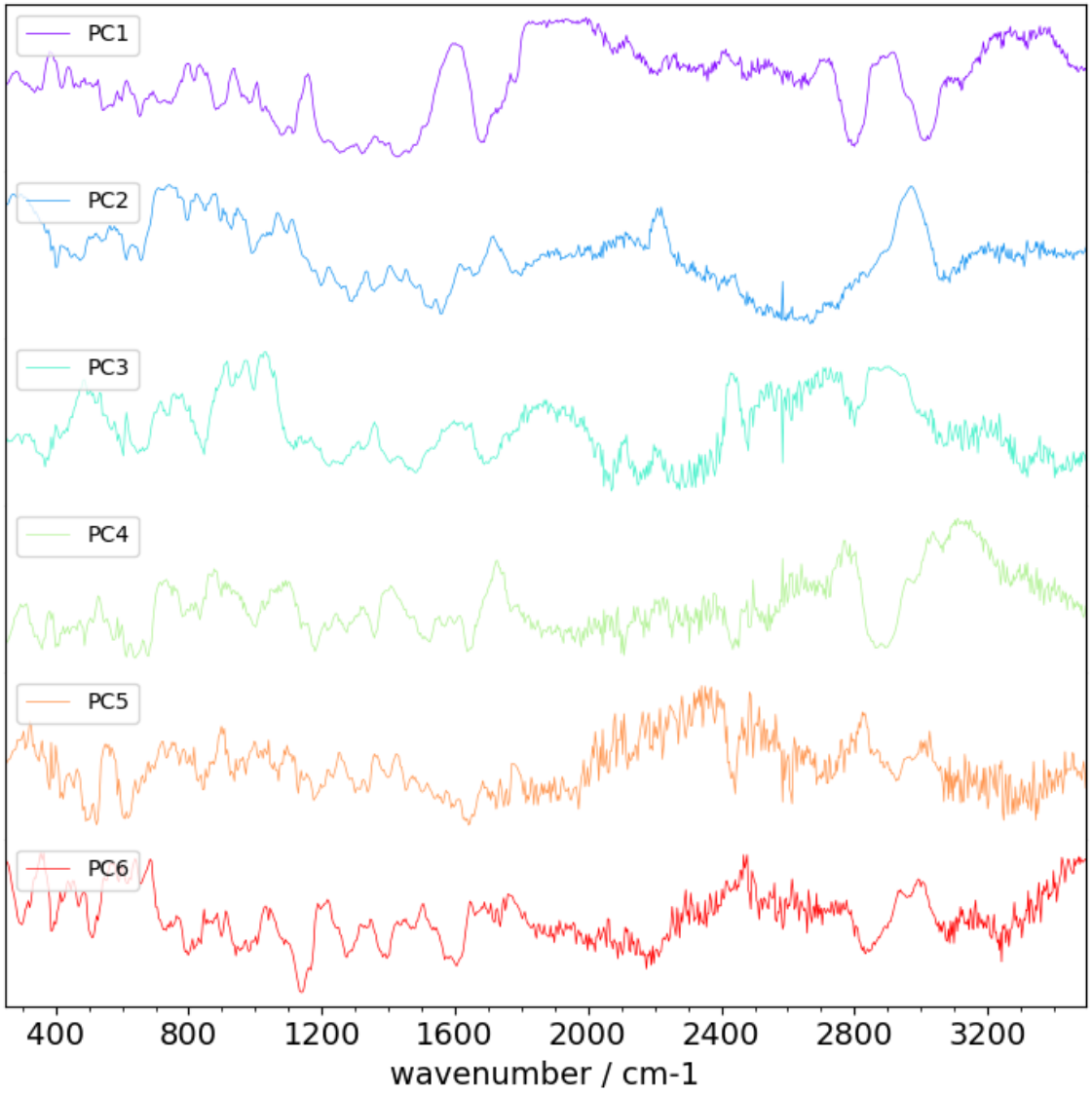

Figure A.22: Loadings plot of principle components 1 to 6 for all glyphosate spectra.

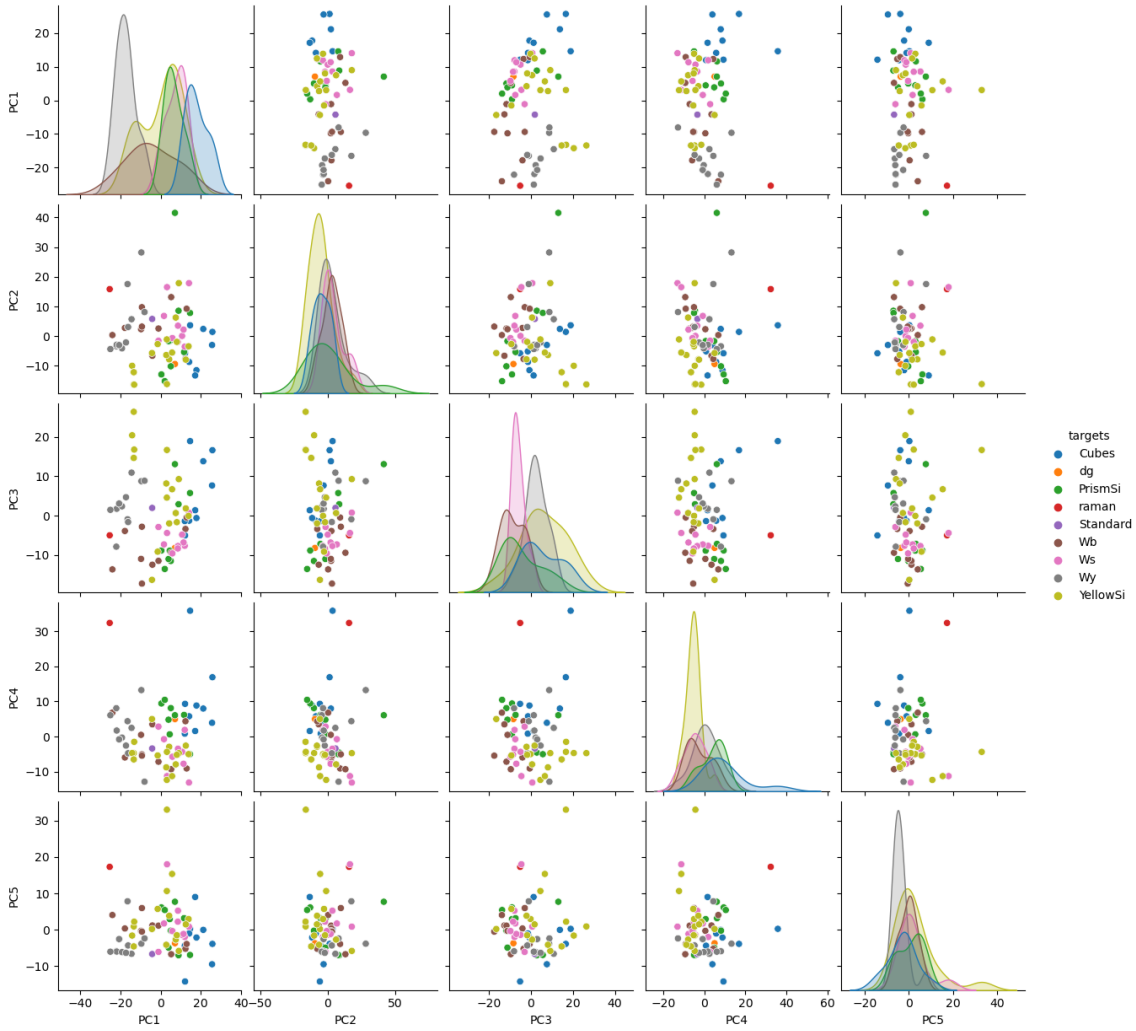

Figure A.23: For the glyphosate spectra, a scattermatrix plot with distribution curves and scatterplots showing the distribution of spectra by the nanoparticle type using their principle components

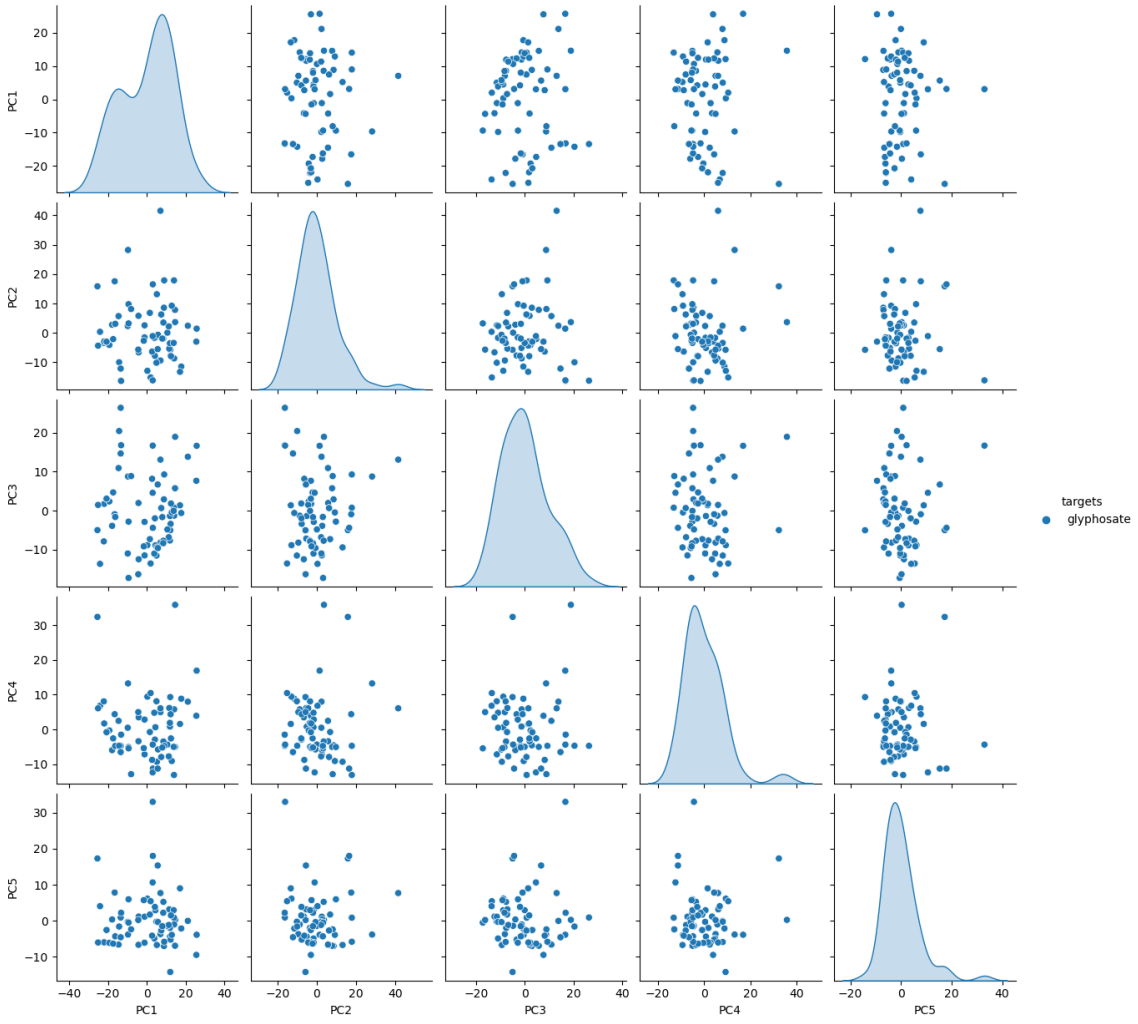

Figure A.24: For the glyphosate spectra, a scattermatrix plot with distribution curves and scatterplots showing the distribution of spectra by the analyte type using their principle components.

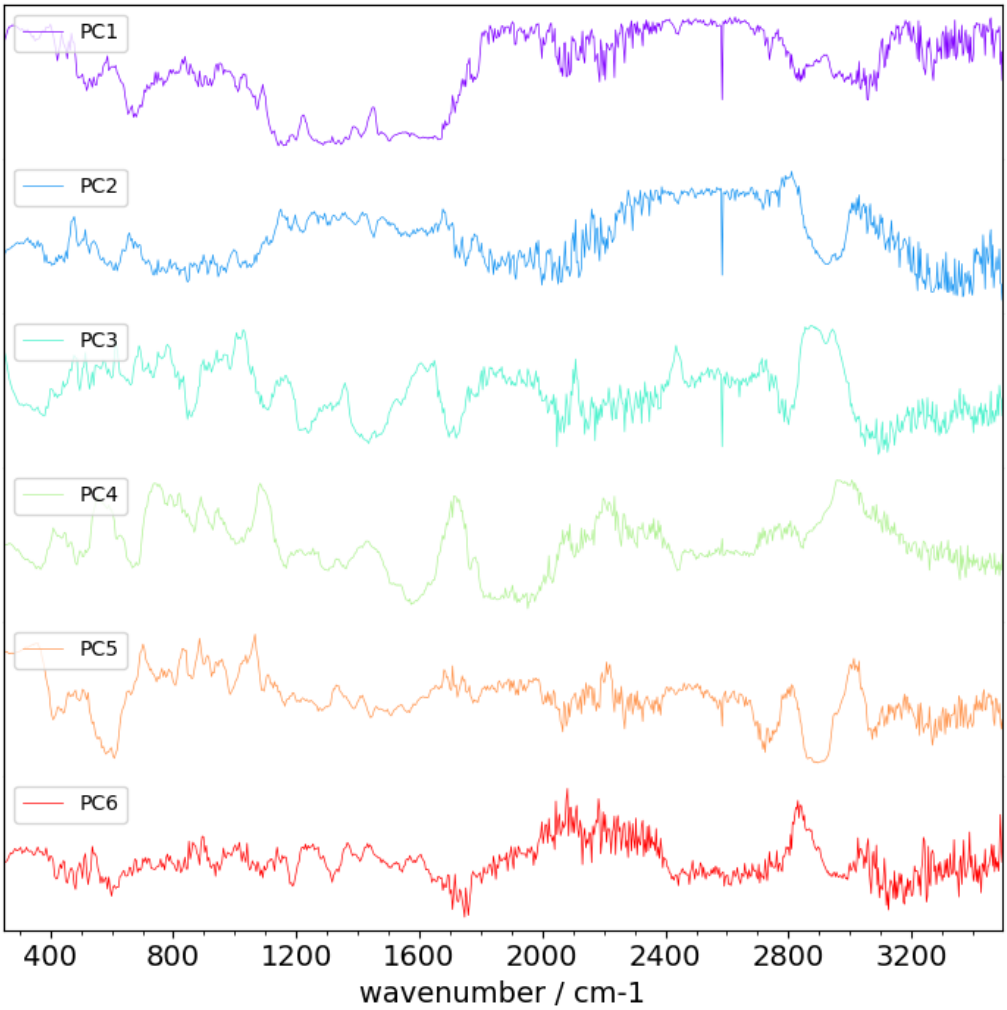

Figure A.25: For the all of the SLIPSERS spectra containing SHINs as nanoparticles and glyphosate and diazinon as analytes, a collection of loadings plots for each principle component show which modes contribute more variation between the samples.

A.2.4 Diazinon

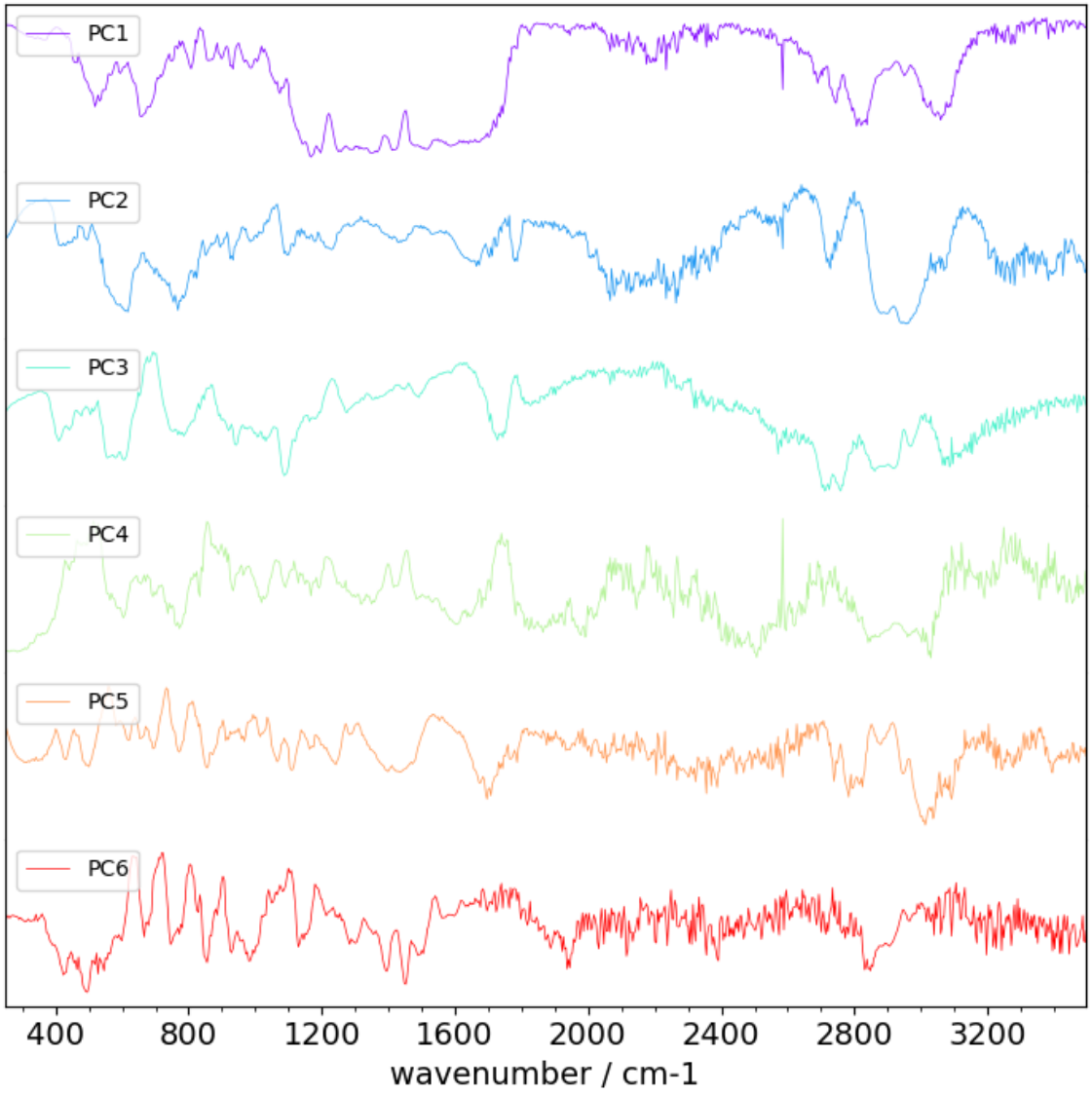

Figure A.26: Loadings plot of the SLIPSERS of diazinon for each of the principle components.

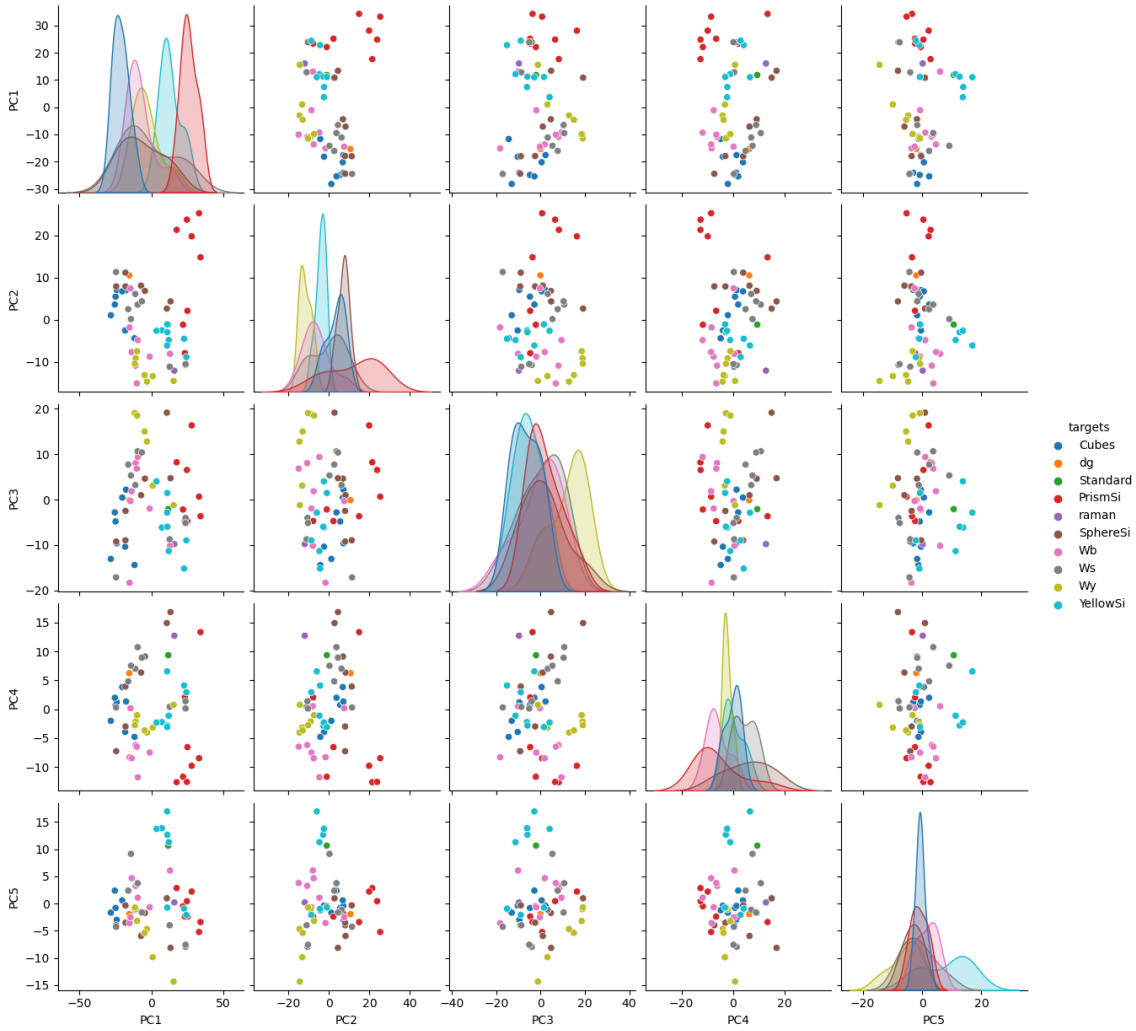

Figure A.27: For the diazinon spectra, a scattermatrix plot with distribution curves and scatterplots showing the distribution of spectra by the nanoparticle type using their principle components.

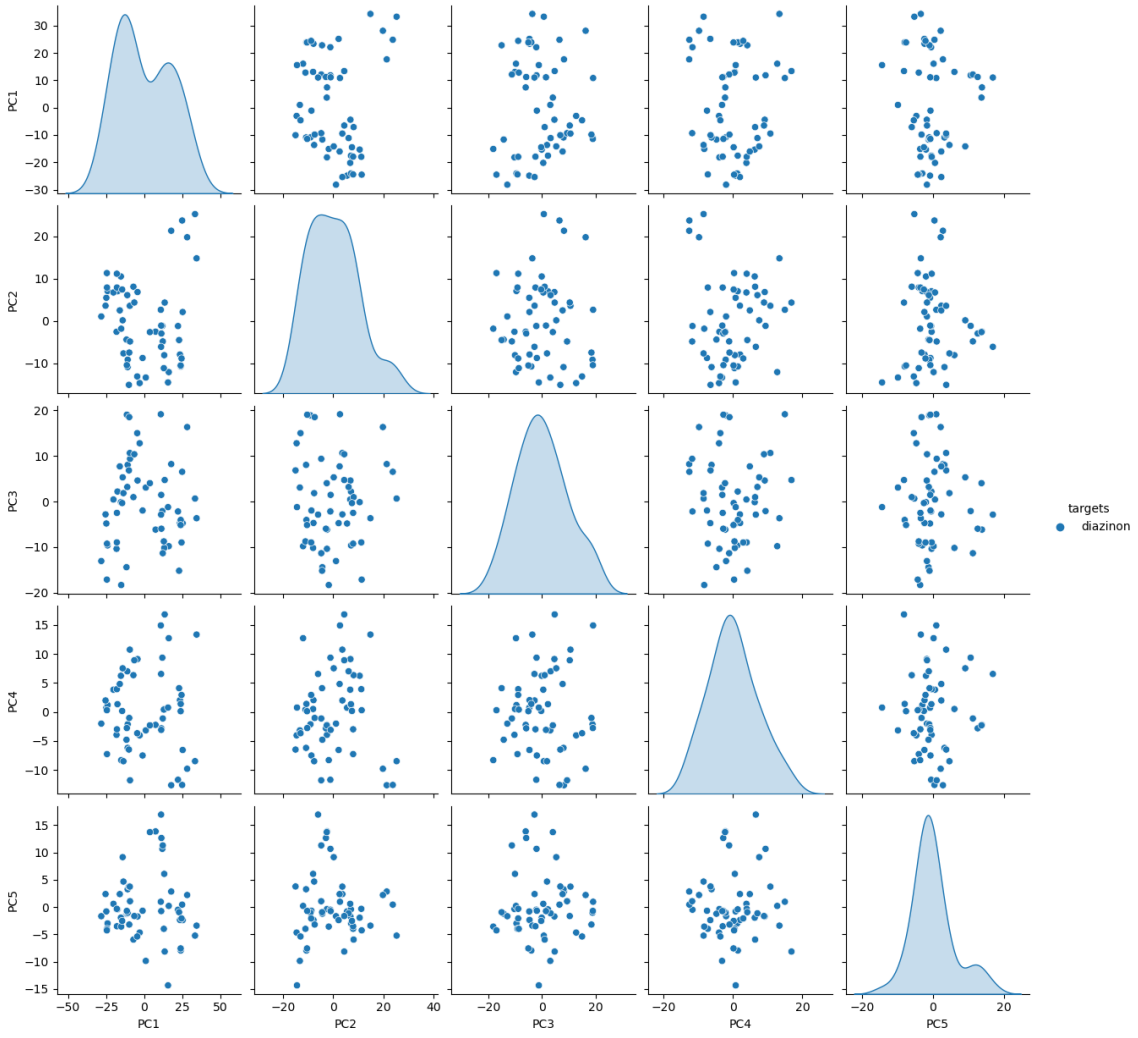

Figure A.28: For the diazinon spectra, a scattermatrix plot with distribution curves and scatterplots showing the distribution of spectra by the analyte type using their principle components.

A.3 Tables

Mode(s)	Raman Shift (cm^{-1})						
	Literature	10^{-6} M	10^{-7} M	10^{-8} M	10^{-9} M	10^{-10} M	10^{-11} M
C-C-C in-plane ring bend	612	631	631	622	671	680	671
C-H out of plane bend	774	737	737	737	710	706	–
C-H in plane bend	1185	1196	1196	1196	1129	1129	1121
Aromatic C-C stretch	1311	1284	1284	1284	1275	1271	1304
Aromatic C-C stretch	1364	1362	1362	1362	1383	1387	1342
	1510	1517	1517	1517	1581	1597	1573
	1652	1649	1649	1649	–	–	–

Table A.1: Table of modes common for each initial concentration of R6G for the silver nanocube substrate.